Characterization of HV-MAPS for the Future LHCb Downstream Tracker and Development of the DAQ System MARS

Dissertation
zur
Erlangung des Doktorgrades (Dr. rer. nat.)
der
Mathematisch-Naturwissenschaftlichen Fakultät
der
Rheinischen Friedrich-Wilhelms-Universität Bonn

vorgelegt von
Hannah Schmitz
aus
Mechernich

Bonn 2025

Angefertigt mit Genehmigung der Mathematisch-Naturwissenschaftlichen Fakultät der Rheinischen Friedrich-Wilhelms-Universität Bonn

Gutachter/Betreuer:	Prof. Dr. Sebastian Neubert
Gutachter:	Prof. Dr. Jochen Dingfelder

Tag der Promotion: 19.12.2025
Erscheinungsjahr: 2026

“When all you got to keep is strong
Move along, move along like I know ya do
And even when your hope is gone
Move along, move along just to make it through
Move along”

– The All-American Rejects

Für meine Familie

♡

Deutsche Zusammenfassung

Mit Beginn von Run 5 des LHC wird das LHCb-Experiment in die High-Luminosity Phase des LHC eintreten. Eine Erhöhung der instantanen Luminosität um eine Größenordnung von $1 \cdot 10^{33}\,\mathrm{cm}^{-2}\mathrm{s}^{-1}$ auf $1 \cdot 10^{34}\,\mathrm{cm}^{-2}\mathrm{s}^{-1}$[1] ermöglicht es im Laufe der Lebensdauer des Experiments $300\,\mathrm{fb}^{-1}$ an Daten zu sammeln. Mit den gesammelten Daten kann das Flavor-Physik Potenzial von LHCb voll ausgeschöpft werden, um Physik jenseits des Standardmodells zu erforschen und Observablen mit bisher unerreichter Präzision zu vermessen.
Infolgedessen wird die Anzahl der Proton-Proton Wechselwirkungen innerhalb einer Strahlkreuzung von 6 auf 40 erhöht. Eine effiziente Spurrekonstruktion in einer stark strahlungsbelasteten Umgebung ist entscheidend, um die Leistung des Detektors zu erhalten und sogar zu verbessern. Daher werden mit Beginn des Long Shutdown 4 alle Subdetektoren einer umfassenden Aufrüstung unterzogen. Strahlungstolerante Technologien, die präzise Zeitinformation mit hoher Granularität bereitstellen, sind vorgesehen.
Ein Schlüsselelement wird der neue Downstream-Tracking-Detektor, genannt Mighty-Tracker, sein. Dieser besteht im zentralen Bereich nahe des Strahlrohrs aus einem monolithischen Pixeldetektor, namens Mighty-Pixel, und im äußeren Bereich aus einem Szintillationsfaserdetektor, namens Mighty-SciFi. Diese hybride Lösung garantiert eine hohe Granularität, Strahlungstoleranz und Zeitauflösung bei gleichzeitig kosteneffizientem Aufbau. Für den Mighty-Pixel sind High-Voltage Monolithic Active Pixel Sensors HV-MAPS vorgesehen, die erstmals am Karlsruher Institut für Technologie [2] entwickelt wurden. Der finale Sensor, genannt MightyPix, wird auf der Entwicklung vorheriger HV-MAPS aufbauen, die für die Experimente Mu3e [3] und ATLAS [4] entwickelt wurden. Folgende Anforderungen sind zwingend erforderlich, um einen effizienten Langzeitbetrieb des Detektors zu gewährleisten: Eine Strahlungstoleranz bis zu einer Fluenz von $3 \cdot 10^{14}\,\mathrm{MeVn_{eq}cm}^{-2}$ und 40 MRad bei einer Zeitauflösung von ≤ 3 ns sowie einer Detektionseffizienz von ≥ 99 % [5].
Die Charakterisierung von HV-MAPS-Prototypen, insbesondere des TelePix2-Sensors [6], mit Fokus auf Performanzstudien ist eines der Hauptthemen dieser Arbeit. Zur Durchführung dieser Studien wurde ein neues Auslesesystem entwickelt, das für die Evaluierung von HV-MAPS im Labor und an Teststrahlanlangen unerlässlich ist. Die Entwicklung und Inbetriebnahme des Mighty ASIC Readout Systems MARS [7] bildet das zweite Hauptthema dieser Arbeit. Untersuchungen zur Leistungsfähigkeit von HV-MAPS mit Schwerpunkt auf deren Zeitauflösung, Sperrspannungsverhalten und Detektionseffizienz in Abhängigkeit verschiedener Arten von Strahlenschäden werden präsentiert. Zu diesem Zweck wurden mehrere Bestrahlungskampagnen am isochronen Zyklotron in Bonn sowie an einer Röntgenröhre durchgeführt. Die

durchgeführten Messverfahren und die erzielten Ergebnisse werden im Hinblick auf die Anforderungen des Mighty-Pixel diskutiert.
Als zentrales Ergebnis konnte die Zeitauflösung im Hinblick auf die Strahlungstoleranz untersucht werden. Von allen evaluierten Sensoren wurde die geforderte Zeitauflösung von ≤ 3 ns erfüllt. Ebenso wurde eine Detektionseffizienz von ≥ 99 % bis zu einer Fluenz von $1 \cdot 10^{14}\,\mathrm{MeVn_{eq}cm^{-2}}$ und einer Dosis von 40 MRad für den TelePix2 Sensor gemessen, was die Eignung von HV-MAPS für den Einsatz im Mighty-Pixel demonstriert.

Abstract

By the beginning of Run 5 of the Large Hadron Collider, the LHCb experiment will enter the High-Luminosity LHC era. An increase by one order of magnitude of the instantaneous luminosity from $1 \times 10^{33}\,\mathrm{cm^{-2}s^{-1}}$ to $1 \times 10^{34}\,\mathrm{cm^{-2}s^{-1}}$ [1] will allow the collection of $300\,\mathrm{fb^{-1}}$ data over the lifetime of the experiment. The collected data enables the LHCb experiment to fully exploit its flavor physics potential, exploring physics beyond the Standard Model of particle physics and probing observables with unprecedented precision.
As a consequence, the number of proton-proton interactions per bunch crossing will increase from 6 to 40. Efficient particle tracking in a harsh radiation environment is crucial to maintain and even improve the detector's performance. Therefore, all sub-detectors will undergo a major upgrade with the beginning of Long Shutdown 4. Radiation tolerant technologies, providing precise time information with high granularity are essential.
A key element will be the new downstream tracking detector, referred to as Mighty-Tracker, consisting of a monolithic pixel detector, called Mighty-Pixel, in the innermost region close to the beam-pipe and a scintillating fiber detector, called Mighty-SciFi, in the outermost region. The hybrid solution offers high granularity, radiation tolerance and timing information while being cost-effective.
For the Mighty-Pixel detector High-Voltage Monolithic Active Pixel Sensors, invented at the Karlsruher Institut für Technologie [2], are planned to be installed. The production sensor, MightyPix, will inherit the development of predecessor HV-MAPS designed for the Mu3e [3] and ATLAS [4] experiments. The following requirements are mandatory to ensure an efficient long-term operation of the detector: A radiation tolerance up to a fluence of $3 \times 10^{14}\,\mathrm{MeVn_{eq}cm^{-2}}$ and 40 MRad with a time resolution of ≤ 3 ns and hit-efficiency of $\geq 99\%$ [5].
Characterization of prototype HV-MAPS, mainly the TelePix2 sensor [6], with focus on performance studies is one of the main topics of the presented thesis. To perform those, a new Data Acquisition System, mandatory for the evaluation of HV-MAPS in a laboratory and testbeam environment, has been developed. The development and commissioning of the Mighty ASIC Readout System MARS [7] is the second topic of this thesis.
Investigations of the performance of HV-MAPS, with emphasis on their time resolution, bias behavior and hit-efficiency in dependence of different kinds of radiation damage, will be presented. Therefore, several irradiation campaigns have been performed at the Bonn isochronous cyclotron and at a x-ray tube. Measurement procedures and obtained results will be discussed with respect to the Mighty-Pixel requirements.

As a main result, the time resolution has been probed in terms of radiation tolerance. For all evaluated sensors the required time resolution of ≤ 3 ns could be fulfilled. In addition, a hit-efficiency of $\geq 99\%$ up to a fluence of $1 \times 10^{14}\,\mathrm{MeV n_{eq} cm^{-2}}$ and a dose of 40 MRad has been confirmed for TelePix2 - demonstrating the viability of HV-MAPS for the Mighty-Pixel.

Acknowledgments

Five years ago I started as the first student at the Bonn LHCb group - young and full of enthusiasm to characterize the MightyPix sensor. When Sebastian offered me this Master Project, I had no idea what to expect and which direction the project would take. It turned out to be a turbulent journey with many ups and downs or, in this case, a lot of downs, but finally great ups.
Now, while writing my thesis and finishing the journey, I reflect all the help I got from so many people over the last years and it is time to say thank you.
First of all, I have to thank you, Sebastian, not only for the chance to do my PHD in your group, but also for the possibilities I got. Besides of developing my knowledge about detector physics, you offered me the chance to participate at unforgettable international conferences and supported my personal development. I always had the autonomy to decide how to determine the direction of each project - a privilege I appreciate a lot. Moreover, you always kept an eye on non-forgetting the physics of LHCb.
Secondly, I want to thank Prof. Dr. Jochen Dingfelder for reviewing my thesis as the second reviewer. At each step in my studies, I asked you for a project. However, I never made it into your group, but due to the similarities to your research projects, I had great discussions with your group members.
At this point I would like to thank the SiLab crew, especially Christian Bespin and Lars Schall, who always tried to answer my questions.
Next, I want to thank PD Dr. Bastian Kubis and Prof. Dr. Björn Krüger for agreeing to review my thesis.

The whole project would not be there without Klaas Ole Padeken (you know how much I appreciate middle names). We started together in Sebastian's group, not knowing each other and without a real idea about the Mighty-Tracker, but we managed to get our feet into the project and not only got good colleges but even friends. I remember many, I mean MANY (!), frustrating moments sitting in the laboratory trying to develop MARS's firmware, configuring sensors, trying to understand the sensor documentation, discussing late in the evenings or on weekends, but in the end we did it. Once we got MARS running and performed first measurements, our progress speed up immensely. I have to thank you not only for the physics knowledge you shared with me, but also for our great discussions, coffee breaks, lunch break discussions, a really good cheese fondue dinner and many more. Moreover, we survived in total four testbeam campaigns without serious damage - a great success. Besides, I could

learn many words of wisdom from you. Unfortunately, I have no space to write all of them down, but there is one I have to share: ”Drei Meter vorm Klo scheißt du dir auch nicht mehr in die Hose”. That being said - I will finish my thesis.
Reflecting discussions, not only about physics, I want to thank my PHD mates in Bonn: Elli, Piet, Kai, Henry, Niclas and non-forgettable Mindaugas. It was a great pleasure to work together with you. We not only shared a lot of time and frustration together at the University, but also had great times outside at team building events - latest at the Bobby Car Race. Do not forget to inform me next year - I am ready to win. We should bring a penguin as mascot.
Further, I would like to thank all Bachelor and Master students who joined the group in the past. Without your researches, many parts of the project would not have been possible.
At this point I have to thank the FTD ELAB crew, the HISKP cyclotron crew, our radiation safety officers and the FTD staff who helped at various points over the last years - in particular, Dennis Sauerland and Marco Vogt. Without you, none of the irradiation campaigns would have been possible.

Gathering knowledge about HV-MAPS would not have been possible without the help of Toko Hirono, Ivan Péric, Lennart Huth, Jan Hammerich and Lucas Dittmann. Discussions with you were really helpful and crucial for the project.
In that manner, I want to thank the whole Mighty-Sensor team and especially our conveners Sebastian Bachmann and Atanu Modak. It was a pleasure to present my work at weekly meetings and discuss results and ideas with you. Also the testbeam campaigns have been more than just a collaborative experience, where I quite literally grew up - since I ate more than just a children’s meal - one of my favorite jokes from you, Sebastian.
It still impresses me how many Haribos a person can eat within a day, Jonas. Thanks to you and the other Mighty-Pixel PHD students - Donatha, Ruben, Lucas and Niclas - I had great times at various collaboration meetings and at the Wasen. Hopefully, we keep our PHD meeting tradition alive and meet regularly, whereby I can do without burglars.

I have to thank some of you again for proof-reading my thesis and trying to get the best out of it. Thank you, Sebastian, Klaas, Niclas, Elli, Kai, Philip, Toko and Lucas for all your feedback!

Of course, I would not have made it to this point without my friends. Without you - Thomas, Christian, Clara, Amelie, Andreas, Kai, Larissa, Lars, Karl - my studies, especially the lectures and lab courses, would have been by far more boring and not so successful. We started with a quite wild party time, but grew up together and now everyone of us is somehow finding his/her own way. I hope we never forget all the funny moments we shared and will keep meeting for a long time.
While trying to understand what I do at the University - but trying even harder to simply have a good and relaxing time - I have to thank Meike, Fabi, Laura, Svenja, Birgit and Mona. We know each other for so long and you have always supported me - thank you!
One person I have to thank especially is you, Karl. We shared so many fantastic moments and always tried to understand and support each other as best as we could. I know that you

are proud of me - but I am also proud of you and your work as a physicist. There are not enough or the right words to express everything, but truly: Thank you!
Maybe you thought I had forgotten you, but I have not. Niclas, you made my PHD time a truly great and enjoyable experience - a real amusemeng! Especially during the last two years and throughout all the irradiation campaigns, your extensive knowledge about electronics was invaluable. It is incredible what we established together! Moreover, we have become an unbeatable team - not only at the laboratory, but also outside of it. You are my partner in crime, and we will always defeat the others at bumper cars. Your wisdom made even the longest working hours feel short - what an eggcelent eggperience, Dackel.

Last but not least, everything is just possible because of my fantastic and lovely family.
Simon und Sophia - Auch wenn ihr nie versteht warum ich Physik studiert habe, habt ihr zumindest versucht Interesse zu zeigen und mich nie aufgehalten - Danke!
Mama und Papa - Ohne euch wäre nichts davon möglich gewesen. Ihr habt mich immer bei meinen Träumen unterstützt, nie an mir gezweifelt und hattet immer ein offenes Ohr - egal wie frustriert ich war. Von euch habe ich gelernt, dass man für seinen Erfolg selber verantwortlich ist und alles erreichen kann, wenn man hart genug dafür arbeitet. Danke für alles, was ihr mir ermöglicht habt. ♡

Contents

1 Introduction **1**

2 The LHCb Experiment **5**
2.1 The Large Hadron Collider 7
2.1.1 The High Luminosity LHC 10
2.2 The Beauty of the LHC - LHCb 11
2.3 The LHCb Detector System 16
2.3.1 Tracking at LHCb 18
2.3.2 Particle Identification System 22
2.3.3 Data Acquisition System - DAQ 26
2.4 Mighty-Tracker 27
2.4.1 Mighty-Tracker Design 27
2.4.2 Mighty-SciFi 29
2.4.3 Mighty-Pixel 29
2.4.4 MightyPix 31

3 Principles of Silicon Detector Technology **35**
3.1 Interaction of Particles with Semiconductor Detectors 36
3.1.1 Energy Loss of Charged Particles 36
3.1.2 Multiple Scattering 39
3.1.3 Energy Loss of Photons 40
3.2 Semiconductors as Particles Detectors 44
3.2.1 Theoretical Concept of Semiconductors 44
3.2.2 Silicon as a Semiconductor 45
3.2.3 Doped Semiconductors 46
3.2.4 The pn Junction 46
3.2.5 Movement of Charge Carriers 51
3.2.6 Signal Generation of Charge Carriers 53
3.2.7 Readout Electronics - MOSFET 54
3.3 Radiation Damage 57
3.3.1 Bulk Damage 57
3.3.2 Surface Damage 65
3.4 Monolithic Active Pixel Sensors 70

4 Introduction of HV-MAPS used within the Mighty-Pixel Project 77
4.1 Development of HV-MAPS towards the MightyPix . . . 78
4.2 Design of TelePix2 . . . 80
4.2.1 Pixel Cell Design . . . 81
4.2.2 Digital Periphery Design . . . 85
4.2.3 Configuration Registers of TelePix2 . . . 89
4.2.4 Power Consumption of TelePix2 . . . 90
4.3 Comparison of HV-MAPS . . . 91

5 Mighty ASIC Readout System - MARS 95
5.1 Requirements . . . 96
5.2 Hardware Design . . . 98
5.2.1 DUT Board . . . 99
5.2.2 FPGA Carrier Board . . . 101
5.2.3 Adapter board . . . 103
5.3 Firmware Design . . . 104
5.3.1 Simulation . . . 110
5.4 Software Design . . . 113
5.5 The TelePix2 Software . . . 115
5.6 MARS compatibility . . . 117
5.6.1 Available DUTS . . . 117
5.6.2 Testbeam Usability . . . 118
5.7 Quality Assurance for MARS . . . 118
5.8 Summary and Outlook . . . 119

6 Characterization of non-irradiated HV-MAPS 121
6.1 Experimental Setup . . . 122
6.2 Commissioning Measurements . . . 124
6.2.1 Calibration Measurements . . . 124
6.2.2 Analog Measurements . . . 125
6.2.3 Pixel Response Measurements . . . 128
6.2.4 Threshold Dispersion . . . 129
6.3 Performance Measurements . . . 134
6.3.1 Biasing Studies . . . 134
6.3.2 Discussion on Measurement Uncertainties . . . 141
6.3.3 Time Resolution . . . 142
6.4 Summary . . . 154

7 Characterization of Bulk Damage on HV-MAPS 155
7.1 Irradiation Side - Bonn Cyclotron . . . 155
7.1.1 Irradiation Setup and Procedure . . . 156
7.1.2 Experimental Procedure . . . 157

7.2 Impact of Proton Irradiation on the Performance of TelePix2 158
7.2.1 Bias Dependence of Proton-Irradiated TelePix2 158
7.2.2 Time Resolution Measurement 166
7.3 Summary 172

8 Characterization of Surface Damage on HV-MAPS 175
8.1 Experimental Setup 176
8.2 Irradiation Campaigns 179
8.3 Irradiation Plan 182
8.4 Results 183
8.4.1 Bias Behavior 183
8.4.2 Low Voltage Power Consumption 188
8.4.3 Run2021 - Annealing Studies 191
8.4.4 Simulation of the Expected Power Consumption of the Mighty-Pixel 193
8.4.5 DUT Performance - Time Resolution 196
8.4.6 DUT Performance - Threshold Dispersion 199
8.4.7 Run2021 - On-Chip DAC behavior 206
8.5 Summary 210

9 Performance Studies of TelePix2 in a Testbeam 213
9.1 The DESY II Testbeam Facility 214
9.2 Experimental Setup 214
9.2.1 Integration of MARS into the EUDAQ2 Software Framework . . . 218
9.2.2 Integration of MARS into the Corryvreckan Testbeam Analysis Framework 219
9.3 Efficiency Studies of TelePix2 220
9.3.1 Analysis Procedure 220
9.3.2 Hit-Efficiency of TelePix2 226
9.4 Time Resolution Studies of TelePix2 231
9.4.1 Time Resolution of TelePix2 232
9.4.2 Comparison with Laboratory Measurements 235
9.5 Summary 236

10 Conclusion and Outlook 239

Bibliography 245

A Appendix 259
A.1 MARS - Latest FPGA Carrier Board 259
A.2 Universities using MARS 260
A.3 Get Started with MARS 261
A.4 Configurable on-chip DACs of TelePix2 263

A.5 Discussion on the Uncertainties of IV- and VV-Measurements 265
A.6 Commissioning Measurements of TelePix2 266
A.7 Matrix Tuning of the Run2021 Sensor 268
A.8 Characterization of Bulk Damage on HV-MAPS 269
A.9 Characterization of Surface Damage on HV-MAPS 271
A.9.1 Calibration of the Comparator Threshold 271
A.9.2 Power Consumption of the First TelePix2 Irradiation 272
A.9.3 Annealing Measurement of the Threshold Dispersion of the Run2021 Sensor 273
A.9.4 Summary of the On-Chip DAC Measurement of the Run2021 Sensor 274
A.9.5 Comparison of the Threshold Scans between the Run2021 and TelePix2 Sensors 275
A.9.6 Investigation of the Amplifier Gain 277
A.10 Performance Studies of TelePix2 in a Testbeam - Observed Time Shifts . . 282
A.11 Sensor Configuration Settings 283
A.12 Glossary 284

List of Tables **287**

CHAPTER 1

Introduction

When was the last time you felt curious about something you did not fully understand? Probably quite often. But when was the last time you were truly fascinated - so fascinated that you began to explore, to question, to expand your knowledge, to learn and to grow?
As a physicist you know this feeling of curiosity and drive to satisfy it. But science goes beyond curiosity. You have the urge not only to solve problems, but first to define them, then to understand them and find solutions, with which you are not satisfied, but continuously strive try to improve them.
In high energy particle physics, scientists have been trying to understand the origin of the universe and its nature since years. It has resulted in the development of the **S**tandard **M**odel SM of particle physics, which - thanks to continuous theoretical and experimental efforts - defines a comprehensive and successful theory of particle interaction. At the **L**arge **H**adron **C**ollider LHC, the world's leading circular particle accelerator located at the European laboratory for particle physics CERN, outstanding results have been obtained in the first two run periods at the four big experiments: ATLAS, CMS, ALICE and LHCb. While ATLAS and CMS explored the Higgs sector and ALICE the quark-gluon plasma, LHCb achieved tremendous results in flavor physics and hadronic spectroscopy. Up to now, no significant ambiguity between the SM predictions and experimental findings have been reported. Nevertheless, the SM cannot describe all observations in the universe, resulting in open questions including the origin of the matter-antimatter asymmetry, neutrino masses and the nature of dark matter.
To investigate their origin and seek answers, scientists are preparing for a new data-taking period at the LHC. In order to enable the collection of larger datasets, improving sensitivity to rare processes, the limits of the accelerator have to be pushed further by increasing the instantaneous luminosity. The new era of the **H**igh-**L**uminosity HL-LHC will offer unique physics research opportunities for the four experiments.
At the LHCb experiment the full flavor physics potential will be exploited. To date, no new massive elemental particles have been discovered by any experiment, likely because their mass scale is not directly accessible at the LHC. However, with the upgraded LHCb detector

the effects of New Physics on the SM can be investigated with unique sensitivity, enabling the probe of mass scales beyond the direct accessibility of production measurements.
Achieving this requires an increase in instantaneous luminosity at LHCb by one order of magnitude from $1 \times 10^{33}\,\mathrm{cm}^{-2}\mathrm{s}^{-1}$ to $1 \times 10^{34}\,\mathrm{cm}^{-2}\mathrm{s}^{-1}$ [1], foreseen for Run 5. As a consequence, the number of visible proton-proton interactions per bunch crossing will increase from 6 to 40, resulting in $300\,\mathrm{fb}^{-1}$ of collected data at the end of the detector's expected lifetime [5].
In order to study rare processes and ensure high precision reconstruction, the separation of primary and secondary vertices from pp interactions and a high tracking efficiency under Upgrade II are crucial. Therefore, fast-timing information from the detectors are mandatory. Moreover, the increase in instantaneous luminosity requires radiation-tolerant particle detectors. Accordingly, the full LHCb detector system has to be upgraded. With the beginning of Long Shutdown 4, the LHCb Upgrade II detector will be installed.
A key element is the installation of the new downstream tracker - the Mighty-Tracker - a hybrid detector equipped with monolithic pixel detectors in the central high occupancy region around the beam-pipe and scintillating fibers covering the outer area. The pixel and fiber detector are called Mighty-Pixel and Mighty-SciFi, respectively.
The Mighty-Tracker is a precise tracking and radiation tolerant detector while being cost-effective. Due to the synergy of high efficiency, good time and position resolution and radiation tolerance, while keeping the material budget low, **H**igh-**V**oltage **M**onolithic **A**ctive **P**ixel **S**ensors HV-MAPS are foreseen for the Mighty-Pixel. The production sensor will be called MightyPix.
HV-MAPS have first been proposed by I. Péric [2] and have been used in various experiments, e.g. the Mu3e experiment [3]. However, it has to be demonstrated that the technology fulfills the Mighty-Pixel requirements. Therefore, an intensive research and development phase has started in 2020. Several prototype HV-MAPS have been characterized by performance studies.
Key elements are the radiation tolerance, time resolution and hit-efficiency. At the Mighty-Pixel the HV-MAPS will be exposed up to a fluence of $3 \times 10^{14}\,\mathrm{MeV n_{eq} cm}^{-2}$ and dose of 40 MRad [5]. A time resolution of ≤ 3 ns and hit-efficiency of $\geq 99\%$ are required [5].
Investigation of both, the time resolution and hit-efficiency, for irradiated and non-irradiated HV-MAPS are main topics of this thesis. As a predecessor to the MightyPix, the TelePix2 sensor [6], featuring a comparable analog sensor design, was characterized.
Since this thesis is the first thesis at the University of Bonn studying HV-MAPS, a new **D**ata **Acq**uisition DAQ system had to be developed to configure and operate the devices as well as read-out and process the collected data. The system, called **M**ighty **A**SIC **R**eadout **S**ystem MARS, was first published in [7]. MARS is the foreseen DAQ system for further sensor characterization studies within the Mighty-Pixel project at all collaborating institutes.

Outline of the Thesis

In order to understand the requirements for the Mighty-Pixel, the LHCb experiment and its planned upgrade, including a comprehensive outline of the physics program, are introduced in chapter 2. Each subdetector and the foreseen upgrade are discussed but special emphasize is given on the Mighty-Tracker in section 2.4.
To understand how silicon detectors are used as particle tracking detectors, the principles of silicon detector technology are explained in chapter 3. Firstly, the interactions of particles with semiconductors are introduced in section 3.1, followed by the theory of semiconductors in section 3.2. The theoretical concept of semiconductors and how to use them as a detector, including the discussion of signal generation and readout electronics, are main topics of the section. Further, the radiation damage in terms of bulk and surface damage is presented in section 3.3 in order to understand its importance for the Mighty-Pixel. Finally, the theory of HV-MAPS is discussed in section 3.4
Subsequently, HV-MAPS designed for the Mighty-Pixel project are introduced in chapter 4. Special focus is on the design of TelePix2, a predecessor of the MightyPix. Its design is explained in section 4.2. Since the MightyPix sensor was not available by the start of this thesis, most measurements have been conducted with TelePix2.
The DAQ system MARS used for all conducted measurements has been developed by the author. Its concept is explained in chapter 5.
Obtained results are structured into three dedicated chapters, covering non-irradiated HV-MAPS (see chapter 6), proton irradiated (see chapter 7) and x-ray irradiated HV-MAPS (see chapter 8). For each case, the emphasis is placed on evaluating the performance in terms of bias and time resolution measurements.
Finally, the hit-efficiency and time resolution were measured at a testbeam campaign in December 2024 at the DESY II testbeam facility [8], using the MARS DAQ system. The setup, integration into the testbeam facility and obtained results are presented in chapter 9.
A summary of the main derived results and outlook of the project will be given in chapter 10.

Each chapter is structured as follows: first, an introduction and explanation of the covered topics is provided; second, the main topics are discussed; and third, the chapters presenting results conclude with a comprehensive summary and a first outlook.

Contributions of the Author

The author was not involved in the design of any HV-MAPS discussed within this thesis. However, results obtained by the author have been considered in the design of MightyPix2.
The author made major contributions to the development of the MARS DAQ system, published in [7]. Mainly, the complete firmware and software have been developed and tested. Hardware elements have not been actively designed by the author, but in collaboration with K. Padeken. Moreover, all hardware components were intensively tested by the author and issues reported for further iterations.
The author conducted all presented measurements on her own with the support of the LHCb Bonn hardware group.
In total, the author attended four testbeam campaigns during her PhD, where only the last was used to gather the results presented within this thesis. The integration of the MARS DAQ system into the testbeam software and the offline data analysis have been developed by the author.
The first two testbeam campaigns were collaborating campaigns with the goal to investigate the performance of ATLASPix3.0(1). The author not only took actively part in the testbeam operation, but also in the data analysis. Main results have been published in [9]. The third testbeam campaign was used to first commission the MARS DAQ system at a testbeam facility. The final commissioning was done at the latest.
Further, the author led seven irradiation campaigns from April 2024 to Mai 2025 at the University of Bonn. In total, three proton irradiation campaigns at the Bonn isochronous cyclotron [10] have been conducted for three different flavors of HV-MAPS used in the scope of the Mighty-Pixel project. Results obtained with the proton irradiated TelePix2 sensor are presented within this thesis, results from the MightyPix1 irradiation in [11] and from the Run2021 irradiation will be presented in [12]. The remaining four irradiations have been performed at the x-ray tube located at the FTD in Bonn [13]. Results from all campaigns are discussed in this thesis. Further two campaigns were supported by two Bachelor students: L. Ernst and M. Liebetrau [14].
Besides, the author supported the supervision of three Master students, C. Arslan [15], N. Sommerfeld [16] and S. Hermann and one other Bachelor student, J. Günther [17]. Results and developments from each are embedded within this thesis.
Next to the main topic of the presented PhD thesis, the author helped to set up the Bonn LHCb hardware group, since she and K. Padeken were the first members who started the whole project at an empty laboratory.
In addition, contributions to simulation studies using the FLUKA software [18] investigating the air activation at the Bonn isochronous cyclotron have been conducted by the author.
As an outreach contribution, the author helped to establish the LHCb international Masterclass at the University of Bonn and partially supervised the Bachelor thesis of L. Exner [19].

CHAPTER 2

The LHCb Experiment

Located at the **L**arge **H**adron **C**ollider LHC, LHCb is one of the four big experiments - seeking answers to questions human beings nowadays ask about the nature of the universe and its beginning:
Why is there more matter than antimatter? What is the origin of mass? What is dark energy? What is dark matter?
Answering these questions requires recreating the conditions of the early universe and probing the smallest building blocks of matter. To probe the building blocks of matter, physics at small length scales must be explored. Therefore high energies are essential. A powerful tool is the acceleration of particles to those energies and their collision.
The most powerful accelerator to date is the LHC where conditions similar to those at the beginning of the universe are recreated by colliding high energy particles at dedicated points. Specialized experiments are situated at those points to study the resulting processes. The LHC acceleration structure is introduced in section 2.1.
Answering the question of the matter-antimatter asymmetry is one of the main research goals of the LHCb experiment. Part of the research is to probe the **S**tandard **M**odel SM of particle physics and search for physics beyond it. Only through contributions beyond the SM certain physics phenomena, such as the matter-antimatter asymmetry, can be explained. The research approach of LHCb is discussed within this chapter.
An important quantity to probe the SM is precision. LHCb, for example, offers precision measurements in the heavy-flavor physics sector. However, the precision is limited by systematic uncertainties. To reduce these uncertainties, additional statistics and more precise measurements are crucial.
One Ansatz are longer measurement times at the LHC. But, in order to obtain the necessary statistics, the experiment would have to run several years longer. Another approach is to increase the instantaneous luminosity.
The new high luminosity era of the LHC, called **H**igh-**L**uminosity HL-LHC, is foreseen to start in 2030. A description of required changes and goals of the HL-LHC is presented in section 2.1.1.

Consequently, experiments at the LHC have to be upgraded to cope with the requirements imposed by the HL-LHC. Therefore, LHCb plans a major upgrade of the whole detector system - called Upgrade II. Without this, an operation at a performance similar to the current LHCb detector system would not be possible. Furthermore, the physics program will be enhanced through operation of the experiment during the HL-LHC era. For example, precision measurements of SM variables, such as the CKM angle γ, will be are carried out with unprecedented precision.
Outstanding results and planned measurements are presented in section 2.2. Motivating the experiment's goals with that, the detector system and its planned upgrades are discussed in section 2.3 and following sub-sections.
Since the measurements presented in this thesis focus on the detector planned for installation downstream of the detector system, special emphasis is placed on it. The Mighty-Tracker is introduced in section 2.4. Its design and hybrid technology approach are discussed in sections 2.4.1 to 2.4.3. Finally, the chapter concludes with section 2.4.4, explaining the requirements and design of the sensor, based on the technology of textbfHigh-**V**oltage **M**onolithic **A**ctive **P**ixel **S**ensors HV-MAPS, foreseen for the Mighty-Pixel.
Introducing and discussing the requirements is required in order to understand the performance studies presented within this thesis because the overall goal is to show this technology being compatible with the experimental requirements.

2.1 The Large Hadron Collider

Exploring the universe with its unresolved questions - such as the matter-antimatter asymmetry or the origin of mass - inevitably leads to probing the fundamental building blocks of matter. As mentioned earlier, probing physics at these scales requires very high energies. Therefore, particle accelerators are essential in order to accelerate particles and bring them into collisions. Specialized experiments located at the collision points are designed to study the resulting processes.
The LHC - located at **C**onseil **E**uropéen pour la **R**echerche **N**ucléaire CERN at the Swiss-French border - is the most powerful particle accelerator up to now.
Since 2010, the 27 km long LHC is the largest circular accelerator complex [20]. Future projects, such as the **F**uture **C**ircular **C**ollider FCC, are planned to further exploit the physics potential and enable new researches in the TeV energy scale in order to study known physics with unprecedented precision as well as beyond Standard Model physics [21].
At the LHC proton beams are accelerated up to 6.8 TeV [22] before they collide at dedicated collision points, enabling a center-of-mass energy of $\sqrt{s} \approx 13$ TeV [23]. Besides physics programs with protons, dedicated studies using heavy ion (lead) beams are also conducted to investigate the quark-gluon plasma, with the goal of further understanding the strong nuclear force. In fig. 2.1 the CERN accelerator complex is depicted [1].
Firstly, negative hydrogen ions (consisting of a hydrogen atom with an additional electron) are accelerated at the linear accelerator LINAC4 up to 160 MeV. At the injection into the **P**roton **S**ynchrotron **B**ooster PSB both electrons are stripped of such that the remaining proton can be further accelerated. With an initial energy of 2 GeV, its energy is ramped up to 450 GeV by the **P**roton **S**ynchrotron PS and the **S**uper **P**roton **S**ynchrotron SPS.
Finally, the protons are injected into the LHC, split into two counter-circulating beams, accelerated to their target energy, and brought to collision at four points.
The four big experiments, located at the interaction points, are: ATLAS, CMS, ALICE, and LHCb.
While **A** **T**oroidal **L**HC **A**pparatu**S** ATLAS [24] and **C**ompact **M**uon **S**olenoid CMS [25] focus on addressing fundamental questions - such as the building blocks of matter, the interaction between particles, and the existence of dark matter - the **A** **L**arge **I**on **C**ollider **E**xperiment ALICE [26] and **L**arge **H**adron **C**ollider **b**eauty LHCb conduct more specialized, but still broad, research.

Instead of a continuous particle beam, the LHC beam structure consists of bunches. 2808 bunches collide every 25 ns with each other, resulting in a bunch crossing frequency of 40 MHz [28]. Per bunch crossing a pile-up [2] of ≈ 27 was foreseen at experiments operating at the peak luminosity of $L = 1.18 \times 10^{34}\,\mathrm{cm}^{-2}\mathrm{s}^{-1}$, e.g ATLAS and CMS. Nevertheless, the design value was exceeded at both experiments.

[1] The main reference for the following specifications of the acceleration complex are taken from [22].
[2] The amount of proton-proton interactions per bunch crossing is defined as pile-up.

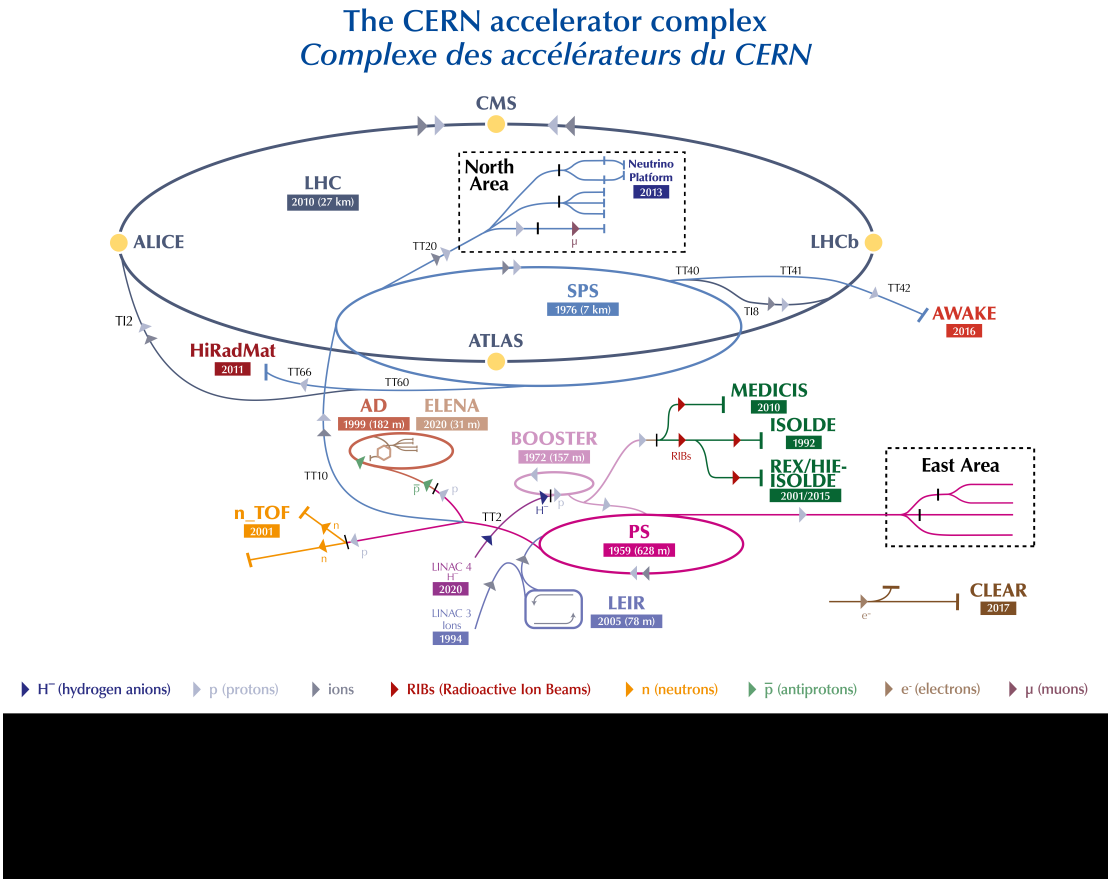


Figure 2.1: Overview of the CERN accelerator complex with all pre-accelerators, main experiments and the LHC (colored in dark blue). The four collision points are labeled with yellow dots to the corresponding experiments: ATLAS, CMS, ALICE, LHCb [27].

At the LHCb experiment, the luminosity was leveled to $L = 2\times10^{32}$ to 4×10^{32} cm^{-2}s^{-1} during the first two run periods, to keep the average number of visible proton-proton interactions per bunch crossing close to one [29], thereby ensuring a high reconstruction efficiency and decay-time resolution for flavor-physics. However, the experiment was successfully operated at a higher pile-up of up to 2.5 [30].
As a result, all experiments conducted an outstanding physics program. In 2012 one of the most publicly celebrated discoveries was made by the ATLAS [31] and CMS [32] collaboration: the observation of the Higgs boson, the last elementary particle of the SM, predicted in 1964 [33].
To study rare processes (characterized by small production cross sections σ), large data samples are essential. As mentioned in the introduction, one way to increase the number of events N is by raising the instantaneous luminosity L_{inst} [34]:

$$\dot{N} = L_{inst} \cdot \sigma \qquad . \tag{2.1}$$

Since the cross section is defined by the physics process, the rate of events $\dot{N}$ is limited by the luminosity. In other words, by the luminosity the ability to produce the required number of particle interactions is described. For a circular collider the following relations are found [3] [35] [34]:

$$L = \gamma \cdot \frac{n_b N^2 f_{rev}}{4\pi\beta^* \epsilon_n} R \qquad L = \frac{N_1 N_2 n_b f_{rev}}{A} \tag{2.2}$$

- γ - Relativistic γ factor
- n_b - Number of bunches: 2808
- N - Bunch population (protons per bunch): 1.15×10^{11}
- f_{rev} - Revolution frequency
- β^* - Beam beta function at a collision point
- ϵ_n - Transverse normalized emittance
- R - Geometrical reduction factor due to the beam crossing angle
- N_i - Number of bunches in respective beams
- A - Cross section area at the collision points

By tuning the beam parameters, the luminosity and hence, the number of detectable events can be enhanced. The design luminosity of $1 \times 10^{34}\,\mathrm{cm}^{-2}\mathrm{s}^{-1}$ was reached in 2016 while a peak luminosity of $2 \times 10^{34}\,\mathrm{cm}^{-2}\mathrm{s}^{-1}$ was achieved in 2018 by the ATLAS experiment [20]. Experimentally this value is limited by the current design of the LHC. With this, an integrated luminosity of $40\,\mathrm{fb}^{-1}$ per year [4] has been recorded by ATLAS [20]. To increase the data collection, the LHC must be upgraded. The planned upgrade and data-taking phases are referred to as the **H**igh **L**uminosity HL-LHC program.

[3] Both formulas can be adapted into each other.

[4] The integration of the (instantaneous) luminosity over time gives the integrated luminosity L_{int} - a measurement of recorded data.

2.1.1 The High Luminosity LHC

By the end of Run 3 the LHC is expected to deliver 350 fb^{-1} [20]. With the HL-LHC upgrade program, over the course of 12 years of planned operation, a total integrated luminosity of 3 000 fb^{-1} [20] will be collected - representing a tenfold increase compared to Run 3.
The peak instantaneous luminosity will increase by a factor of 7.5, reaching $L = 7.5 \times 10^{34}\,cm^{-2}s^{-1}$, which is expected to result in ≈ 200 events per bunch crossing at ATLAS and CMS [20].
By optimizing the parameters, introduced in eq. (2.2), the luminosity can be maximized. Besides optimizing the number of bunches per beam (2808 $\rightarrow$ 2748) and a higher beam current (0.58 A $\rightarrow$ 1.09 A), the optical beam parameters as well as the machine parameters are tuned. To fulfill the target goals [5], new technologies are required. A few examples are given next:
Focusing magnets with 12 T (so far 8 T) magnetic fields will concentrate the beams such that the number of collisions per bunch crossing is enhanced. Further, crab cavities will be used to tilt the beginning and end of each bunch at the interaction point while the center is kept. Therefore, the overlap of bunches increases, resulting in higher pile-up. To reverse the rotation, a further cavity is used.
To protect the superconductors from quenching caused by the increased particle flux, resulting from the enhanced beam optics, new crystal collimators will replace the existing graphite-based ones.
A key feature of the HL-LHC is so called lumi-leveling, which was pioneered by the LHCb experiment. Due to the beam collisions, the luminosity is unstable over time as protons are "burned-off", and is therefore not stable over a run. By applying lumi-leveling, the average luminosity is maintained throughout the entire run period. To achieve this, the beam's beta function β^* is dynamically adjusted - starting with a larger beam cross section and gradually squeezing it to its target value. Upgraded beam optics are required [28].
The overall HL-LHC upgrade will take place in **L**ong **S**hutdown LS3 - scheduled to start in mid 2026 [36] [37]. Within four years all upgrades have to take place such that at beginning of Run 4, in the middle of 2030, all experiments can start data taking. Besides the LHC itself, the experiments will upgrade their machines to ensure stable and precise data taking under the new conditions as well as enhance their physics potential by updating the used detector and data acquisition technologies.
While ATLAS and CMS are planning to operate at the design HL-LHC luminosity with the beginning of Run 4 (2030), ALICE and LHCb will enter the HL-LHC era at the start of Run 5 (2036) [37].
Key element of all detector system upgrades is the incorporation of radiation tolerant, precise and fast detector technologies with a low material budget. How this is done at the LHCb experiment and the planned physics program, is discussed in section 2.2 and section 2.3.

[5] A detailed discussion of all specifications and their implementation is provided in [20]and [28].

2.2 The Beauty of the LHC - LHCb

Since 2008 the LHCb experiment is under operation at **I**nteraction **P**oint IP8 at the LHC. With the physics program and detector layout first proposed in the **L**etter **o**f **I**ntent LoI in 1995, the LHCb collaboration delivered precise and outstanding measurements in flavor physics and beyond.
LHCb is designed as a single-arm forward spectrometer to perform precision measurements in the heavy flavor physics regime (in fig. 2.3 the current detector system is depicted). Consequently, large data samples are essential.
Operating the experiment at an instantaneous luminosity of $4 \times 10^{32}\,\mathrm{cm}^{-2}\mathrm{s}^{-1}$ and a center-of-mass energy of $\sqrt{s} = 7$ to 13 TeV during the first two data collection phases, Run 1 and Run 2, enabled the collection of $9\,\mathrm{fb}^{-1}$ of proton-proton collision data [29]. The dataset allows ongoing efforts to address many fundamental and still unresolved questions about the universe. As previously stated, one puzzle is the matter-antimatter asymmetry of the universe. When matter and antimatter come into contact, they annihilate, releasing energy. The Big Bang should have produced matter and antimatter in equal amounts. However, the universe as known today consists mostly of matter. Understanding this imbalance has become a key challenge.
The violation of the **C**harge-**P**arity CP condition in the **S**tandard **M**odel SM of particle physics is necessary to explain this. But, the **CP V**iolation CPV observed so far within the SM is too small to account for the matter-antimatter imbalance. Precise measurements of the SM predictions therefore enable the search for New Physics, as deviations may indicate its existence. To stress the importance of CPV, a few highlight measurements are presented:

While the first CPV was observed in the Kaon system in 1964 [38], no CPV had been measured in the baryon and charm sectors until the LHCb experiment began operating. The high b-quark production rate enables the possibility of measuring CPV in beauty baryon decays. In 2017, the first observation of CPV was reported with a significance of $3.3\,\sigma$ in the decays of $\Lambda_b^0 \to p\pi^-\pi^+\pi^-$ and $\Lambda_b^0 \to p\pi^-K^+K^-$ [39]. From a theoretical point of view, the amplitudes of both SM processes (W^- emission and gluon emission) are expected to be of similar magnitude. A deviation, and hence CPV, can arise from the interference of both processes. The significance found in [40] is lower, while a larger data sample was analyzed, indicating that the data remains insufficient to establish CPV.
Two new studies, published in [41] and [42], observed CPV in baryonic decays, as well as in beauty hadrons decaying into charmed particles, using data collected during Run 1 and Run 2.
The first one found evidence for CPV with $3.2\,\sigma$ significance in the decay $\Lambda_b^0 \to \Lambda K^+K^-$ by measuring the difference between the Λ_b^0 and its anti-particle decay [41].
The second showed first CPV in beauty to charmonium decays again with $3.2\,\sigma$ significance by measuring the decay rate difference and branching fractions of $B^+ \to J/\Psi\pi^+$ to the favored decay $B^+ \to J/\Psi K^+$ and its anti-process [42].
Another hint for CPV was found measuring the oscillation frequency Δm_s in $B_s^0 - \bar{B}_s^0$ mixing

with $\Delta m_s = (17.7683 \pm 0.0051 \pm 0.0032)\,\mathrm{ps}^{-1}$ [43]. Since the B_s^0−meson consists of a heavy and light mass eigenstate, the oscillation frequency is related to the mass difference Δm_s. A precise measurement is required to constrain the SM quark-mixing prediction by the **C**abibbo-**K**obayashi-**M**askawa CKM matrix [44] [45]. Using data collected during Run 2, a world-leading result was obtained for the $B_s^0 \to D_s^- \pi^+$ decay.

Beyond CPV measurements, LHCb reported outstanding physics results of benchmark measurements of the SM, hadron spectroscopy, lepton flavor universality studies and a first observation of the rare decay $B_s^0 \to \mu^+\mu^-$ [46]. Further, heavy ion physics as well as fixed target experiments and studies in the dark sector have been performed during Run 1 and Run 2. Some landmark measurements are presented in the following.

Hadron spectroscopy is a central element of LHCb's physics program, enabling investigations of the hadron internal structure and formation mechanism. In addition, it provides information about the quark production process. As a result, important measurements for the **Q**uantum **C**hromo**d**ynamics QCD theory are contributed, enabling research of the strong interaction. Part of this is the study of hadronic states, which are separated into conventional and exotic states. While baryons and mesons are classified as conventional hadrons, states with other quark content, for example tetra- and pentaquarks, are considered as exotic hadrons. In 2003 the first tetraquark $\chi_{c1}(3872)$ [47] was observed by the Belle collaboration.
Since the start of the LHCb experiment, numerous exotic states have been discovered. Prominent candidates are the P_c^+ pentaquark [48] [49] and the doubly charmed T_{cc}^+ tetraquark [50] [51].
The decay $\Lambda_b^0 \to J/\psi K^- p$ is dominated by $\Lambda_b^0 \to J/\psi \Lambda^* (\to K^- p)$ but can have exotic contributions. This contribution was found to be produced by two charmonium pentaquarks with quark content $c\bar{c}uud$ with masses of $(4\,380 \pm 8 \pm 29)$ MeV and $(4\,449.8 \pm 1.7 \pm 2.5)$ MeV [48]. In the follow-up analysis published in [49], the $P_c(4450)^+$ was validated and could be resolved into two narrow resonances. Additionally, a new state $P_c(4312)^+$ has been found with $7.3\,\sigma$ significance.
Tetraquark states such as the doubly charmed tetraquark $T_{cc}(3875)^+$ consist of four quarks - in case of the T_{cc}^+ two charm quarks and $\bar{u}\bar{d}$ quark pair. For a long time the existence of such a state was unclear. The analysis performed in [51] observed this state in the $D^0 D^0 \pi^+$ spectrum close tho the $D^{*+} D^0$ threshold. Reconstruction of the D^0-mesons is done via the $D^0 \to K^- \pi^+$ decay channel.
One key question is the arrangement of the quarks in such a state. Two possible bindings are predicted by theorists. Color singlet hadrons are either bound loosely into hadronic molecules or tightly into compact multiquarks. Due to the closeness of $T_{cc}(3875)^+$ to the $D^{*+} D^0$ threshold the nature might be a hadronic molecule. However, a compact multiquark cannot be excluded with the available data from Run 1 and Run 2. Consequently, further statistics are required.

For all presented results and precision measurements conducted at LHCb, large data

samples and excellent detector performance are essential to ensure high significance of measurements at the precision border.
As already said, LHCb is designed as a single-arm forward spectrometer. Due to the predominant production of $b\bar{b}$ pairs by gluon-gluon fusion and the low B-hadron masses compared to the center-of-mass energy, produced beauty and also charm hadrons are boosted into the forward direction. Covering a pseudorapidity range [6] of $2 \leq \eta \leq 5$, the detector system enables measurements of those by design.

A higher precision and enhanced physics program became possible with a first upgrade of the overall detector system - called Upgrade I which is under operation since Run 3.
Running at an instantaneous luminosity of $L_{inst} = 1 \times 10^{33}\,\mathrm{cm}^{-2}\mathrm{s}^{-1}$ a total dataset of $50\,\mathrm{fb}^{-1}$ will be recorded until the end of Run 4. The detector is read-out by a newly installed full software **D**ata **Acq**uisition DAQ system operating at 40 MHz. Thus, the selection efficiency for hadronic modes could be substantially improved [30].
Before Upgrade I, the readout rate of the initial DAQ system was limited to 1.1 MHz [30]. Consequently, a complete upgrade of the DAQ architecture was necessary to increase the signal yield in response to the increased luminosity. Removing the 1.1 MHz limitation of the $L0$ hardware trigger, is indispensable to profit from the increased luminosity since the $L0$-hadron efficiency saturates at luminosities $L_{inst} \geq 2 \times 10^{33}\,\mathrm{cm}^{-2}\mathrm{s}^{-1}$ [30]. In addition, more information about each event is required to trigger.
Removing the $L0$ hardware trigger, is the most efficient way to access the full event information. As a consequence, the detector must be read-out at 40 MHz, with each event analyzed online.
Thus, New Physics studies and precision measurements of the SM became possible. Benchmark measurements are among others: CPV studies in $B_s \to \phi\phi$, lepton-flavor violating τ-decays and precision measurements of charm CPV of order 10^{-4} [30].

However, the full physics potential of the Upgrade I LHCb detector (shown in fig. 2.3) is still limited but can be further enhanced running the experiment during the HL-LHC era at an even higher luminosity of $L_{inst} = 1 \times 10^{34}\,\mathrm{cm}^{-2}\mathrm{s}^{-1}$ [7] [1]. To motivate the physics goals, some landmark measurements are presented:

To further exploit CPV, the SM unitarity triangle apex will be measured to unprecedented precision. Therefore, tree-level processes, measuring the CKM angle γ, and flavor-changing neutral current loop-processes, observed in B-meson oscillations, are target measurements. The systematic uncertainties in the decay channel $B^- \to DK^-$ will decrease with increasing

[6] Pseudorapidity defines the particle's angle relative to the beam axis: $\eta = \ln[\tan(\Theta/2)]$ [34].

[7] The available publications at the point writing this thesis have foreseen a target luminosity of $L_{inst} = 1.5 \times 10^{34}\,\mathrm{cm}^{-2}\mathrm{s}^{-1}$. Therefore, most cited numbers for Upgrade II are derived using this luminosity scenario. During the evaluation and possible scoping scenarios of the detector, published in [1], a reduced luminosity of $L_{inst} = 1 \times 10^{34}\,\mathrm{cm}^{-2}\mathrm{s}^{-1}$ is anticipated for Upgrade II. However, expected specifications such as particles rates and radiation doses have not been adapted and publicized at this point. If more accurate numbers are available, remarks are given.

data samples. Hence, this channel provides excellent precision measurements. A reduction of the uncertainty of γ of 1° down to 0.35° is expected by Upgrade II [52].
Further New Physics in CPV will be targeted by measuring the CP-violating weak phase ϕ_s in $B_s^0 \to J/\psi\phi$ and $B_s^0 \to \phi\phi$. Since the weak phase is very small and precisely predicted by the SM, its measurement is highly sensitive to possible contributions from New Physics. To date, the precision is insufficient to claim a deviation from the SM prediction. But, with the amount of collected data in Run 5 and Run 6 the uncertainty on the determination of ϕ_s will be significantly reduced. Combining multiple decay modes is expected to yield a precision on the order of the SM uncertainty.
As in the initial physics program and Upgrade I the charm sector will be further studied. The first hinting measurement in this sector (discussed earlier within this section) showed evidence of CPV, but with insufficient statistical significance. Hence, more measurements are needed to validate CPV in these processes.
LHCb is the only experiment (up to now) which is sufficiently sensitive to $D_0 - \bar{D}_0$ mixing allowing precise measurements of the asymmetry [5].

Similarly, the hadron spectroscopy program will be continued, trying to understand the nature and dynamics (including their decay and interaction) of exotic states. While lots of observed exotic hadrons appear close to the meson-antimeson/meson-baryon threshold, being explained by molecular or hadron re-scattering models, some states differ from this and indicate tight bindings. One example is the Pentaquark P_c^* ($c\bar{c}uud$) in the decay $\Lambda_b^0 \to P_c^*[\to \Lambda_C^+ \bar{D}^{*0}]K^-$ which nature can be described by either a hadronic molecule or tightly bound states [53].
With Upgrade II unprecedented sensitivity in those measurements will be possible. Measuring of the so far not possible measurements of width and excitation spectrum is foreseen and will help understanding hadronic binding [52].

In contrast to Upgrade I, the foreseen physics program is not possible with the Upgrade I detector under Run 5 and Run 6 conditions. Besides the fact that most subdetectors will not be able to cope with the experimental requirements, the foreseen physics is only possible with excellent vertex reconstruction and information including low momenta measurements as well as an improved energy resolution of the electromagnetic calorimeter. Moreover, the DAQ system has a roughly six times higher throughput of 200 TB of data per second compared to Upgrade I [1]. A reduction of ≈ 4 orders of magnitude is crucial before the data can be stored on disk [1].
Taking the experimental requirements, caused by the HL-LHC environment, into account, the overall detector system has to be upgraded to withstand the radiation environment and operate at the expected data rates. Main challenges for all sub-detectors are radiation damage, high multiplicity and particle rates.
To address this and achieve the anticipated physics goal, the LHCb collaboration has undertaken an intensive **R**esearch and **D**evelopment R&D program elaborating possible technologies. A detailed discussion of the current project status is published in the **F**ramework **T**echnical

Data **R**eport FTDR [52] and possible scoping scenarios in the Scoping Document [1]. With the planned upgrade a dataset corresponding to an integrated luminosity of 300 fb^{-1} is expected to be collected by the end of Run 6 which is a factor 5 higher than collected by the Upgrade I detector. A time evolution of peak luminosity (colored in blue) and recorded luminosity (colored in red) is presented in fig. 2.2.

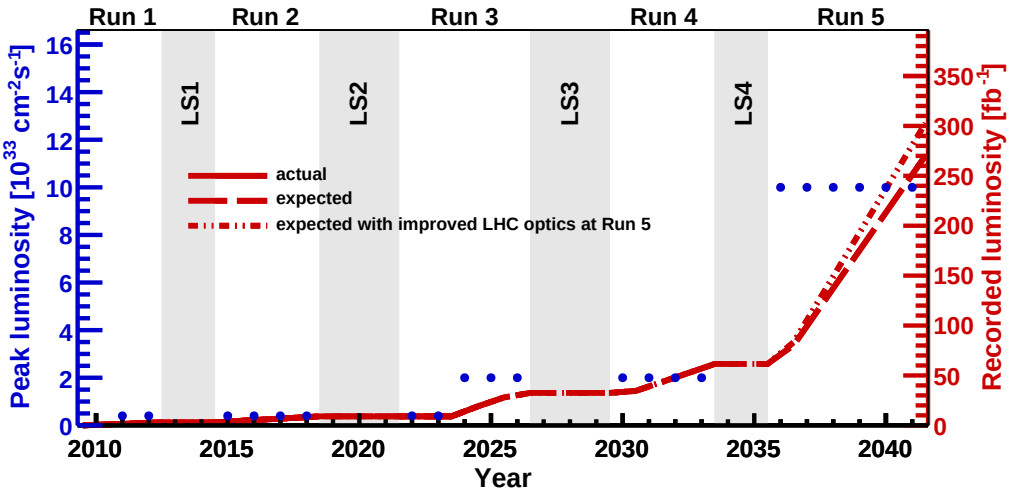


Figure 2.2: Overview of peak luminosity (blue colored) and integrated luminosity (red colored) for all Run periods of LHCb over the years starting with its beginning in ≈ 2010 and ending at the end of Run 6 after 2040 [1].

Because of the raised luminosity, the number of visible pp interactions will increase from ≈ 6 (Upgrade I) to 40 [1]. To increase the luminosity, adjusted beam optics close to the interaction point have to be installed. A summary of needed adjustments is given in [5] and references therein.
To achieve the presented physics goals, a reliable and excellent detector performance is unavoidable. A main challenge will be the operation of all sub-systems at high multiplicity and particle rates. Furthermore, radiation tolerant technologies are essential.
Precision measurements and excellent vertexing, essential for LHCb's pysics program, is only possible with 4D-tracking (including fast time information) and radiation tolerant technologies.
The foreseen upgrades of each system and their current status are discussed in the following section 2.3.

2.3 The LHCb Detector System

Designed as a forward spectrometer LHCb covers 20 m length and 10 m hight. A side-view of the currently running Upgrade I detector is shown in fig. 2.3.
Nearly all sub-systems are split into two halves: (1) *A*-side and (2) *C*-side. Accessing the system is possible at the *A*-side while cryogenic cooling is located at the *C*-side.
The detector complex can be functionally divided into tracking and **P**article **Id**entification PID detectors .
The **Ve**rtex **Lo**cator VELO, **U**pstream **T**racker UT, the dipole magnet and the **Sci**ntillating **Fi**ber tracker SciFi form the tracking system. Particle identification is done via two **R**ing **I**maging **Ch**erenkov RICH detectors, the **E**lectromagnetic and **H**adronic **Cal**orimeter (ECAL and HCAL) and the Muon chambers.
All systems are read out at 40 MHz - meaning zero-suppressed without any hardware trigger. As mentioned previously, the establishment of this DAQ architecture was one of the key upgrade installations of Upgrade I and is unique within all LHC experiments.

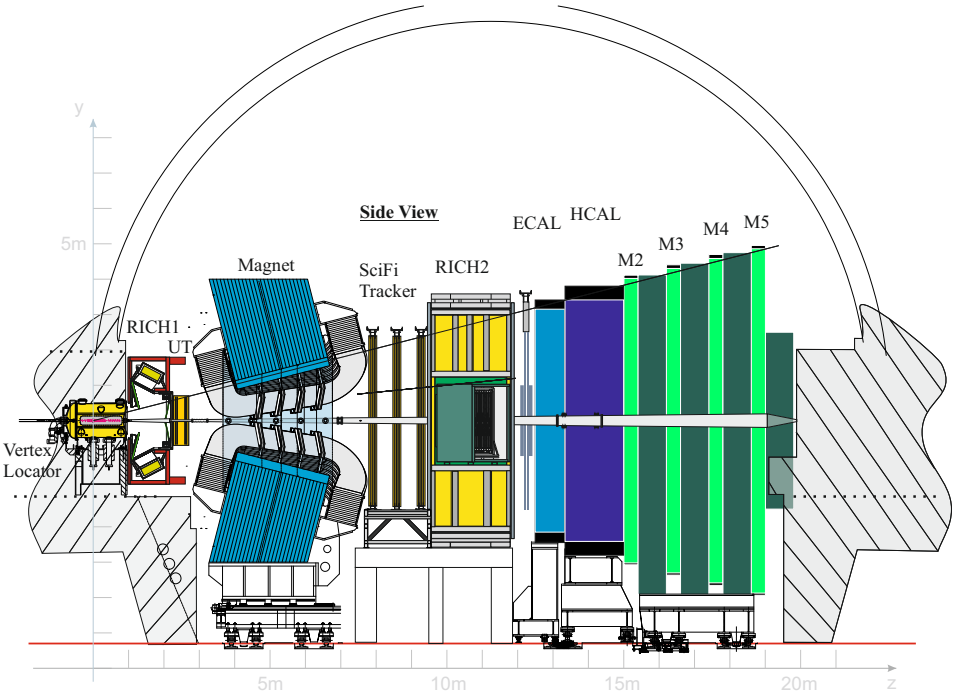


Figure 2.3: Side-view of the Upgrade I LHCb detector system. All subdetectors including tracking parts (VELO, UT, Magnet, SciFi) and PID detectors (RICH1, RICH2, ECAL, HCAL, Muon) are labeled and schematically drawn. The coordinate system points in z in beam direction [29].

As motivated in section 2.2 the overall detector system will undergo a major upgrade in LS 4. The re-designed detector system is presented in fig. 2.4.

While the initial approach, dividing the system into tracking and PID detectors, stays, each sub-system will be upgraded and some even removed while new parts will be installed.
The Upgrade II tracking system will consists of the VELO, the **U**pstream **P**ixel UP, magnet stations and the **M**ighty-**T**racker MT. The foreseen upgrade plans will be discussed in section 2.3.1.
Particle identification is achieved using information from the RICH1 and RICH2 detectors, the newly installed **T**ime **o**f internally **R**eflected **Ch**erenkov TORCH detector and the PicoCAL calorimeter.

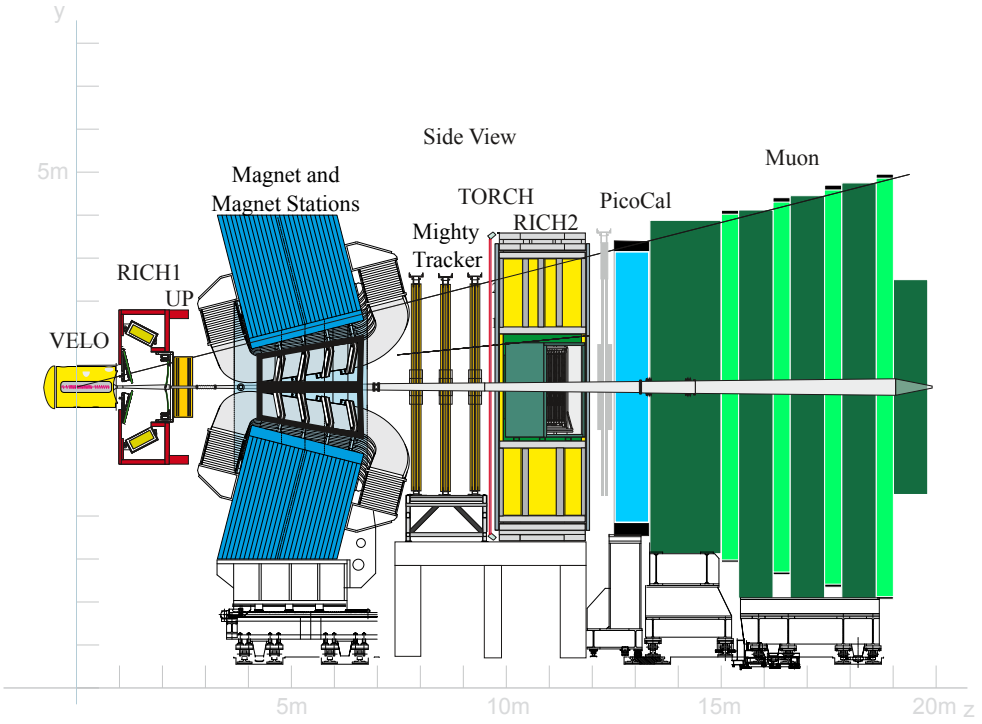


Figure 2.4: Side-view of the Upgrade II LHCb detector system. All subdetectors including tracking parts (VELO, UP, Magnet Stations, MT) and PID detectors (RICH1, RICH2, TORCH, PicoCAL, Muon) are labeled and schematically drawn. The coordinate system points in z in beam direction [1].

The challenges faced by each system at the start of Run 5 are presented in the following sections. To motivate each upgrade, an introduction of the current detector system is provided, followed by a discussion of the Upgrade II improvements.

2.3.1 Tracking at LHCb

Operation of the LHCb Upgrade II detector at a peak luminosity of $1 \times 10^{34}\,\mathrm{cm}^{-2}\mathrm{s}^{-1}$ will increase the amount of charged particles per bunch crossing immensely [8]. Hence, efficient tracking with a low fake rate is essential. Moreover, the correct association of secondary vertices to primary vertices of heavy flavor decays is crucial. The improvement of the tracking system includes the installation of new technologies enabling high granularity, fast time information and radiation tolerance. In addition to upgrading the current tracking detectors, the inner magnet walls will be equipped with magnet stations - covering the low momentum acceptance.
Foreseen plans for the magnet stations are described within this section. The Upgrade I VELO, UT, and SciFi and their upgrades towards the VELO, UP and MT are discussed in the following parts.

The Magnet System

A 4 T m dipole magnet divides the LHCb detector system into an upstream and downstream part. While currently two tracking systems (VELO and UT) are located upstream and one (SciFi) downstream, for Upgrade II additional tracking stations inside the magnet - called magnet stations - are foreseen.
Two saddle-shaped coils made up of aluminum make up the magnet [29]. Charged particles are bent in the $x - z$-plane, enabling momentum reconstruction. To overcome a polarity bias, the polarity is switched regularly.
Physics potential of LHCb can be enhanced by tracking low momenta particles. To date, particles with a momentum below $p = 5\,\mathrm{GeV}$ are not covered efficiently as most tracks are deflected into the magnet. Installing tracking stations inside the magnet overcomes this boundary. Four panels of scintillating fibers are foreseen. Consequently, particles with $p \geq 500\,\mathrm{MeV}$ are covered within the detector acceptance [5].
Ensuring operation under high irradiation causes placement of the readout electronics outside the magnet. Therefore, the light will be guided by clear fibers towards **Si**licon **P**hoto-**m**ultipliers SiPMs.
Ongoing R&D focuses on the performance at the expected radiation dose as well as on the readout architecture. Therefore, the for the SciFi developed readout chip PACIFIC is used as a base (see section 2.3.1 for more information about the SciFi). The installation of the main hardware is scheduled to LS 3. Improvements are expected by a new readout ASIC which will be installed in LS 4. Further, this ensures the possibility to replace hardware that might be damaged due to radiation in Run 4 [5].

[8] 2000 charged particles, produced within the detector acceptance, per pp crossing are expected at $L_{inst} = 1.5 \times 10^{34}\,\mathrm{cm}^{-2}\mathrm{s}^{-1}$ [1].

Vertex Locator - VELO

The VELO is positioned around the interaction point to track particles and reconstruct decay vertices produced in collisions. High tracking efficiency and granularity are essential to distinguish primary and secondary vertices. Therefore, the VELO is equipped with silicon pixel detectors and a readout ASIC operating at 40 MHz.
A key quantity for physics analyses is the impact parameter resolution - the resolution of the closest distance of the primary vertex to a reconstructed track. A good resolution is fundamental for LHCb's physics program.
Maximizing the impact parameter resolution is possible by minimizing the distance of the innermost pixels to the interaction point. Consequently, the VELO is designed to be movable close to the beam. If beams are stable and hence, unwanted radiation damage due to unstable beams is less probable, the VELO modules are moved from an *open* to a *closed* position with the closest pixel 5.1 mm away from the beam line [20].
Two movables halves are equipped with 26 modules each [20]. A high granularity and spatial resolution is ensured by a pixel pitch of 55 µm. At the end of Run 4 a radiation dose of 8×10^{15} MeVn$_{eq}$/cm^2 and 4 MGy are expected for the central pixels [20].
A dedicated hybrid sensor, consisting of a planar silicon sensor of 256 x 256 pixels [20] and a readout ASIC - called VeloPix - based on the Timepix3, have been designed to cope with this.
Under Upgrade II conditions the VELO has to be operational at higher radiation levels and particle rates. To ensure a similar performance and even improve the current, the detector system must be upgraded. Physics improvements by a suppressed combinatorial background can be achieved by adding fast time to spatial information.
Without this additional information, correct association of vertices and differentiation between them will be challenging, since the primary vertex separation is reduced to 1.5 mm (for Upgrade I: 4.2 mm) [5], due to a higher primary vertex density caused by the increased pile-up. The Upgrade II VELO is foreseen to be the first 4D tracking detector with a track timestamp resolution of 20 ps and radiation tolerance up to 6×10^{16} MeVn$_{eq}$/cm^2 for the central pixels at the end of Run 6 [5].
A 28 nm (for Upgrade I: 130 nm) technology has to be used for the ASIC to provide the needed time resolution and radiation tolerance [20] [5]. Moving from planar to 3D silicon sensors improves timing and radiation tolerance for the sensing part of the hybrid detector.
Current R&D investigations focus, among others, on reducing the material of the **R**adio**f**requency RF foil, separating the detector and the LHC vacuum, to increase the impact parameter resolution. Further, performance studies on the sensor and ASIC are ongoing with emphasis on timing performance under irradiation. Cooling technologies, using Krypton or CO_2, as well as the readout architecture and electronic system of the modules are investigated.
More information about the current status and all requirements can be found in [5] [1] [54].

Upstream Tracker - UT

Upstream between RICH1 and the dipole magnet the UT is located. Due to possible incorrect matches of long tracks between the VELO and SciFi, a substantial number of so-called ghost tracks may result. Requiring a particle to be additionally detected in the UT, significantly reduces the amount of ghost tracks. As a consequence, the trigger can process more events per time. Additionally, the track reconstruction of tracks traversing the SciFi is improved by a first charge and momentum estimation by the combination of the information from the UT and VELO. With a significance of 15% the track momentum can be derived [29]. Furthermore, the UT detects long lived particles, e.g. Λ baryons, which have no tracks in the VELO. Hence, the UT has a significant impact on charged particle tracking and thus, physics performance of LHCb.
Four layers of silicon strips arranged in a *xuvx* geometry [9] are installed in the Upgrade I UT. Depending on the occupancy and radiation damage, different pixel pitches and strip lengths are used.
The maximum dose for the innermost sensors at the end of Run 4 is 4×10^{14} MeVn$_{eq}$/cm^2 (NIEL damage) and 1 kGy (TID damage), while for most of the detector 2×10^{13} MeVn$_{eq}$/cm^2 are expected. Accordingly, different sensor types are installed. Central regions are equipped with n-in-p sensors with a pitch of 93.5 µm, while p-in-n sensors with a pitch of 187.5 µm are used for the outer parts. Further, sensors in the innermost regions are half the strip length to cope with the occupancy and allow a module design with central sensors placed 34 mm away from the beamline [29].
A specific readout ASIC, called SALT, was developed and fabricated in a 130 nm process for the UT [29].
Because of the increased occupancy under Upgrade II, silicon pixel detectors are required. Besides high granularity, fast time information and high radiation tolerance are essential to at least maintain the Upgrade I performance.
A detector consisting of four planes based on MAPS is foreseen - called **U**pstream **P**ixel UP. The used silicon pixel technology is currently investigated. Due to similar requirements with the technology foreseen for the Mighty-Pixel (see section 2.4 for more information), common efforts are ongoing. Hence, performance studies of HV-MAPS conducted for the Mighty-Pixel are also investigated under UP Upgrade II conditions. Moreover, commonalities of module and electronic architecture are shared.
Radiation tolerance has to be validated up to 3×10^{15} MeVn$_{eq}$/cm^2 and 240 MGy [5].
Studies of HV-MAPS regarding radiation tolerance have been performed within this thesis and are presented in chapter 7 and chapter 8.
Comparing the requirements with the MP requirements (presented in section 2.4), the expected data rate (74 MHz/cm^2), four times higher hit rate (150 MHits/cm^{2}s) and radiation tolerance are the main differences [55]. Therefore, these topics are evaluated in more detail.

[9] The two innermost layers *uv* are tilted by a stereo angle of 5° with respect to the outer *x* layers to obtain 2D spatial information.

Current investigations and design decisions can be found in [5] [1] [55].

Scintillating Fiber Tracker - SciFi

Downstream of the dipole magnet, three tracking stations, equipped with four layers of scintillating fibers each, are located.
To cover the full acceptance after the magnet, the SciFi has a dimension of 6 m x 5 m [29]. At each station the layers are arranged in *xuvx* geometry with a stereo angle of $\pm 5^{\circ}$ for the inner two layers and held by C-frames.
The main task of the SciFi is to reconstruct charged particle tracks and estimate their momentum. Therefore, a high hit reconstruction efficiency of 99%, mechanical stability, a material budget of $\leq 1\%$ and radiation tolerance compatible with Run 3 and Run 4 conditions are required [29]. In addition, the detector has to be granular enough to cope with the occupancy.
Hence, plastic scintillating fibers with 270 µm [29] diameter, read out by SiPMs, have been chosen. Six layers of fiber are wound in a hexagonal matrix, creating a fiber mat of 2 424 mm length and 130.6 mm width [29]. A module consists of eight fiber mats. At the center of the SciFi a mirror is positioned in order to increase the light yield. A schematic overview of the front view of one station consisting of eight mats and two half panels as well as the side view of one stations is illustrated in fig. 2.5. Fiber mats are colored in light blue and covered by black polyimide foils, helping with light shielding and supporting mechanical stability [29].

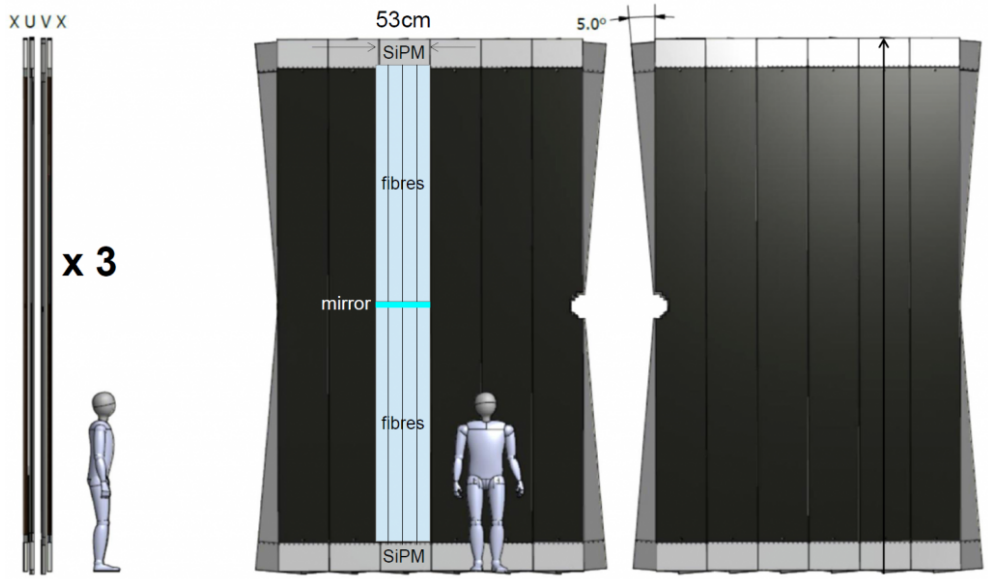


Figure 2.5: Schematic overview of one SciFi station. Fiber mats (colored light blue) are light tight and mechanically stabilized by black polyimide foils. The readout electronics as well as the mirror position are shown [56].

To ensure efficient photo-detection, SiPMs produced by Hamamatsu [57] with a pixel pitch

of 250 µm, slightly smaller than the fiber diameter (270 µm), are used [58].
The performance of both fibers and SiPMs degrades due to radiation induced damage. A signal reduction up to 40% [29] of the fibers due to transparency loss is expected. In addition, the SiPMs will suffer from the damaged silicon lattice, increasing the dark count rate significantly and resulting in the need of cooling to $-40\,^{\circ}$C [29].
Therefore, the SiPMs are glued to a titanium cold bar and enclosed, along with the fiber connection, inside a cold box. Liquid cooling and constantly flushing the system with dry gas is required to ensure those low temperatures without condensation.
Readout of the FE is realized via dedicated hardware - consisting of the PACIFIC ASIC, a clustering and master board. Firstly, received analog signals are digitized by the PACIFIC. Secondly, clustering and zero-suppression is done at the clustering board. Voltage and clock distribution as well as slow and fast control are transmitted via the master board. In addition, the data is serialized and further transmitted via optical links.
Maintaining the performance of the downstream tracker under Upgrade II conditions is a key element to ensure sufficient particle tracking at high particle and hit rates. Challenging is to find a cost-efficient solution covering the huge dimension of the SciFi tracker coping with the experimental requirements. The solution will be the Mighty-Tracker - a hybrid tracking system consisting of a monolithic pixel and a scintillating fiber detector. A detailed discussion of the Mighty-Tracker is provided in section 2.4.

2.3.2 Particle Identification System

Particle identification is a crucial element in flavor physics. Successfully studying B-physics demands precise B-hadron reconstruction. Hence, all decay products have to be well known. Therefore, knowing the interaction, mass and momentum of a particle is essential. Momentum information is provided by the tracking system while the mass can be reconstructed by the information of the PID system. With the system operated during Run 1 and Run 2 excellent hadron identification was possible.
Distinguishing kaons, pions and protons is a key element of LHCb and unique within the LHC experiments. As a result, CPV measurements of $B_s^0 \to D_s^{\pm} K^{\mp}(\pi^{\mp})$ are possible although the final state have similar topologies [5]. Moreover, lepton universality studies and measurements including electrons and neutral hadrons have been made possible by the ECAL.
Identifying muons μ is essential for many measurements at LHCb. Without precise muon detection the measurement of the rare decay $B_s^0 \to \mu^+\mu^-$ would have been impossible [5].
The Upgrade I PID system consists of two RICH detectors, a calorimeter systems and four muon stations. In the following the currently installed detectors are introduced and the need for an upgrade of those is discussed. Furthermore, planned new subsystems for Upgrade II will be introduced.

RICH

At LHCb charged hadron discrimination is possible through two RICH detectors. Thus, final states including pions, kaons and protons can be distinguished - allowing a low combinatorial background, flavor tagging and providing information for the HLT2 [29].
A momentum range of 2.6 to 100 GeV [29] is covered by the system. The system is divided into two detectors: (1) RICH1 is located upstream between the VELO and UT, covering the full angular acceptance while (2) RICH2, located downstream between the SciFi and ECAL, covers the more central region [1].
Both use Cherenkov photons to detect particles. Cherenkov light is produced by the Cherenkov effect [59]:

> If a charged particle traverses matter with a velocity larger than the speed of light in it, an electromagnetic wave is created which may polarize the lattice of the medium. Because of the particle's velocity, the relaxation time of the perturbation is shorter than the excitation. Accordingly to Huygens [60], interference occurs. If there is constructive interference, a wavefront is built - called Cherenkov radiation.
> For RICH detectors mirrors are used to focus the produced light rings onto planes. Reconstruction of the angles allows velocity reconstruction and in combination with the momentum PID.

At RICH1 C_4F_{10} is used while CF_4 at RICH2. Consequently, two different momenta regimes are covered. Namely, 2.6 to 60 GeV by RICH1 and 15 to 100 GeV by RICH2 [29].
Produced Cherenkov light is detected by **M**ulti-**a**node **P**hoto**m**ultiplier **t**ubes MaPMTs compatible with the required 40 MHz readout rate.
To maintain the Upgrade I performance and extend the PID performance further, the system will be upgraded within Upgrade II to operate in the HL-LHC era [5].
Necessary will be an improved Cherenkov angle reconstruction to enhance the upper limit of the momentum range and thus, allow a reduction of the combinatorial background [5]. Therefore, the MaPMTs need to be replaced by fast and highly granular photodetectors, e.g. SiPMs or **M**icro**c**hannel **P**late **P**hoto**m**ultiplier MCP-PMTs [1]. A time resolution of ≤ 100 ps for a single photon [61] is necessary to operate at 10 MHz/mm^2 [61] photon density.
Current R&D focuses on a suitable photodetector technology since none of the existing fulfills the experimental requirements. Hence, cooling of SiPMs to cryogenic temperatures to control the dark count, radiation tolerance and possible mechanical and cooling system solutions are investigated.
Due to the small pixel pitch and fast time information a new **F**ront-**E**nd FE-ASIC, called FastRICH, is developed to cope with the increased data throughput of 30 Tbit/s (Upgrade I: 8 Tbit/s) [5].
Information about the current status and investigated technologies are explained in [5] [1] [61].

TORCH

Improving charged hadron separation in the low momenta regime would significantly improve the flavor tagging efficiency, crucial for CPV measurements, and hadron spectroscopy. Hence, a new sub-detector called TORCH, located in front of RICH2, is planned to be installed during LS 4, covering the momentum range below the Cherenkov light emission threshold. TORCH stands for **T**ime **o**f internally **R**eflected **Ch**erenkov light and relies on the **T**ime-**O**f-**F**light TOF detection principle:

> The time needed two traverse the space two detection stages is measured by TOF detectors. Due to the relation of mass and speed, PID is possible with those detectors. Detectors consist mostly of scintillating materials and photodetectors.

For the planned detector, quartz plates are foreseen to produce Cherenkov photons. Via internal reflection the light is guided towards MCP-PMTs where focus elements focus the light. The MCP-PMTs detect and further process the signal [5].
To separate kaons and pions over a flight path of $\approx 10\,\text{m}$, a time resolution of 15 ps is required. Hence, a photo-detection with a good time resolution is essential. The time difference is measured between the detection of the photon and the corresponding track originating from the primary vertex.
As a result, kaon, pion and proton separation up to 20 GeV [5] is possible.
Due to commonalities with the RICH system, similar DAQ architecture is evaluated for TORCH. In addition, SiPMS are investigated as an alternative to MCP-PMTs.
Project milestones and the module design are described in [5] [1] [62].

Calorimeter

Particle decays including photons and neutral charged hadrons can be observed by a calorimeter system. The initial LHCb detector stack and also the Upgrade I detector consist of an ECAL and HCAL.
LHCb physics performance relies on precise electron and photon identification. The main task of the HCAL was to provide information for the $L0$ trigger.
Both detectors are separated in different regions depending on the hit density. Therefore, the dimension of the used scintillator modules varies accordingly.
The created scintillation light is collected via wavelength shifting fibers and transported towards the PMTs. A shashlik geometry of active scintillator and passive absorber media is currently installed. For the ECAL 2 mm lead absorber plates are used while iron is used for the HCAL [29].
For Upgrade II, the calorimeter system must cope with the anticipated high pile-up, requiring increased granularity and fast time information. Further, an increased radiation dose is expected. The upper limit of 40 kGy of the current ECAL modules will be reached by the beginning of LS 3 for the innermost modules.

Taking these considerations into account, and given that the HCAL is no longer strictly required due to the removal of the $L0$ trigger, the calorimeter system will be re-designed towards the PicoCal, compromising only an ECAL [5].
The new ECAL has to withstand a radiation dose of 1 MGy in the innermost region, needs a time resolution of tens of picoseconds [1] and high granularity. Therefore, a **Spa**ghetti **Cal**orimeter SpaCal design is foreseen for the central part while the outer region will be equipped with an upgraded version of the current modules. New wavelength shifting fibers will be installed for the shashlik modules to ensure fast timing.
To match the radiation tolerance, crystal fibers are foreseen for the central SpaCal with tungsten as absorber medium. For the middle part of the PicoCal plastic fibers with lead as absorber material are planned [63]. Clustering and timing improvement for the central region will be achieved by splitting the modules and reading them out at both ends.
Investigations of the scintillation materials, photodetectors and DAQ architecture are ongoing with focus on timing, radiation tolerance and processing the amount of data. More information are given in [5] [1] [63].

Muon Stations

Muon identification is a key element of many LHCb physics analyses and hence, high efficiency is mandatory. The four muon stations M2-M5 consist of 276 **M**ulti-**W**ire **P**roportional **C**hambers MWPCs, each made up of four gas gaps, and iron absorber elements to stop low momentum particles [5]. According to the occupancy and hence, required readout channels the dimension of each station is adjusted, resulting in 16 different types of chambers [29].
Keeping the Upgrade I detector performance under Upgrade II conditions, requires replacement of the current system. At the expected high luminosity the MWPC will saturate leading to dead times and therefore, in-efficient operation [5]. A highly granular detector operating at high particle rates can be achieved by a hybrid solution where the central regions will be equipped with μ-RWELL chambers [10] and the outer with newer MWPCs, possible to be operated at higher rates [5].
To reduce the expected rate, an iron-concrete shielding in front of the first station is planned to be installed.
Additionally, the FE ASIC and DAQ architecture must be upgraded to cope with the high occupancy.
The status of the developed FATIC ASIC as well as the R&D status is summarized in [1] [5] [64].

[10] μ-RWELL detectors are **G**aseous **E**lectron **M**ultiplier GEM based detectors where the μ-RWELL consists of a micro-patterned amplification stage (well) made out of Kapton embedded in a readout layer with a resistive layer in-between. The resistive layer is used for spark protection.

2.3.3 Data Acquisition System - DAQ

The LHCb **D**ata **A**cq**q**isition System DAQ reads out all subdetectors synchronously at the bunch crossing frequency of 40 MHz. In contrast to the other LHC experiments, no $L0$ hardware trigger is required, making LHCb's DAQ unique. As an advantage a high data throughput is processed, essential to obtain sufficient statistic to observe rare decays. Challenging is to reduce 4 Tbit/s of incoming data to 10 Gbit/s, retaining the interesting physics processes that can be stored.
The DAQ consists of an **E**vent **B**uilder EB farm and the **H**igh **L**evel **T**rigger HLT farm - performing a **R**eal-**T**ime **A**nalysis RTA [29]. Data from all subdetectors is sent via optical links from the cavern to the data center where the EB collects them. The back-end hardware used for this are TELL40 boards flashed with subdetector specific firmware. Collected data is pushed to the first HLT stage, called HLT1, and buffered. At this point, on **G**raphics **P**rocessing **U**nits GPUs running application, inclusive data selection of beauty and charmed hadrons based on charged particle reconstruction is done. The accepted data is sent to the second stage - HLT2. A full offline reconstruction and selection is performed. Data accepted at this stage is buffered and stored on disk.
For all readout protocols a custom designed hardware board - PCIe40 - is used. In the DAQ mode, where data from the front-ends is received and decoded, the board is called TELL40 with only receiver lines equipped. Usage for slow control needs bidirectional links. In that mode the board is called SOL40. Controlling the whole DAQ and hence, operating as a master of all modules is possible with a specialized firmware. The board is then called SODIN.
As a user the main interface to each subdetector is the SOL40. All readout boards and FE electronics are connected to SODIN to forward clock, timing and trigger information. Additionally, the **E**xperimental **C**ontrol **S**ystem ECS information is distributed.
The ECS is used to configure, monitor, control and operate the detector system. Hence, low and high voltage, cooling systems as well as configuring the FE and backend DAQ is possible with that.
For Upgrade II the main challenge is to operate the DAQ cost-efficiently at a data throughput of 200 Tbit/s [5]. The overall architecture will be the same as for Upgrade I. A new custom hardware board is designed to replace the PCIe40, namely the PCIe400, allowing faster data links of 56 Gbit/s (Upgrade I: 10 Gbit/s) as well as a network connection of 400 Gbit/s using Ethernet protocols or the PCIe Gen5 [5].
The integration of the new LHC clock distribution, called White Rabbit [11], available hardware components and the current project status are discussed in detail in [5] [1] [65].

[11] The White Rabbit allows synchronized clocks at multiple nodes in the detector system with unprecedented accuracy.

2.4 Mighty-Tracker

Covering an area of $\approx 30\,\mathrm{m}^2$ [5] and operating at high efficiencies with low material budget while being read out at 40 MHz, makes the SciFi an excellent tracking detector. Increasing the luminosity to $1.5 \times 10^{34}\,\mathrm{cm}^{-2}\mathrm{s}^{-1}$ [12] leads to particles rates of up to $17\,\mathrm{MHz/cm}^2$ and hit rates of $34\,\mathrm{MHzcm}^{-2}$ [66] at the innermost region of the downstream tracker. Additionally radiation damage of $3 \times 10^{14}\,\mathrm{MeVn_{eq}cm}^{-2}$ (NIEL) and 40 MRad (TID) [66] are expected. Besides the induced radiation damage of the installed scintillating fibers, the occupancy leads to nearly 100% ghost rate if the current SciFi would be operated under Upgrade II conditions. Charged particle tracking would be impossible and hence, LHCb physics measurements could not be continued at Upgrade I level. In addition, the track reconstruction time would increase by a factor of two [5]. To overcome these challenges and keep the performance of LHCb's tracking system at least as high as it is now, the whole downstream tracking system must be upgraded.
A cost-effective solution is found by a hybrid detector - the **M**ighty-**T**racker MT - consisting of a silicon pixel detector, called Mighty-Pixel, covering the innermost region and scintillating fibers, called Mighty-SciFi, in the outer areas.
Both detector parts are developed separately by two different development teams pushing each technology towards its best. Challenging is the common integration of both keeping, the same envelope of the current SciFi tracker.
An overview of the Mighty-SciFi is given in section 2.4.2. The Mighty-Pixel is introduced in section 2.4.3. Since performance measurements within the R&D phase of the foreseen silicon pixel technology are done within this thesis, the pixel part is emphasized.
It should be mentioned and pointed out that the R&D phase of the Mighty-Tracker is not finalized at the point writing this thesis. Hence, lots of developments are ongoing and not publicly available. Therefore, the status of the system available at this point and published in [5] [1] [66] is used as a base to describe the detector.

2.4.1 Mighty-Tracker Design

Similar to the SciFi, the MT will consist out of three tracking stations. Four layers of scintillating fibers in the same *xuvx* arrangement will be deployed. At each station, before the first and behind the last layer, silicon pixel layers will be installed, resulting in total in six layers. Each layer will cover $2.1\,\mathrm{m}^2$ for $1.5 \times 10^{34}\,\mathrm{cm}^{-2}\mathrm{s}^{-1}$ while smaller modules are foreseen for the $1 \times 10^{34}\,\mathrm{cm}^{-2}\mathrm{s}^{-1}$ scenario, which will reduce the area per layer to $1.3\,\mathrm{m}^2$ and in total to $8\,\mathrm{m}^2$ [1].
In addition, the geometry of the Mighty-SciFi, the fiber only part, will change at a lower luminosity. Two scenarios have been studied and presented in [1]. It was concluded that

[12] Since the specifications of the Mighty-Tracker are not adapted for the new luminosity scenario of $1 \times 10^{34}\,\mathrm{cm}^{-2}\mathrm{s}^{-1}$, the initial baseline scenario is quoted here to give a consistent picture of the detector design. However, reducing the luminosity would not affect the choice of technology, but rather the Mighty-Pixel design. A discussion of this is given in the corresponding sections.

shortening of the fiber modules is preferred instead of reducing detection layers. Consequently, a small loss in acceptance is expected.
The front view of the baseline geometry [13] is shown in fig. 2.6. Fiber modules are colored in light blue and cover the outermost area while the silicon part (colored brown/black) is arranged in the central region according to the hot occupancy region. At the top and bottom of each half the fiber readout and services are located. The whole detector is held by C-frames similar to the SciFi.
Their design and shared infrastructure of both detector parts is investigated at the time of this thesis.

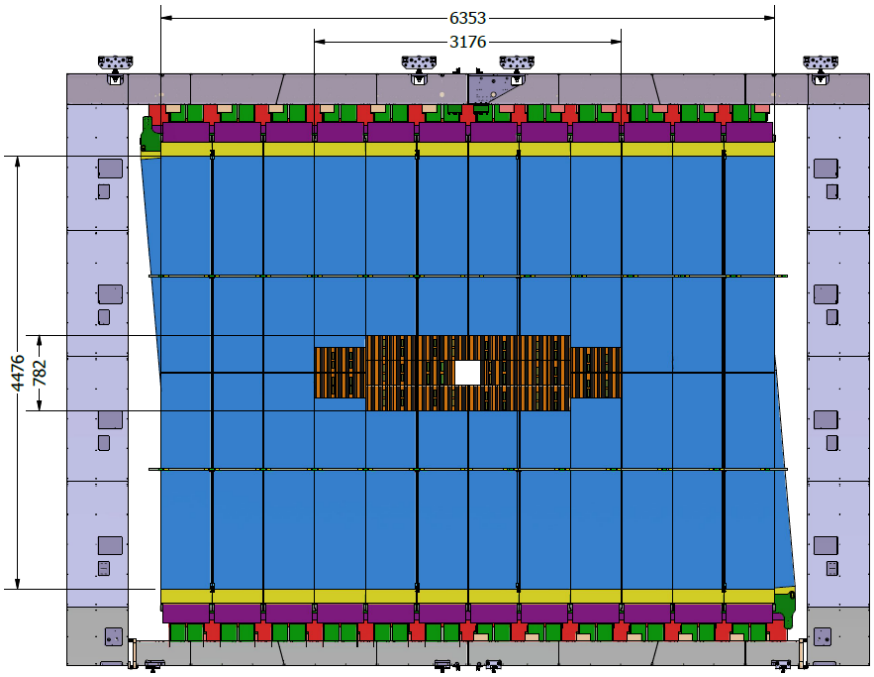


Figure 2.6: Front view of the MT with fiber modules (colored in blue) in the outer detector regions and silicon pixel modules (colored brown/black) in the innermost area where the occupancy is maximal. The detector is held by C-frames (colored in gray). Additionally, the readout electronics at the top and bottom of each halves are indicated as well as the dimensions for the baseline scenario [1].

[13] To be consistent with the terminology in [1], the baseline scenario covers the detector design and specifications for 1.5×10^{34} cm^{-2}s^{-1}.

2.4.2 Mighty-SciFi

The design of the Mighty-SciFi will inherit knowledge gained by the SciFi. Hence, the most critical points are radiation tolerance of the fibers and an acceptable dark count rate of the SiPMs.
Current fiber developments have proven green fibers to be more radiation tolerant than blue emitting fibers [5]. Currently installed SiPMs would have an unacceptable **D**ark **C**ount **R**ate DCR while being operated at similar temperatures as for Upgrade I. Reducing the DCR is mandatory to use them. In addition, a radiation tolerance of $3 \times 10^{12}\,\mathrm{MeVn_{eq}cm^{-2}}$ [1] is required. Studies operating them at cryogenic temperatures have proven the radiation tolerance. Thus, cryogenic cooling is foreseen for Upgrade II. Therefore, a cold box with vacuum insulation is designed with a vacuum feed-through for the connection between fiber mats and flex PCBs.
Moreover, a high photon detection efficiency must be ensured. Micro-lenses are investigated in order to concentrate the light on the detection area. As a result, 20% [1] light yield improvement was measured for the smaller pixel sizes. Consequently, the recovery time can be improved, cross talk between pixels reduced and self-heating reduced due to operation at lower gain [5].
Investigations on the number of fiber layers within a fiber mat are ongoing. The goal is to reduce the cluster size derived by the amount of triggered SiPM channels. Four instead of six fiber layers show a reduced cluster size while maintaining a similar hit detection efficiency [5]. In addition, the geometrical efficiency will be increased by overlapping the mats and modules. Furthermore, the module size varies accordingly to the area covered by the Mighty-Pixel. In the central part, mechanical support is provided by honeycomb structures between each layer, supported by C-frames at the end of each module [1].
Due to the long signal tails of the cooled SiPMs a new readout ASIC version is required. The PACIFIC++ will be the successor of the SciFi PACIFIC. Besides adjusted signal shaping, a simplified clustering compared to Upgrade I is implemented [67]. Hence, no FPGA is required which reduces the power budget. Furthermore, the **T**ime-**o**f-**A**rrival ToA information is obtained by a **T**ime-to-**D**igital **C**onverter TDC with a resolution of ≤ 1 ns [1].

2.4.3 Mighty-Pixel

Covering the central region of another tracking detector using a different detector technology, leads to challenges of the mechanical design itself and support structures. Simulations of the expected occupancy and track reconstruction efficiency for Upgrade II conditions have lead to different geometrical design scenarios. Following the baseline luminosity scenario, the design of the **M**ighty-**P**ixel MP covers the innermost region where the fibers cannot cope with the occupancy and hence, expected radiation damage. An overview of the front of one MP layer is shown in fig. 2.7 [14].

[14] Disclaimer: All shown schematics are are intended only as illustrations and not as final design schematics.

The module design follows the stave topology. Hence, the readout electronics (colored in green) are relocated outside the active area of the module (colored in brown) and connected via flex cables, resulting in reduced dead area, less material budget and less radiation damage of the electronics.

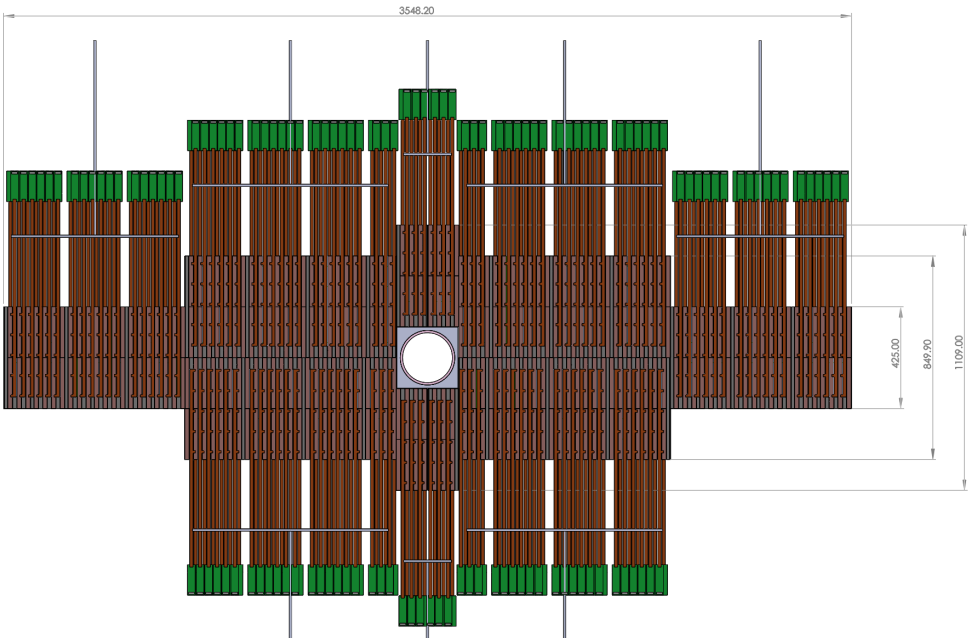


Figure 2.7: Front view of one MP layer for the baseline luminosity scenario. Readout electronics (colored in green) are positioned at the top/bottom of one module, connected via flex cables, following the stave topology. Modules (colored in brown) are arranged around the beam hole to cover the highest occupancy region. Dimensions of modules and the whole MP layer are indicated [66].

One module consists of a sandwich structure shown in fig. 2.8. Each stave is double-sided instrumented with four columns per side containing four hybrid flexes with five sensors each to reduce gaps and thus, dead areas. Two columns (one double-column) are connected to a tape for data transmission and power distribution which is connected to a **H**igh **D**ensity **I**nterconnect HDI, containing optical links and data processing hardware.
Cooling of the module is unavoidable to ensure the required performance under irradiation. Therefore, a titanium cooling pipe is embedded in the central part of each module, enabling 2-Phase CO_2 cooling. A thermal connection as well as mechanical support is provided by carbon foam and fiber sheets.

The main task of the hybrid is to provide electrical connections to five sensors simultaneously, including high and low voltage supply, as well as transmitting clock, TFC, and ECS signals. Investigations on the data transmission and power distribution connector are ongoing [66]. Serial powering of the hybrids is targeted since other powering schemes, e.g. point-to-point powering, are not feasible. The final scheme is still under investigation. Studies using sensors

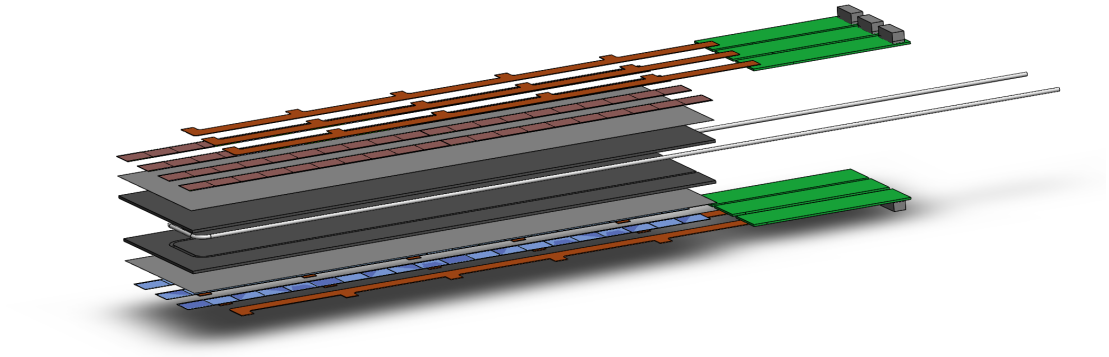


Figure 2.8: Exploded view of one stave with HDI PCBs (colored in green) at one end. One stave is double-sided equipped with pixels to reduce dead areas. Mechanical stability and a thermal connection is provided by carbon foam and fiber sheets. Titanium cooling pipes are located in the middle to cool the module. Data links and power are distributed by a tape on top of the sensors and connected to the HDI PCB. [66].

developed for the ATLAS experiment show promising results powering two columns [15] connected to one HDI via one tape. Hence, eight hybrids are powered via one serial power chain at the same time while four chains are required to power one double-sided instrumented stave [66].
For the high voltage distribution a possible switch connecting two columns is discussed. Consequently, only one HV feed per serial power chain would be needed [66].

2.4.4 MightyPix

Due to the increased luminosity a high occupancy is expected. Specifications for the baseline luminosity scenario derived an expected maximum particle density of $17\,\mathrm{MHz/cm^2}$ and hit rates up to $34\,\mathrm{MHzcm^{-2}}$ [66] in the central detector region. In addition, radiation doses of $3 \times 10^{14}\,\mathrm{MeVn_{eq}cm^{-2}}$ (NIEL) and 40 MRad (TID) [66] are estimated. Moreover, a time resolution of $\leq 3\,\mathrm{ns}$ is required to associate hits to the correct bunch crossing with a 4σ significance [66].
Furthermore, a power budget of $\leq 150\,\mathrm{mW/cm^2}$ [66] and low material budget are crucial to minimize multiple scattering and ensure precise particle tracking.
Finally, covering a large area with silicon detectors is cost-intense. A cost-effective solution possible to fulfill the experimental requirements are **H**igh-**V**oltage **M**onolithic **A**ctive **P**ixel **S**ensors HV-MAPS [16].
The sensor developed to fulfill all requirements, summarized in table 2.1, is called MightyPix. The interplay of all requirements makes this sensor unique within full size HV-MAPS used at

[15] A column represents one longitudinal side of a module. One module contains four columns per side.
[16] The technology of HV-MAPS and silicon pixel detectors in general are described in chapter 3.

Parameter	Specification
Pixel size (bending plane)	$\leqq 100\,\mu m$
Pixel size (non-bending plane)	$\leqq 200\,\mu m$
Substrate thickness	$< 100\,\mu m$
Maximum particle rate	$17\,MHz/cm^2$
Maximum hit rate	$34\,MHzcm^{-2}$
Maximum data word length	32
Mighty-Pixel efficiency (including dead areas)	$> 96\%$
In-time efficiency	$> 99\%$
Maximum noise rate	$\leq 400\,kHz/cm^2$
Data transmission rate	4x 1.28 Gbit/s
Radiation damage: NIEL	$3 \times 10^{14}\,MeVn_{eq}cm^{-2}$
Radiation damage: TID	40 MRad
Power consumption	$\leq 150\,mW/cm^2$

Table 2.1: Summary of the experimental requirements of the Mighty-Pixel and hence MightyPix. Numbers are taken from [66].

LHC experiments. Particularly challenging is the required time resolution at the expected radiation damage for the anticipated power budget.
Currently a first version, MightyPix1, is available. The next sensor iteration, MightyPix2 [68], is planned to be fabricated until beginning of 2026. MightyPix3, the final sensor, will be designed based on MightyPix2 and other predecessors. Performance studies are incorporated to guide possible design adaptions. Common for all iterations of the MightyPix is the HV-CMOS technology which is explained in section 3.4.

All sensors are based on the HV-MAPS designed at KIT [17]. The development of these sensor types and predecessors are discussed in chapter 4.
Since the sensor, called TelePix2, characterized within this thesis is part of the predecessors, a detailed explanation of the sensor design is given in chapter 4, as well.
In the following the design specifications of the MightyPix and the current R&D status is explained in more detail.

Because of the high occupancy a good spatial resolution is crucial. Simulations have shown that sensors of size 100 µm x 200 µm would be sufficient to fulfill the requirements. Current developments have shown that squared pixel sizes are advantageously in terms of signal collection efficiency and charge sharing. Therefore, MightyPix2 is designed with a pixel size of 84 µm x 84 µm [66]. In contrast to the final MightyPix, MightyPix2 has a reduced sensor size of 2 cm x 1.66 cm instead of 2 cm x 2 cm [66].

[17] At the **K**arlsruher **I**nstitut für **T**echnologie KIT the group of I. Péric designs all MightyPix prototypes as well as sensors similar to it such as the TelePix2.

The final substrate thickness is still under discussion. Thinning of the sensors is definitely required to reduce the material budget. However, studies using these type of sensors thinned to 50 µm have shown worse performance compared to sensors with a thickness of 100 to 200 µm [69].
To ensure the sensor's functionality at the expected data rates, simulations have been performed [70]. Measurements proving this are not yet done and part of the ongoing R&D projects.
Testing the efficiency, time resolution and in-time efficiency for non-irradiated as well as irradiated sensors is crucial to fulfill the experimental requirements. Since performance studies regarding this are done within the scope of this thesis, no detailed discussion is given here. The need for those measurements, results and possible impacts on the MightyPix and overall Mighty-Pixel design are explained in the corresponding parts of this thesis, starting with chapter 6.
A crucial aspect not tested so far is the power budget in dependence on the operation temperature. Because most predecessors have not been designed to fulfill the MightyPix requirements and for LHCb Mighty-Tracker project, they were not designed to meet the required power budget. In addition, pixel and sensor sizes differ as well as the embedded ASIC electronics. Hence, meaningful conclusions cannot be done without hesitations. However, testbeam campaigns with the ATLASPix3.0 and ATLASPix3.1 (both are part of the predecessors for the MightyPix) have shown operating the sensors at cold temperatures, especially after irradiation, increases the performance significantly [9] [18].
The first sensor of the MightyPix developments, MightyPix1, was produced in a 180 nm CMOS process at TSI [71]. With the analog part, featuring all specifications, the sensor was intended to be a dedicated test sensor with a pixel size of 165 µm x 50 µm and sensor size of 0.5 cm x 2 cm [66]. The digital part is not fully compatible with the LHCb DAQ. Hence, testing most of the required digital features will first be possible with MightyPix2 [19].
Due to a design flaw of MightyPix1 the bias load line was grounded such that the sensor could not be configured coming from the manufacturer. A **F**ocused **I**on **B**eam FIB surgery was required to correct the issue and enabled the configuration of the sensor. A few sensors were operated successfully afterwards. However, the configuration is not stable due to the constant load. Because of that and the small amount of repaired sensors, no systematic studies with MightyPix1 have been performed. But, laboratory measurements of the time resolution have shown promising results and will be presented in [69].
Hence, detailed studies with predecessors, such as the previously mentioned ATLASPix and TelePix2, were essential to investigate the performance of HV-MAPS to show the technologies compatibility with the Mighty-Pixel requirements.

[18] It should be mentioned that the author of this thesis participated at both testbeam campaigns presented in [9] and contributed significantly to the data analysis and understanding of the results.
[19] MightyPix2 and successors will be produced the 180 nm process at AMS [72]. Further fabrication at TSI is not possible since the production line was closed. Because of that, slight changes in the sensor design were required. An overview is given in [68].

CHAPTER 3

Principles of Silicon Detector Technology

The working principles of semiconductors are commonly exploited for particle detection in **H**igh **E**nergy **P**hysics HEP experiments such as the LHCb experiment at CERN (introduced in chapter 2). To understand the working principle and the challenges of such detectors, it is necessary to discuss the fundamental principles of semiconductors, which is the goal of this chapter.
Firstly, the detection of particles requires their interaction with matter. Thus, the interaction of particles with matter with focus on typical particles at high energy experiments (heavy charged particles, light charged particles and photons) is explained in section 3.1. Further, the influence of scattering of particles with matter and its consequences are introduced in section 3.1.2.
The measurable signals produced by those interactions can be detected with semiconductor detectors. Hence, their working principle - starting with an introduction of the underlying theory - is explained in section 3.2. Moreover, the movement of charge carriers, the generation of a signal at the readout electrodes, and the readout electronics themselves are discussed.
Since such detectors are operated over a long period in high-radiation environments (see chapter 2 for more information), damages due to radiation occur. Those are discussed in section 3.3. Measurements concerning the radiation tolerance are presented in chapter 7 and chapter 8.
The introduced concept of silicon as pixel detectors and its challenges in harsh radiation environments led to the development of different silicon-based technologies. The technology foreseen for the Mighty-Pixel (introduced in section 2.4.3) is a **M**onolithic **A**ctive **P**ixel **S**ensor MAPS, which is introduced in section 3.4.
How **H**igh **V**oltage HV-MAPS are characterized and the obtained results are presented in chapter 6 and chapter 9.

3.1 Interaction of Particles with Semiconductor Detectors

When particles traverse matter, various interactions occur with probabilities that depend on the particle type and the material properties. Thus, the design of a particle detector depends on the occurring processes. Since silicon is used for the active area of the Mighty-Pixel detector, the main energy loss happens via ionization and excitation.
Depending on the particle type different processes have to be taken into account. For charged particles these are discussed in section 3.1.1 and for photons in section 3.1.3.

All explanations in this chapter are mainly based on detailed studies and derivations presented in [34], [73] and references therein. If other references are used, citations are provided.

3.1.1 Energy Loss of Charged Particles

If a charged particle traverses matter, energy loss due to collisions with the mediums' atoms occur. The amount of transferred energy T depends on the interaction cross section σ_A, the mass M and velocity β of the particle [34]:

$$-\left\langle \frac{\mathrm{d}E}{\mathrm{d}x} \right\rangle = n \int_{T_{min}}^{T_{max}} T \frac{\mathrm{d}\sigma_A}{\mathrm{d}T}(M, \beta, T)\mathrm{d}T \tag{3.1}$$

with the target particle density n. Due to electromagnetic interaction between the incoming particle and the atom's Coulomb field, the scattering process is described by Rutherford scattering [74]. Including the cross section in eq. (3.1) the Bethe equation (see eq. (3.2)) can be derived [34]. Since the transferred energy is often small and fluctuates, the mean energy loss per path length $\left\langle \frac{\mathrm{d}E}{\mathrm{d}x} \right\rangle$ is quoted [34] [73]:

$$-\left\langle \frac{\mathrm{d}E}{\mathrm{d}x} \right\rangle = K \frac{Z}{A} \rho \frac{z^2}{\beta^2} \left[\frac{1}{2} \ln \frac{2 m_e c^2 \beta^2 \gamma^2 T_{max}}{I^2} - \beta^2 - \frac{\delta(\beta\gamma)}{2} - \frac{C(\beta\gamma, I)}{Z} \right] \tag{3.2}$$

with:

- Constant terms: $K = 0.307\,\mathrm{MeV cm^2/mol}$ depends on the electron mass and its radius; the electron mass $m_e = 511\,\mathrm{keV}$; speed of light $c \approx 300\,000\,\mathrm{km\,s^{-1}}$
- Material properties: Z/A is the fraction of protons per nucleus; material density ρ
- Particle properties: charge number z; $\beta\gamma$ relativistic properties; maximal possible energy transfer to an electron for a single collision T_{max}
- Mean excitation energy I of the material

- Density correction $\frac{\delta(\beta\gamma)}{2}$ for high energies
- Shell correction $\frac{C(\beta\gamma,I)}{Z}$ for low energies

Important is that this equation describes the mean energy loss $\left\langle \frac{dE}{dx} \right\rangle$, often called the mean/mass stopping power when the energy loss is normalized to the material density.
The energy dependence of the mass stopping power is shown in fig. 3.1. As an example the energy loss of a positively charged muon in copper can be seen.

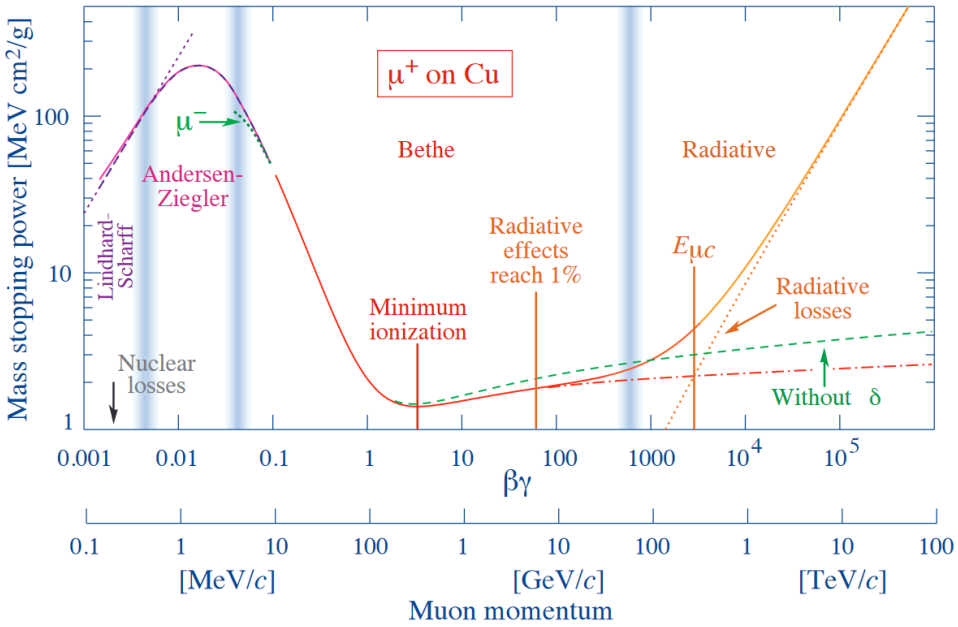


Figure 3.1: Dependence of the mass stopping power in units of MeVcm^2/g for different particle energies in terms of $\beta\gamma$ and the momentum p of a muon in copper Cu [73]. Different regimes depending on the ongoing interaction processes and corrections are visualized.

The regime labeled "Bethe", typically between $0.1 < \beta\gamma < 1000$, refers to the ionization dominated regime and is described by eq. (3.2).
At low energies of $0.1 \leq \beta\gamma \leq 1.0$, the $1/\beta^2$ dependence dominates, which can be explained by an increasing momentum transfer at low velocities. With increasing energy the stopping power increases due to two effects: (1) Kinematics and (2) relativistic. Firstly, the transferred energy T increases with γ. Secondly, the transverse electrical field increases with γ, too - increasing the impact parameter and hence, the mass stopping power. However, the increase is limited by the density effect. Because of the larger electrical field, surrounding atoms get polarized and thus, counteracting the extension of the field.
In-between the $1/\beta^2$ and logarithmic-rise regime, a minimum at $\beta\gamma \approx 3 - 3.5$ of $(1 - 2)$ MeVcm^{2}g^{-1} is observed. Particles within this region are called **M**inimum **I**onizing **P**articles MIP. Since those particles spend a minimal time in the vicinity of the atom, their

energy loss is minimal. Muons, which have typically an energy of 1 to 100 GeV, are mostly of this nature. Therefore, muon detection is done separate from other light charged particles. At very high energies of $\beta\gamma \geq 1000$ radiative effects occur which are not described by eq. (3.2). The other extreme occurs at very low energies. Within this regime the particle's velocity is close to the velocity of electrons in the shell. Hence, shell corrections have to be taken into account [73].

Energy Loss of Light Charged Particles

Since eq. (3.2) shows a mass dependence, the interaction of light particles, e.g. electrons/positrons, with matter differs from the previously discussed heavy charged particles.
At very low energies ionization is the dominating interaction for electrons/positrons. However, this differs compared to heavy charged particles due to possible different spins, in-distinguishability between electrons and the medium's electrons and their kinematics [34]. Furthermore, other processes as annihilation for positrons have to be taken into account. A more detailed description can be found in [75].
At higher energies electrons/positrons mainly lose their energy via Bremsstrahlung which describes the energy loss by radiation of photons due to scattering of the electron off the Coulomb field [34] [75]. The amount of lost energy depends on the particle energy E and the radiation length X_0 of the material [34]:

$$\left(\frac{\mathrm{d}E}{\mathrm{d}x}\right)_{rad} = -\frac{E}{X_0} \tag{3.3}$$

After one radiation length X_0 the electron energy is reduced to $1/e$ of its initial energy. Often the thickness x of a detector is described by fractions of X_0 - called material budget x/X_0. The point where both processes (Bremsstrahlung and ionization) have the same rate of energy loss is called critical energy E_C [75].

Fluctuations in Energy Loss

δ-Electrons

For very large energy transfers ($T \gg I$) δ-electrons can be produced. These are shell-electrons that are 'kicked' out of the shell by up to 90° in central collisions.
Due to the $1/T^2$ [34] energy dependence the energy distribution has a large tail towards high energies which is especially important for highly relativistic particles.
If the detector is thin, δ-electrons can escape the active area which results in a loss in the detected energy. In addition, photons produced via Bremsstrahlung or by annihilation can escape the detector. Hence, it is common to modify the Bethe formula by restricting the maximum energy transfer to $T_{cut} < T_{max}$.
Moreover, the spatial resolution of a detector is impacted by δ-electrons. The produced ionization track is broadened by electrons ejected perpendicular to the initial particle's track.

In addition, low-energy electrons increase the amount of ionization of the material due to the $1/\beta^2$ dependence, which can lead to the formation of clusters.

Statistical Fluctuations

Although the energy loss is described as the mean energy loss per path, the total energy loss fluctuates due to the statistical nature of collisions which can be described by a Landau distribution [75]. Two main effects lead to fluctuations: (1) Number fluctuations and (2) energy fluctuations.
Number fluctuations originate from the Poisson statistic of the number of ionization processes N. Energy fluctuations stem from fluctuations of the transferred energy between single processes [34]. This results in a long tail in the energy loss distribution towards large energy depositions. Therefore, the measured mean energy loss is highly influenced by those fluctuations. A more reliable variable is the **M**ost **P**robable **V**alue MPV because of its long tail independence.
Depending on the detector thickness different models have been derived to characterize the energy loss distribution. For thin detectors, such as HV-MAPS (see section 3.4) with a typical thickness of 50 to 200 µm, the model developed by Landau and Vavilov can be used [76] [77].
From a statistics point of view, a Gaussian distribution is expected by the Central Limit Theorem [75] if enough random variables are summed. In thick detectors more collisions take place compared to thin detectors, such that the core of the energy loss distribution is more Gaussian-shaped.
However, for thin detectors the Central Limit Theorem cannot be applied since the Landau distribution is only defined to the maximal energy transfer T_{max}.

3.1.2 Multiple Scattering

Charged particles traversing matter not only lose energy, as discussed in section 3.1, but also scatter by the electric field of a nucleus which is described by Rutherford scattering [34] [74]:

$$\frac{\mathrm{d}\sigma}{\mathrm{d}\Omega}_{Rutherford} = z^2 Z^2 \alpha^2 \hbar^2 \frac{1}{\beta^2 p^2 \sin^4(\theta/2)} \tag{3.4}$$

with the scattering angle θ, the charge z, velocity β and momentum p of the incoming particle and the nucleus number Z. Due to the high energies at the LHC the scattering angles are small. In theory a Gaussian distribution for an infinite number of scattering processes is expected. However, for a finite number of processes the scattering angle distribution is described by the Molière distribution [78]. Especially at tails towards large scattering angles, the distribution models differ while measured data are described more reasonable by Molière [34].
For thick detectors the Gaussian approximation can be used to describe the scattering angle θ_{MS} [34]:

$$\theta_{MS} = \frac{13.6\,\mathrm{MeV/c}}{p\beta} z \sqrt{\frac{x}{X_0}} (1 + 0.038 \ln(x/X_0)) \tag{3.5}$$

with the charge z, velocity β and momentum p of the scattered particle, the material thickness x and the radiation length X_0.
Since multiple scattering worsens the spatial resolution, particle tracking detectors are designed such that multiple scattering is minimized. Thus, semiconductor based detectors are build as thin as possible with high X_0 material leading to a small material budget x/X_0 (see table 2.1 for the requirements of the Mighty-Pixel).

3.1.3 Energy Loss of Photons

In contrast to the energy loss of charged particles in matter, the energy loss of photons is of different nature. Photons are either absorbed or scattered. Hence, the number of photons N follows an exponential decay [34]:

$$N(x) = N_0 \exp(-\mu x) \tag{3.6}$$

with the absorption coefficient μ which can be expressed by the mean free path length $\lambda = \mu^{-1}$ [34]. Further the following dependency can be derived [34]:

$$\lambda = \frac{1}{n\sigma} \tag{3.7}$$

where n describes the target density and σ the cross section. Due to the dependence of the cross section on the material properties the cross section differs for different materials. In fig. 3.2 the cross section in dependence of the photon energy for lead is depicted.

The total cross-section is affected by various types of photon interactions. Main interactions are:

- **Photoelectric Effect - Absorption with emission of a shell-electron:**
  If a photon interacts via the photoelectric effect, its full energy is absorbed by the atom. Thus, a shell-electron can leave the shell if the transferred energy E_γ is larger than the binding energy E_B. The electron has the kinetic energy $T = E_\gamma - E_B$ [34].
  Since the absorption probability is given by the binding energy, jumps in the cross section are observed (see fig. 3.2: $\sigma_{p.e.}$), originating from the energy levels in the atomic shell structure. Depending on the photon energy, electrons from higher shells (with larger binding energy) can leave the atom. Hence, edges in the spectra occur. Electrons from outer shells may fill the created vacancy by emission of a x-ray with discrete energy which can be used to characterize and identify elements.

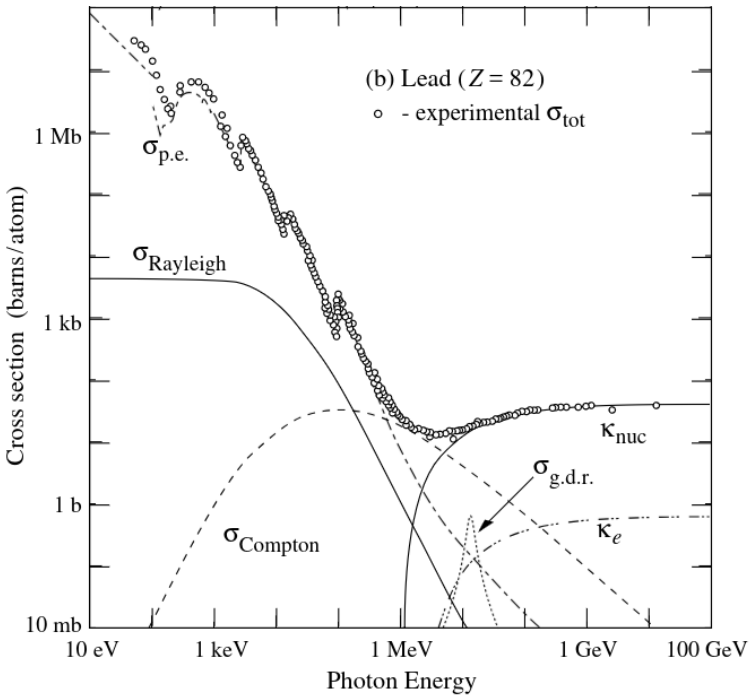


Figure 3.2: Cross section in barns/atom for different photon energies of photons in lead. Most important contributions of the cross section are depicted [75]

The dependence on the shell structure Z and the energy E for the K-shell is given by [34]:

$$\sigma_{p.e} \propto E_\gamma^{-m} Z^n \approx E_\gamma^{-3.5} Z^{(4-5)} \tag{3.8}$$

where m, n depend on the ratio of the binding and kinetic energy of the shell electron. A decrease of the cross section with increasing energy due to an increased discrepancy between E_γ and E_B is visible in fig. 3.2. For very high energies the energy dependence has to be corrected to E_γ^{-1}. However, at such high energies the cross section is not dominated by the photoelectric effect but by pair production and the Compton effect. To detect photons, the deposited energy in the detector is measured. If the full photon energy is deposited, a characteristic peak - called photopeak - is visible. Further structures depending on secondary photons can occur. More information can be found in [34].

- **Compton Effect - Inelastic scattering with an shell-electron:**
  If the photon energy ($\mathcal{O}(1\,\text{MeV})$) is much larger than the binding energy, the electron is called quasi-free. Thus, the cross section is proportional to the atomic number Z. The

scattering process of a photon off such an electron, is described by the Compton-effect. Due to the scattering process the photon's energy and flight direction are changed with respect to its initial properties. The scattered photon energy E'_γ depending on the scattering angle Θ can be derived in compliance with energy and momentum conservation [34]:

$$E'_\gamma = \frac{E_\gamma}{1 + \epsilon(1 - \cos\Theta)} \tag{3.9}$$

with $\epsilon = \frac{E_\gamma}{m_e c^2}$. For a scattering angle of 180° the transferred energy is maximal. In the measured energy spectrum a sharp edge occurs - called Compton edge. Other scattering angles lead to smaller deposited energies in the detector resulting in a continuous spectrum - called Compton continuum.
Besides scattering inside the active detector material, Compton scattering can happen outside the detector. If the scattered electron deposits its energy inside the detector, a backscatter peak in the energy spectrum is observed [34].

- **Pair Production - Creation of an electron-positron pair:**
  If the photon energy is larger than the rest mass of an electron and a positron, a conversion into those is possible. This process is called pair production.
  Due to energy and momentum conservation this is only possible within a Coulomb field of a nucleus. The recoil energy is (mostly) negligible due to the mass difference [34].
  The inversion of this interaction is the previously discussed Bremsstrahlung (see section 3.1. The Bethe-Heitler process models both interactions and the cross section [34]:

$$\sigma_{p.p} \approx \frac{7 \cdot A}{9 \cdot X_0 \cdot N_A \cdot \rho} \tag{3.10}$$

  with the Avogadro constant N_A, the particle density ρ and the atomic mass number A. Due to the dependence on the atom's electric field an implicit dependence of the cross section on Z^2 can be deduced [34].

A comprehensive summary of the dependence on the atomic number Z on the photon energy E_γ is illustrated in fig. 3.3. The different regimes for the main photon interactions are indicated.
At low energies ($\mathcal{O}(keV)$) the photoelectric effect dominates while at high energies ($E_\gamma \geq 2m_e c^2$) the leading process is pair production. In between Compton scattering dominates.
For silicon ($Z = 14$) Compton scattering has a large contribution over a wide energy range while the photoelectric effect and pair production are comparatively minimal. With increasing

Z Compton scattering is only dominating at a small energy range. Taking these dependencies into account detectors can be specialized depending on their operational goal.

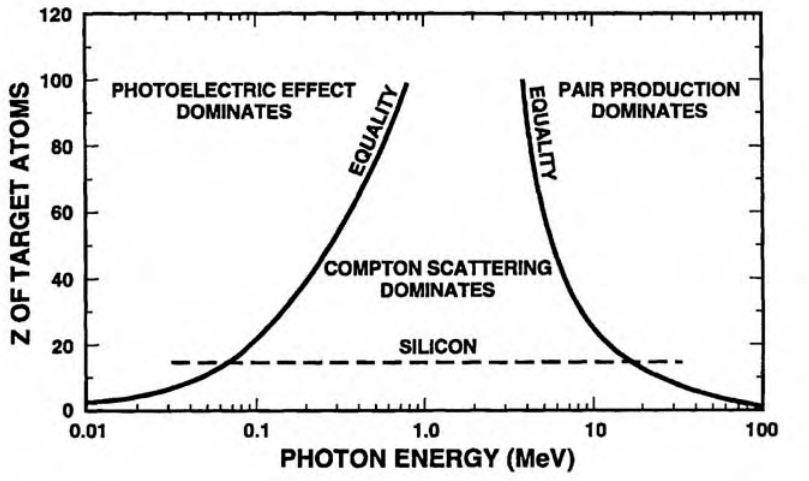


Figure 3.3: Dependence of the atomic number Z on the photon energy for the main photon interaction processes. The different regimes for the processes are labeled as well as the atomic number of silicon ($Z = 14$) [79].

A more detailed description for all processes can be found in [34] and [75].

3.2 Semiconductors as Particles Detectors

Since MAPS are the foreseen technology for the Mighty-Pixel, the fundamentals of semiconductors as particle detectors are discussed within this section. Therefore, the underlying theoretical concept of a semiconductor is discussed in section 3.2.1. Next, silicon as a semiconductor material is introduced in in section 3.2.2, followed by a discussion of doping in section 3.2.3, and the formation and characteristics of the pn junction in section 3.2.4, including its operation as a detector. How charge carriers move and create signal inside the detection medium is explained in section 3.2.5 and section 3.2.6. Finally, the electronics used inside a monolithic sensor are introduced in section 3.2.7.

Theories and concept introduced in this section are based on [34], [80], [81] and references therein. If other references are used, citations are given.

3.2.1 Theoretical Concept of Semiconductors

The lattice structure of silicon leads to a periodic electrostatic potential $V(\vec{r})$ - built by the lattice atoms where an electron can move through. Its states are described by the time-independent Schrödinger equation [82] [83]

$$\left(-\frac{\hbar^2}{2m}\nabla^2 + (V(\vec{r}))\right)\Psi(\vec{r}) = E\Psi(\vec{r}) \tag{3.11}$$

with the effective mass m, the envelope of the wave function $\Psi(\vec{r})$ and energy E. The wave function can be solved by a Bloch wave [84] [83]:

$$\Psi(\vec{r}) = \exp(i\vec{k}\vec{r})u_{\vec{k}}(\vec{r}) \tag{3.12}$$

where $u_{\vec{k}}(\vec{r})$ describes the lattice periodicity and $\vec{k}$ the momentum of the crystal.
The introduced model is valid for an ideal, infinite lattice. In a real, finite lattice the energy of single atoms is split-up in discrete energies. Since the energy difference between these is close for different atoms, so called energy bands are formed [34].
Two bands (at $T = 0\,\mathrm{K}$) are relevant to define the material properties in terms of conductivity: (1) Conduction and (2) valence band.
Within the conduction band the states of the lowest occupied band are summarized while the band shortly below it is called valence band. The energy region separating both is called bandgap. Inside it, no energy states are allowed.
Depending on the size of the bandgap at 0 K the material can be classified in three types: (1) Conductor, (2) semiconductor and (3) insulator.
For conductive materials (mostly metals) both bands overlap such that no bandgap exists. A

current flows as soon as electrons occupy different states which is possible in a metal without external energy.
In contrast to that, insulators are non-conductive. Electrons inside the valence band are strongly bound between the atoms while no charge carriers occupy the conduction band. Because of the large bandgap ($\approx 9\,\text{eV}$) charge carriers cannot overcame the gap by thermal excitation at room temperatures resulting in non-conductivity [34].
Valence electrons in semiconductors are bound less leading to a reduced bandgap of $O(1\,\text{eV})$ [34]. Hence, electrons can overcome the barrier and occupy states in the conduction band - resulting in an electron current. The created vacancies in the valence band lead to a possible current flow, too. Depending on the semiconductor material thermal excitation is sufficient to overcome the bandgap [34].

3.2.2 Silicon as a Semiconductor

A typical material for semiconductor based detectors in HEP is silicon. At room temperature the bandgap energy is $1.12\,\text{eV}$ [34]. Therefore, external excitation is necessary to conduct a current. Increasing the temperature T leads to a reduced gap while lowering T increases the bandgap energy. Hence, a dependence of the conductivity on the temperature can be deduced. The Fermi-Dirac distribution for spin-$1/2$ particles describes the probability distribution for electrons by [80]:

$$f(E) = \frac{1}{1 + \exp((E - E_f)/k_B T)} \tag{3.13}$$

with the Boltzmann constant k_B and E_F denoting the Fermi energy which is the energy at where the occupation probability is 50%. In silicon, the Fermi energy is located at the midpoint of the bandgap at $T = 0\,\text{K}$. The number of electrons n is then derived by [80]:

$$n = \int_{E_C}^{\infty} N(E) f(E) dE \tag{3.14}$$

where $N(E)$ describes the energy states and E_C the conduction band energy. A detailed derivation for $N(E)$ can be found in [34].
With this the intrinsic charge carrier concentration n_i in silicon for a thermal equilibrium[1] can be derived [34]:

[1] The number of recombination and excitation processes between the conduction and valence band are equal leading to an equal amount of electrons n and holes p.

$$n_i = \sqrt{N_C N_V} \exp\left(\frac{1}{2}\frac{E_g}{k_b T}\right) \approx 1.01 \times 10^{10}\,\mathrm{cm}^{-3} \tag{3.15}$$

N_C and N_V being the effective densities in the conduction and valence band and the bandgap energy $E_g = E_C - E_V$. Due to temperature dependence of $N_{C,V}$ the charge carrier concentration has a strong temperature dependence.
Further, the conductivity σ_i can be calculated considering the charge carrier mobility μ_i [34]:

$$\sigma_i = n_i e(\mu_e + \mu_h) \approx 2.8 \times 10^{-4}\,(\Omega\mathrm{m})^{-1} \tag{3.16}$$

where e denotes the electrical charge. This quantity can be related to the resistivity $\rho_i = \frac{1}{\sigma_i}$ [34].

3.2.3 Doped Semiconductors

To enhance the poor intrinsic conductivity of silicon, doping of the material with other elements is a common technique. Depending on the element the number of free charge carriers is increased.
Elements of the third group in the periodic system of elements have one electron less compared to silicon in the unfilled shell. Thus, doping with elements as boron or aluminum results in additional holes. Since the dopant accepts a charge carrier it is called acceptor and the doped material p-doped.
In contrast to that, elements of the fifth group (e.g., Lead, Arsenic) have one electron more than silicon in the unfilled shell. Hence, additional electrons are added by doping with those so-called donors. The electrical conductivity of such n-doped semiconductors is enhanced by this since the electron is loosely bound and can by excited by small thermal excitations.
Although the thermal conductivity is influenced by doping, the electrical charge of the semiconductor is still neutral [34].
Further, doping changes the number of energy states since new energy bands depending on the dopant are introduced. In n-doped semiconductors an energy band - called donor level - shortly below the conduction band is introduced while for p-doped materials an acceptor level is created, lying above the valence band. Because of that the Fermi level is shifted towards the corresponding doping level [34] [80].

3.2.4 The pn Junction

A pn junction is created when a p-doped and n-doped semiconductor are brought into contact. At their interface the junction is built. Devices like this are called diode and are the basic elements of a detector and transistors (see section 3.2.7).
Because of the difference in majority charge carriers between both parts a concentration

gradient arises - resulting in a diffusion current I_{diff}. Hence, electrons of the n-doped part diffuse into the p-doped part and vice-versa. Both charge carriers recombine at the boundary with the majority charge carriers of the other part forming a region - called depletion zone - where no mobile charge carriers are left which results in an isolating area.
In fig. 3.4 a schematic illustration of the process is shown. Due to the ionized atoms at the boundary a space charge region (shown by the charge distribution $Q(x)$ in fig. 3.4) is formed - leading to an intrinsic electrical field creating a drift current I_{drift} that counteracts the diffusion current. Hence, an intrinsic potential, called built-in potential V_{bi}, is formed of $\approx 0.6\,\text{V}$ [34] for silicon.

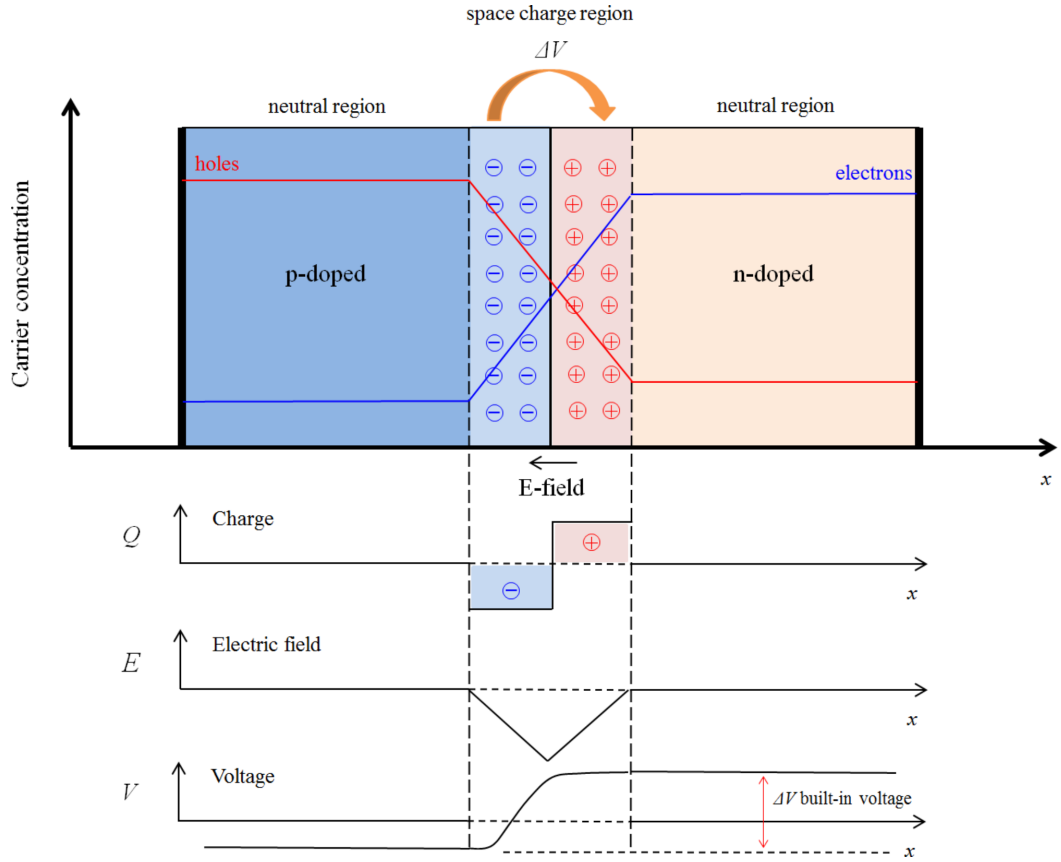


Figure 3.4: Schematic illustration of pn junction where holes (colored red) diffuse from a p-doped (colored blue) into a n-doped semiconductor (skin-colored). The resulting space charge $Q(x)$, the electrical field $E(x)$ and potential $V(x)$ distributions are shown [85].

In thermal equilibrium [2] the space charge density $\rho(x)$ depends purely on the doping concentration N_i [34]:

[2] Without external bias diffusion and drift compensate each other.

$$\rho(x) = \begin{cases} -eN_A & -x_p < x < 0, \\ +eN_D & 0 < x < x_n. \end{cases} \tag{3.17}$$

Including neutrality $N_A x_p = N_D x_n$ [34] and using Maxwell's equations, the electrical field $E(x)$ can be derived [34]:

$$E(x) = \begin{cases} -\frac{eN_A}{\epsilon\epsilon_0}(x + x_p) & -x_p < x < 0, \\ +\frac{eN_D}{\epsilon\epsilon_0}(x - x_n) & 0 < x < x_n \end{cases} \tag{3.18}$$

where ϵ describes the permittivity. Integrating the electrical field yields the built-in potential U_{bi} [34]:

$$U_{\text{bi}} = -\int_{-x_p}^{x_n} E(x)d(x) = \frac{e}{2\epsilon\epsilon_0}(N_A x_p^2 + N_D x_n^2). \tag{3.19}$$

Finally, the depletion width d can be derived including the depths x_i and effective doping concentration $N_{eff} = N_D - N_A$ [34]:

$$x_p = \sqrt{\frac{2\epsilon\epsilon_0}{e} U_{\text{bi}} \frac{N_D}{N_A(N_D + N_A)}} \tag{3.20}$$

$$x_n = \sqrt{\frac{2\epsilon\epsilon_0}{e} U_{\text{bi}} \frac{N_A}{N_D(N_D + N_A)}} \tag{3.21}$$

$$d = x_p + x_n \approx x_p \approx \sqrt{\frac{2\epsilon\epsilon_0}{e|N_{eff}|} \cdot U_{\text{bi}}} \tag{3.22}$$

In eq. (3.22) a typical scenario for a silicon based semiconductor is assumed: The doping concentration between p- and n-doped silicon differs by several orders of magnitude. Thus, the depletion zone grows mostly towards the less doped part.
For most modern applications the charge collection electrode is n-doped while the bulk has a low p-doping concentration (see section 3.4) resulting in a depletion region predominately growing from the electrode towards the bulk.
Without an external applied bias voltage the depletion depth is only a few µm wide. To ensure efficient particle detection, the depletion depth has to be enhanced. Hence, an external bias voltage U_{bias} is applied resulting in [34]:

$$d = x_p + x_n \approx x_p \approx \sqrt{\frac{2\epsilon\epsilon_0}{e|N_{eff}|} \cdot (U_{\text{bi}} + U_{bias})} \tag{3.23}$$

Depending on U_{bias} the depletion zone is either enhanced or reduced which is depicted in fig. 3.5. On the left hand-side in fig. 3.5 the scenario without external bias voltage is shown as previously discussed. Both scenarios for external bias voltage are illustrated on the right hand-side. If the external bias voltage (labeled U_{ext}) is positive (positive voltage at p-doped part), the depletion width is reduced. In contrast to that, a negative bias voltage increases the width. Hence, reverse bias is the usual operation mode for semiconductor particle detectors.

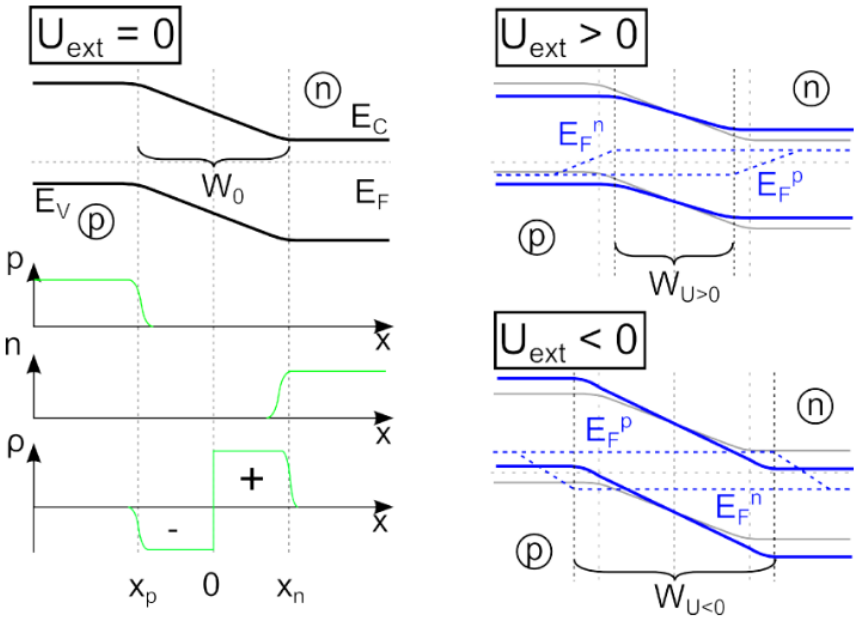


Figure 3.5: Illustration of the three possible bias scenarios: (1) Without external bias (shown on the left hand-side), (2) forwards bias (shown on the top right hand-side), (3) reverse bias mode (shown on the bottom right hand-side). For all the energy levels of conduction and valence band as well as the Fermi energy is marked [86].

To achieve a highly efficient particle detection, detectors are usually operated nearly fully depleted - meaning the depletion zone extends the full detector volume (typically on the order of (100 to 200 µm). Hence, the depletion voltage U_{dep} can be expressed in dependence of the detector thickness d and the doping concentration [34]:

$$U_{dep} = \frac{ed^2}{2\epsilon\epsilon_o} \cdot N_{eff} \quad . \tag{3.24}$$

Detector Operation Mode - Reverse Bias

The introduced model describes an ideal scenario where no current in the depletion zone is allowed. Therefore, the current I can be described by the current of a Shockley diode [34]

$$I = I_S(e^{eU_{ext}/(kT)} - 1) \tag{3.25}$$

with the reverse bias saturation current I_S. An exponential dependence on the bias voltage and temperature can be derived. In fig. 3.6 the typical current-voltage (IV) behavior is shown for forward and reverse bias.

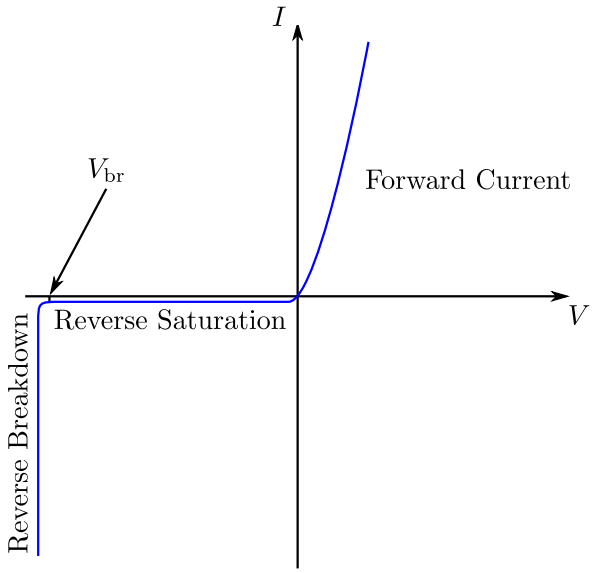


Figure 3.6: Illustration of the current-voltage behavior of a diode for forward and reverse bias. The breakdown V_{br} in reverse bias mode is labeled [87].

For a realistic detector the main contribution to the leakage current in reverse bias operation mode is not I_S but thermal generated current in the depletion zone - which is usually meant by the term leakage current I_L. Thus, a dependence on the depletion volume V can be deduced [34]

$$I_L = e \cdot V \cdot \frac{n_i}{2\tau} \tag{3.26}$$

where τ denotes the mean lifetime of charge carriers and e the elementary charge. Further, a temperature dependence [34]

$$I_L \propto T^2 \cdot e^{\frac{-E_G}{2k_B T}} \tag{3.27}$$

is derived. Increasing the temperature results in an increased leakage current. In a worst case scenario thermal runaway occurs - meaning the detector heats up, increasing the leakage current further and eventually destroying the device [81].
If the applied external bias is too large, a strong increase of the leakage current can occur. The voltage where this happens is called breakdown voltage. Two different kinds of breakdown are distinguished: (1) Tunneling and (2) Avalanche breakdown.

- **Tunneling Breakdown:** For strongly bent energy bands an electron from the valence can tunnel into the conduction band. For increasing temperature the bandgap decreases such that the tunneling probability increases, too. Hence, a breakdown can occur at lower voltages. Thus, the breakdown voltage decreases with increasing temperature [88].

- **Avalanche Breakdown:** If the electric field is strong enough to accelerate electrons such that new electron-hole pairs are generated by impact ionization, an avalanche can occur if the number of generated charge carriers is larger than their absorption. Inelastic scattering of electrons with lattice phonons increases with increasing temperature resulting in a reduced mean free path and an increased energy loss. Therefore, a higher potential is necessary for electron-hole pair creation, leading to an increased breakdown voltage with increasing temperature [88].

The introduced theoretical concepts of current-voltage behavior in reverse bias mode as well as the leakage current and its temperature dependence are important to understand the presented measurements in section 6.3.1.

3.2.5 Movement of Charge Carriers

The movement of charge carriers in semiconductor particle detectors depends on the operation mode of the detector. Therefore, the two main types of movement in a detector are introduced in the following: (1) Diffusion and (2) drift.
If a charge carrier moves freely through a semiconductor, its movement is random and dominated by scattering with, e.g., the lattice or impurities [81]. The superposition of this statistical movement with diffusion and drift is described by the Boltzmann transport equation [34].
A charge concentration gradient effects diffusion of charge carriers corresponding to the gradient. Hence, carriers from the high concentration part diffuse in the lower concentrated part. The conducted diffusion current $\vec{j}_{D,i}$ depends in the diffusion constant D_i and the charge carrier gradient ∇i [81]:

$$\vec{j}_{D,i} = (-)D_i \nabla i \tag{3.28}$$

where i denotes the charge carrier (either electrons e or holes p). The direction of the current depends on the charge concentration gradient. A relation of the diffusion constant to the charge carrier mobility μ is given by the Einstein relation $D_i = \frac{k_B T \mu_i}{e}$ [81].
If multiple charge carriers are created, they can diffuse as a charge cloud with a spatial distribution described by a Gaussian function [34]. The width $\sigma(t)$ [34]

$$\sigma(t) = \sqrt{2Dt} \tag{3.29}$$

depends on the diffusion coefficient D and time t leading to a spread of it over time. Depending on the size of the cloud, signal on multiple pixel electrodes [3] is generated - known as charge sharing. Effectively this leads to cluster of hits and thus has to be taken into account when reconstructing the signal position.
In an electrical field charge carriers are accelerated between collisions resulting in a drift current. The compensation of acceleration and scattering leads to an equilibrium such that the drift velocity $\vec{v}_D$ is described by the Drude model [34]:

$$\vec{v}_D = \frac{q\tau}{m_{eff}\vec{E}} = \mu\vec{E} \tag{3.30}$$

with the effective mass m_{eff} and the relaxation time τ - defining the mean time between two collisions. Since the mobility depends on τ, a dependence on the temperature, doping concentration and lattice impurities is given [81].
Typical values for electrons and holes in silicon at room temperature are [34]:

$$\mu_e = 1\,450\,\mathrm{cm}^2/(\mathrm{Vs}) \qquad \mu_h = 500\,\mathrm{cm}^2/(\mathrm{Vs}) \quad . \tag{3.31}$$

An approximately three times higher mobility of electrons compared to holes is deduced which is of importance for radiation damage (discussed in section 3.3).
The resulting drift current $\vec{j}_{Drift}$ [34]

$$\vec{j}_{Drift} = e(p\mu_p - n\mu_e)\vec{E} = \sigma\vec{E} \tag{3.32}$$

depends on the mobility μ_i and charge carrier density n, p. The conductivity σ is referred to the resistivity $\frac{1}{\rho}$.

[3] Typically segmented semiconductors are used for particle detectors.

3.2.6 Signal Generation of Charge Carriers

Created charge carriers induce a signal in the readout electronics due to their movement inside the electric field. As discussed previously, electrons move towards the n-doped part and holes towards the p-doped part of the semiconductor. Hence, the n-doped part is used as charge collection electrode. The signal generation is described by Shockley and Ramo [89] [90].
In this model the induced current i_S on an electrode i of a segmented system is given as [34]

$$i_{S,i} = q\vec{E_{w,i}}\vec{v} \tag{3.33}$$

with the weighting field $\vec{E_{w,i}} = -\vec{\nabla}\phi_{w,i}$ [34] depending on the weighting potential $\phi_{w,i}$.
This Ansatz is valid by the superposition principle where the overall potential of a system of k electrodes is given by the unit potential of electrode i if all other potentials are set to zero. Thus, a weighting potential for each electrode can be derived.
The induced signal dQ_i is expressed in terms of the weighting field [34]

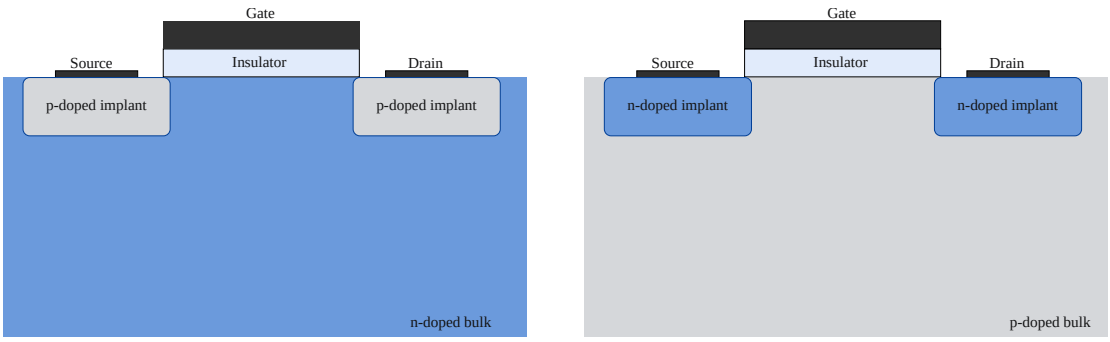
$$dQ_i = -q\vec{E_w}d\vec{r} \quad . \tag{3.34}$$

Hence, a moving charge q induces a current. The induced signal depends on the field configuration while being independent of the field strength and the applied external voltage. While charge carriers move towards the corresponding electrode, the induced current decreases with increasing time and decreasing distance to the electrode. Once they arrive at the electrode, the induced current vanishes. Due to the different mobility of electrons and holes the induced current of electrons has a fast rise compared to holes. Therefore, the induced signal on the electrode arises faster as for holes.
Since the drift time depends on the applied voltage, the charge collection time depends on it, too. To ensure fast charge collection, a high voltage is necessary [34].
In a real pixelated detector (segmentation in two dimension) [4] the largest signal is created close to the readout electrode. Thus, the induced signal is dominated by the type of charge carrier moving towards the electrode. Depending on the position of the charge creation, the contribution of the charge to the total signal differs which is known as the small pixel effect [34].

[4] So far only systems without segmentation of the electrodes have been considered.

3.2.7 Readout Electronics - MOSFET

Monolithic silicon pixel detectors are read-out by integrated circuits. The used electronics are based on a **M**etal-**O**xide **S**emiconductor MOS and realized in **F**ield-**E**ffect **T**ransistors FET - called MOSFET - allowing complex integrations of integrated circuits on the same substrate as the sensitive detection volume.
The advantage of it is that both transistor types - PMOS and NMOS - can be realized within standard CMOS processes [5] by embedding the transistors in corresponding wells. E.g., a PMOS transistor consists of p-wells inside n-doped bulk material. Moreover, the technology enables low power consumption and resistor-less designs [34].
The principle of a transistor is described in the following. As depicted in fig. 3.7 a MOSFET consists of four parts: (1) Gate, (2) Source, (3) Drain and (4) Bulk/Substrate.
The working principle is based on a voltage regulated conductivity. To change the conductivity between source and drain, a control voltage between gate and bulk is applied. A dielectric layer - mostly silicon dioxide SiO_2 - separates the gate electrode (realized as a metal contact) and the other elements. Depending on the doping of the bulk, the source and drain contacts are embedded in different wells. For a PMOS transistor p-wells are used since the bulk is n-type while for NMOS transistors p-type bulk is used and thus n-wells.



(a) PMOS (b) NMOS

Figure 3.7: Schematic illustration of a MOSFET from the side. Both types (PMOS and NMOS) are shown. Drain, source, gate, bulk and their corresponding doping as well as the insulator layer (mostly) SiO_2 are labeled.

The interface between implants and bulk material forms diodes, creating a depletion zone without which current would flow without any external applied gate voltage. By applying a control voltage the current is regulated. Four different operation modes can be distinguished [6] [91], visible from the characteristic MOSFET curve in fig. 3.8.

[5] With standard CMOS processes, standard available implementations of commercial CMOS processes are meant.

[6] All explanations are valid for a NMOS transistor. PMOS transistor are operated in the same way but the majority charge carriers are holes instead of electrons.

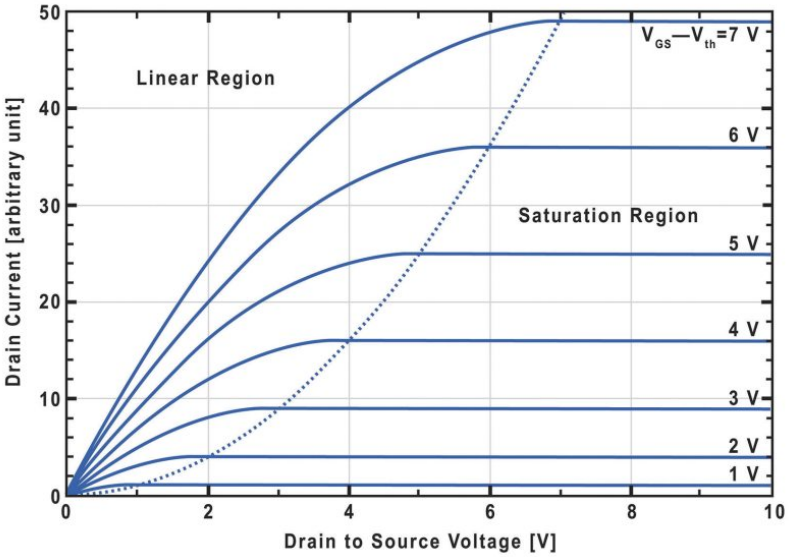


Figure 3.8: Characteristic drain-to-source current I_{DS} to drain-to-source voltage U_{DS} curve of an NMOS transistor. By the dashed line the linear operation and saturation region are separated [92].

- **Cutoff Region:** In an ideal state no current flows between drain and source. This is given if $U_{GS} < U_{thr}$ where U_{thr} denotes the threshold voltage. Below U_{thr} electrons are not sufficiently excited to reach the drain electrode [83].

- **Linear Region:** A positive gate potential [7] creates an electron accumulation below the gate electrode - called weak inversion because the majority charge carriers are electrons in a p-doped bulk. If $U_{GS} > U_{thr}$ and $U_{GS} - U_{thr} > U_{DS}$, the current between drain and source depends linearly - analogously to an ohmic resistor - on U_{GS}, defining the linear operation regime [91].

- **Saturation Region:** A quadratic dependence of the drain-source current on U_{GS} occurs if $U_{GS} > U_{thr}$ and $U_{GS} - U_{thr} \leq U_{DS}$. Although U_{DS} increases further, the current saturates - defining a saturation regime where the current is independent of the voltage [91].

- **Body Effect:** Changing the voltage U_{BS} between source and bulk results in a changed threshold voltage. Hence, the bulk acts as a second gate [93].

The most simple design of a transistor - as shown in fig. 3.7 - is a linear transistor, illustrated in fig. 3.9. Its resistance is defined by the geometry given by the ratio of length L and width W [91] [94]. Increasing the length results in a longer transistor and thus, an increased resistance. On the other hand, a wider transistor yields more current.

[7] The potential's polarity is positive relative to bulk, source and drain.

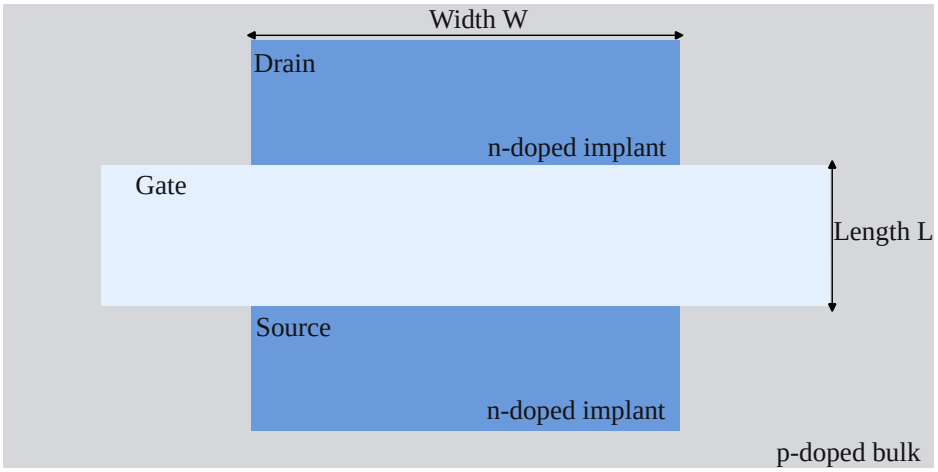


Figure 3.9: Top view of a linear transistor with p-doped bulk and n-doped implants. Length L and width W of the electrodes are indicated.

Besides possible spatial limitations in the design of linear transistors, this type is more prone to radiation induced damages [94]. Radiation generated electron-hole pairs increase the leakage current due to tunneling through the insulation layer. Further, parasitic channels between drain and source can occur. While electrons leave the insulation layer due to their higher mobility, holes are trapped (a more detailed discussion is given in section 3.3). Hence an electric field due to radiation damage arises, resulting in a parasitic channel and therefore, an increased leakage current [94].
To overcome this, **E**nclosed **L**ayout **T**ransistors ELTs are often used in ASICs used for HEP experiments. A schematic illustration of the top view of an ELT is shown in fig. 3.10

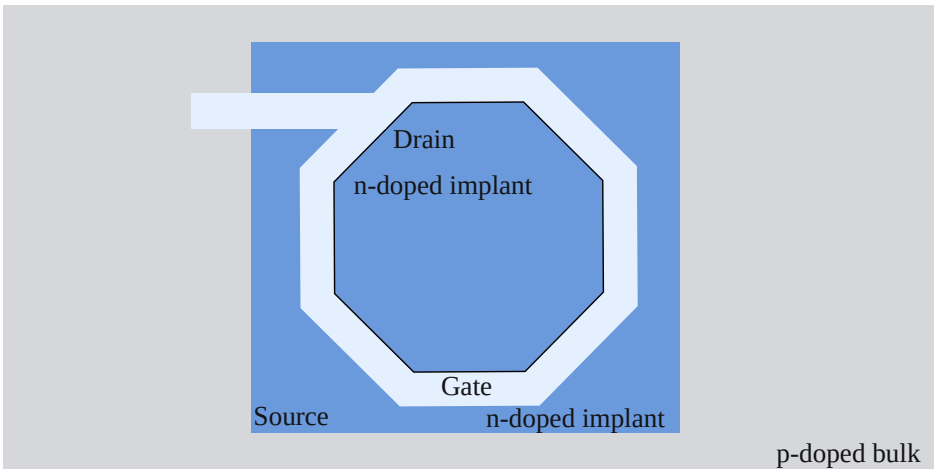


Figure 3.10: Top view of an ELT is shown where the gate is annular. For more information: [94].

As a consequence, no edges between source and drain occur such that parasitic channels

cannot built up. For this type different designs of the gate geometry are possible. More information can be found in [94].

3.3 Radiation Damage

The high particle rate expected for the LHCb Upgrade II detector will lead to a high radiation environment. Therefore, the overall detector system will be exposed to extreme radiation. Up to $3 \times 10^{14}\,\mathrm{MeV n_{eq} cm^{-2}}$ and 40 MRad of radiation induced damage are expected for the Mighty-Pixel at the end of its lifetime (for more details see section 2.4).
An introduction of possible radiation damages and its effects on the operation of silicon pixel detectors is given within this section.
Depending on the effect of radiation damage two types are distinguished: (1) Bulk damage (discussed in section 3.3.1) and (2) surface damage (discussed in section 3.3.2).
While bulk damage affects mainly the particle detection sensitive volume of a detector, surface damage alters the readout electronics of the device. For monolithic particle detectors (introduced in section 3.4) the understanding of both effects and their interplay is of crucial importance to ensure efficient detector performance under irradiation.

3.3.1 Bulk Damage

While particles traverse the detector, energy is lost via interaction (mainly ionization and excitation) of the incident particle with the medium (as discussed in section 3.1). Since ionization is reversible, this process does not contribute to stable radiation damage in silicon [34]. Besides this, incident particles undergo scattering processes (inelastic and elastic) with the lattice atoms. This can lead to so called **P**rimary **K**nock on **A**toms PKA if the particle energy is above a threshold energy $E_d \approx 25\,\mathrm{eV}$ [95]. Hence, silicon atoms are dislocated from their primary lattice position and can move through the crystal at room temperature while interacting with it, further [95]. Depending on the energy, ionization and non-ionization interactions occur whereby non-ionization interactions may result in defects. An comprehensive overview of possible defects is given in fig. 3.11 and explained in the following:

- Vacancy V: Unoccupied position of a silicon atom. This defect can form more complex structures, e.g., a di-vacancy V^2.
- Interstitial I: Silicon atom placed in-between the silicon lattice.
- Frenkel pair: Combination of an interstitial and a vacancy next to each other.
- Impurity/Interstitial substitute: Substitution of a silicon atom or an interstitial with other atoms.

Moreover, impurities within the silicon lattice [8] can form more complex defects, e.g., OC complexes.
All of these effects belong to point-like damages in the crystal. Depending on the incident particle energy, the PKA energy differs. Hence, further interactions with the material are possible. If the energy is sufficient, further **N**on **I**onizing **E**nergy **L**oss NIEL interactions occur, resulting in a cascade and thus, a cluster defect may arise. If not, the defects are localized and separated into the introduced types of point-like defects.

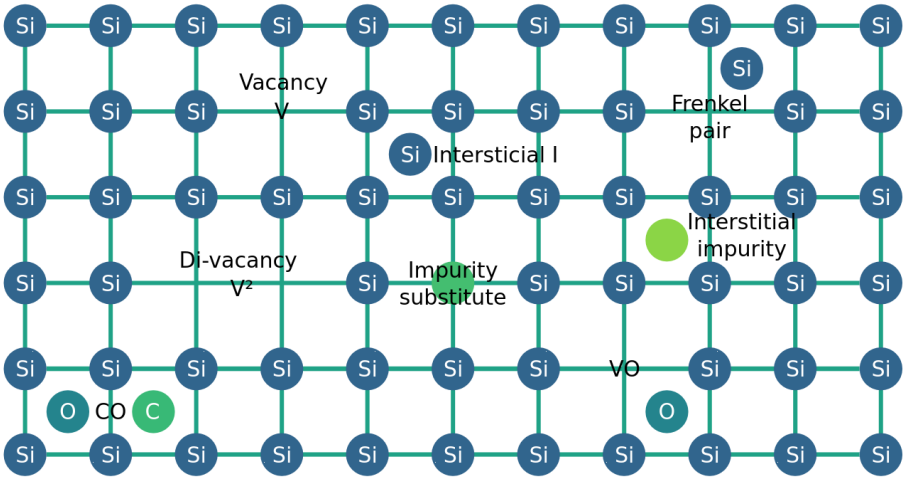


Figure 3.11: Overview of possible defects on NIEL induced damages in a silicon lattice. Silicon lattice atoms are colored in blue. Defects are labeled according to their type [96].

Besides the dependence on the incident particle energy, the type of particle causes differences in the damages since the maximum energy transfer $E_{R,max}$ [95]

$$E_{R,max} = 4E_P \frac{m_P m_{Si}}{(m_P + m_{Si})^2} \tag{3.35}$$

in an elastic collision depends on particle mass m_P and kinetic energy E_P [9]. Taking eq. (3.35), the threshold energy E_d and the energy needed to create a cluster $E_{th,c} = 5\,\text{keV}$ [95] into account, it can be concluded that protons create more point-like defects while neutrons create more cluster-like [95].
Hence, the irradiation of silicon detectors with different types of particles (here protons and neutrons) can cause differences in the observed performance of the device.

[8] The material can be enriched by oxygen O or carbon C or by other atoms depending on the doping concentration.

[9] The introduced relation is valid for an non-relativistic approach. For relativistic particles a relation is derived in [34].

NIEL Hypothesis

The amount of energy lost by **N**on **I**onizing **E**nergy **L**oss NIEL is parametrized in terms of NIEL damage which includes the energy that is transferred to phonons, too [97]. Within this model the damage scales linearly with the transferred energy to the PKA and thus, with the NIEL damage - independently of the initial spatial and energy distribution and annealing [10] [95]. The displacement cross section - mostly called damage function - $D(E)$ parametrizes the NIEL in dependence of the particle energy E [95]

$$D(E) = \sum_{\nu} \sigma_{\nu}(E) \cdot \int_{0}^{E_r^{max}} f_{\nu}(E, E_R) P(E_R) \mathrm{d}E_R \tag{3.36}$$

including all possible interactions ν leading to displacements, the interaction dependent cross section σ_{ν} and the probability $f_{\nu}(E, E_R)$ to generate a PKA. How much energy of the PKA energy is needed to create displacements is modeled by Lindhard partition functions $P(E_R)$ [95].
Following the NIEL hypothesis, the produced damage can be scaled in terms of NIEL damage where a normalization to the damage produced by 1 MeV neutron is done. The hardness factor κ [95]

$$\kappa = \frac{\int D(E)\phi(E)dE}{D(E_n = 1\,\mathrm{MeV}) \cdot \int \phi(E)dE} \tag{3.37}$$

is used to relate the produced damage to those of a 1 MeV neutron. Consequently, the irradiation fluence ϕ can be expressed in terms of the neutron equivalent fluence ϕ_{neq} and vice versa [95]

$$\phi_{neq} = \kappa\phi = \kappa \int \phi(E)dE \quad . \tag{3.38}$$

The hardness factor used within this thesis for a proton irradiation at the Bonn cyclotron (more information in chapter 7) for 13.5 MeV protons is $\kappa \approx (3.71 \pm 0.11)$ [98].
NIEL scaling, however, is not universally valid as shown in [99]. Within this research the acceptor removal effect was studied in detail - showing discrepancies between the induced defects of protons and neutrons in p-doped silicon pixel detectors. Further, NIEL does not take into account all types of effects of bulk damages on silicon detectors (explained in the following sub-section), e.g., the change of the effective space charge.

[10] Annealing is discussed later within this section

Effects of Bulk Damage on Silicon Detectors

The radiation induced damages can alter the detector performance due to new energy levels in the energy bandgap. Three macroscopic measurable effects are observed: (1) Change of leakage current, (2) trapping of mobile charge carriers and (3) change of the effective doping concentration. Each effect is described within the **S**hockley-**R**ead-**H**all (SRH) model [100] [101]. A more detailed derivation is presented in [95].
In the following the observed effects of bulk damage with the corresponding modeling within the SRH are discussed.

Leakage Current
Defects close to the middle of the bandgap behave like recombination/generation centers such that the distance towards both bands (conduction and valence band) is reduced - impacting the leakage current. Thus, the leakage current I_{leak} of an irradiated device is affected by the generation current which scales linearly with the detector volume $V = A \cdot d$ [97]

$$I_{leak} = q_0 \cdot A \cdot \sum_{defects} G_t \tag{3.39}$$

with the electrical charge q_0 and the sum over all possible defects. One single defect of type t is described by the generation rate $G(t)$ [97]

$$G(t) = N_t f_t e_n = N_t (1 - f_t) e_p = N_t \frac{e_n e_p}{e_n + e_p} \tag{3.40}$$

where f_t denotes the defect occupancy for electrons, n/p the electron/hole emission rates and N_t the charge carrier concentration. Defects close to the middle of the bandgap increase the leakage current as charge carriers are generated efficiently.
Moreover, a fluence and temperature dependence is observed. Increasing radiation fluence ϕ increases the generation current resulting in a higher leakage current. An expression by the current-related damage factor α [97]

$$\alpha = \frac{\Delta I}{V \phi_{neq}} \tag{3.41}$$

shows a linear relation between the radiation induced leakage current ΔI and fluence in dependence of the detector volume V. Its dependence normalized to the volume is presented in fig. 3.12. An annealing treatment of 80 min at 60 °C was performed while the leakage currents were measured at 20 °C [95].

Further, a dependence of the leakage current on the temperature T can be derived from eq. (3.40) [97]

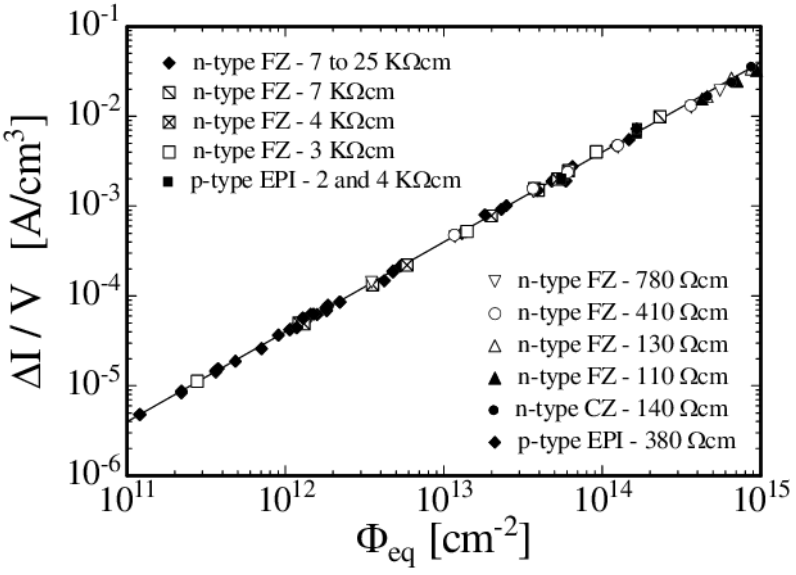


Figure 3.12: Dependence of the radiation induced leakage current normalized to the detection volume on the fluence. Data for various types of silicon with different doping concentrations and from different manufacturers are presented. For all an annealing treatment of 80 min at 60 °C was performed [95].

$$I(T) \propto T^2 \exp(-E_{eff}/(2k_B T)) \tag{3.42}$$

with the activation energy $E_{eff} = (1.214 \pm 0.014)\,\text{eV}$ for silicon [97]. Reducing the temperature by a degree centigrade results in a reduced leakage current of $8\% - 10\%$ in the temperature range from $-20\,^{\circ}\text{C}$ to room temperature [97].
Due to the strong temperature dependence, irradiated devices are operated at cold temperatures to avoid high leakage currents. In a worst case scenario the dissipated power can lead to self-heating - increasing the leakage further and resulting in so-called thermal runaway which can destroy the detector.
Since the defect formation is temperature dependent, a temperature treatment affects the defect generation and its development - called annealing (discussed in section 3.3.1). Measurements presented in [95] show a temperature dependent decrease of the damage rate over time with a parametrization of [97]

$$\alpha = \alpha_1 \cdot \exp(-t/\tau_1) + \alpha_0 - \alpha_2 \cdot \ln(t/t_0) \quad . \tag{3.43}$$

A set of parameters and their description is given in [95].

Trapping

Charge carriers can be trapped by defects and released after a certain time. If the release time is longer than the readout time, the signal charge induced at the charge collection electrode is reduced. Hence, the signal amplitude depends on the amount of trapped charge carriers [97]. The trapping time τ_e, τ_h for electrons and holes is given by [97]

$$1/\tau_e = c_n(1 - f_t)N_t \qquad 1/\tau_h = c_p f_t N_t \tag{3.44}$$

with the constants $c_i = v_{th,i}\sigma_i$ [11]. Summing over all possible effects yields the effective trapping times τ_{eff}. Consequently, the loss of charge [97]

$$Q(t) = Q_0 \exp(-t/\tau_{eff}) \tag{3.45}$$

is derived. For increasing radiation fluence the probability of trapped charges increases, too. Therefore, highly irradiated samples suffer from decreased charge collection efficiency [97]. Similar to the leakage current, a linear fluence dependence is observed [97]

$$1/\tau_{eff} = 1/\tau_{eff,0} + \beta\phi_{neq} \quad . \tag{3.46}$$

where β denotes the effective trapping damage constant and $\tau_{eff,0}$ the charge carrier lifetime without irradiation [97].
Additionally, a dependence of β on the annealing state of the device was measured. Depending on the charge carrier type, the damage rate either increases (for holes) or decreases (for electrons) over time [97].
From the derived equations, a reduction of charge carrier trapping can be achieved by short drift paths and fast charge collection time. To achieve this, a high electric field and a reduction of the detector thickness is necessary. Thinned devices also show less leakage current since the overall detection volume is reduced.

Effective Space Charge

The doping concentration determines the space charge density. By irradiation acceptor and donor levels can be introduced to the existing energy levels. Thus, the effective doping concentration is altered. Since this effect on the sensor bulk is highly material and radiation type dependent, NIEL scaling does not hold.
The amount of donors N_D and acceptors N_A after irradiation defines the effective space charge density N_{eff} depending on the defect type t [97]

[11] The product is given by the thermal velocity of electrons/holes $v_{th,i}$and their capture cross section σ_i [95].

$$N_{eff} = \sum_{donors} (1 - f_t) N_t - \sum_{acceptors} f_t N_t \quad . \tag{3.47}$$

Changing N_{eff} results in a changed depletion voltage. Since (introduced in eq. (3.24))

$$V_{dep} = \frac{q|N_{eff}|d^2}{2\epsilon\epsilon_0} \tag{3.48}$$

the acceptor/donor level concentration changes the operation voltage of the device [95]. For n-type sensors an effect called type inversion is observed. With increasing radiation fluence the positive space charge is compensated by radiation induced negative space charge. At larger fluences the negative space charge increases further, resulting in change of the effective doping concentration. Accordingly to eq. (3.48) a higher voltage is necessary to deplete the device. For p-type devices no type inversion is possible since the space charged density is negatively charged without irradiation. However, another effect - called acceptor removal - is observed [99].
An explanation is given in the following:

Acceptor Removal:
As introduced in section 3.3.1 interstitials and vacancies move freely at room temperature through the silicon lattice. P-doped material can be enriched with boron, oxygen and carbon. Therefore, chemical reactions of the defects with those dopants are possible, creating complex defects. For example, the reaction of an interstitial I with boron B_s can produce $I + B_s \rightarrow B_i$ boron interstitials moving freely through the lattice [99]. Further, the interaction of created interstitials with others can form even more complex defects. One is the boron-oxygen defect B_iO_i with an energy level in the upper half of the silicon bandgap [99]. Hence, it acts as positive space charge.
Depending on the radiation type, different amounts of this defect have been found. Proton irradiated samples showed a higher concentration compared to neutron irradiated devices. Besides this, other measurements (see [99] and citations therein) obtained a higher acceptor removal for proton than for neutron irradiated detectors.
Further, the acceptor removal rate depends on the initial acceptor concentration. Devices with higher acceptor concentration (low resistivity materials) show an increased acceptor removal rate [99]. No clear explanation for this can be given, but in [99] two different effects are discussed.

Similar to the leakage current and charge carrier trapping, the effective space charge density depends on the annealing state. The effective change of doping concentration ΔN_{eff} is parametrized by [95]

$$\Delta N_{eff}(t) = N_A(t) + N_C + N_Y(t) \quad . \tag{3.49}$$

Three components determine the change [12]:

- **Stable damage N_C:** Damage, independent of the temperature and thus, annealing. Defects due to donor removal and acceptor creation are described by it. Therefore, it is material and fluence dependent.
- **Short term damage N_A:** Short term or beneficial annealing describes the initial decrease of effective doping concentration because the depletion voltage is reduced. For p-type semiconductors the depletion voltage increases.
- **Reverse annealing N_Y:** Reverse annealing behaves as the opposite of beneficial annealing. For annealing treatments longer than 80 min at 60 °C acceptor states start to formate, increasing the depletion voltage.

To keep the detector in a beneficial annealing state, an operation at low temperatures and storage at low temperatures is necessary. Thus, the defects are 'frozen'. Further, an operation at low temperatures reduces the leakage current.
Additionally to an annealing dependence, the effective space charge density and its radiation induced change are highly material dependent. Measurements showing this can be found in [97] and references therein.

Annealing of Irradiated Silicon Detectors

The work presented in [95] studied bulk damage and the effects of it on the detector operation in detail. Within the study an annealing treatment of irradiated samples for 80 min at 60 °C was derived. After this, the detector is at a beneficial annealing state, enhancing its performance. A reduced leakage current enables higher bias voltages and thus, a more efficiently operating device.
The irradiated samples (presented in chapter 7) have been annealed using those parameters. To keep the samples in this annealing state, a long-term storage at cold temperatures is chosen [13].

The discussed theory about bulk damage assumed a homogeneous distribution of defects over the detection volume. In reality this is not given. Additionally, the space charge density is not constant over the depletion volume. Especially after irradiation, the electric field is not linear but highly non-trivial. Defects as the double junction effect can occur. A more detailed discussion is provided in [95] [97].

[12] A detailed discussion of all components and their parametrization is given in [95].

[13] Not only for long-term storage but also for short-term in-between measurements, the devices are stored at a freezer.

3.3.2 Surface Damage

Radiation induced defects on the surface of semiconductor based detectors are summarized by the term surface damage. By surface the part above the bulk material including the sensor electronics is meant.
As introduced in section 3.2.7, the surface of a device is equipped with MOSFETs. Hence, the term surface includes the SiO_2 layer itself as well as the SiO_2-Si interface.
In contrast to the Si bulk, the SiO_2 lattice is highly irregular with intrinsic defects (explained in the following) [102]. The origin of surface damage is therefore due to the interaction of generated charge carriers with the intrinsic defects, resulting in an altered electrical state of those. Hence, surface damage activates intrinsic defects.
Charge carriers are generated by ionization. Similar to Si bulk, ionization can be reversible by recombination but due to the insulating properties of SiO_2, this process is not fully reversible. Additionally, deep level defects in the energy bandgap can trap charge carriers. A release of those into the conduction or valence band is highly suppressed due to the large bandgap energy of $E_G^{SiO_2} = 8.8\,\text{eV}$ [102]. Further, the mobility of electrons ($\mu_e^{SiO_2} \approx 20\,\text{cm}^2\text{V}\,\text{sec}^{-1}$) is much higher than for holes ($\mu_h^{SiO_2} \approx 2 \times 10^{-5}\,\text{cm}^2\text{V}\,\text{sec}^{-1}$) compared to silicon [102] - resulting in a separation of those. Depending on the gate voltage electrons drift towards the metal while holes slowly propagate through SiO_2 towards the interface region. Therefore, holes are the major contributor to surface damage.
Two main effects of surface damage are: (1) The build-up of positive charges and (2) an increased leakage current. In the following the main processes leading to these effects are discussed.
The amount of surface damage is often referred as **T**otal **I**onizing **D**ose TID damage since the damage originates from ionization in SiO_2 [102].

Production Induced Defects

To use silicon as a semiconductor, a mono-crystal is required. However, silicon occurs in nature mainly in compound forms. Hence, different production processes exist to produce mono-crystalline silicon. One possible production is the Czochralski process (more information in [95]) where a silicon ingot is pulled out of poly-silicon. Therefore, the poly-silicon is melted, doped and a single crystal seed is placed on its surface. While rotating the crucible, the crystal seed is pulled upwards such that a silicon ingot grows. Due to the production process, impurities in the melt occur inhomogeneously in the pulled crystal. At a further production step, silicon wafers are cut out of the ingot. After mechanical processing in order to reduce surface damages, the wafers are oxidized to reduce leakage currents and insulate them by a silicon dioxide SiO_2 layer - built due to the reaction of silicon and oxygen. Further, the layer acts as a mask at subsequent photographical processes where wafer parts are doped and dedicated structures embedded.
At the oxidation and further production steps, hydrogen impurities may form in the SiO_2, resulting in irregularities of the lattice. Those can either establish connections with SiO_2

lattice atoms or move through the lattice acting as donor effect levels and thus, introducing more positive space charge.
At the Si-SiO_2 interface lattice mismatches occur - enhancing the defect concentration in that region. Trivalent silicon can form bindings with three other silicon atoms by having one dangling bond extending towards the oxide. During manufacturing dangling bonds are in purpose electrically deactivated by saturating them with hydrogen atoms H forming, e.g., Si-H connections [103] [104].

Ionizing Energy Loss

High energy particles can ionize the material creating electron-hole pairs. In a p-substrate MOSFET electrons drift towards the positively charged metal contact while holes drift slowly towards the Si-SiO_2 interface. The fraction of charge not recombining and hence, may introducing damages, is called charge yield [104]. Depending on the radiation type and the electrical field, the charge yield differs [105].
In fig. 3.13 the formation process of defects is depicted.

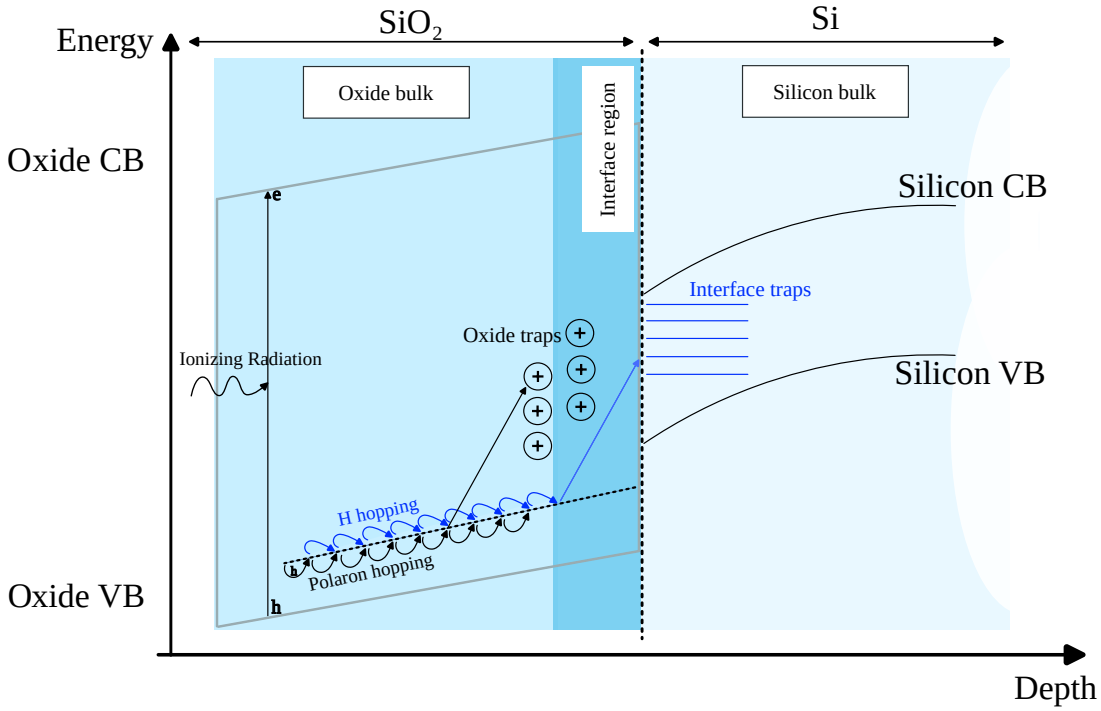


Figure 3.13: Schematic illustration of IEL induced damages and their formation. Ionizing radiation creates an electron-hole pair in the SiO_2 (colored in light blue). Holes are transported via polaron hopping towards the interface region (colored in blue) and can form oxide and interface traps. Interface traps force a bending of the energy levels in silicon (colored in very bright blue). The energy bands in silicon and SiO_2 are labeled as well as the different regions.

Holes interact with the SiO_2 bulk and traverse it via a hopping process. At the interface region positive oxide charges can be created by trapping those [104].
While moving towards the interface, hydrogen atoms H are released by hole hopping. Those can move towards the interface creating interface traps.
In the following a summary of both defects and their formation is given [104] [105] [106]:

- **Oxide traps:** In the SiO_2 bulk electrons and holes can be trapped.
  While holes move through the lattice, they cause a distortion of the local potential resulting into 'self-trapping' and the creation of polarons (describing the combination of holes and their field). Therefore, the hopping process is often called polaron hopping.
  In the Si-SiO_2 vicinity the defect concentration is enhanced due to the lattice mismatch and out-diffusion of oxygen. Hence, oxygen vacancies can trap polarons. The amount of trapped polarons depends on the capture cross section which itself depends on the electrical field and the manufacturing process.
  Oxide traps undergo annealing by two mechanisms: (1) Due to the localization of oxide traps close to the silicon bulk, electrons from the silicon bulk can tunnel to the trap and neutralize it or (2) by thermal excitation of electrons from the valence band of the SiO_2. Tunneling annealing is more probable for higher electric fields due to a reduced potential barrier. Both annealing mechanisms start while the sensor is operated and thus, already during the irradiation itself - depending on the operation temperature, the irradiation rate and the electric field.

- **Interface traps:**[14] At the Si-SiO_2 interface so called interface traps can occur which affect both - the silicon bulk and the SiO_2 layer. Depending on their position in the band gap, they act as donor/acceptor levels or are neutrally charged if close to the mid-gap energy.
  The nature of interface traps is due to dangling bond defects. So called dangling bond defect centers P_b occur when hydrogen passivated dangling bonds are activated by removing the hydrogen atom via an interaction with a proton. Hence, the 'activated' dangling bond acts as an interface trap. The proton is created by a preceding polaron hopping where it was freed.
  Since its position at the interface, the energy levels of the silicon are affected changing the space charge distribution. Resulting effects on the operation are discussed in section 3.3.2.
  In contrast to oxide traps, annealing is more complex and slower for interface traps. A clear annealing treatment cannot be given, but a trend towards annealing at temperatures above 100 °C has evolved.

[14] The formation of interface traps is under steady investigations since the formation of those is not yet fully understood. Two different models give an explanation of it. More information about those (**W**inokour-**M**c**L**ean MCL and hole hopping) is given in the quoted references.

While oxide trapping is a 'fast' process, interface traps evolve due to the low ion mobility slowly over time [104]. Measurements discussed in [104] and references therein showed that interface trap build-up does not depend on the radiation rate - becoming relevant for measurements presented in chapter 7.

Effects of Surface Damage on Silicon Detectors

Interface traps as well as oxide traps effect the operation of silicon detectors since they alter the properties of MOSFETs. The main effects are a threshold shift, change of leakage current and a decreased charge carrier mobility and transconductance [106]. Those are discussed in the following [106] [102] [104]:

- **Threshold voltage shift:** By the term threshold voltage shift the shift of the threshold voltage of a MOSFET before irradiation to the value after irradiation is meant. Due to the contribution of interface and oxide traps, the total shift ΔV_{thr} is the sum of both $\Delta V_{thr} = \Delta V_{ox} + \Delta V_{it}$. Both components can be determined from the charge distribution and oxide capacitance. Due to their charge dependence, a positive charge induces a positive threshold voltage shift and vice-versa.
  The oxide trapping component depends on the oxide trap density and the position in the Si-SiO_2 interface. Hence, traps closer towards the border region increase the threshold shift while traps far away have less impact. By the nature of positively charged traps, the induced threshold shift is negative. Depending on the MOSFET type, the radiation induced threshold shift differs to the non-irradiated threshold. For PMOS the threshold voltage increases, while it decreases for NMOS transistors [15].
  In contrast to oxide traps, the charge of interface traps differs depending on their energy levels. Since NMOS transistors have a positive gate voltage, electrons move towards the interface - making the transistor conductive. Therefore, the probability of interface trap build-up increases under irradiation for this biasing. PMOS transistors, instead, are negatively biased and thus, non-conductive such that under irradiation less interface traps are generated.
  In total, the threshold voltage shift for PMOS transistors has always two positive contributions (in absolute values) - increasing the shift. For NMOS transistors the total threshold shift shows a time-dependent shape. In a first stage, the oxide trapping component is dominant while at a later stage, the slowly evolving interface states contribute more and more. At high TIDs the oxide traps are saturated and the threshold shift is dominated by interface states. Hence, depending on the amount of TID, the threshold voltage first decreases down to its minimum and then increases (in absolute values).
  How the threshold voltage shift affects the performance of HV-MAPS has been investigated within this thesis and is presented in section 8.4.6.

[15] A decrease for NMOS transistors means the threshold voltage is becoming more negative.

- **Leakage current:** The leakage current of a MOSFET is the current between drain and source if no gate voltage is applied when the transistor is turned 'off'. Irradiation induced damage effects only the leakage current of NMOS transistors. Two reasons are responsible for the increased leakage current: (1) Parasitic channels and (2) subthreshold currents.
  Parasitic channels are the main contributor to the increased leakage current. Its natures is explained in section 3.2.7. Due to the parasitic paths between drain and source, currents occur increasing the leakage.
  Subthreshold currents are composed of two underlying contributions. Firstly, at low TIDs the threshold voltage decreases due to oxide charge trapping resulting in an increased leakage current. Secondly, the slope changes due interface trap build-up.
  A change towards the pre-irradiation state is possible due to the interface build-up which can compensate the negative threshold voltage and the changed slope. In section 8.4.6 and section 9.3 the effect of it on the performance of HV-MAPS is discussed.

- **Mobility and transconductance:** Since interface traps trap charge carriers in the interface region, the conduction of a MOSFET is reduced resulting in a decreased mobility. Further, the transconductance is decreased by that. For NMOS transistors this effect is stronger than for PMOS transistors since more interface traps are built.

3.4 Monolithic Active Pixel Sensors

Pixel Sensor Technologies

The technology of semiconductor particle detectors has developed over the last decades in different ways, optimizing the detection performance depending on the individual application. Besides the usage for, e.g., particle tracking in HEP experiments such as the Mighty-Pixel at LHCb (introduced in section 2.4.3), semiconductor detectors are used for various applications in astronomy and medicine. High granularity and efficiency, a good spatial resolution and fast charge collection make this technology usable for the foreseen goals.
Spatial determination of the incident particle is achieved by structured electrodes. As discussed in section 3.2.5, charges move via drift and diffusion through the medium while their spatial resolution is given by $\sigma = \sqrt{2Dt}$ (see eq. (3.29)). For digital readout where the only information is if the signal is readout by the electrode or not, the spatial resolution is determined by the electrode pitch. If the device - consisting of two electrodes with pixel pitch p - is hit at a position x between those, the spatial resolution σ is given by [34]:

$$\sigma^2 = \int_{-p/2}^{p/2} \frac{x^2}{p} \mathrm{d}x = \frac{p^2}{12} \quad . \tag{3.50}$$

Hence, lowering the pixel pitch enhances the spatial resolution. Further, clusters [16] can improve the resolution since neighboring pixels detect the signal - effectively reducing the pitch.
In general two kinds of technology are defined: (1) Hybrid and (2) monolithic detectors. The concept of both as well as their disadvantages and advantages are discussed in this section.
Both technologies underlie the same working principle. Impinging particles generate electron-hole pairs in the sensitive medium - created by a pn-junction of a low-doped substrate and high-doped implant. Hence, the depletion regions grows mainly towards the substrate. By an electric field the charge carriers are separated and further collected at the corresponding electrodes [17]. The induced signal is amplified and further processed depending on the readout design.
In fig. 3.14 a generic signal processing chain of a monolithic sensor is illustrated. The created signal charge Q is amplified and shaped by a **C**harge **S**ensitive **A**mplifier CSA. Afterwards, the analogue output signal is discriminated and digitized to be further processed by the digital readout [18].

Since the signal processing is comparable for both technologies, they suffer from similar noise sources degrading the signal. Besides signal fluctuations the readout electronic itself is

[16] Clusters are formed when the induced signal is shared by more than one electrode.

[17] The relevant processes of particle interaction with mater as well as signal generation in silicon are discussed in previous sections (see section 3.1 and section 3.2.6).

[18] A detailed description of the signal processing chain for sensor used within this thesis is given in chapter 4.

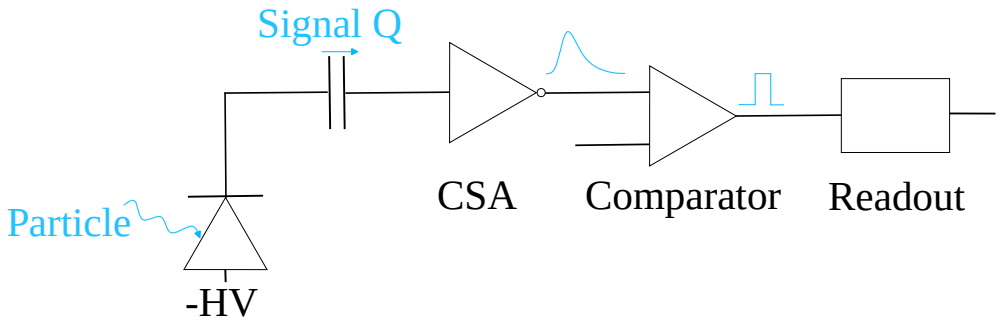


Figure 3.14: Illustration of a signal processing chain in a monolithic detector. An incident particle creates a signal in the sensing diode. The signal charge Q is amplified, discriminated and further processed towards the digital readout block.

affected by electronic noise which is the dominating source of noise in a silicon detector [34]. The noise density in a frequency interval df of a system is defined by the power density dP_n/df [34]. Depending on the frequency dependence within a defined bandwidth, noise is classified into white (non-frequency dependent) and frequency dependent noise.
Mainly three types of noise contribution can be distinguished: (1) Shot noise (white noise), (2) thermal noise (white noise) and (3) $1/f$ noise [34]:

- **Shot noise:** Statistical fluctuations of charge carriers passing a potential wall are described by Shot noise. In a semiconductor detector this occurs when charges in the bias diode are created. Hence, the leakage current of the detector contributes to Shot noise.
- **Thermal noise:** Thermal noise is induced by thermal motion of free charge carriers - described by Brownian motion [107]. Due to the temperature dependence a reduction by cooling is possible.
- **$1/f$ noise:** The origin of $1/f$ noise are number fluctuations. In MOSFETs trapped and released charge carriers at the oxide-substrate interface change the conductivity and hence, contribute to this noise source.

How noise affects a system is determined by the **S**ignal-to-**N**oise **R**atio SNR. Signal is measured as the signal amplitude while noise is defined as the noise voltage at the same measurement point [103]. For a SNR equal to 1 the charge is defined as the **E**quivalent **N**oise **C**harge ENC representing the electronic noise.
For a generic readout as shown in fig. 3.14 noise contributes at several points to the system.

One main contributor is the CSA. While thermal and $1/f$ noise occurs at all transistors, Shot noise degrades the signal due to the leakage current from the sensing diode. To reduce the amount of noise, the leakage current should be minimized. Additionally, a small detector capacitance results in lower noise. Thermal noise in transistors can be reduced by a high transconductance. However, an increased power consumption of the CSA is caused by that - resulting in the necessity of cooling the system which has further effects on the overall detector system design.
Furthermore, the detector capacitance C_D effects the amplifier rise time τ_r. Since $\tau_r \propto C_D$, reducing the capacitance reduces the rise time [34] [81]. On the one hand, its advantageous for noise reduction since the bandwidth is reduced while on the other hand, the time resolution [19] is worse.

Hybrid Pixel Detectors

To obtain a better spatial resolution of a signal, silicon strip detectors were further segmented resulting in a pixel detector. As a further advantage, high granularity is enabled by that, which is necessary for applications with high particle rates, e.g., HEP experiments at the LHC. In the following a brief discussion about the technology of hybrid pixel detectors is given because the development of monolithic sensors, e.g. foreseen for the Mighty-Pixel (see section 2.4.3), is based on the knowledge obtained by them.
Hybrid pixel detectors consist of two parts - a sensitive pixel diode and a readout pixel. The electrical output signal of the diode is electrically connected via solder bonds to the readout ASIC where amplification and digitization take place. The process of connecting both is called bump-bonding. In fig. 3.15 a typical hybrid detector with a readout cell and pixel diode, electrically connected, is illustrated.

Usually, the diode substrate is highly doped such that lots of charge carriers are available while the readout ASIC is fabricated in standard CMOS processes using lowly doped silicon [34].
Having two separate parts, enables the possibility to develop and study both individually. Hence, both can be optimized as best as possible. One limiting factor is the fit between the two. The readout **A**pplication-**S**pecific **I**ntegrated **C**ircuit ASIC must match the sensor diode dimension [81]. Hence, the sensor dimension is limited by the ASIC size and vice versa.
Besides high granularity, hybrid pixel detectors have a fast charge collection time and high radiation tolerance. Thus, they are the state-of-the-art technology for tracking detectors at HEP experiments. For example, the ATLAS **I**nner **T**rac**k**er ITk has to withstand a radiation dose of $2 \times 10^{16}\,\mathrm{MeVn_{eq}/cm^2}$ and 10 MGy [109]. To cope with this requirement, silicon pixel and strip hybrid detectors are foreseen. Two different types of hybrids - planar and 3D sensors - depending on the required specifications within the ITk are used [109].
Although planar pixel detectors are well established and used in several applications, they

[19] The time resolution specifies the minimum time required to resolve two consecutive events. The importance of this quantity for the Mighty-Pixel is explained in section 2.4

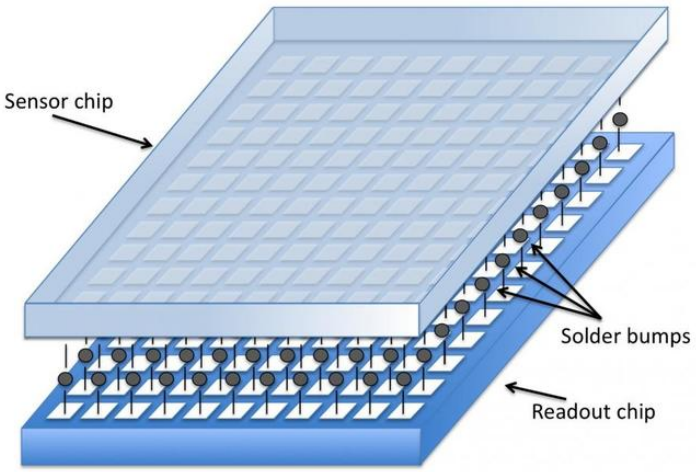


Figure 3.15: Illustration of a hybrid pixel detector with a sensor chip (colored in light blue) connected via solder bumps to a readout ASIC (colored in blue) [108].

suffer from long charge collection times and are prone to radiation induced damages [34]. A newer development are 3D silicon pixel detectors. In contrast to planar sensors, the charge collection electrodes are etched vertically into the substrate enabling a fast collection time due to short drift paths and improved radiation tolerance [34]. A drawback of this technology is the complex production and its high costs. Hence, planar sensors are used whenever possible.

Another drawback due to the design of hybrid pixel detectors, consisting of two parts, is the material budget increase because of the bump bonding. Reducing the material budget is necessary for high rate environments and precise tracking applications. One possible solution are monolithic pixel detectors.

Monolithic Pixel Detectors

Monolithic pixel detectors combine a sensing diode and the readout ASIC within one substrate. Besides a reduced material budget, costs are reduced as bump bonding is no longer necessary and commercial CMOS processes can be used for fabrication. **M**onolithic **A**ctive **P**ixel **S**ensors MAPS have integrated amplifiers in each pixel making them active pixel cells. Mainly two different types are distinguished: (1) MAPS with epitaxial layer and (2) MAPS with high resistivity substrate.

In standard CMOS processes lowly doped silicon substrate wafers are used. To enhance charge collection a thin (0.5 to 20 µm [81]) highly doped epitaxial layer is grown on top of them. On top the readout electronics are embedded. In fig. 3.16 a monolithic sensor with epitaxial layer and electronics on the topside is illustrated.
Charge carriers created by an impinging particle are separated and move towards the electrodes. Since the abundance of a high electrical field and small depletion region, charge carriers move via diffusion (see section 3.2.5). Electrons are collected at the n^+ electrode realized by an embedded n-well. Hence, only charge carriers close to the collection electrode are collected fast and efficiently.
Deep p-wells are necessary if PMOS electronics are used to prevent competing charge collection by n-wells used in the PMOS transistors.

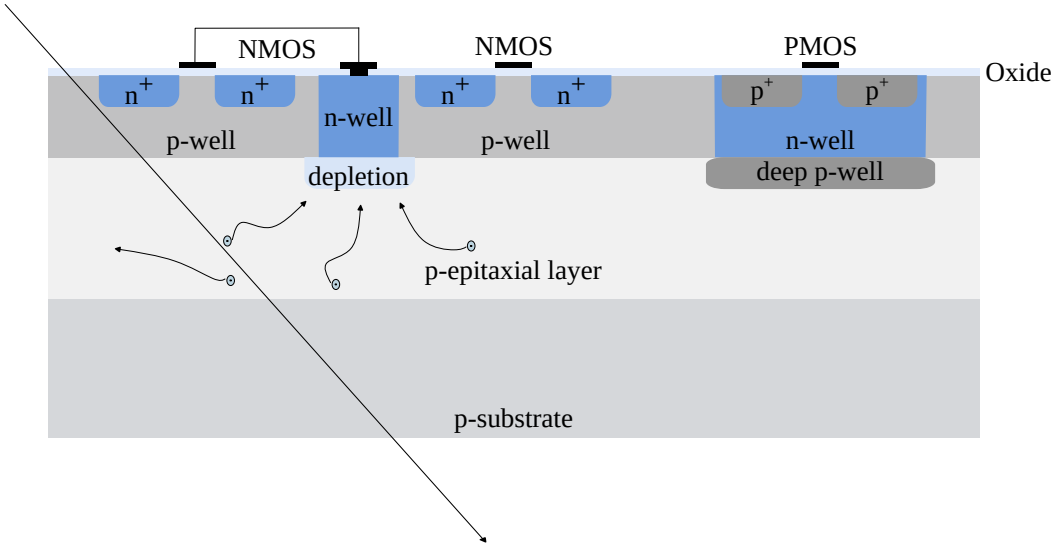


Figure 3.16: Side view of a monolithic pixel sensor with lowly doped p-substrate (colored in gray), a thin epitaxial layer (colored light gray) and embedded readout electrode on top. The growing depletion layer towards the epitaxial layer as well as freely moving charge carriers are indicated. For more information: [34].

Enhanced charge collection efficiency is possible by enlarging the charge collection n-well electrode to embed more complex CMOS electronics inside, reduce drift paths and increase the depletion region. Further, the usage of **H**igh **V**oltage HV is enabled by that. The corresponding MAPS are called HV-MAPS. Without this enhancement those type of MAPS are not suitable for fast tracking applications since the charge collection is too slow ($\approx$ 100 ns [34]) and not efficient enough.
The second type of MAPS is fabricated without an epitaxial layer. Instead, non-standard high ohmic p-doped silicon wafers are used as substrate material. Together with a large collection electrode this enables a large depletion area and thus, efficient charge collection. By high

electric fields due to HV bias, the charge collection time is significantly reduced, making this type of MAPS suitable for HEP experiments.
A cross-section of one HV-MAPS pixel is depicted in fig. 3.17. Besides the deep n-well with embedded readout electronics and the p-substrate two contacts for high voltage biasing of the substrate are illustrated.

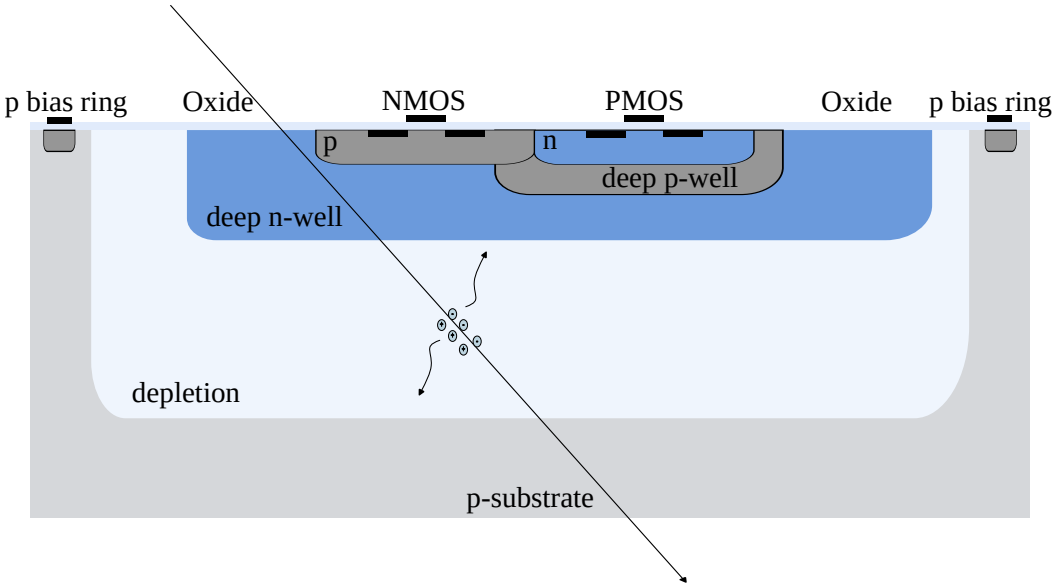


Figure 3.17: Cross section of one pixel cell of a monolithic pixel sensor with high doped p-substrate (colored gray) and large charge collection electrode (colored blue). The readout electronics are integrated within the deep n-well. High voltage biasing is possible by p-implants. The depletion region (colored light blue) and created charge carriers are indicated. For more information: [34] and [81].

The depletion depth d depends on [34]

$$d \propto \sqrt{\rho \cdot U} \tag{3.51}$$

the substrate resistivity ρ and external applied voltage U. Hence, high resistivity substrate has an intrinsically deeper depletion. Due to non-standard production steps and other wafers the production costs are higher compared to MAPS with epitaxial layer.
By applying high voltage at the sensor edges the electric potential is not homogeneous over the sensor area. To avoid high electric fields regions, causing unwanted avalanches in a worst case scenario, the electric potential gradient and hence, the electric field is smoothened by guard rings. How the breakdown of the characterized sensor within this work is affected by high electric fields, is discussed in later sections (see section 6.3.1).

As for MAPS with epitaxial layer two types of charge collection electrode exist: (1) Large and (2) small collection electrode [20]. Since large collection electrodes shield electronics, high electric fields and a large depletion volume are possible. Further, charge carriers are less trapped because of shorter drift paths - improving the radiation tolerance. As a drawback the sensor capacitance and hence, the electronic noise is larger compared to MAPS with a small collection electrode. Therefore, these devices have a better Singal-to-Noise ratio as well as a lower power consumption [102].
HV-MAPS with low doped p-substrate and a highly doped large collection electrode were realized for the first time in 2007 by I.Peric [2]. A cross section of a HV-MAPS consisting of four pixels is presented in fig. 3.18.

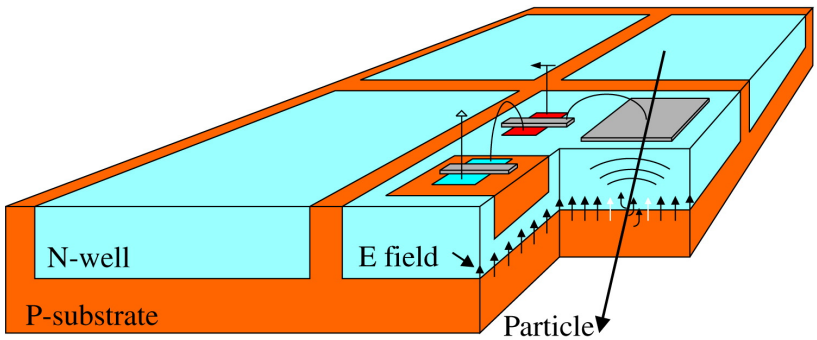


Figure 3.18: Schematic cross section of a HV-MAPS with four pixels. Charge collection electrode (colored light blue), substrate (colored orange) and the readout electronics are indicated [2].

Based on this sensor concept the final MightyPix sensor is developed. Hence, all predecessors are based on it, as well. A more detailed description of the design at the example of the sensor investigated within this thesis is given in chapter 4.

[20] The sensor types developed at KIT and investigated within this work are all large collection electrode MAPS without an epitaxial layer.

CHAPTER 4

Introduction of HV-MAPS used within the Mighty-Pixel Project

A deep understanding of the technology of HV-MAPS and their performance not only in general but also with respect to the requirements of the Mighty-Pixel is essential to validate the technology's compatibility with the experimental requirements.
To develop a production sensor for the Mighty-Pixel detector, knowledge of the foreseen technology and evaluation are crucial. Therefore, an intensive R&D phase towards the production sensor - MightyPix3 - is, at the time writing this thesis, ongoing. Its predecessor MightyPix2 is foreseen to arrive at all participating laboratories in 2026. The first sensor of the MightyPix development chain - MightyPix1 - is available but has no stable configuration due to a design flaw and limited in availability (see section 2.4.4 for more information).
However, the MightyPix development inherits its design of HV-MAPS designed by the group of Ivan Péric at KIT for the Mu3e [3] [110] and ATLAS experiments [4] [110].
Part of these developments are two engineering runs with the Run2020 and Run2021 sensors [111] as dedicated test devices compromising different ASIC electronics and pixel sizes. The successor sensor - TelePix2 [6] - is the latest predecessor of the MightyPix development chain. Due to several commonalities in the design of TelePix2 and MightyPix1, the sensor is an excellent device to study the technology of HV-MAPS in order to probe the technology with regards to the requirements of the MightyPix.
The design of all sensors can be separated into two parts: (1) Analog pixel cell and (2) digital periphery. While the analog part has several similarities between the three predecessors and the MightyPix developments, the digital part is different since MightyPix is designed dedicated to be operated within LHCb's DAQ system. Because the other sensors have been designed as part of developments of the Mu3e experiment, their digital design is not compatible with the LHCb DAQ system.
Taking the mentioned issues of MightyPix1 into account, TelePix2 is an excellent device to test the analogue performance with respect to the Mighty-Pixel requirements. Hence, most studies done within this thesis have been performed with TelePix2. Since some studies and

also the integration of the Run2020 and Run2021 sensors in the laboratory DAQ system MARS (see chapter 5) have been conducted as well, those sensors will be shortly introduced in section 4.3.
To understand the developments, similarities and differences between used devices with respect to MightyPix an overview is given in section 4.1.
Although, the design of TelePix2 and the other sensors are not part of this thesis, a deep understanding is unavoidable due to two reasons. Firstly, a major part of this thesis was the development of the MARS DAQ system (see chapter 5) usable in the laboratory and at testbeam campaigns for single sensor characterization with the possibility to test modules as well. Secondly, performance measurements and understanding of those are not possible without knowing the sensor's architecture. Hence, the architecture of TelePix2 is described in detail in section 4.2. Afterwards, a comparison between used HV-MAPS within this thesis is presented in section 4.3.
Additionally, it should be mentioned that this thesis is the first LHCb thesis working on KIT developed HV-MAPS at the University of Bonn. All necessary knowledge was acquired through measurements, public documentation, discussions with experienced scientists from the LHCb Heidelberg group, and consultations with the designers at KIT.
Theses used to obtain knowledge are: [112] [113] [114] [93] [83].

4.1 Development of HV-MAPS towards the MightyPix

The dedicated development of MightyPix was built upon a long HV-MAPS development phase. Building on this foundation, the MightyPix design was further strengthened. An overview of developed HV-MAPS leading towards the MightyPix is given in the following. Since the proposal of HV-MAPS in 2007 by I. Péric, several HV-MAPS have been designed not only by the KIT designer team but also by other designers at different institutes. An overview of the development chain of HV-MAPS designed at KIT towards MightyPix2 is given in fig. 4.1.

First developments were done for the Mu3e experiment. Starting with test structures in 2011, produced in the H18 line at AMS, several iterations up to the production sensor, MuPix11 - produced in the H18 process at TSI in 2022, were evaluated.
A second development line with HV-MAPS dedicated for the ATLAS experiment started in 2017. With the knowledge gained from ATLASPix3(.1) a third development towards the MightyPix started in 2020 with a first engineering sensor: Run2020. While the Run2020 sensor and its successors the Run2021, TelePix2 and MightyPix1 sensors have been produced by TSI, further sensors, such as MightyPix2, will be submitted at AMS due to the shutdown of the H18 process at TSI.
Another sensor - the P2Pix - is part of the overview, belonging to the P2 experiment [116]. Knowledge will be shared between the two experiments and influence the design of MightyPix2. In addition, a further sensor - LF-MightyPix - is included. The sensor was produced at LFoundry [117] to evaluate another process by a different manufacturer as fall-back solution

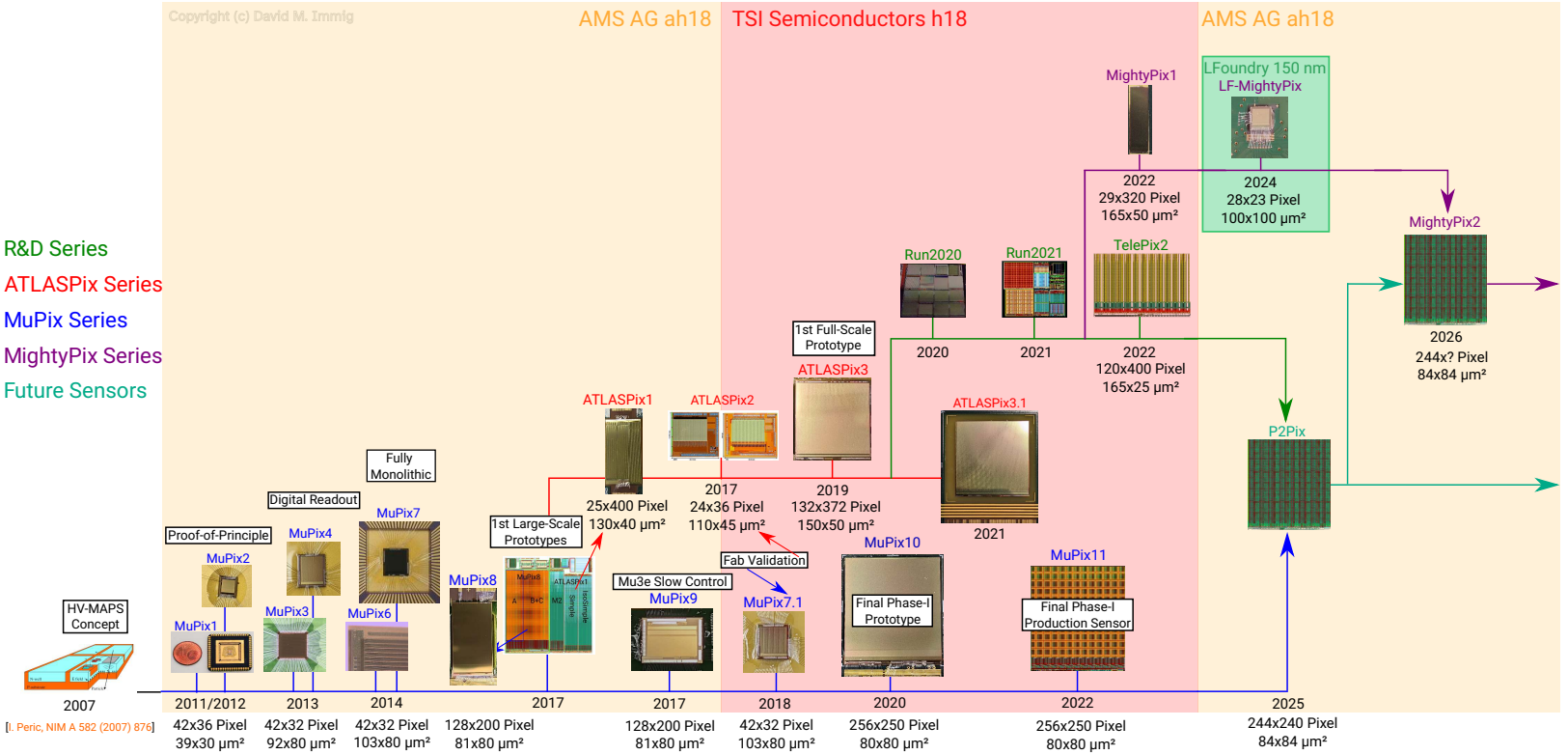


Figure 4.1: Historical overview of HV-MAPS designed at KIT by I. Péric for the Mu3e and ATLAS experiments. Based on this, the MightyPix family is developed. Main features, e.g. number of pixels and pixel size, is shown as well as the foundry [115].

to AMS and LHCb specific digital features.
As mentioned in the beginning, TelePix2 is the latest predecessor to the MightyPix development chain. Therefore, the sensor is an excellent candidate to understand the technology and validate its compatibility with the Mighty-Pixel.

4.2 Design of TelePix2

TelePix2 [6], depicted in fig. 4.2, has been designed with the purpose to be used as a fast Region-of-Interest trigger and time information providing sensor for EUDET-type beam telescopes - specialized to fulfill the requirements at the DESY II testbeam facility [8].
For the design, presented in the following, and measurements, discussed in chapter 6, it has to be taken into account that this sensor was not designed to meet the Mighty-Pixel requirements. However, its pixel cell design, described in section 4.2.1, shares commonalities with the MightyPix and hence, can be used for performance measurements.

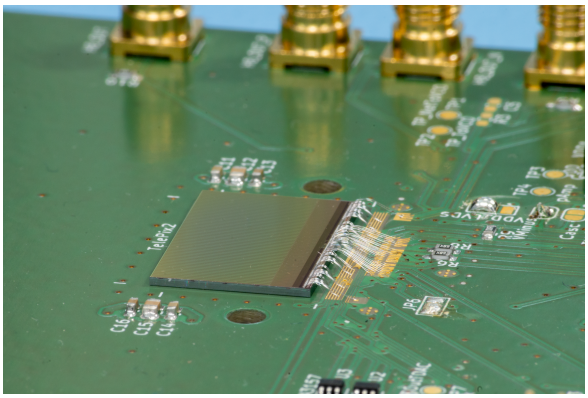


Figure 4.2: TelePix2 glued and bonded to a MARS carrier PCB.

Intended to operate within a telescope, TelePix2 has a total sensor size of 20.015 x 13.130 mm^2 to cover the area of sensors used in the EUDET-type telescopes [118]. With a matrix of 120 columns and 400 rows and a pixel size of 165 x 25 μm^2 TelePix2 was produced in a 180 nm process on a 200 to 400 Ω cm p-type Czochralski wafer at TSI [71].
The sensor consists of active pixel cells and a digital periphery. Each column, consisting of 400 pixels, is point-to-point connected to 400 hit digitizers in the digital periphery, and one **E**nd-**o**f-**C**olumn EoC buffer. At the digital periphery the asynchronous data enters the synchronized domain. Located in the digital periphery, the **R**eadout **C**ontrol **U**nit RCU processes the signals and sends a zero-suppressed data link with 1.25 Gbit/s.
To place all needed connections inside the sensor, several metal layers are needed. Within the used technology seven layers of metal are available with the top layer used for power distribution and timing signals [6].

The active pixel cell and digital periphery design are described in section 4.2.1 and section 4.2.2. How the sensor is configured, is explained in section 4.2.3. Finally, the chapter concludes in section 4.3 with a comparison of HV-MAPS used within this thesis .

4.2.1 Pixel Cell Design

The active pixel cell consists of three main parts: (1) Sensor diode, (2) **C**harge **S**ensitive **A**mplifier CSA, (3) comparator. If a charged particle traverses the reverse biased sensor diode, ionization can occur. Generated electron-hole pairs are separated by the electrical field and drift towards the corresponding electrode. The induced signal is amplified and shaped by the CSA - generating an analog output signal that is processed by the comparator. If the signal, surpasses the detection threshold of the comparator, a digital pulse is generated.
In the following the pixel cell design of TelePix2 is explained in more detail. An overview of the pixel design is presented in fig. 4.3.

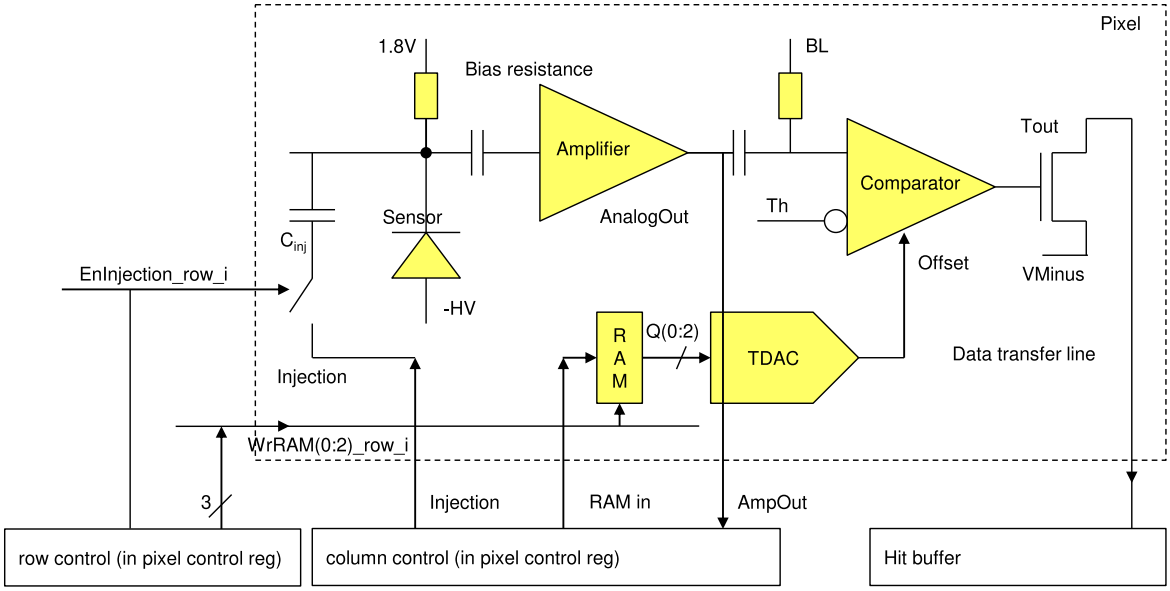


Figure 4.3: Schematic of the pixel cell design with the CMOS amplifier and comparator. Connections to the pixel control register as well as the charge injection circuit are shown. The discriminated output signal is sent to the hit buffer [119].

Sensor Diode

In its simplest approximation, the sensor diode is a pn junction. A depletion region forms at the junction, and reverse biasing enhances the region - essential for providing a large active detection volume. If sufficiently depleted, the active detection volume can be extended to the full sensor depth, enabling a large sensitive area. If a charged particle ionizes the sensitive

medium, electrons are collected by the collection electrode.
In more detail, a deep n-well is embedded in a p-type Czochralski wafer. The n-well has a large fill factor and hence, follows the large collection electrode approach (see section 3.4). As indicated in fig. 3.17 the sensor is top-side biased via the top metal layer with a metal contact on a p^+-implant outside of the pixel matrix - called chip bias.
Neighboring pixels are isolated by a trench isolation separating each and a p-implant forming a guard ring - called pixel guard ring [120]. By the implementation cross-talk is reduced. If a signal received by one pixel is capacitively coupled into adjacent pixels, one speaks of cross-talk. Consequently, this has to be taken into account for particle tracking. In addition, conductive electron layers at the Si-SiO_2 interface are interrupted by trench isolation. These can be built up by IEL damages (see section 3.3.2) due to trapped holes which attract free negatively charged carriers. Depending on the p-stop doping concentration, electron accumulation and as a consequence cross-talk can be reduced.
However, high electric fields at the p-implant influence the breakdown behavior (see chapter 6). Since the p-stop acts as a guard ring, it is either floating or set externally to a potential. Thus, the contact can be used to bias the substrate as well - called pixel bias.
The collection electrode itself is biased via a resistor placed between the n-well and the external power supply of a nominal voltage of $\approx 1.8\,\mathrm{V}$. By an on-chip configuration DAC, *VNBias* [1], the bias strength can be adjusted. However, for all investigated devices the DAC did not have an effect on the biasing behavior.
The generated signal is further processed by the CSA.

CSA

The main task of a **C**harge **S**ensitive **A**mplifier CSA is to integrate collected charge over a time period and amplify the signal while offering a high gain and low power consumption.
Signals collected by the collection electrode are AC-coupled into the CSA. Because the DC-levels of the amplifier and the sensor diode differ, AC coupling is needed.
Since the CSA is implemented inside the deep n-well, its input node is coupled to the n-well causing a parasitic capacitance. In the same manner the output node is coupled to the n-well as well. Usually, this causes capacitive loads but can be used advantageously as feedback via coupling the parasitic capacitance of the amplifier output back into the amplifier input via a feedback capacitance (for more information see [120]). In addition, a resistive feedback circuit is implemented to constantly discharge the CSA.
Depending on the settings of involved transistors, the rise and fall time of the signal is tunable. The feedback capacitance determines the rise time while the fall time is regulated by the feedback resistor. Shaping of the signal is done via the on-chip DAC *VNFB* regulating the discharge resistance. An overview of the in-pixel electronics is given in the transistor level schematic in fig. 4.4.

[1] Typically all on-chip DACs starting with "V" are used to regulate voltages while DACs starting with "I" are current regulators.

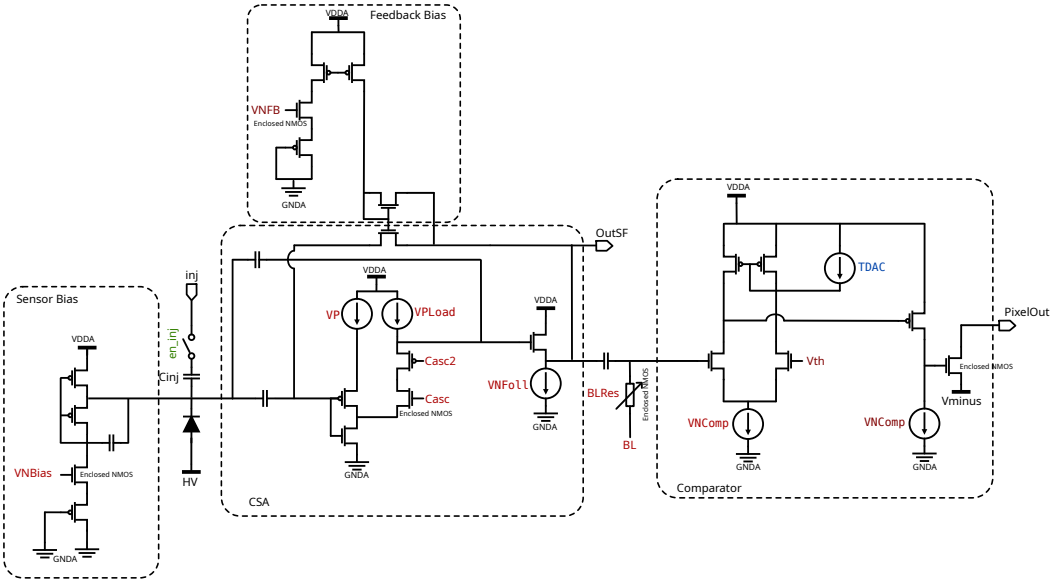


Figure 4.4: Schematic of the transistor level of the amplifier and comparator including the sensor bias and feedback circuit. Configurable on-chip DACs are labeled in red [121].

Via *VP* the bias voltage of the CSA can be adjusted. With *VPLoad* [2] the input bias of the transistor, acting as a resistive element, of the CSA and the feedback circuit are tuned. The source follower at the output of the CSA is AC-coupled to the comparator input, isolating the CSA output from the high impedance RC filter. As a result, the effective resistance compared to the following capacitance is reduced which subsequently reduces the delay caused by the RC-element. In addition, the feedback current is produced. The current of the source follower at the CSA output is controlled via *VNFoll*.
For the most bottom pixel of each column the amplifier output signal *AmpOut* is accessible, usable to optimize the on-chip DACs while visualizing the analog signal with an oscilloscope. Via *IPFoll* the current source of the output signal is controlled.

Comparator

The main task of the comparator is to convert an analog input signal into a digital output signal by comparing it to a defined threshold voltage - discriminating if a signal is detected or not. The length of the digital pulse corresponds to the amount of detected charge.
In TelePix2, but also all other HV-MAPS with an in-pixel comparator, the CSA output is capacitively coupled to a configurable baseline voltage *BLPix*. Hence, the baseline potential is modulated by the CSA output signal. Via a resistor, tunable by the on-chip DAC *BLRes*, the voltage is coupled into the input of a 3-bit tunable CMOS comparator, depicted in fig. 4.4. If the BL voltage, modulated by the output signal of the CSA, passes the threshold, the

[2] *VPLoad* is implemented as *IPLoad* in the configuration file. For historic reasons the naming scheme was not adjusted for each device although the DAC configuration in the DUT might has changed.

comparator output switches - creating a digital output signal. Its length is defined as the **T**ime-**o**ver-**T**hreshold ToT, correlated to the amount of signal charge.
The biasing of the comparator is controlled by the on-chip DAC *VNComp*. Because of process variations every pixel reacts differently to a given threshold resulting in a dispersion of the threshold over the full sensor matrix. Minimizing the dispersion is possible using three tune bits - called *TDAC*. Current drawn by the TDACs and provided by transistors is controlled via *IPDAC* [3].
Disabling noisy pixels is possible via a switch in the hit buffer enabling/disabling the comparator output.
The comparator output signal is sent out and received by the hit buffers, described in section 4.2.2. By the difference of the digital power domain and *VMinus* the voltage amplitude of the signal line is defined. Small *VMinus* values increase the probability for cross-talk between adjacent lines, while large values decrease the signal amplitude. In a worst case scenario, signals cannot be detected by the receiver.

Injection Circuit

To evaluate the functionality of the sensor, usually a particle source is mandatory. However, a particle source may not always be available. Furthermore, testing the sensor electronics without requiring ionizing particles is beneficial. Therefore, an on-chip injection circuit is implemented.
The test pulse is generated by discharging a capacitance inside the pixel cell as indicated in fig. 4.4. As a consequence, the induced signal can be used to test the complete readout chain.
The injection signal itself is produced in the periphery and routed towards each pixel cell. In TelePix2 the injection can be enabled for individual pixels via the *En_inj* bit. Pixels without enabled injection are connected to ground to avoid unintended signals.

[3] It should be mentioned that different TDAC implementations exist for the sensors used within this thesis. While TelePix2 has TDACs placed in the hit-buffer cell, the Run2020 sensor has two flavors of TDACs. Firstly, similar to TelePix2 located in the hit-buffer and secondly, located in the pixel cell.

4.2.2 Digital Periphery Design

At the digital periphery digital information is associated to the pixel cell output. Most important are row/col addresses and timestamp information.
The periphery is located at the bottom of the pixel matrix - an arrangement that is crucial for minimizing dead areas in the Mighty-Pixel by allowing non-sensitive regions of adjacent sensors to overlap. A simplified overview is illustrated in fig. 4.5.

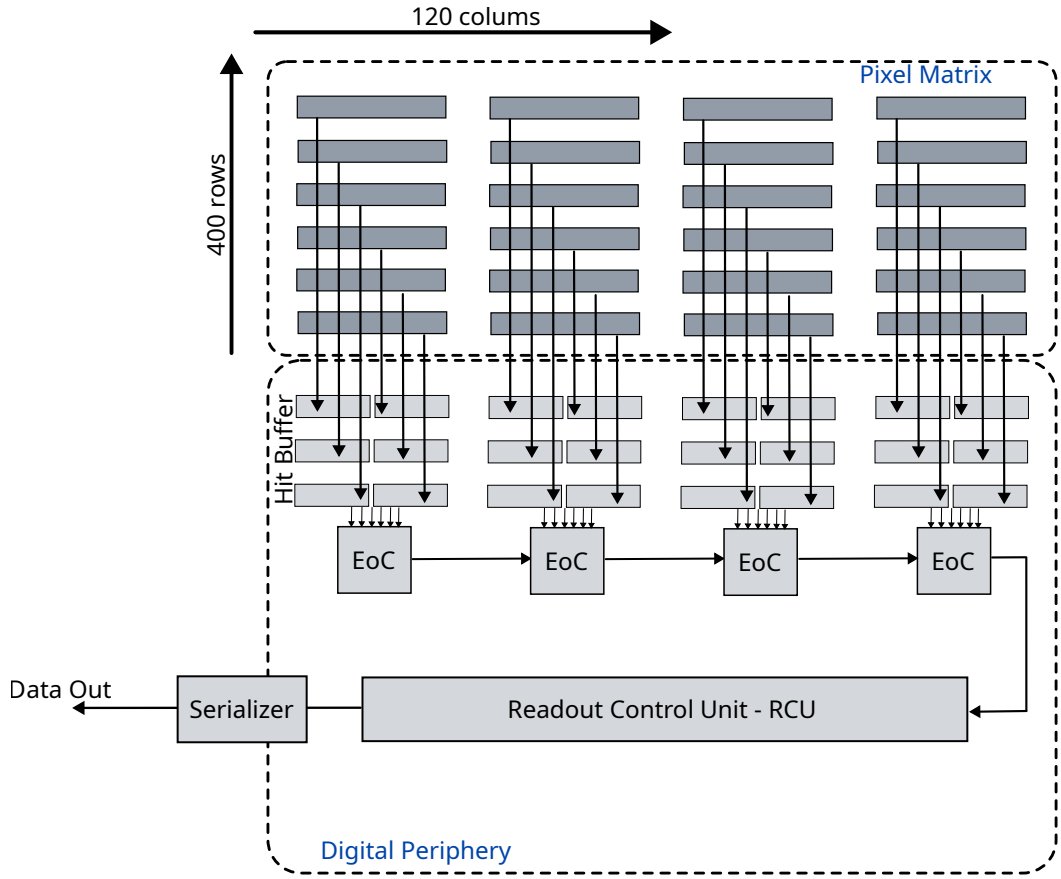


Figure 4.5: Simplified schematic of the building blocks of the digital periphery of TelePix2 including the hit buffers, EoC buffer and the RCU.

It consists mainly of two blocks: (1) The RCU and (2) a custom-designed Phase-Locked Loop (PLL) and data serializer.
The output of the pixel cells is received and stored at the hit buffer cells - digital partner cells for each pixel cell. Before the data is read-out by the RCU, it is transmitted to the **E**nd-**o**f-**C**olumn EoC buffer.
In the following each component is explained, starting with the hit buffer cells.

Hit Buffer

Every pixel cell is connected to a readout cell which generates its address and timestamp information. Because of many needed connection lines, multiple metal layers are used which can influence the recorded data - an effect observed in the time resolution studies of TelePix2 (see section 6.3.3).
The hit buffer consists of RAM cells, a digital receiver and edge detector as well as hit flags, priority logic and memory needed for data processing. The line signal of the pixel cell output is received by the receiver, illustrated in fig. 4.6.

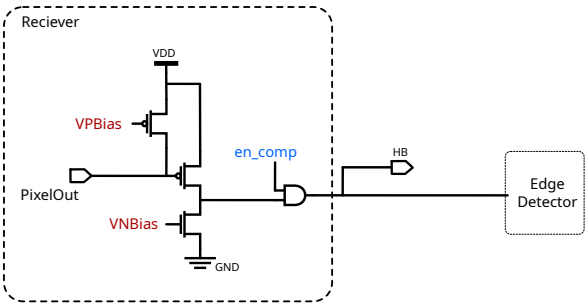


Figure 4.6: Transistor level schematic of the receiver located in the hit buffer. On-chip regulator DACs are colored in red. Enabling/Disabling of the comparator is done via the RAM value *en_comp*. Voltage domains are indicated [121].

A digital signal with a voltage level between ground GND and the digital voltage level VDD is created if the line signal surpasses the detection threshold. Its pull up current to the VDD potential of 1.8 V is regulated by *VPBiasRec* and the detection threshold by *VNBiasRec*. The hit edge detector, located at the right edge in fig. 4.6, digitizes the signal by the generation of a pulse at the leading edge of the signal hit, externally delayable by the on-chip DAC *VNDel*.
At the stage of the hit detection, the asynchronous data is synchronized into the clock domain. Recording a hit, raises the storage of its arrival time buffered into *TS1*. The timestamp, based on the timestamp clock, is captured asynchronously at the signal edge.
A 19 bit Gray encoded timestamp is generated, along with a 1-bit counter triggered on the falling edge. Therefore, the recorded timestamp of the hit is sampled with twice the reference clock speed, doubling the timestamp precision.
The falling edge of the hit signal is sampled with 10 bit and a timestamp *TS2* is stored as soon as the signal falls below the comparator threshold. A combination of both enables ToT measurements. Further, a digitized timestamp is sampled by a seven bit **T**ime-to-**D**igital **C**onverter TDC producing a digital time information [4].
Between the receiver and edge detector a output signal of the comparator, called *Hitbus*, is tapped out. In contrast, to the *AmpOut* not only the signal of the most bottom pixel of a

[4] The TDC is not used within this thesis. Further, it should be mentioned that the TDC cannot be turned off in TelePix2 due to a design flaw, resulting in an unintended high power consumption (see section 4.2.4).

column but the OR of a column is connected out - used as the fast RoI trigger to provide time information for the EUDET-type beam telescopes.

End-of-Column Buffer EoC

At the end of the hit buffers the **E**nd-**o**f-**C**olumn EoC buffer are located. For each column the hit information (address and timestamps) are stored and provided to the **R**eadout **C**ontrol **U**nit RCU. Per readout cycle data with the lowest row address is stored in the EoC buffers - giving the readout its name: *Column-Drain Readout*. How the EoC buffer are read out, is determined by a priority logic which is described within the following section.

Readout Control Unit

Reading hits, formatting the information and sending the data out serially is task of the **R**eadout **C**ontrol **U**nit RCU - directly transferring data from the EoC buffers to the data serializer without intermediate buffering. It comprises a configuration register, a state machine and a data formatting block including 8b/10b encoding and the top module of the data serializer.
The state machine controls the readout of the pixel matrix, reads the data and transmits it to the serializer. In fig. 4.7 a schematic overview of the state machine is presented, detailing each state along the corresponding output data words.
Each state has a dedicated purpose. By an identifier flag the state machine distinguishes each state. If the identifier flag is a ”1”, the 8b/10b data word contains only a control pattern and not valid data. The states including valid data are further identified by a two bit identifier at the beginning of the data word.

A summary of the most important tasks of the state machine states is given in the following:

1. Sync state: State machine stays for configurable numbers of clock cycles in this state. The output consists of the 8b/10b symbol K28.5, used to align the 8b/10b codes in a bit stream.

2. Pull Down: If the pull down signal is activated, the column data busses are discharged.

3. Load Column: The start of a readout cycle is defined by generation of the load column signal. The signal is transmitted to the hit buffers → Data of the highest position buffer is loaded into the column bus, used to buffer the data of a column, and copied to the EoC buffer.

4. Load Pixel: Hit buffers are activated if they have stored hits.

5. Load Pixel: If hits are available, a valid data word containing timestamp information is sent out.

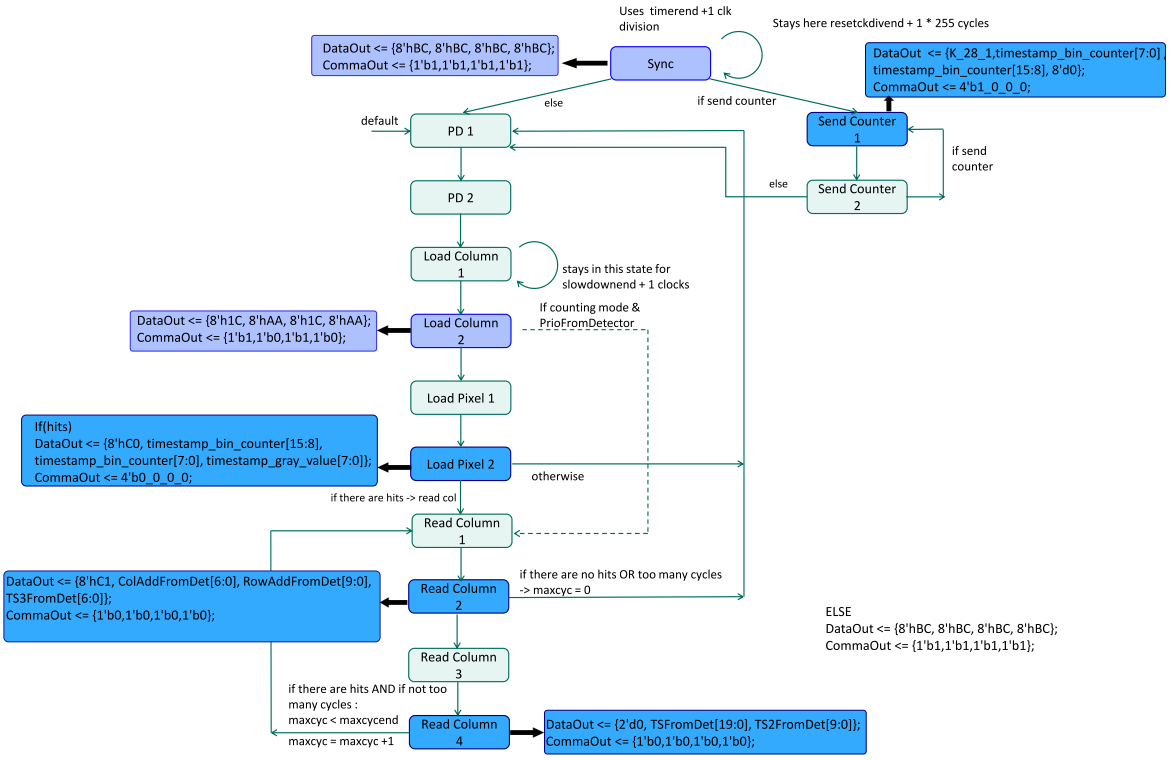


Figure 4.7: Schematic of the state machine of TelePix2. States in which valid data is transmitted are highlighted in blue and in which 8b/10b control symbols in light blue. Adapted from [119].

6. Read Column: EoC buffers with data are activated to send the data via the data bus.

7. Read Column states: Data is transmitted to the serializer.

For all states the first state ”1” generates the signal while the second state ”2” deactivates the signal and sends the data output. The duration of the first load column state is configurable via *slowdownend*. Via *timerend* the overall state machine can be slowed down.
The output data is sent in two states with the following content:

- Row and column address and the TDC information
- Time information containing the ToA information *TS1* and *TS2*

The understanding of the state machine and its data format was essential to develop the firmware of MARS (introduced in section 5.3). Two examples regarding - (1) 8b/10b encoding, and (2) clock domains - are explained in the following:
The 8 bit data output is 8b/10b encoded to DC balance the transmission and reduce error probabilities. Via a custom serial protocol the output is sent on the falling and rising clock edge - resulting in a doubled data output rate which was taken into account in MARS’s firmware.

Understanding of the sensor internal clock domains is crucial to configure the sensor. For example, the clock of the state machine has to be ten times faster than the bit clock to ensure sufficient time to serialize the data in time. The serializer transmits two bits per cycle - one on each clock edge of the bit clock. Therefore, up to 20 bit can be sent per state machine cycle if the state machine clock is ten times faster. By sending data only in every second state to the serializer, sufficient time to transmit 40 bit is ensured.

Phase Locked Loop

On-chip clock generation is possible via an implemented **V**oltage **C**ontrolled **O**scillator VCO. An external (on FPGA level created) reference clock is received and processed to a five times faster base clock. Synchronizing and stabilizing both clocks is regulated via a **P**hase **L**ocked **L**oop PLL. Operating the sensor without the PLL is possible if a direct external reference clock with five times the base clock frequency is provided. Via two switches the operation mode is selectable.

4.2.3 Configuration Registers of TelePix2

TelePix2 has in total five registers: (1) Configuration register in the RCU, (2) DAC register in the RCU, (3) **V**oltage **DAC** VDAC register in the RCU, (4) Column-row register in the **C**onfiguration **R**egister **B**lock CRB and (5) TDAC register in the CRB.
All registers are implemented as shift registers sharing the same clock input, except for the configuration register, which uses two separate clocks.
Via the VDAC register on-chip voltages are controllable. For example, the baseline voltage or threshold of the comparator, can be defined. Global signals to control the digital periphery are stored in the configuration register, while on-chip DACs are controlled by the DAC register. An overview of configurable on-chip DACs and voltages of the in-pixel electronics is given in table A.3. In table A.2 a similar overview of global DACs of the configuration register is provided. Both tables summarize the most relevant DACs for this thesis.
The configuration of the pixel matrix is managed by the two registers stored in the CRB - explained in the following.

Configuration Register Block

Per column one CRB controls four pixel-rows. Besides the row-column register, the CRB comprises a TDAC register - dedicated to store RAM. Both have similar clocks, serial input and read-back signals but two independent global load signals to write data from the shift register to the pixel memory cell.
Register cells, storing bits, are implemented triple-redundant to reduce error probability by **S**ingle **E**vent **U**psets SEUs induced by radiation damage.

Row-Column Register

By the seven bit large row-column register, placed between the pixel and hit buffer column, the matrix is configured. Four bits out of these are used to produce **W**rite **RAM** WRAM signals, each for four pixel-rows per column. Enabling injection, the amplifier and hitbus output is controlled via the three remaining bits.

TDAC Register

A one bit TDAC register located per column is needed to store and generate RAM signals. In addition, the possibility to read back the pixel RAM is implemented. Doing so, enables the possibility to read back stored bit content in the register cells and detect radiation induced bit flips.
Whether RAM generation or read-back is foreseen, is controlled via two global signals stored in the configuration register implemented in the RCU.

4.2.4 Power Consumption of TelePix2

As stated previously, TelePix2 has a design flaw causing a high power dissipation. Using the standard configuration (for more information see chapter 6 and appendix A.11), the DUT consumes approximately (380 ± 1) mA in the digital and (339 ± 1) mA in the analog domain without cooling of the device.
One contributor to this consumption is the TDC, which cannot be turned off. To reduce power, the timestamp clock can be disabled, resulting in a power consumption of (119±1) mA (digital) and (360 ± 1) mA (analog). However, disabling the timestamp clock prevents measurement of the time resolution, as discussed in section 6.3.3. Therefore, disabling of the timestamp clock is not feasible. The high power consumption has several consequences on the operation of the DUT:
Firstly, a cooling solution covering the heat dissipation is required. The developed setup is introduced in section 5.2.1.
Secondly, optimizing the sensor configuration (presented in appendix A.11), essential to enhance the sensor performance [5], results in an even higher power consumption of approximately (371 ± 1) mA (digital) and (548 ± 1) mA (analog). Consequently, the cooling approach has to cover this as well.
Thirdly, the operation of irradiated sensors is affected. A detailed discussion of both effects bulk and surface damage is provided in chapter 7 and chapter 8, respectively.

[5] The optimized performs in terms of time resolution is presented in section 6.3.3.

4.3 Comparison of HV-MAPS

An overview of the sensors used within this thesis with respect to the MightyPix is given in table 4.1 [6]
Besides studying the performance of the Run2020, Run2021 and TelePix2 sensor, the author took part in two testbeam campaigns with the ATLASPix3(.1) where contributions to the temperature and humidity monitoring, the overall sensor operation at the campaigns as well as major contributions to the analysis were done.
The sensor design of the Run2020, Run2021 and TelePix2 sensors are very similar except some minor differences. In contrast to TelePix2 and the Run2021 sensor, the biasing scheme differs for the Run2020 sensor because of a missing n-well isolation, essentially shorting chip and pixel bias. Further, the timestamp information is implemented slightly different. For MightyPix1 and MightyPix2 a similar biasing scheme is implemented.
More differences can be found in the foundry, sensor and pixel size, in-pixel electronics (amplifier and comparator). In table 4.1 a summary of those as well as the sensor interface, its data output and decoding are presented.
Variations become apparent when comparing the physical dimensions of the sensors. Because the Run2020/1 sensors are dedicated test sensors, the sensor size is small. Instead, TelePix2 is a full size sensor. Similar, MightyPix1 is the first test sensor of the MightyPix development chain and hence, the sensor size is not full size. In contrast, MightyPix2 will nearly be a full-size sensor [7].
Looking at the pixel sizes and electronics, several differences are observed. Testing pixel sizes and electronics was main part of the engineering sensors. Hence, different flavors have been implemented.
In addition, a CMOS comparator [8] was implemented in the Run2021 sensor due to the possibility of adding a deep p-well into the n-well in the fabrication process. Beneficial are the reduced bias current and fast rise time. Because of the closed manufacturing process at TSI, MightyPix2 will have a NMOS comparator since AMS does not offer the required deep p-well implantation. Studies testing the NMOS comparator performance with the Run2020, performed at the University of Heidelberg [122], showed promising results in terms of time resolution studies.
Still under discussion is the pixel size of the production MightyPix. From tracking studies a slight loss in performance for large squared pixels (100 x 100 μm^2) has been derived. However, squared pixel generate less leakage current which is especially important in terms of radiation damage. On the other hand, rectangular pixel have smaller clusters along the long pixel side and offer an improved track momentum resolution.
Configuration of the sensor is not only relevant for the development of laboratory DAQ system

[6] Emphasis is given on the Run2020, Run2021 and TelePix2 sensors because they were used for laboratory measurements.
[7] The final sensor size is under discussion at the point writing this thesis.
[8] The first CMOS comparator has been implemented in a development sensor as part the ATLASPix development chain.

but also for the overall Mighty-Pixel. Since thousands of sensors have to be configured, the configuration has to be parallelized and its time must be reasonably low. While standard communication via I2C is foreseen for tests in the laboratory, the protocol is not feasible for the experiment. How the slow control is implemented in MightyPix2, is described in [68]. TelePix2 and the Run202/1 sensors are configured via **S**hift **R**egisters SR as explained previously.
The 64 bit output data word is for all sensors besides the MightyPix 8b/10b encoded and sent via one data link operational up to 1.25 Gbit/s. Decoding of the data is done at the readout DAQ (see chapter 5).
Increasing the number of data links for MightyPix2 is necessary to cope with the expected hit rate. In addition, the data word length is shortened when all four links are used. Further, scrambling of the data word is implemented to DC balance the data transmission.
The main difference between the Run2020, Run2021, TelePix2, MightyPix1 and MightyPix2 sensor is the digital design since MightyPix2 will offer LHCb specific digital features - necessary to cope with LHCb's DAQ system. For example, the ECS and TFC systems (introduced in section 2.3.3) can be tested. In addition, the data output and processing will change. Data words with two different lengths (30 bit or 32 bit), depending on the hit rate, are built by the FSM, which is similar to the FSM described in section 4.2.2. However, the subsequent data processing differs from that of the predecessor sensors. To convert the long data words into 30 bit words, a gearbox is implemented. Before the output data is serialized, the sent data is selected at a multiplexer stage. More information is provided in [68].

Chip	Foundry	Size [mm^2]	Pixel size [µm^2]	Amplifier	Comparator	Interface	Data	Decoding
ATLASPix3(.1)	TSI	20 x 20	150 x 50	PMOS	NMOS	SR	1.25 Gbit/s, 64 bit	8b/10b
Run2020	TSI	5 x 5	165 x 25/50/100	all	all	SR	1.25 Gbit/s, 64 bit	8b/10b
Run2021	TSI	5 x 5	165 x 25/50	CMOS/NMOS	CMOS	SR	1.25 Gbit/s, 64 bit	8b/10b
TelePix2	TSI	20 x 10	165 x 25	CMOS	CMOS	SR	1.25 Gbit/s, 64 bit	8b/10b
MightyPix1	TSI	5 x 20	165 x 50	CMOS	CMOS	I2C, SR, TFC	1.28 Gbit/s, 64 bit	scrambler
MightyPix2	AMS	20 x 16 [a]	84 x 84	CMOS	NMOS	I2C, TFC, ECS	4 x 1.28 Gbit/s, 32 bit	scrambler

Table 4.1: Overview of specifications of HV-MAPS used for measurements within this thesis (ATLASPix3(.1), Run2020, Run2021, TelePix2) compared to the specifications of MightyPix1 and MightyPix2. Specifications include production foundry, dimensions, readout electronics, sensor interfaces and implemented data readout.

[a] The sensor size was under discussion at the point writing this thesis.

CHAPTER 5

Mighty ASIC Readout System - MARS

Characterization of HV-MAPS requires a dedicated **D**ata **Acq**uisition system DAQ. As main part of this thesis the DAQ system MARS - **M**ighty **A**SIC **R**eadout **S**ystem was developed and first published in [7].
MARS comprises custom hardware, firmware and software offering a modular and flexible approach in all parts as well as a user-friendly python interface. Its development was a crucial step in the R&D phase of the MightyPix. Other DAQ systems exist, but do not fulfill the requirements on adaptability and availability. Two other systems are the GECCO [86] and MUDAQ used by groups at KIT and the Heidelberg University.
The GECCO system was developed and supported by PHD students at KIT. Hence, long-term support was not provided. In addition, adaptions to operate HV-MAPS foreseen for the Mighty-Pixel project would have been needed on all levels of the DAQ. Moreover, the system can be used within testbeam conditions but is not optimized for this purpose.
The MUDAQ system has been developed by the Mu3e group mainly located at the University of Heidelberg to characterize HV-MAPS. Since the HV-MAPS studied within this project inherit from the MuPix family (see fig. 4.1), the DAQ system is suitable for those sensors [1]. However, the required hardware was not available at the beginning of this thesis.
Hence, a DAQ system covering all requirements was crucial to characterize HV-MAPS in the laboratory as well as at testbeam facilities.
Since the SiLab at the University of Bonn has a lot of of experience with characterization of silicon sensors and a well established DAQ system, BDAQ53 [123], developed as a pixel detector test system for ATLAS and CMS, and based on BASIL [124], MARS follows its design approach and inherits its architecture from BASIL and especially the adapted DAQ system for the TJ-MonoPix2 [125].
Because the tested **D**evices **U**nder **T**est DUTs are designed differently compared to DUTs usually tested within the SiLAB, new hardware had to be designed and produced. Further, changes to firmware and software had to be made. However, for all three building blocks (hard-

[1] The LHCb group at the Heidelberg University is using MUDAQ as a DAQ system to study HV-MAPS for the Mighty-Pixel project.

ware, firmware, software) commonalities with the BDAQ53 can be found since non-device specific building blocks have been adapted. Each design is discussed within this chapter.
Firstly, requirements for MARS are discussed in section 5.1. Based on this, the hardware design is introduced in section 5.2 and the firmware in section 5.3. Testing the firmware without hardware is possible via a simulation which was set-up within this thesis. The architecture is explained in section 5.3.1. Configuration of the sensor is done via a software interface written in python. While an outline of the general software approach is given in section 5.4, a specific example for the TelePix2 sensor is shown in section 5.5. Finally, MARS's compatibility is summarized in section 5.6 including available devices and hardware. As an ongoing project and outlook **Q**uality **A**ssurance QA is introduced in section 5.7.

Disclaimer

Since the development of MARS is a challenging project, the author did not develop all parts on her own. The start of the project was done in 2020 by K. Padeken and is based on BDAQ53. With the start of this thesis in 2022 main contributions to all building blocks have been made. While the hardware was mainly designed by K. Padeken and later by N. Sommerfeld, debugging and testing was done by the author. Large parts of the firmware and the software setup were developed by the author. All implemented scan routines and analyses programs have been setup within this thesis and were tested for different devices. Moreover, the integration into a testbeam setup at DESY (see chapter 9) has been done by the author.

A short introduction on how to get started with MARS is given in appendix A.3.

5.1 Requirements

Two main applications were taken into account designing MARS: (1) Studying single DUTs in the laboratory and (2) studying single DUTs at testbeam facilities as part of a beam telescope. Moreover, MARS must be suitable for different DUTs. Therefore, the overall design approach is a highly modular and flexible system.
MARS's hardware is split-up into three main parts: (1) An **F**ield **P**rogrammable **G**ate **A**rray FPGA placed on a FPGA carrier board, (2) a DUT carrier board and (3) an adapter board. Their design is discussed in section 5.2.
Separation into different components allows compatibility with different DUTs without major change of the full hardware. In particular, the DUT carrier board has to be specialized for each DUT. Separating it from the remaining system enables the possibility to keep the main hardware components unchanged for different devices.
Usage within a beam telescope requires minimal material budget to ensure low multiple scattering and thus, a high tracking efficiency. In addition, components which are affected by radiation damage are kept minimal and not in the vicinity of the DUT. A crucial component

is the FPGA itself. Moreover, cables as connectors between the adapter and DUT board are beneficial in terms of modularity. Consequently, the FPGA together with its carrier board can be positioned away from radiation-critical areas.
Furthermore, cables are needed to test the data link quality over a long distance which is required by the experiment (see section 2.4.3).
Keeping the experimental requirements and in particular the MightyPix specifications (presented in table 2.1) in mind, DUTs have to be studied at different temperatures to understand the performance-temperature dependence and find the optimal operation temperature. Therefore, cooling and temperature controlling is required (see section 5.2). Additionally, high and low voltage have to be provided and controlled (see section 5.2).
Studying the time resolution is crucial to ensure that the MightyPix specifications are met. Therefore, inputs for trigger signals are needed. Connectors for this are available on the adapter board (see section 5.2.3). Further, MARS is compatible with a **T**rigger **L**ogic **U**nit TLU (see section 5.2.2 and chapter 9) [126].
Besides the data link quality, the data rate has to be studied. For the MightyPix sensor an output rate of $4 \times 1.28\,\mathrm{Gbit/s}$ [55] is required. Testing necessitates an FPGA capable of this. The `Mercury KX1` [127], an `AMD Kintex 7` FPGA, and its successors fit these requirements. At the point writing this thesis MARS was not yet designed for operation at the maximum rate of all links because MightyPix2 will be the first sensor enabling those tests.
Next to the required flexible hardware design, the firmware and overall software have to be highly flexible, too. In addition, the software interface has to be user-friendly. Because of that python was chosen as the main software language.
Similar firmware and software should be used for different devices as well as laboratory tests and testbeam campaigns. Hence, both are designed modular as well. Each part is discussed in section 5.3 and section 5.4, respectively.
Finally, MARS is used at different universities and will be used at even more (see the summary in table A.1) to test MightyPix2 and hybrids (see section 2.4.3). Consequently, needed software, firmware and hardware has to be accessible which is ensured by the CERN hosted version control system `GitLab` [128] and a documentation given by this thesis. An additional documentation webpage [129] is under development as well.
Characterization of hybrids with MARS is possible since this application was kept in mind from the beginning on. Adapting the firmware and software is mandatory but due to their flexible design possible. Hardware components have to be exchanged depending on the final hybrid design and to enable high data rates for multiple links.

5.2 Hardware Design

Disclaimer

The hardware was initiated by K. Padeken and later within this thesis in collaboration with N. Sommerfeld. The author tested all pieces for functionality and contributed feedback for subsequent iterations and improvements.

MARS hardware design is versatile allowing to test different HV-MAPS in the laboratory as well as at testbeam campaigns. Three main components can be distinguished: (1) a DUT carrier board, (2) a FPGA with FPGA carrier board and (3) an adapter board.
In fig. 5.1 a top view of MARS is shown. The FPGA is covered by a blue heat sink and slotted into to the FPGA carrier board. Via a `PCI Express` connector the FPGA and adapter board are connected. The DUT carrier board is connected to the adapter via two `Display Port` cables for external voltages and data transmission. Shown is a DUT carrier board hosting a TelePix2 sensor covered by a protection cap.

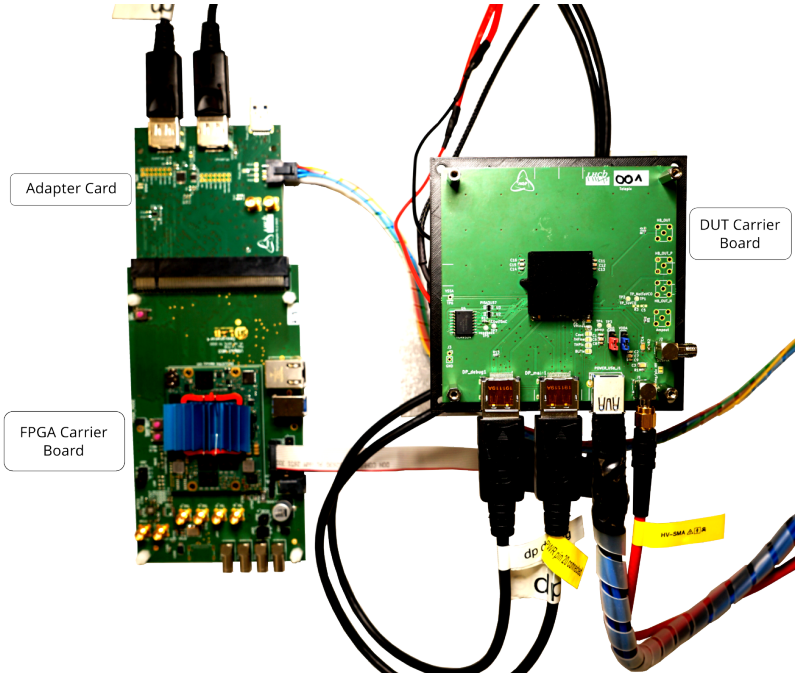


Figure 5.1: Top view of MARS consisting of a TelePix2 carrier board, located on the right hands-side, a FPGA covered by a blue heat sink and slotted into the FPGA carrier board and the adapter PCB connecting all pieces. `Display Port` cables for data and signal transmission as well as low voltage cables are connected.

The design of each **P**rinted **C**ircuit **B**oard PCB depends on its corresponding purpose. A schematic overview of the system and needed data and signal transmission is illustrated in fig. 5.2.

The FPGA board is powered externally and connected to the back-end computer for data transmission via Ethernet and for configuration via a JTAG programming cable. In addition, commands to execute scan routines are transmitted via Ethernet from the back-end computer to the FPGA board. The board offers an additional connector to use a TLU - needed for, e.g., testbeam campaigns (see section 5.6.2). Signals transmitted and received by the FGPA - adapter board connection are shown. Details are given in the following sections.
Similar external inputs for the connector and DUT carrier board are shown as well shared signal lines.

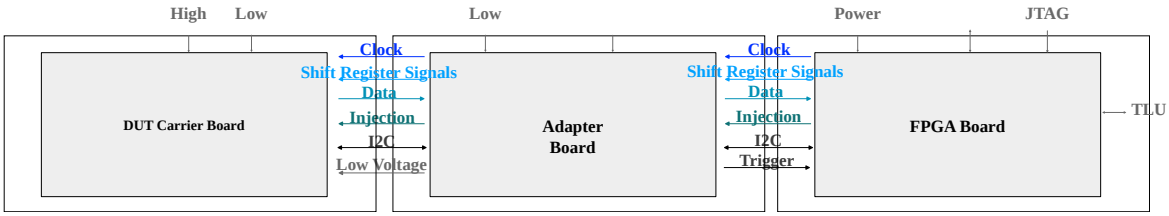


Figure 5.2: Schematic overview of MARS. Signal and data transmission with their direction between all pieces are indicated. Low voltage can be supplied either via the adapter board or directly to the DUT carrier board. High voltage is applied directly to the device. The FPGA board is powered externally and connected to the back-end computer via Ethernet for data transmission and a JTAG programming cable to configure the FPGA. External inputs as trigger signals to the adapter board and a TLU connection to the FPGA are indicated as well.

5.2.1 DUT Board

The main purpose of the DUT carrier board is to house the DUT itself. Since this part has to fit in beam telescopes and in laboratory setups for irradiation campaigns, a minimal amount of electronic components are placed on the PCB. An example of the TelePix2 carrier board is shown in fig. 5.3.
Bias voltage is supplied externally via SMA connectors, while low voltage to power the device is either applied directly by an external power supply or routed through the adapter board. For both, shielded USB3.0 type A connectors are used. Data and signal transmission is done via Display Port cables offering a locking connection with shielded conductors over variable distances.
For TelePix2, a GPIO **I**ntegrated **C**ircuit IC is placed on the DUT board, since the number of available connections on the Display Port cables is insufficient to configure the DUT. The load signals are fanned out to control the five shift registers (introduced in section 4.2.3). Additionally, the PCB offers probe points for the *AmpOut* and *HitBus* signal as well as several voltages, which can be set on- or off-chip, e.g. the comparator threshold *ThPix*. Because some voltages, as well as the on-chip injection, can be set to either external or internal for TelePix2, solder jumpers have been chosen to enable both operation modes.

Temperature controlled operation of the DUT is required to keep the leakage current - especially of irradiated devices - low (see chapter 7 and chapter 8 for more details). Hence,

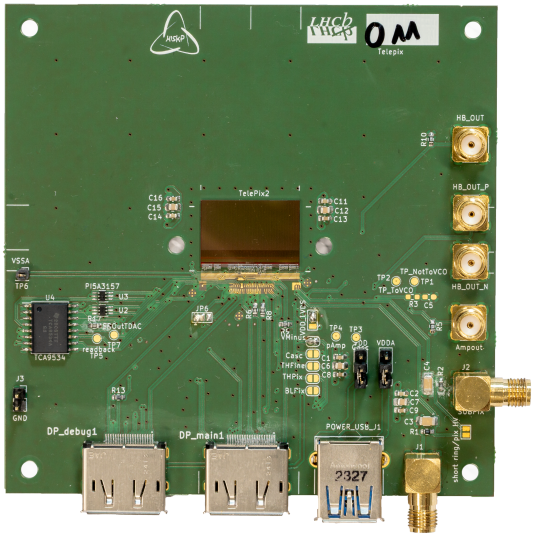


Figure 5.3: TelePix2 carrier board with power and bias connectors as well as data and signal connection to the adapter board via `Display Port` cables.

a hybrid cooling approach, consisting of a water block and Peltier elements, was chosen and designed within a Bachelor Thesis by J. Günther [17]. Due to possible usage within a testbeam, the aim was to minimize the material budget in the active area. Moreover, the cooling has to be placed outside the beam. As a consequence, direct cooling of the sensor is not possible. Instead, the area around it is cooled. Therefore, the thermal transfer of the PCB can be used. Accordingly, the PCB was designed with minimal component placement on its upper half, allowing for uniform and efficient cooling. The latest iteration of the cooling setup is shown in fig. 5.4.

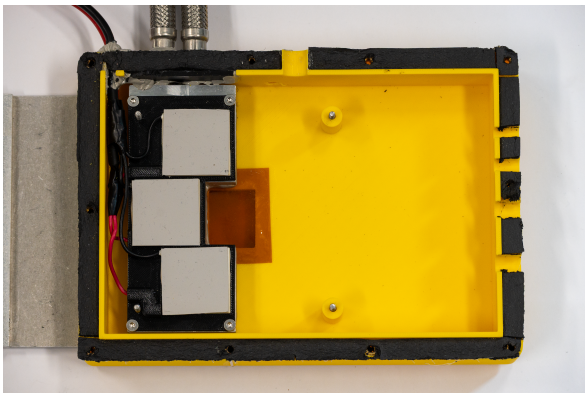


Figure 5.4: Top view of the aluminum water block with Peltier elements on top to cool the DUT from the bottom side placed inside the testbeam enclosure.

Three Peltier elements are thermally connected to the water block with thermal paste on

their hot side and held in place by a 3D printed frame such that the produced heat is efficiently transferred to the water block. Thermal connection to the DUT is done via thermal pads allowing a quick and clean exchange of different DUTs.
Externally cooled water is floating through a meandering pattern, milled inside the block, to promote turbulent flow and maximize the surface area. Cooling the water block is needed to ensure efficient operation of the Peltier elements at low temperatures to efficiently transport the heat away from the DUT board.
Depending on the intended use, different arrangements are possible. Under testbeam conditions the PCB is cooled from the back or front side. The cut-out is fit to the arrangement of the Peltier elements on the PCB to reduce multiple scattering. As a result, temperatures of $-21\,^{\circ}\mathrm{C}$ at the position of the DUT on the PCB can be achieved [17].
Operation in the laboratory does not require keeping the area behind the DUT clear of additional material which enables positioning of the Peltier elements at the position of the DUT at the back-side of the PCB. Temperatures of $-38\,^{\circ}\mathrm{C}$ [17] could be measured by the arrangement, required to operate irradiated TelePix2 sensors efficiently (in section 7.1.2, the setup used for irradiated sensors is explained in more detail).

5.2.2 FPGA Carrier Board

The `Mercury KX1` [127] FPGA is connected to the FPGA carrier board via two `Hirose FX10` [127] connectors. Interfaces as USB 3.0, PCIe-x16 and gigabit Ethernet are available. A schematic overview of the board and important connections are illustrated in fig. 5.5.

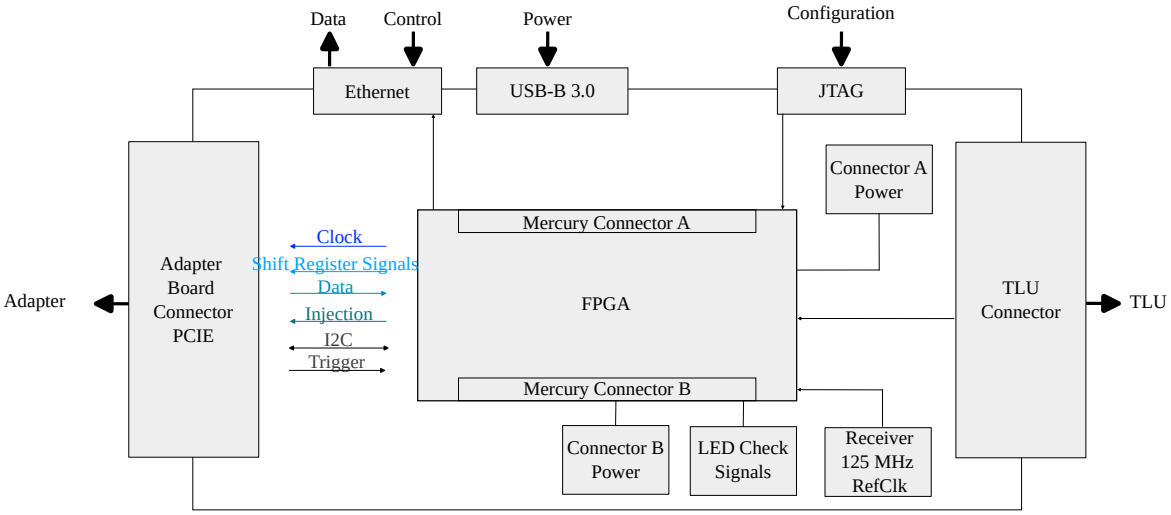


Figure 5.5: Schematic illustration of the FPGA carrier board. Signals received and transmitted by the FPGA are indicated. Important connectors for powering and input and output signals are labeled.

Signals from and to the DUT are routed via the adapter card, connected with a `PCIe` connector, towards the corresponding pins at the `Hirose FX10` connectors [130] to the FPGA

module. Depending on the transmitted signals different design parameters are important. For the design short path lengths, no or less amount of probe points and impedance matching were taken into account. Without, signal integrity cannot be ensured.
Shielded routing is enabled by a stack-up PCB of four layers: (1) Signal, (2) ground, (3) power and (4) signal. Power distribution is done via a power plane and grounding, also for the signals of the first layer, via a ground plane. High-speed signals, as timing and data, are differentially routed via the first plane. The exact route design depends on the signal itself, e.g. differential or single ended, and its location on the `Hirose FX10` connectors, since dedicated signals belong to dedicated connector pins. Consequently, important and sensitive signals are routed first and the remaining in descending priority.
Main purpose of the FPGA board is to provide and transmit all required signals of the DUT beside powering. Hence, configuration, clock, injection and I2C signals are transmitted. Data is received and processed by the FPGA (see section 5.3 for the FPGA implementation) before being sent to the back-end computer.
In the first version of the board, shown from top in fig. 5.6, data is sent through a 1 Gbit/s Ethernet communication implemented via a corresponding `SiTCP` [131] protocol. To overcome this limitation for higher data rates, a 10 Gbit/s `SiTCP` Ethernet protocol will be used in the future. Increasing the bandwidth requires a dedicated hardware component - the `SFP+` connector. With it comes a second version of the FPGA carrier board, shown in fig. 5.7. Due to issues of said board another iteration was required (see appendix A.1). Tests of the latest board are ongoing [2].
The FPGA can either be powered via `USB-B 3.0` or through an external power supply using a `Molex` connector. The latter is needed in the 10 Gbit/s `SiTCP` mode to supply the required power.
Configuring the FPGA is done by flashing the bitstream of the synthesized firmware via a `JTAG` programming cable. The possibility to store the bitstream in EEPROM is available but was not implemented within this thesis.
Connection to a TLU is foreseen via a `HDMI Port` and was used during the testbeam campaign. An issue with the implementation of the connection was found and corrected for the third version of the carrier board.

[2] Mostly all measurements have been performed with the first version of the FPGA carrier board. Testbeam measurements (see chapter 9) have been done with the second version.

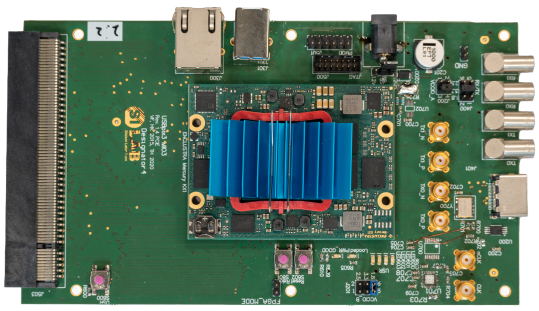


Figure 5.6: Top view of the first version of the FPGA carrier board with the FPGA covered by a blue heat sink.

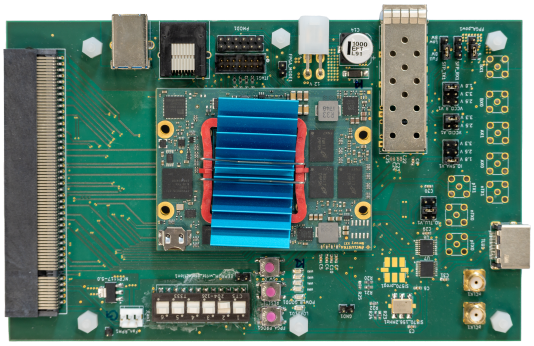


Figure 5.7: Top view of the second version of the FPGA carrier board with the FPGA covered by a blue heat sink

5.2.3 Adapter board

In-between the FPGA and DUT carrier board, an adapter is located. Two main purposes are foreseen. Firstly, components needed to provide external voltages and signals for the DUT, which are not provided by the FPGA, are placed on it. Secondly, probe points of signals from either the FPGA or the device are embedded. For example, clocks or injection signals produced by the FPGA can be tested. The final injection signal is created on the adapter board. Further, external trigger signals are received by `SMA` connectors and transmitted towards the FPGA connection.
One possible application is receiving external trigger signals from a scintillator usable for time reference measurement. A dedicated time reference layer was developed within the Master Thesis of N. Sommerfeld [16]. The setup itself is shown in fig. 7.3.

The adapter card supports low voltage biasing up to 5 V. Moreover, low voltage for the DUT can be transmitted from the adapter card via `USB 3.0 type A` to the DUT carrier board. However, it can also be supplied directly to the DUT board.
`Display Port` has been chosen due their locking connection and shielded data transmission over various distances.

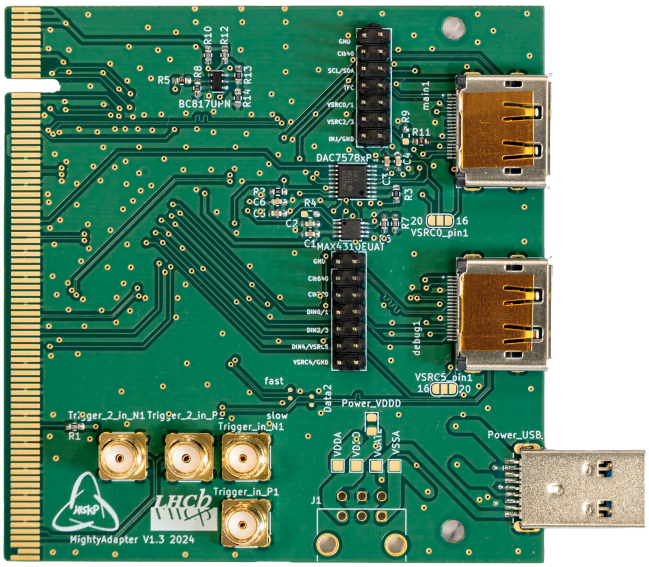


Figure 5.8: Top view of the adapter card with a PCIE connector towards the FPGA carrier and Display Port connectors to the DUT carrier board. Low voltage is applied via a MOLEX connector. SMA connectors are used for external trigger inputs.

5.3 Firmware Design

Intended to be usable for various DUTs, MARS's firmware architecture is designed to be modular. Since its purpose is to enable communication with the DUT and the back-end computer and process incoming data, dedicated modules are implemented. Specialized communication and data processing routines are required for different DUTs. Hence, modules concerning those purposes have to be adapted accordingly.
For common and non-DUT-specific functionalities custom Xilinx and generic BASIL modules are used. Accordingly to each BASIL firmware module, python modules are available for controlling. Similar, a python class for MARS was developed with the main purpose to configure external voltages.
A schematic overview of the four MARS specific firmware modules is depicted in fig. 5.9: (1) A non-hardware specific top module, (2) a hardware specific core and (3)(4) a DUT specific data receiver.
Two different directions are distinguished for all signals and data: (1) Signals/Data received by the FPGA and (2) signals/data transmitted from the FPGA. While data from the DUT is always received and after processing transmitted from the FPGA to the back-end computer, signals are either transmitted to the DUT or received from external hardware, e.g. trigger signals from an external trigger.
In fig. 5.9 the illustrated data path, colored in red, indicates how the data is processed within

MARS before being sent to the PC.
Incoming external signals, e.g. trigger signals and the TLU clock, are received and further processed in the top module. Clocks needed within MARS and for the communication with the DUT are derived within the top module.

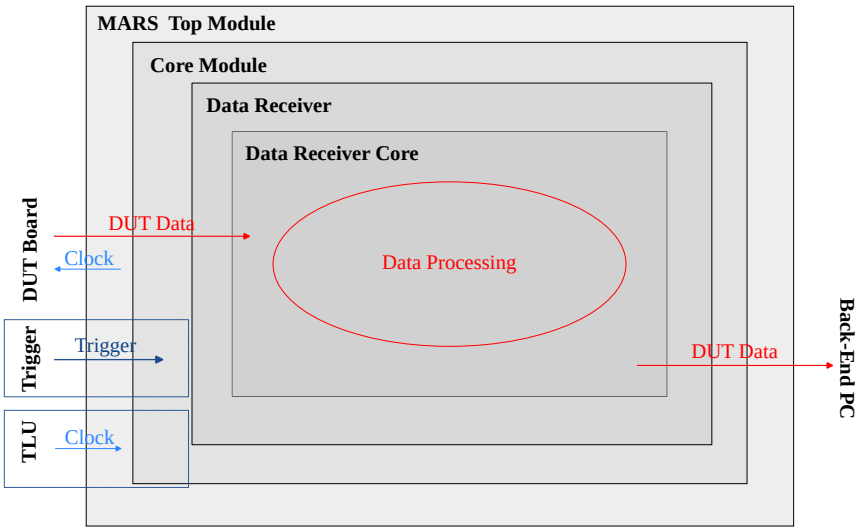


Figure 5.9: Schematic overview of MARS firmware design. Main modules, incoming and outgoing data (colored in red) as well as trigger and TLU signal inputs (colored in dark and light blue) are labeled.

A 100 MHz input clock, generated via an oscillator located on the FPGA board itself, is used as the main input clock to derive all needed clocks. Two PLLs are used in the top module to generate clocks needed for the FPGA-DUT and FPGA-PC communication. An overview of the architecture is illustrated in fig. 5.10.
For the FPGA-PC communication five clocks with frequencies depending on the used communication protocols are derived. In addition, a $(1\,\text{GHz}/7) \approx 142.86\,\text{MHz}$ bus clock is synthesized - used to transport signals via the BASIL bus between the firmware modules.
At least five different clocks are necessary for the FPGA/DUT communication. Since the DUT can either generate clocks via an on-chip oscillator (see section 4.2), a 100 MHz input clock is transmitted to the DUT or the DUT uses a faster clock directly. For the latter, the reference clock has to be five times faster than the input of the on-chip PLL. Hence, a 500 MHz reference clock is generated and transmitted.
Timestamp TS generation can be either triggered by an external trigger or by data. Therefore, two clocks, 100 MHz for the FPGA data triggered TS and 500 MHz for the external trigger

TS, are derived.
Since the incoming data is de-serialized in 10 bit chunks by the data receiver, a 100 MHz clock is needed to process those chunks. To process individual bits, a ten times faster clock is essential. Thus, a 1 GHz clock is generated by the PLL and transmitted to the receiver.
Important for clock signals is a clear separation between those signals on the FPGA. In addition, bad signal routing can cause slight delays affecting the operation of the DUT. In order to avoid this, constraints on the routing have to be set. Those are defined in a *constraints* file - specific for each DUT.
Further, hardware-pins and corresponding signals are associated within it. For example, dedicated pins have to be used for differential input/output lines. Moreover, depending on the signal, on-FPGA terminations and dedicated power banks are specified.
To summarize, the purpose of the DUT-specific constraints file is to associate the hardware signals to the firmware signals and set specifications on the firmware signals.

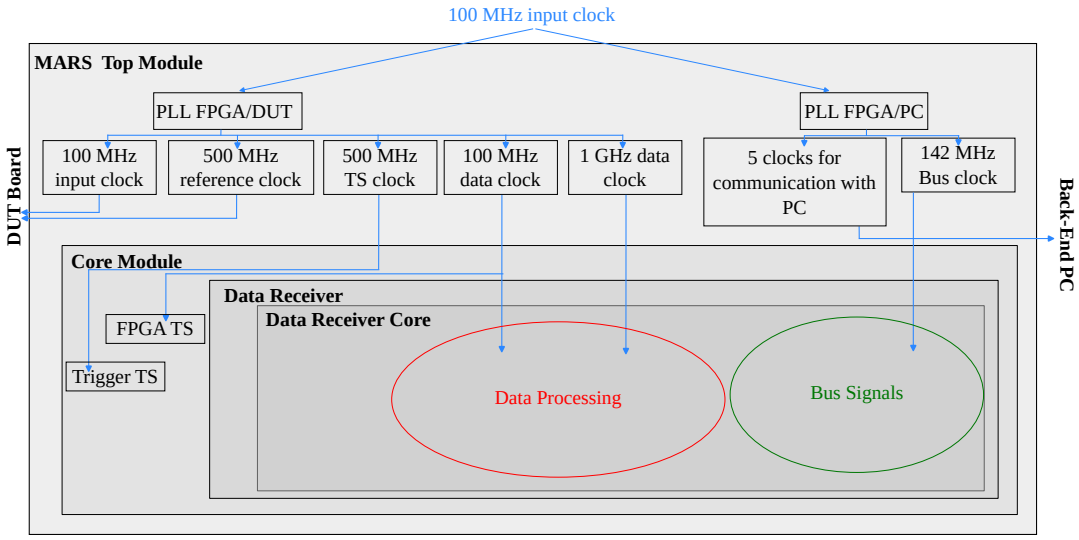


Figure 5.10: Schematic overview of the clock architecture (colored in blue) in MARS is shown. Via two PLLs clocks for the FPGA-PC and FPGA-DUT communication are derived from a 100 MHz input clock.

The first stage of the defined signals is the top module. Its main purpose is to set up necessary clock signals for the FPGA-DUT and FPGA-PC communication. In fig. 5.11 a schematic illustration of its main building blocks is given. As discussed, clocks are generated by two PLLs.
Configuration and controlling of the firmware modules is done via the **U**ser **D**atagram **p**rotocol UDP steering the BASIL bus system. Via this system MARS is controllable through a python

software interface.
Processed data is stored in a **F**irst **I**n **F**irst **O**ut FIFO buffer before being transmitted via SiTCP to the back-end computer. Depending on the hardware version of the FPGA carrier board (see section 5.2.2), two Ethernet speeds can be used, either 1 Gbit/s or 10 Gbit/s [3]. Both communication protocols, UDP and SiTCP, use the same Ethernet and IP address. Each has been chosen due to their advantageous for each purpose. While UDP enables high speed signal transmission, error checks are lacking and data is un-ordered, SiTCP allows ordered data transmission with accurate error checks and handshakes [123].

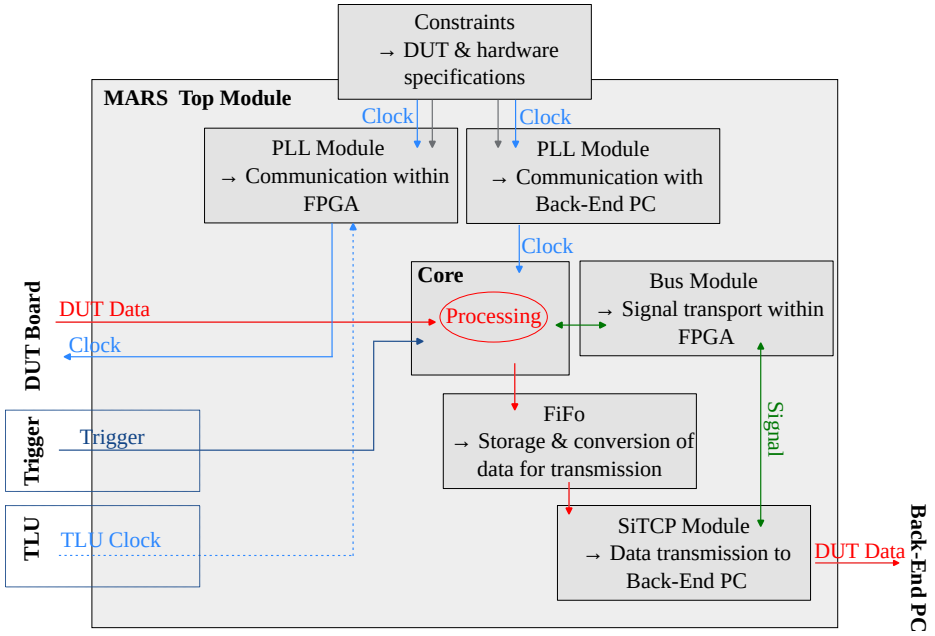


Figure 5.11: Schematic overview of top module. Main modules are included as well as the clock (colored in blue) and data (colored in red) path.

Hardware specifications and communication protocols are defined and implemented in the MARS core module. An illustration of its architecture and included building block is depicted in fig. 5.12.

Addresses for each module are defined and communication made possible by the bus system. To enable direct access between the firmware, software and hardware, a **G**eneral

[3] Measurements done within this thesis have been performed with 1 Gbit/s data link speed since the used FPGA does not support 10 Gbit/s. In contrast, its successors offer faster data transmission. The required protocol is implemented and has to be tested.

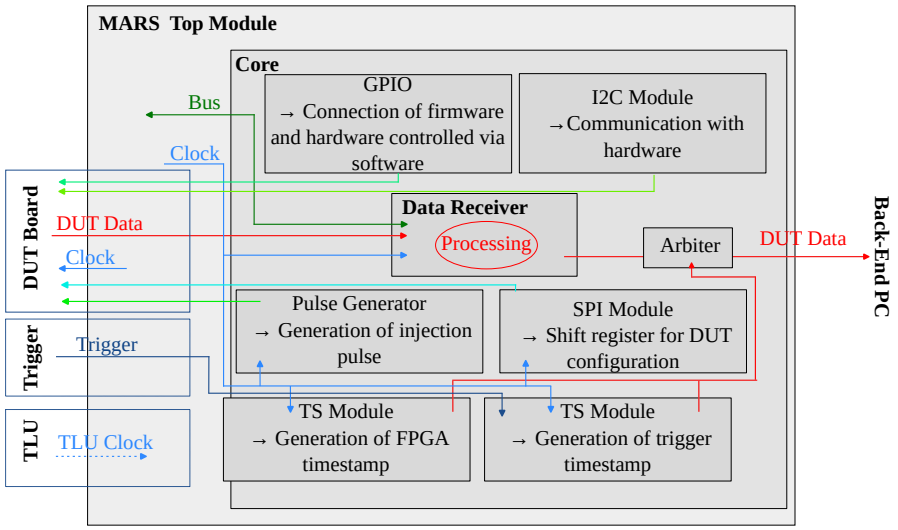


Figure 5.12: Schematic overview of the FPGA core module. Main modules are illustrated as well as the clock (colored in blue) and data (colored in red) path. Additional signals transmitted to the DUT are indicated and colored in green.

Purpose **I**nput/**O**utput GPIO register is implemented. It can be used to control registers and single signals. One example are reset signals of the DUT, which can be set in software. Those are received by the firmware and transmitted towards the DUT. Another example is the read-back of firmware registers. Since the output data of the DUT is processed in the data receiver (explained later within this section), false decoded data words can occur. To monitor the amount of wrongly decoded data words, the registers are used.
The main used communication protocols are I2C [132] and **S**erial **P**eripheral **I**nterface SPI. Via I2C hardware components on the adapter board (see section 5.2.3) are controlled. To configure the sensor, a **S**hift **R**egister SR is essential, matching the on-chip SR implementation (see section 4.2).
A dedicated pulse generator is implemented to generate an injection pulse used for injection signals. Timestamp generation is handled by two timestamp modules, allowing the creation of an external triggered TS as well as a data triggered FPGA timestamp. Since the DUT itself includes timestamps in its data-stream, in total three time information points are available. Matching of those is done in software. However, FPGA and trigger TS are only sent if DUT data is available. Hence, the inherent precision of the TS is higher but its effective precision is limited by the data accuracy. This approach was chosen to reduce the amount of junk output data.

A continuous output data-stream is provided by a round-robin arbiter. Processed DUT data, trigger TS and FPGA TS are combined in one data-stream.
Incoming data is processed in the core of the data receiver module. The data receiver itself initializes a bi-directional bus to transport data.
The data processing architecture, displayed in fig. 5.13, is distinguishable in five different stages:

1. Via a `Xilinx` specific DDR receiver module the incoming data link is received. Since data is sampled on both edges, the **D**ouble **D**ata **R**ate DDR module is necessary.

2. Next, the data is aligned via a custom alignment module checking the 10 bit data chunks for the idle pattern. If the pattern is found, a synchronization flag is set.

3. A 8b/10b decoder module decodes the data link into 8 bit chunks. Decoding errors are counted and transmitted via the bus system to access the information in software.

4. According to the on-chip state machine (see section 4.2) a custom counterpart state machine is implemented on the receiver side. Control pattern checks are performed and junk data removed.

5. Finally, data is stored zero-suppressed in a two-stage FIFO system where the clock domain is changed to further process data. Decoration of data with control flags is possible and done at several stages to enable data interpretation in software (see section 5.4).

Read-back of registers containing, for example, error information is possible via the BASIL bus system. Further, write signals can be transmitted through it such that, for example, reset signals are sent or clocks enabled/disabled.

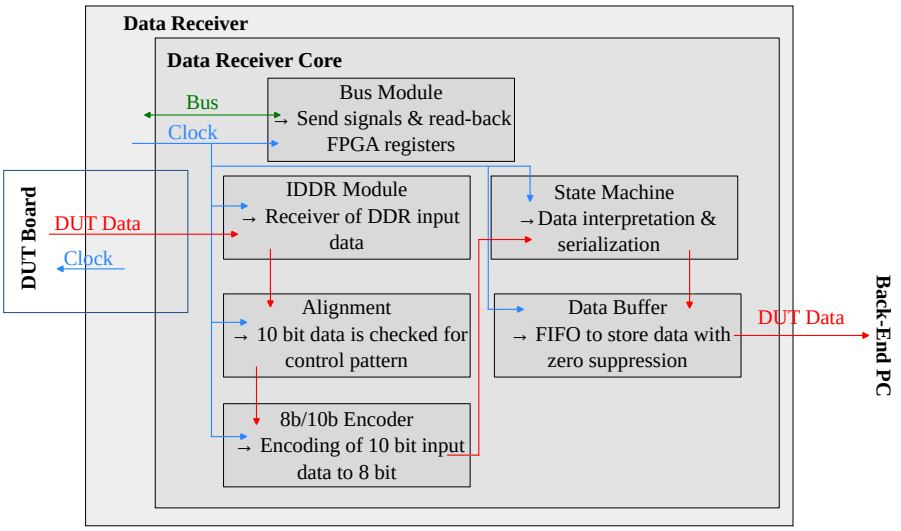


Figure 5.13: Schematic overview of the DUT-specific data receiver core module. Main modules for data processing are illustrated as well as the clock (colored in blue) and data (colored in red) path. The bi-directional BASIL bus signal is colored in green.

Testbeam Mode

Using MARS as a DUT DAQ system for testbeam campaigns is planned and has been successfully tested (see chapter 9). To change the operation from default laboratory mode into testbeam mode, the original input clock has to be changed to the TLU clock. Without, the DUT DAQ would not be synchronized to the clock of the telescope layers and scintillators, resulting in individual non-synchronized data-streams such that no particle track reconstruction would be possible.
For each purpose two different top modules are available. In addition, the constraints file differs since different hardware pins are used for the input clock.
In order to make the operation more user-friendly, each configuration mode can be synthesized with a corresponding compilation program. Similarly, the synthesized firmware is loaded to the FPGA via two different upload scripts.

5.3.1 Simulation

Testing the firmware as well as the software (see section 5.4) requires available hardware and comes with a lot of potential error sources. If, e.g., the DUT is not operational or the data processing in the firmware does not work as intended, it is difficult to isolate the cause. Hence,

simulations are important and essential to test the firmware and software without hardware. Furthermore, developing both is possible without an available DUT which is important for time-critical projects without dedicated time for software/firmware development.
Since both are written in different languages, the co-simulation framework Cocotb [4] was chosen and set up.
Cocotb offers simulation of the python software interface, the verilog firmware modules and the digital chip interface. The latter one is not yet included in the developed simulation since no chip emulation is available.
A verilog simulator runs the firmware modules without needed hardware connections. Because of that the top module of the firmware stack is replaced. As the digital chip interface is not available, the input data must be simulated. At the moment a dedicated data pattern based on real data is used.
Main purpose of the MARS simulation is to prove data processing and signal/clock transmission. Including the simulation in MARS's development, errors in the data processing could be identified and solved. In addition, constraints on time critical signals were optimized with the goal to reduce delays and possible data losses.
At the time writing this thesis the python software interface has been included in the simulation by K. Padeken. In future python tests will be available to test its functionality further. Moreover, continuous integration is planned, including unit tests.
An example of the simulation showing the clock signal transmission between each module is depicted in fig. 5.14 with a color coding marking each clock. From the 100 MHz origin clock, the 100 MHz input clock, colored in green, is transmitted to the FPGA core module. Further, the five times faster reference clock, colored in purple, is shown. Important for data processing are the 100 MHz and the 1 GHz clocks, colored in yellow and orange, respectively. The expected dependencies between each clock are confirmed and no delay is observed.

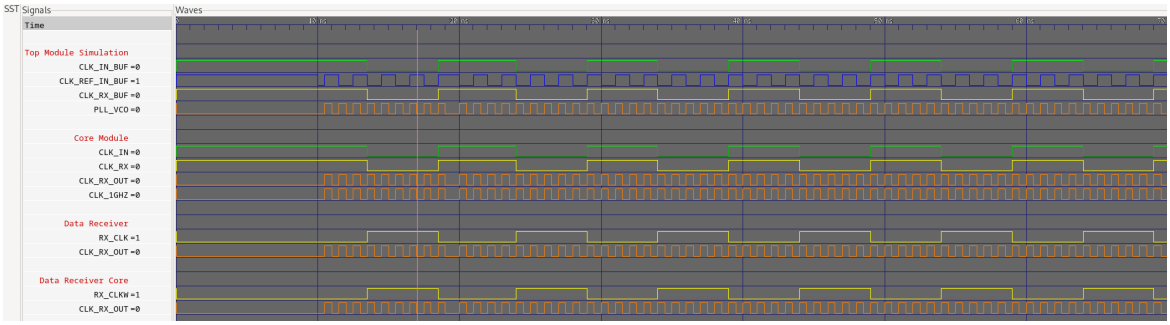


Figure 5.14: Example of the MARS simulation output. Shown are important clock signals for data processing starting with clocks generated in the top module and ending with those used by the data processing receiver core.

In fig. 5.15 a simulation of the data processing in MARS is displayed. As mocked data input a realistic data pattern is simulated in the top module. The data is transmitted into the

[4] **CO**routine based **CO**simulation **T**est**B**ench Cocotb

receiver module where a interpretation of the non-aligned data stream takes place.
The DDR over-sampled data (*RX_DDR*) is formatted into 10 bit data chunks in order to decode the encoded input data via a commercial 8b/10b decoder (The data pattern is explained in section 4.2.2). The encoded 8 bit chunks (*dec_data*) are serialized. Therefore, a state machine, similar to the on-chip state machine (see fig. 4.7 for information about the on-chip FSM), is used.
After serializing, 28 bit data words are buffered in the two-stage FIFO with the following output words: *Wdata* of the first FIFO and *cdc_data_out* of the second.
Decorated with a data identifier, the 32 bit output data (*FIFO_DATA*), is transmitted to the core module where a continuous data stream is generated by a round-robin arbiter. Its output, *ARB_DATA_OUT*, is sent via Ethernet, implemented in the top module, to the back-end computer.

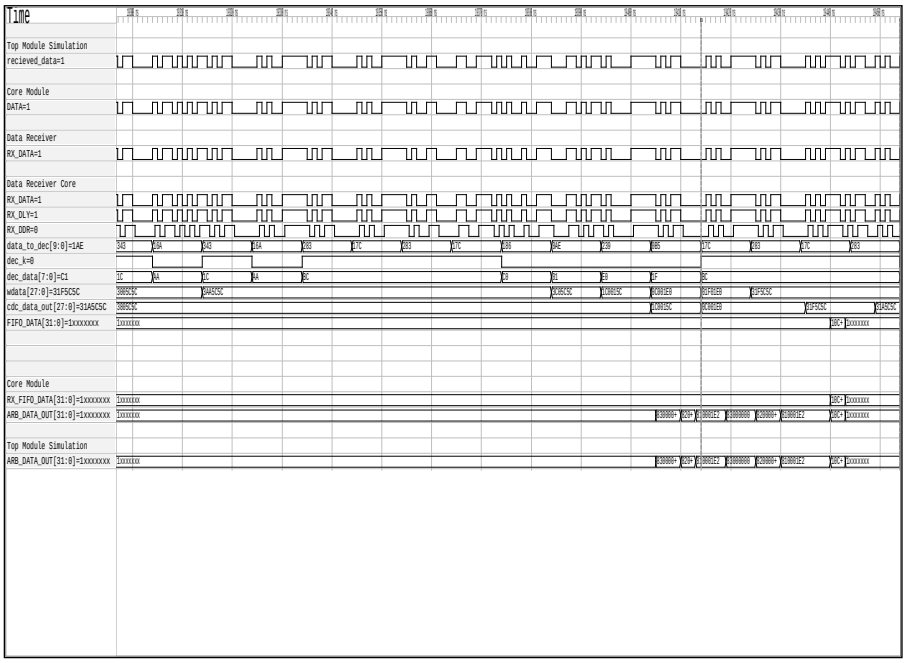


Figure 5.15: Example of the MARS simulated data flow. Shown is how received data is transmitted towards the data receiving core module, processed by it and sent backwards to the round-robin arbiter.

5.4 Software Design

MARS's software architecture is designed based on the BDAQ53 [123] and TJ-MonoPix2 [125] DAQ systems. Its main design objectives are flexibility and user-friendliness. Hence, the overall software interface is python based. A script-based user interface was chosen to provide insight into the DUT configuration.
The setup and development of the software was the main part of the author in collaboration with K. Padeken. An overview of the architecture is shown in fig. 5.16.

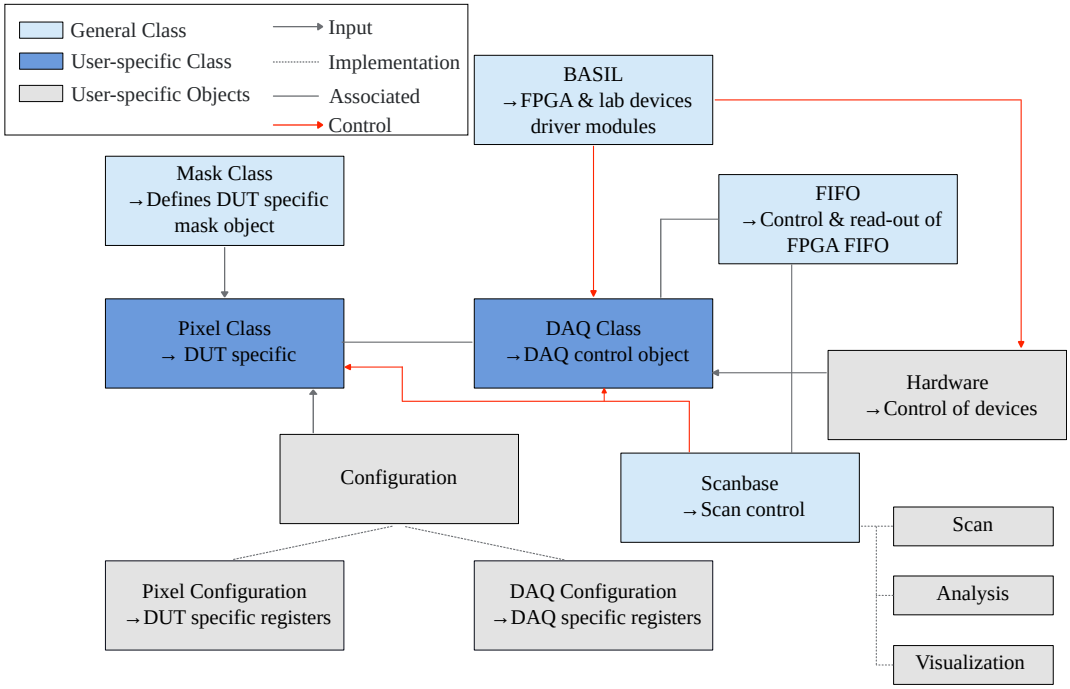


Figure 5.16: Schematic overview of MARS software architecture. General classes are colored in light blue, user specific in blue and user-specific objects in gray. Dependencies between each part is illustrated by different arrows and colors, explained in the legend. Adapted from [123].

General classes are colored in light blue and user-specific in blue. Objects depending on the DUT are colored in gray. Different types of relations between them are distinguishable. Classes that can inherit from each other, are associated to objects or control devices.
Evident by fig. 5.16, MARS software stack consists of three main building blocks: (1) A pixel element, (2) a DAQ element and (3) BASIL.
The pixel element compromises a DUT specific pixel class and configuration file. Its purpose is to handle the chip communication, define DUT specific commands and functionalities, set default settings and voltages. The configuration itself is defined in a configuration file. Part of this is, for example, a register with on-chip DACs which have to be set to configure the device. Therefore, the DUT configuration is a register object inheriting from the BASIL

register class.
Further, the DUT inherits from a general mask object used to define DUT specific masks. As an example only parts of the DUT can be enabled/disabled - defined by the mask object. In addition, an injection mask is available, defining an injection algorithm dedicated to chosen pixels.
The DAQ class is independent of the DUT and includes functions and commands specific for the DAQ. Since the DUT communication happens via the DAQ, the pixel class inherits from it.
FPGA firmware modules are controlled via BASIL. In addition, hardware devices, for example power supplies or ICs on the PCBs, can be controlled via BASIL.
The *scanbase* houses scan routines which are generalized by the DAQ and pixel class. Routines are user and DUT specific but follow a common strategy initialized and controlled via the *scanbase*. Firstly, the DUT is initialized. Secondly, it its configured. Thirdly, the scan is performed. Depending on the routine, data can be analyzed and visualized offline. For both classes are available.
Besides this, the *scanbase* and DAQ class are associated to a FIFO readout class used to communicate with the FPGA FIFO. States of the FIFO can be read out and commands to empty it sent.
Since data analysis can be done offline, raw data is saved into an `HDF5` [133] file format. The data buffering starts as soon as the data read out is enabled. Additionally, further information about used settings and the configuration are saved.
Analysis of the data can be performed offline or online. With the online analysis, the data are processed in real time. Direct access to the results is provided through a dedicated web interface. But, in contrast to the offline mode, a reduced data analysis is performed. For example, the hit occupancy and ToT information are available but no complete analysis chain, e.g. the time resolution analysis, explained in section 6.3.3, is executed. For both a dedicated and DUT-specific *interpreter* class, required to interpret the data, was developed.
To visualize measured data, a class containing several visualization objects (different plot formats) is available. Furthermore, default analysis methods, e.g. Gauss fits, are implemented. Moreover, calibration parameters could be fed into the visualization class. Although the interface exists, it was not used within this thesis.

The complete architecture is saved in a version controlled git repository made available via `GitLab` [134]. Besides the software stack, the firmware is part of it, too. Due to different types of software objects, the repository has a corresponding structure.
Objects belonging to the system, e.g. the Pixel and DAQ class, belong to *system* objects. Configuration files for each are part of the *config* folder. Functionalities used to analyze and visualize the data are grouped into *analysis*. Scans itself are part of the *scans* object.

5.5 The TelePix2 Software

In this section the TelePix2 software is discussed in more detail. It compromises an explanation of the TelePix2 pixel class with its DUT specific functionalities, an overview about available scan routines and analyses. For each the corresponding measurements is referred to. TelePix2 has five configuration register (see section 4.2 for more information): (1) Column/Row, (2) TDAC, (3) configuration, (4) DAC, (5) on-chip voltage register - defined in the configuration file. The same data line of the SPI (see section 5.3 for more information) is used for each but different load signals.
Initialization, implemented as part of the pixel class, is used to configure the TelePix2 sensor to its default settings. Depending on the set defaults, DUT specific voltages, e.g. the comparator threshold, are set on-chip or off-chip.
The following functionalities, according to the design of TelePix2 discussed in chapter 4, are available:

- Set voltages: Voltages, not set on-chip, are set externally via a GPIO component on the adapter board. For TelePix2 *VMinus* has to be set externally.
- Enable amplifier output *AmpOut*: Measuring of the analog amplifier output signal is possible for the bottom most pixel of each column and done by tapping the amplifier output out to a pad on the chip.
- Enable *HitBus* output: The digital *HitBus* output signal is accessible per column.
- Enable injection: Injection can be enabled per pixel. Its signal amplitude is either set on- or off-chip.
- Set TDAC: Tuning of the comparator threshold is possible via an implemented tuning algorithm where TDACs are set per pixel to optimize either the threshold dispersion or reduce the amount of noisy pixels by increasing their threshold.

According to those, user- and DUT-specific scan routines are implemented and have been tested. Commissioning measurements, presented in section 6.2, include measurements of the *AmpOut* and *HitBus* output. A `Jupyter` notebook is available to test if the DUT is operational.
Further, threshold and injection scans are performed (see section 6.2). For the latter a global comparator threshold is set and the injection amplitude is varied while for the first the injection amplitude is fixed and the threshold varied. With both the pixel response is studied. The threshold scan can be used for source scans where for a certain time the pixel response to a radioactive source is measured.
Moreover, the tuning strength is measurable, allowing the optimal value to be selected for tuning the DUT via its TDACs. Three types of tuning methods are available.
Firstly, the noise level of the overall DUT can be reduced by optimizing the comparator threshold per pixel. Secondly, a global threshold value can be found and thirdly, a per pixel

tuning towards the global target threshold is performed with the goal to reduce the threshold dispersion of the DUT. The latter two are mostly performed consecutive.
Besides those scan routines, a full integration into the `EUDAQ2` [118] and `corryvreckan` [135] software packages for testbeam applications has been done (see chapter 9).
Additionally, scan routines can be decorated by measuring the power consumption and leakage current to study their behavior. Standalone measurements of those, e.g. leakage current measurements, presented in chapter 6, are also possible with the devices used in the Bonn laboratory.
For all measurements different analysis scripts are available. The main analysis and data interpretation routines use a common approach. DUT data is interpreted by an DUT-specific interpreter and analyzed within the analysis routine. Part of this is a clustering algorithm, inherited from [136], to construct clusters of neighboring pixels responding to a signal detected at a similar time. In addition, data measured with laboratory devices, e.g. the power consumption, is analyzed in the analysis routine.
The output information enables more specific analyses such as studying the time resolution in dependence of the bias voltage chapter 6).

5.6 MARS compatibility

Since MARS is intended as a laboratory and testbeam DAQ system, it offers both compatibilities. A brief summary of already included and tested devices for measurements is given in section 5.6.1. How to operate MARS at a testbeam facility and needed adaptions is explained in section 5.6.2 and chapter 9.
Both integrations have been developed by the author.

5.6.1 Available DUTS

MARS is specialized to test HV-MAPS designed for the Mighty-Pixel project or HV-MAPS originating from the KIT developments (see fig. 4.1). Besides TelePix2 [137], the Run2020 [138] and Run2021 [139] HV-MAPS have been implemented in hardware, software and firmware and successfully operated in laboratories. The integration of the LF-MightyPix and in the future, of the MightyPix2 is ongoing. For both dedicated DUT carrier boards have to be designed and pixel classes with corresponding configuration files implemented. Moreover, a new data receiver in the firmware is needed.
Besides this, MARS is compatible with DUT carrier boards from other DAQ systems such as the GECCO and MUDAQ DUT carriers. Therefore, adapter boards are available. Characterizing similar devices with different DAQ systems enables reduction of systematic effects. Moreover, during the development phase of MARS MUDAQ proven DUTs have been used to get MARS running.
Both adapter cards are shown in fig. 5.18 and fig. 5.17.

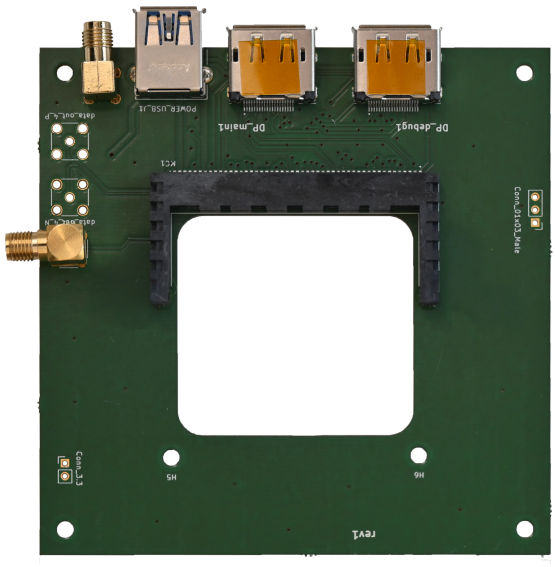


Figure 5.17: Top view of the MUDAQ connector.

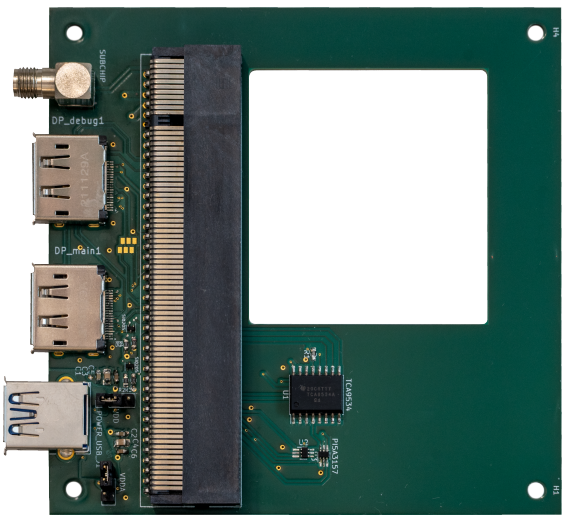


Figure 5.18: Top view of the GECCO connector.

5.6.2 Testbeam Usability

To use MARS during a testbeam campaign as the DAQ system for a DUT as part of a particle beam telescope as e.g., at DESY [140], the hardware can be used without any adaptions. Cooling of the DUT is possible via a hybrid cooling solution as explained in section 5.2.1. Since the beam telescope and MARS have to be operated with the same clock, a TLU is needed. As introduced in section 5.2.2 a connection is available. A dedicated firmware is necessary to use the TLU inputs properly and derive the required clocks. A specialized version, available here [141], was developed and successfully used (see chapter 9).
Similar, specific scan routines as part of the software interface are essential. To ease the operation, MARS offers the possibility to be operated via the EUDAQ2 [142] interface [5].

5.7 Quality Assurance for MARS

Since MARS is planned to be the default DAQ system for the R&D phase of the HV-MAPS MightyPix family, its quality has to be ensured. Therefore, all its building blocks (hardware, firmware, software) have to be proven to be operational before distributed to and used by collaborating institutes.
MARS hardware is internally reviewed before ordered and tested in-house. In future, the review process will be extended to collaborating institutes such as the University of Dortmund.
Firmware and software are part of the simulation. Hence, their functionality can be proved without any hardware. The firmware simulation is up to the writing of this thesis fully functional and usable. Simulating the python software is functional but still under development. Test routines are planned to be implemented to test various functionalities. In addition, continuous integration is supported. If a user uploads changes to the repository, the simulation will run and check for issues - ensuring a working firmware and software.
Test routines for a fully equipped system are offered. As a first test initial supplied voltages have to be verified on the PCB. Therefore, several probe points at the different hardware pieces are available. For example, low voltage can be either measured at the DUT carrier or adapter board. Another test measurement is the clock signal quality which can be tapped at the adapter board. If the powering and clock signals are working, the DUT can be configured and first tested by a start-up `Jupyter` notebook where external and on-chip voltages are set as well as data links checked. Set voltages can be measured at the DUT carrier board. Once all voltages are verified and the data link is stable, the system is ready to be fully operational. A simple How-To-Get-Started with MARS is provided in appendix A.3. Besides ensuring MARS quality in terms of functionality, its quality in terms of user-friendly operation has to be ensured as well. Thus, the repository is equipped with a *ReadMe* description explaining how to setup the firmware and software and configure a DUT. In addition, this thesis serves as a documentation. In future, a documentation webpage [129] will be available where MARS developers and user document the system and all its functionalities.

[5] The integration is described in chapter 9.

5.8 Summary and Outlook

To summarize, MARS is a versatile DAQ system coming with three different building blocks: (1) Hardware, (2) firmware and (3) software. Its intended for single chip and hybrid characterization of HV-MAPS for the Mighty-Tracker project. Usage in the laboratory as well as at testbeam facilities is foreseen and has been proven. While single chip studies have been performed successfully in both test environments, hybrid characterization has not yet been done.
Due to its flexible design approach MARS can be used to operate different DUTs. The TelePix2, Run2020 and Run2021 sensors are already included. In future, MARS will offer operation of Mighty-Pixel specific DUTs. Therefore, developments are ongoing.
Changes have to be done for all building blocks. DUT-specific carrier boards have to be designed, a new data receiver core implemented and due to LHCb specific communication protocols, further protocols have to be included in the firmware core.
For the software an adjusted pixel class and configuration file must be set up. Additionally, the data link structure will change. Hence, a suitable data interpreter is required. Common scan, analysis and visualization routines will be kept.
Similarly, MARS will be further developed for hybrid characterization. Therefore, new hardware components are inevitable to connect the hybrid PCB to the adapter card. Moreover, the FPGA carrier board and the FPGA itself have to be suitable to process the expected amount of data links and rates. The `Mercury KX1` cannot be used but its successors. Main changes in the firmware are additional data receivers - one for each chip per hybrid. Via unique chip addresses each can be identified.
Because multi-chip testing was in mind since the beginning of MARS development, the software offers all required capabilities. Thus, no major changes have to be made.

CHAPTER 6

Characterization of non-irradiated HV-MAPS

In the following chapters the characterization of HV-MAPS as part of the R&D phase towards the MightyPix are presented. All measurements are evaluated with the goal to confirm the capability of the technology for use in the Mighty-Pixel. Hence, the sensor performance is investigated and evaluated in terms of the MightyPix requirements, listed in table 2.1. Main focus is on the efficiency, time resolution and radiation tolerance with target values of [68]:

Parameter	Specification	References
Overall efficiency	$> 96\%$	[68]
Time resolution	≤ 3 ns	Corresponds to in-time efficiency $> 99\%$ [1], [5]
Radiation damage: NIEL	3×10^{14} MeVn_{eq}cm^{-2}	[1], [5]
Radiation damage: TID	40 MRad	Simulation in chapter 8

Thus, not only measurements with non-irradiated but also irradiated devices have been performed.
Within this chapter results of the non-irradiated sensor as a baseline for the performance of the irradiated devices are discussed. Two irradiation types have been performed to study the influence of bulk and surface damage on the performance. In chapter 7 results discussing bulk and in chapter 8 discussing surface damage are summarized. Measurement of the performance in terms of hit-efficiency and time resolution was done at a testbeam campaign at DESY II in December 2025 for all devices. The campaign and results are discussed in chapter 9.
Since MightyPix is not available at the time of writing this thesis, all measurements have been performed with TelePix2 (introduced in section 4.2). Further, some measurements have been carried out with its predecessor Run2021 (also known as TelePix1). An explicit specification which measurement was performed with which device is provided in the corresponding

sections.
However, it is important to note that none of the DUTs were originally designed to fulfill the MightyPix requirements. The power consumption and hit rate capability have not been evaluated in detail with the available devices since the results are of limited use for the Mighty-Pixel project. However, first estimations on the expected behavior of the power consumption, especially for irradiated devices, have been conducted (see section 8.4.2 for more information).
Before evaluating the DUT performance, commissioning measurements are carried out to ensure its overall functionality and optimize the configuration settings. Performed commissioning measurements, including tests of the analog and digital functionality, are presented in section 6.2.
Furthermore, the functionality of MARS is validated by those measurements. Hence, they are treated as the commissioning of both the DUT and the readout DAQ system.
The experimental setup is described in section 6.1. After discussing the commissioning measurement results in section 6.2, the performance of the non-irradiated device is presented in section 6.3. The analysis primary focuses on the time resolution and depletion behavior of the DUT, as achieving a time resolution with a standard variation better than $\sigma \leq 3\,\text{ns}$ is a key requirement for the MightyPix.

6.1 Experimental Setup

Characterization of all devices has been carried out with the MARS DAQ system (introduced in chapter 5). A typical laboratory setup is shown in fig. 6.1. The TelePix2 DUT carrier board is connected to the adapter card via two `Display Port` cables. The adapter card itself is connected to the FPGA carrier board equipped with the FPGA. The setup follows the typical MARS setup described in section 5.2.
Low voltage power is directly supplied to the DUT carrier board using four-wire sensing to ensure a stable voltage supply and correct for a voltage drop over the cables. Biasing of the DUT can be done via two bias structures. A detailed description is given in section 6.3.1.
Because of a large heat dissipation of TelePix2 (see section 4.2.4 for more information), the DUT is cooled to keep the leakage current minimal. However, the DUT could be operated at room temperatures as well.
For standard laboratory measurements of non-irradiated devices a Peltier element is placed underneath the PCB at the position of the DUT. To achieve low temperatures on the cold side of the Peltier element, the warm side of it has to be cooled. Therefore, a common CPU cooler is used to dissipate the heat. The stack-up is shown in fig. 6.1.
Since the DUT itself has no on-chip temperature sensor, the temperature can only be measured via external means, e.g. close to the DUT on the PCB using an external temperature sensor. Because measurements at temperatures of $\leq 0\,^{\circ}\text{C}$ of the non-irradiated DUT have not been performed with this setup no temperature limitation can be given for it. The setup used for temperature dependent measurements is important for irradiated devices. Hence, it is

presented in section 7.1.1.

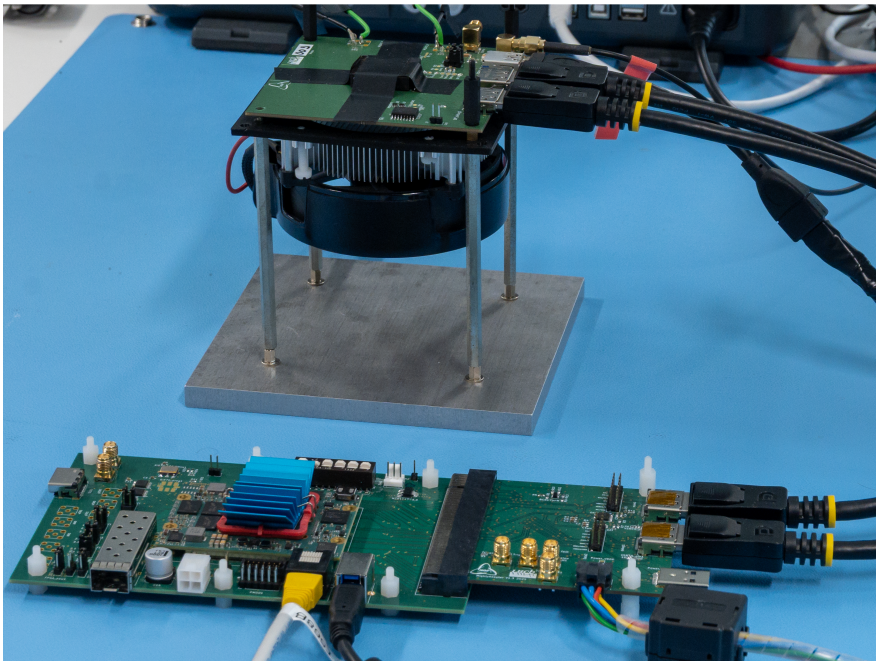


Figure 6.1: Side view of a typical laboratory setup used to characterize TelePix2.

Standard voltages used for the measurements are summarized in table 6.1:

Parameter	Value
VDDD (low voltage for the digital domain)	1.92 V
VDDA (low voltage for the analog domain)	1.92 V
HV - Chip (high voltage using chip biasing)	−120 V
HV - Pixel (high voltage using pixel biasing)	−80 V
BLPix (On-Chip DAC setting the baseline voltage)	127 DAC units
BL (External voltage setting the baseline voltage)	0.97 V
VMinus (External voltage of the hitbus line driver)	0.8 V

Table 6.1: Summary of standard voltage settings for a default operation of a non-irradiated TelePix2 sensor using the MARS DAQ system.

6.2 Commissioning Measurements

Firstly, commissioning measurements of the TelePix2 are presented. At the same time, the MARS DAQ system is proven for its performance requirements necessary to characterize HV-MAPS.
Since TelePix2 has on-chip voltages, a calibration of those was done to ensure that generated voltages correspond to the expectations. In section 6.2.1 the measurement is discussed.
Testing of the analog and digital functionality of the DUT is presented in section 6.2.2 and section 6.2.3. Confirming both, further DUT functionalities can be tested. Important are the **T**une **DAC**s TDACs used to tune the comparator threshold per pixel to minimize the threshold dispersion. A tuning algorithm has been implemented. In section 6.2.4 the algorithm and results are summarized.

6.2.1 Calibration Measurements

TelePix2 has multiple global on-chip voltages. Two of those have been calibrated: (1) Baseline voltage *BLPix* and (2) threshold voltage *ThPix* of the comparator. Both can also be set externally.
Besides, the injection strength can either be set on-chip or externally. Calibration allows to determine the effective comparator threshold since it is the difference of the set comparator threshold and the baseline. On per-pixel level the individual pixel threshold includes the tuned threshold voltage.
Both voltages, *BLPix* and *ThPix*, are implemented as an 8 bit on-chip DAC as part of the VDAC register. Hence, a variation between 0 to 255 DAC units is possible covering the voltage range of 0 to 1.8 V. Theoretically, one DAC unit corresponds to 7 mV.
Calibration measurements of *BLPix* and *ThPix* for the overall DAC range are shown in fig. 6.3 and fig. 6.2.

The applied voltages against the set VDAC value is shown. Dense measurement points have been chosen for the relevant DAC range for standard operation settings. For both measurements the DUT was fully configured and operational.
By a linear regression to both measurements a slope of approximately (6.97 ± 0.01) mV/DAC for *BLPix* and approximately (7.00 ± 0.13) mV/DAC for *ThPix* is obtained. Both agree with the expected linear response and theoretical expectation of 7 mV. Therefore, the functionality of MARS configuring the DUT correctly is validated.
Therefore, the default baseline voltage of $BLPix = 127$ DAC units corresponds to ≈ 889 mV. A typical threshold voltage is at least 50 mV above baseline to be above the noise floor [1]. Hence, $ThPix = 144$ DAC counts ≈ 1.008 V is a valid setting.
Since both voltages are generated on-chip, radiation damage could alter the transistor working points and thus, influence the calibration. Therefore, a re-calibration of an irradiated device is

[1] The noise floor of a DUT is determined by its leakage current. Signals originating from leakage are amplified and processed by the DUT ASICs which corrupts real signals due to their in-distinguishability.

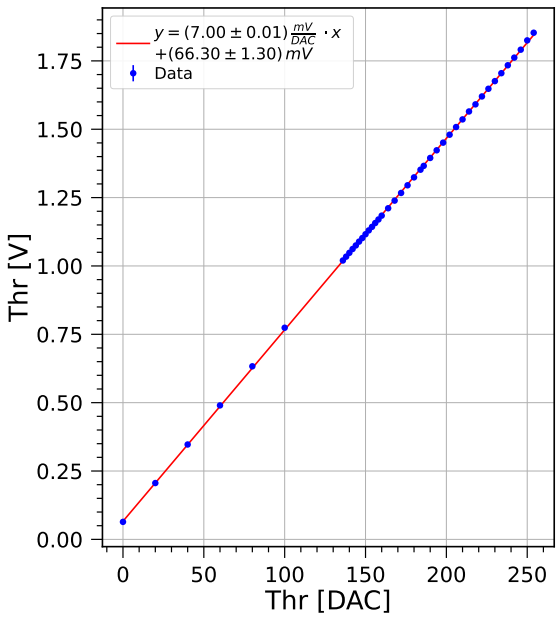


Figure 6.2: Calibration measurement of *THPix* showing the applied voltage for the possible DAC value range.

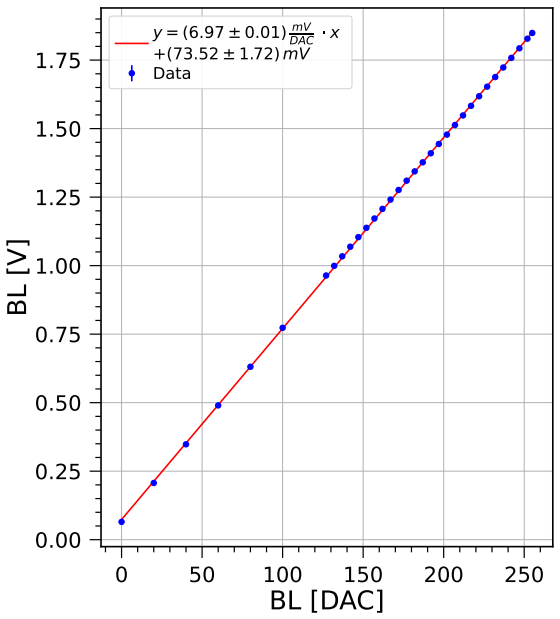


Figure 6.3: Calibration measurement of the *BLPix* showing the applied voltage for the possible DAC value range.

important to validate the performance of the VDACs. In appendix A.9 the result is presented.

6.2.2 Analog Measurements

Before testing digital functionalities of the DUT, the analog part has to be tested. Therefore, a signal is generated to validate the DUT's response. Two different ways of signal generation are possible.
Firstly, a signal can be injected into dedicated pixels using the on-chip injection circuit. Consequently, each pixel and its response can be tested individually, allowing to test the general functionality of the sensor. For the bottom most row the analog *AmpOut* signal can be tapped out and visualized with an oscilloscope, depicted in fig. 6.4 in pink. The digital injection is done on-chip and triggered by the injection pulse colored in yellow. In turquoise the corresponding digitized signal of the comparator output, known as *HitBus*, is shown.

The initial analog measurement validates the basic functionality of both the DUT and the DAQ system. Further, the amplifier and comparator response were optimized in order achieve a trade-off between a good sensor performance and reasonable power consumption by tuning the DAC parameters (listed in table A.3) using the oscilloscope.
Since the DUT must be sensitive to particles and respond to their charge deposition, the injection signal tests are not sufficient to validate its overall performance. Hence, further tests are necessary. Therefore, particle source tests have been performed to ensure the DUT being sensitive to particles. Common used particles sources are a Sr-90 β^--source and a

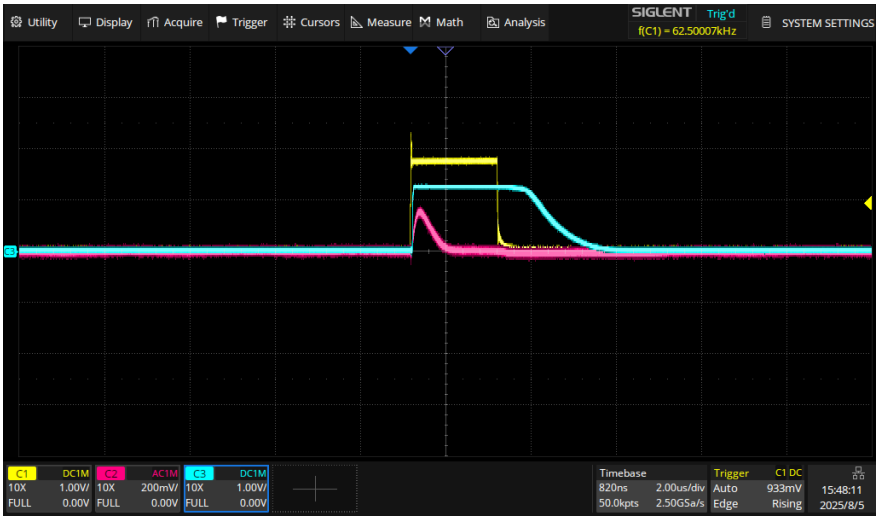


Figure 6.4: Example of an digital injection signal (colored in yellow), the corresponding *AmpOut* (colored in pink) and *HitBus* (colored in turquoise) output signals. Vertical and horizontal scales are depicted in the picture.

Fe-55 γ-source. Fe-55 is used as a representative particle source for MIPs. The characteristic 5.9 keV photon peak from Fe-55 peak serves as a reference for calibrating the injection pulse amplitude by comparing the ToT spectra obtained from Fe-55 with those from the injection pulse. However, the calibration was not accomplished within the scope of this thesis.
An example showing the chip response to Sr-90 is shown in fig. 6.5.

From the measurement it can be seen that all pixels respond to the charge deposition. Moreover, the source profile is visible. Due to a non-central and tilted position of the source, smaller source tip than chip size and the distance between the DUT and source, the occupancy profile is not centralized in the chip and has a diffuse border.
Further, the cluster formation is depicted in fig. 6.6 [2]. Hits with a distance of ≤ 5 pixels and a similar timestamp to the first hit are summarized as a cluster.
As expected, Sr-90 electrons deposit their energy mostly in one pixel. However, a cluster size of ≥ 1 is also observed. A possible reason could be crosstalk, which is not expected here. Another reason is an inclined trajectory. If electrons pass the DUT not by a straight but an inclined trajectory, several pixels are hit and respond, enlarging the cluster size. In addition, low energy electrons can result in clusters with a size ≥ 2.

[2] A logarithmic visualization is provided in fig. A.2

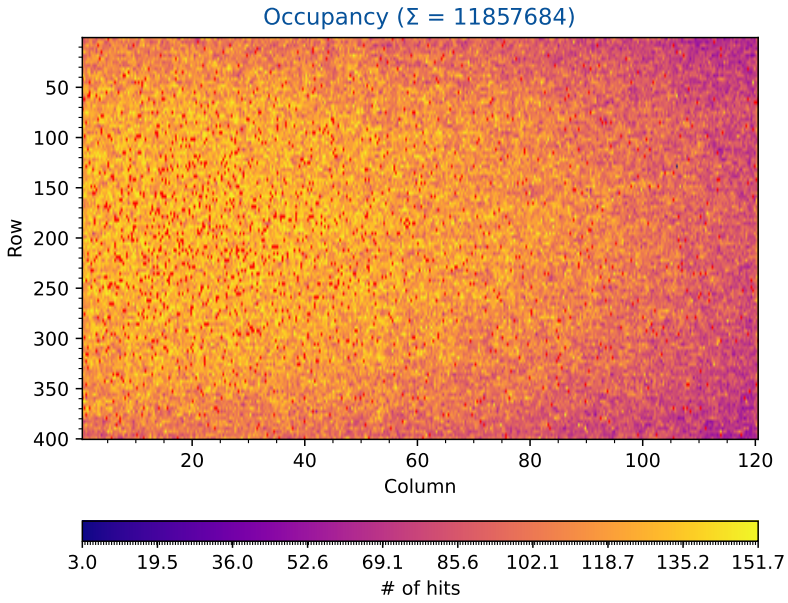


Figure 6.5: Occupancy map of the charge deposition measurement with a Sr-90 β-particle source.

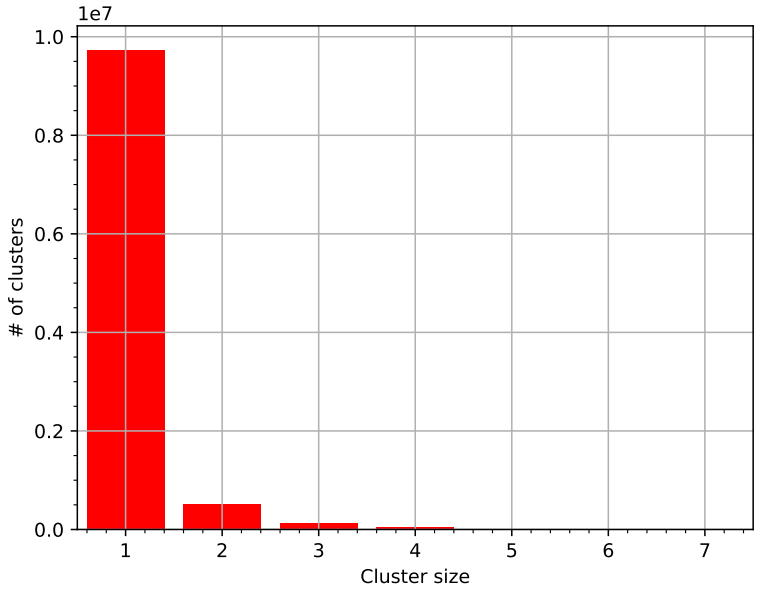


Figure 6.6: Measured cluster size with a Sr-90 β-particle source.

6.2.3 Pixel Response Measurements

Important for particle detection is the detection threshold. The comparator threshold is defined global and applied to each pixel. In addition, a local tuning per pixel is possible via TDACs.
However, the global set threshold is not equal between each pixel due to process variations. A mismatch between individual transistors - and consequently in the response of the resulting circuits - is expected, leading to a threshold dispersion. Causes, among others, can be the following: (1) Variations in the ASIC production, e.g., fluctuations of the baseline voltage or fluctuations of the amplifier gain, (2) variations of the material, e.g., variations in the doping concentration of the implants and, (3) variations in the performance of individual pixels, e.g., fluctuating signal-to-noise ratios or variations in the charge collection efficiency per pixel.
Minimizing the dispersion is possible by tuning each comparator threshold towards a common goal, usually a global threshold, which is explained in section 6.2.4.
Determination of the point where the injection strength is equal to the effective comparator threshold for a fixed baseline voltage can be done in two ways: (1) For a fixed threshold the injection signal is altered and (2) for a defined injection signal the threshold is varied. For both a fixed number of signals are injected. For MARS the default are 100 signals per setting as a compromise between speed and statistics.
In an ideal system the behavior of each pixel is binary. Either 100 % of signals would be detected if the signal amplitude is above the threshold or none. As an result a step function would be expected for both methods. In reality every system is affected by noise. Noise in the pixel comparator and amplifier circuit may arise due to thermal or Shot noise (see section 3.4). Therefore, the step function is smeared resulting in an "s-curve" shaped signature. Mathematically a Gaussian error function describes the number of measured signals $N(x)$ [34]:

$$N(x) = \frac{N_{inj}}{2}\left(1 + \mathrm{erf}\left(\frac{x-\mu}{\sqrt{2}\sigma}\right)\right) \quad . \tag{6.1}$$

Depending on the threshold detection method, x is either the injected signal strength or the varied threshold. The threshold of a pixel μ is defined by the value where 50 % of the injected signals are detected - in the following refereed to as the turning point. The amount of amplifier noise is characterized by the slope σ of the function.
An example measurement for both so-called s-curves or z-curves [3] is depicted in fig. 6.8 and fig. 6.7.
Figure 6.8 shows the measured signals using a fixed injection strength and altering the global threshold in DAC counts. Vice versa, fig. 6.7 shows the measured signal for a fixed global comparator threshold for different injection signal strengths.

[3] The formula in eq. (6.1) can be adapted by introducing a negative sign to model the z-curve.

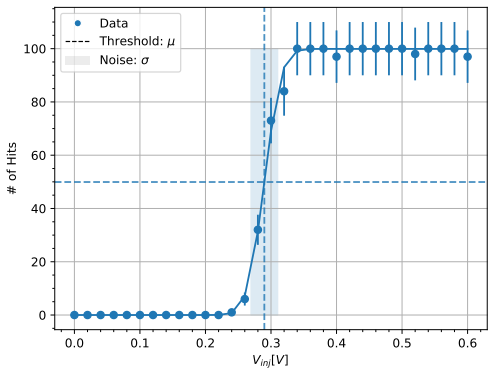


Figure 6.7: S-curve measurement showing the amount of measured signal of a fixed pixel threshold of 145 DACunits for different injection strengths. The uncertainty is given by $\sqrt{N_{hits}}$.

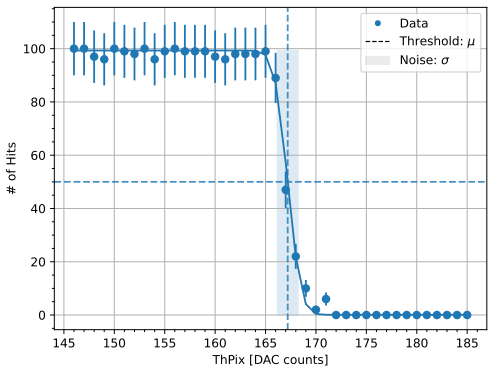


Figure 6.8: Z-curve measurement showing the amount of measured signal of a fixed injection of 400 mV strength for different pixel threshold. The uncertainty is given by $\sqrt{N_{hits}}$.

6.2.4 Threshold Dispersion

The threshold dispersion of the sensor matrix is derived by performing a z-curve measurement on each pixel. Minimizing the dispersion towards the global set threshold is possible by TDACs (explained in section 4.2).
Each in-pixel comparator has three tune bits, called TDAC, used to vary the threshold locally on pixel level. The algorithm to obtain the mean comparator threshold of the sensor matrix is described in the following:

1. Z-curve measurements are carried out for each TDAC setting in the range of 0-7 (3 bit correspond to a range of 0-7).

2. The turning point μ, corresponding to the threshold, of each is determined, and a Gaussian is fitted to the distribution of all turning points. In fig. 6.9 an example is presented.

3. The mean of the fitted Gaussian - representing the mean comparator threshold of the analyzed pixel matrix - shown in fig. 6.9, is extracted.

By design a monotonous shift of the mean of the threshold dispersion for the whole TDAC range is expected. Depending on the current drawn by the TDACs, the shift of the threshold is expected to change. The magnitude of the shift increases with the drawn current, which is controlled by the on-chip DAC *VNDAC*. In addition, no change of the threshold dispersion in dependence of *VNDAC* is expected. In fig. A.3, the threshold dispersion in dependence of *VNDAC* is presented.
The influence of *VNDAC* on the threshold change per TDAC value has been measured and is shown in fig. 6.10. The uncertainty of the mean threshold μ is taken as the statistical

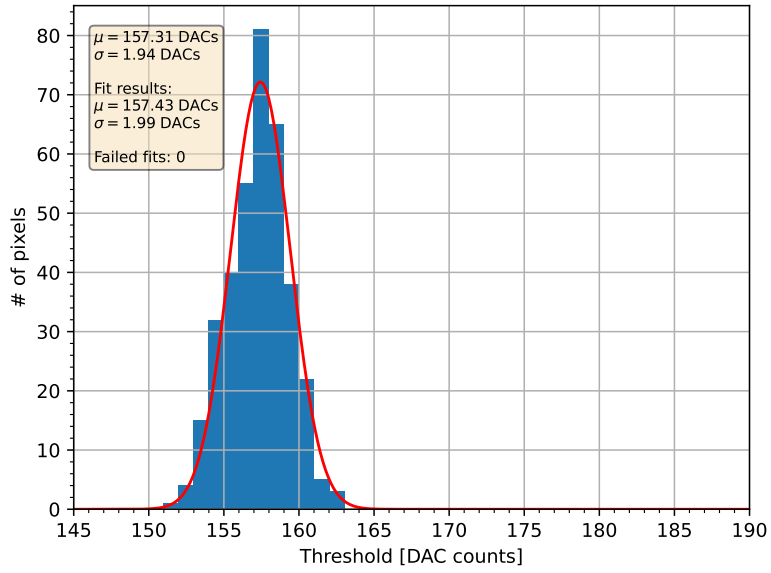


Figure 6.9: Example of the threshold distribution of 400 pixels. A Gaussian distribution is fitted to data. Measurement settings are: *VNDAC*= 0 DAC units and TDAC = 0.

uncertainty $\sigma/\sqrt{N_{inj}}$, where σ is the standard deviation and N_{inj} the number of injections [4]. Since TelePix2 has 120 x 400 pixels and requires at least 30 to 40 s to fully configure due to multiple sensor configuration writes, a z-curve measurement across the entire DUT is not feasible. Hence, the number of pixels was limited to 400 which ensures enough statistics to measure the threshold TDAC dependence.

The mean of the threshold dispersion in DAC units for the TDAC range is shown for *VNDAC* ranging from 0 to 20 DAC units. At TDAC = 0 effectively no current is drawn [5], resulting in a crossing point at a fixed pixel threshold depending on the injection strength. Incrementing the TDAC value results in a decreased detection threshold. The tuning strength per TDAC step increases with *VNDAC*, as a higher current is drawn.
Hence, a large tune strength is achieved for large *VNDAC* values. To enhance the threshold shift per TDAC, *VNDAC* has to be increased. Due to a limited pixel threshold scan range, shifts entering the noise floor are not possible. As a consequence, data points at high TDACs for large *VNDAC* values are not recorded in fig. 6.10. Moreover, large tuning strength limits the resolution since each tune step yields a large change of the threshold. Therefore,

[4] A more accurate estimate of the uncertainty comes from the fit itself, which is not currently implemented in the analysis. For one example, the fit uncertainty of μ was calculated to be on the order of ± 0.1 DAC units, which likely underestimates the measurement uncertainty. An extension of the MARS analysis incorporating a more accurate calculation is planned.

[5] A slight variation between individual measurements may explain the minimal shift observed at TDAC = 0. Additionally, increased on-chip currents resulting from stronger tuning settings could account for the effect.

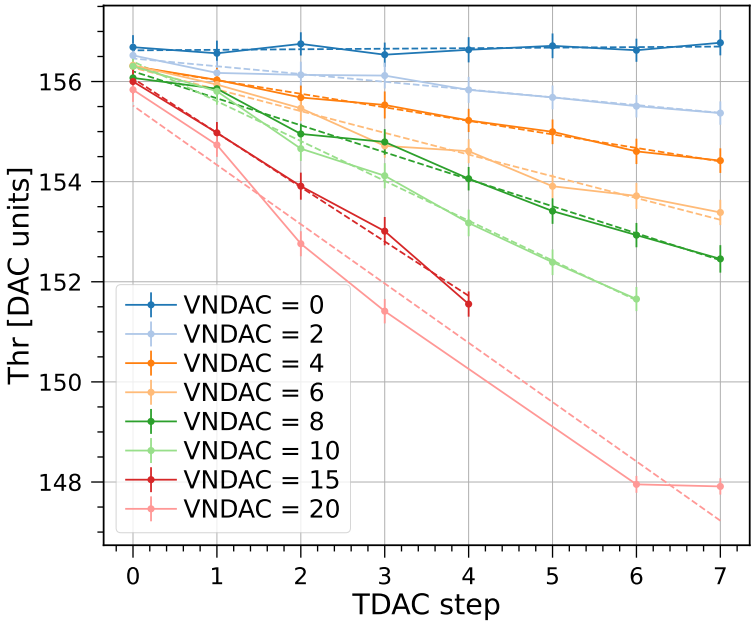


Figure 6.10: Mean pixel threshold versus TDAC for different VNDAC settings in DAC units. A linear regression is fitted to data to show the linear dependence between threshold and TDAC. The uncertainty of μ is the statistical uncertainty $\sigma/\sqrt{N_{inj}}$ with the standard deviation σ and the number of injections N_{inj}.

a compromise between sufficient tune strength and resolution has to be made. Thus, the threshold dispersion has to be taken into account, as the tune strength has to be adequate to optimize the threshold of pixels deviating most from the target threshold.
Optimization of the pixel threshold is done in a step-wise algorithm. Three steps are performed: (1) Measuring the threshold dispersion to define the optimal tune strength, (2) set the global threshold or determine it by a measurement and (3) optimize the threshold dispersion by an binary tune algorithm. In the following each step is explained in more detail.

1. **Definition of the optimal tune strength:** Firstly, the tune strength has to be defined. Depending on the goal of either altering the local pixel threshold a lot or optimize it precisely, the parameter has to be chosen. For both the threshold dispersion of a significant amount of pixels has to be measured. From the tuning strength measurement, shown in fig. 6.10, the on-chip DAC *VNDAC* is chosen. For the default threshold tuning scenario, a *VNDAC* value of 14 DAC units is selected to ensure a fine tuning strength, allowing the local thresholds to be precisely aligned towards the global target.

2. **Definition of the target global threshold:** The global threshold is derived in two ways. Either a fix threshold is set by the user or it is determined by a measurement.
   For the latter case, a threshold scan (z-curve measurement) is done for a statistically significant amount of pixels with a TDAC value of three. Since the threshold-TDAC

dependence (see fig. 6.10) is linearly decreasing with increasing TDAC value, a TDAC value of three is chosen as the starting point to enable tuning the threshold up or down. The 50 % value μ of each z-curve is obtained from the fit and histogrammed for all scanned pixels. By a Gaussian fit the mean of the distribution is derived and defined as the target threshold.

3. **Matrix tuning:** Finally, the threshold dispersion of the pixel matrix of the DUT is optimized towards the global threshold. Therefore, a binary search, schematically illustrated in fig. 6.11, is performed. Starting at a TDAC value of three z-curves are performed in each pixel. The measured pixel threshold is compared to the global threshold. Depending on its deviation, the TDAC value is incremented or decremented by one bit at a time, resulting in the present TDAC algorithm. Repeating this for the whole algorithm results in four z-curves per pixel. The best TDAC value for each pixel is buffered. In the end, the best value is applied to each pixel and a final z-curve is performed.

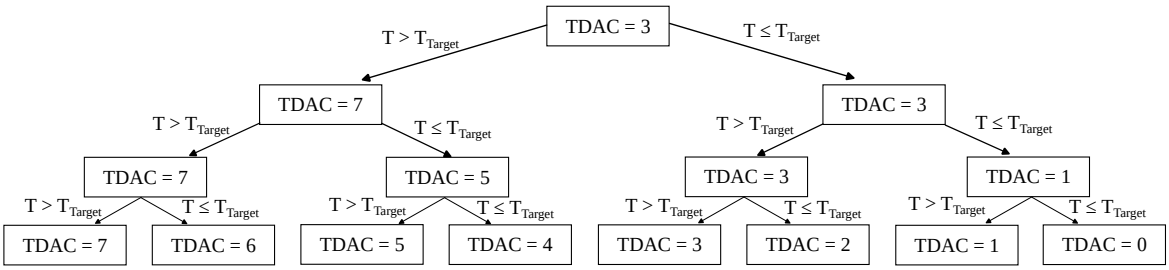


Figure 6.11: Schematic illustration of the TDAC algorithm based on a binary search.

An automated tuning algorithm including the global threshold search and subsequently the matrix tuning is available. In fig. 6.12 the result is depicted. 100 pixels have been evaluated. A tuning of the whole matrix of TelePix2 is not feasible due to its long configuration time [6]. Nevertheless, a similar algorithm has been implemented for its predecessor - the Run2021 sensor. Due to its short configuration time and lower amount of pixels, the matrix tuning is evaluated for the whole pixel matrix. Comparable results are presented in appendix A.7.
The overall threshold dispersion is already low (σ = 2.6 DAC units) without tuning (colored in blue). Applying the algorithm to one row over 100 columns shows a significant decrease of the dispersion (colored in orange). In addition, the anticipated threshold goal of 167 DAC units has been reached after tuning.
The algorithm is working as intended and can be adjusted for other devices.

[6] It has to be noted that the number of pixels was limited to 100 pixels. To obtain a significant amount of statistics more pixels are required. But due a non-optimized injection pattern for a large number of pixels and time-constraints, since the measurement takes up to several days for many pixels, the presented results are limited in the number of used pixels. Further improvement of the algorithm is planned. However, matrix tuning is at the moment not intended for the MightyPix. Consequently, an optimized algorithm does not have main priority.

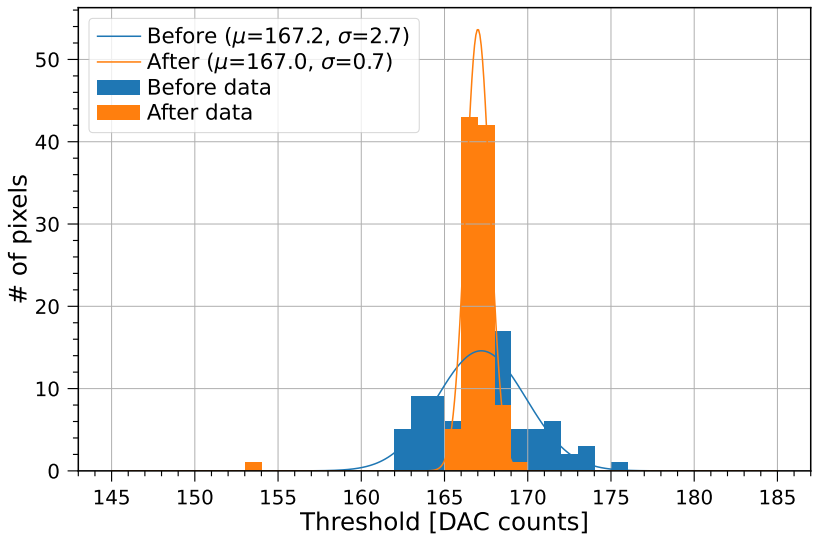


Figure 6.12: Threshold dispersion before (colored in blue) and after tuning (colored in orange). A threshold goal of 167 DAC units was anticipated for 100 pixels using VNDAC = 14 DAC units.

Besides optimizing the pixel threshold dispersion, the matrix can be optimized in terms of noise. Hence, the overall tune goal is to operate the sensor at the lowest possible threshold by optimizing the local pixel threshold such that no pixel enters the noise floor. Therefore, the global threshold search starts at a high threshold at minimal TDAC and iteratively lowers the threshold and repeats the measurement. At each step the occupancy of all scanned pixels is determined and the noise rate derived. Depending on the allowed global noise rate, the global threshold is defined at the minimum threshold - just above the noise floor.
Next, the local threshold is lowered by lowering the TDAC value as long as the sensor noise rate is below the allowed global noise rate.
Vice versa the algorithm could be started the other way around with the highest TDAC value and setting the global threshold as the threshold where the noise floor is entered. The local tuning would optimize each pixel threshold to decrease the noise rate per pixel and hence, the noise of the full matrix. Because the latter method is more prone to end up in the noise floor being stuck, the first method is preferred.

6.3 Performance Measurements

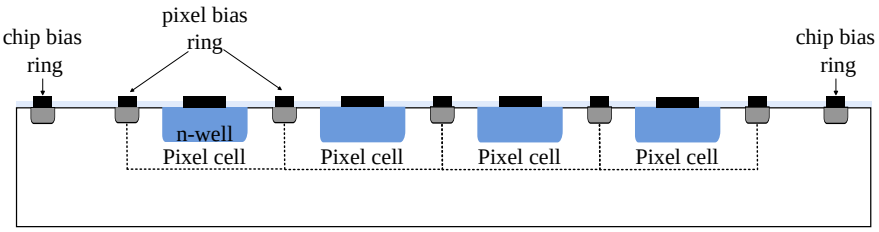
Once the DUT and DAQ system are commissioned, the DUT performance can be studied in detail. In terms of investigating HV-MAPS for the Mighty-Pixel project, the time resolution and particle detection efficiency of non-irradiated and irradiated devices are of main importance.
Therefore, all measurements relevant for irradiated devices have to be performed for non-irradiated devices to obtain a baseline for the investigation of the effects of radiation damage on the performance.
Since both requirements, particle detection efficiency and time resolution, depend on the analog behavior and hence the depletion of the sensor bulk, biasing studies have been performed. Section 6.3.1 discusses those results while in section 6.3.3 a laboratory time resolution measurement is introduced and explained.
Particle detection efficiency is measured at a testbeam facility. Therefore, the results are presented in chapter 9.

6.3.1 Biasing Studies

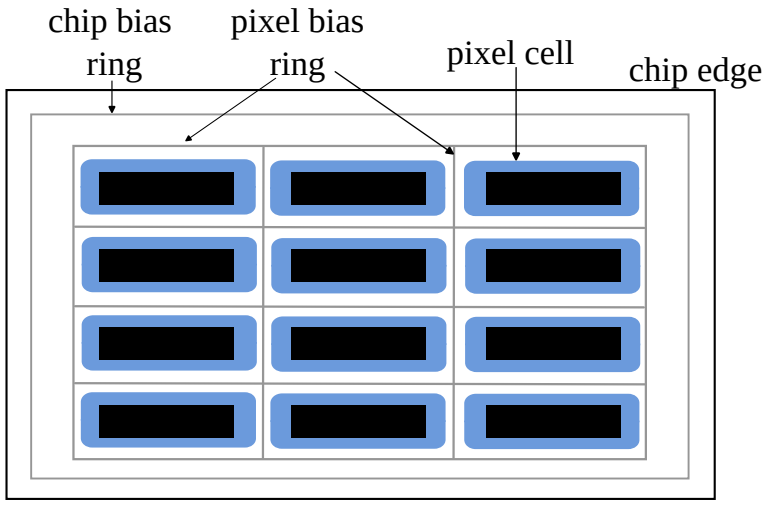
Bias measurements serve as a direct method to probe the bulk properties of HV-MAPS, enabling analysis of the depletion depth and its behavior.
As explained in section 3.2.4, the sensitive detection volume is built by a depletion region whose size depends on the applied bias voltage and bulk resistivity. Enhancement of the depletion region is enabled by increasing the bias voltage. Full depletion is pursued to ensure a maximized sensitive detection volume.
Biasing studies are a powerful tool to understand the sensor diode and depletion region. Therefore, various biasing studies of TelePix2 have been performed. Furthermore, the implementation of measurement routines serves as a foundation to characterize irradiated HV-MAPS (presented in section 7.2.1 and section 8.4.1).

TelePix2 is biased via top-side biasing as shown in fig. 6.13. A deep p-well surrounds the pixel matrix and digital part where the bias voltage is applied via metal contacts which is called chip bias. Moreover, a p-stop implant separates pixels from another used to improve shielding and avoid unintended leakage currents leading to crosstalk. Besides its initial purpose as a guard ring, the so-called pixel guard ring can be used to bias the sensor as well. Hence, two possible top-side bias structures are available: (1) chip and (2) pixel bias.
A schematic illustration of both is shown in a top and side view of a representative matrix in fig. 6.13. In-pixel electronics and the collection n-well electrode are indicated.

A typical measurement is a so called IV-curve. Stepwise the bias voltage is increased while the leakage current is measured. From that the operation of the sensor diode can be proven, the operation bias voltage defined and the breakdown determined. For all presented measurements the breakdown voltage is defined as the voltage where the leakage current increases drastically due to an avalanche effect resulting in an increased leakage current as



(a) Side view



(b) Top view

Figure 6.13: Schematic illustration of the TelePix2 top-side bias structure consisting of the chip and pixel bias ring. The deep n-well is colored in blue and the p-stop in gray. Ohmic metal contacts are colored black. In the top-view the in-pixel electronics is illustrated in dark gray.

explained in section 3.2.4.
Example measurements for TelePix2 are shown in fig. 6.14 and fig. 6.15. In the latter case, TelePix2 is biased via the chip bias ring, whereas in the former it is biased through the pixel guard ring. As stated in section 4.2.4, TelePix2 has a large heat dissipation. Therefore, the intrinsic DUT temperature is $\geq 30\,^{\circ}\mathrm{C}$ without cooling. Consequently, the DUT had to be cooled to ensure operation at room temperature. Nevertheless, TelePix2 can also operate without additional cooling.

With increasing bias U the leakage current I increases up to the breakdown of the diode where a drastic change in the leakage current is observed. While the breakdown occurs at $\approx -143\,\mathrm{V}$ for chip biasing, an earlier breakdown at $\approx -86\,\mathrm{V}$ is measured for pixel biasing. Besides expectations, both do not agree with each other. Since both are connected via the sensor substrate, a correlation is expected. Investigating this is possible via **V**oltage-**V**oltage VV-curves.
For this purpose, one bias contact is used to actually bias the DUT while the other is used to monitor the voltage tapped at the other contact. Both possibilities are presented in fig. 6.16

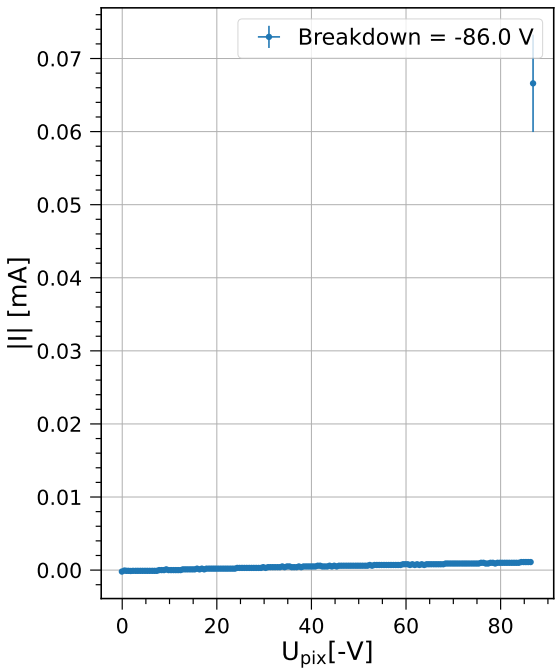


Figure 6.14: IV measurement of TelePix2 with pixel biasing yielding a breakdown at ≈ -86 V.

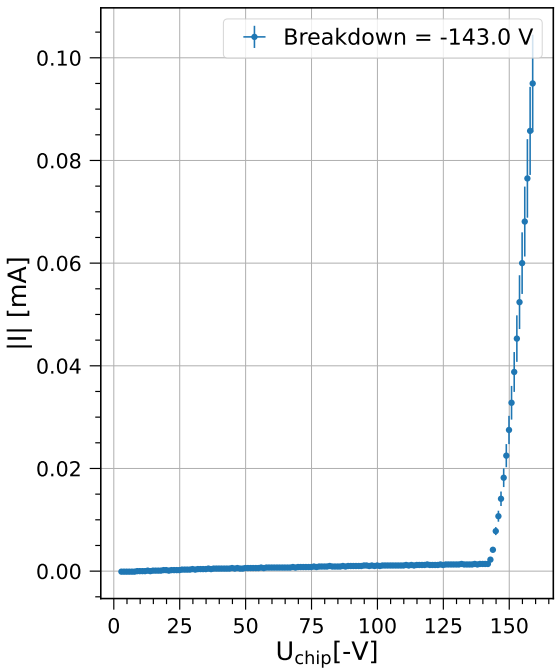


Figure 6.15: IV measurement of TelePix2 with chip biasing yielding a breakdown at ≈ -143 V.

and fig. 6.17. In the first case TelePix2 is biased via the pixel bias ring and the voltage at the chip bias ring is monitored. In the second, the measurement is repeated vice versa. For both three different regions are observed: (1) Linear correlation, (2) square root correlation, and (3) breakdown region.

Firstly, a linear dependence between both is observed. Secondly, a square root correlation up to the breakdown voltage is determined.
Since both bias rings are implemented on top of a p-implant inside the p-bulk, an ohmic connection between both via the substrate exists even without any applied bias. When a bias voltage is applied to one contact, the depletion region predominantly expands from the deep n-well into the substrate. With increasing depletion region the resistance between both bias contacts changes. A simplified thought experiment can be used to visualize the capacitive behavior:

> A depleted sensor diode is in first sense a plate capacitance where the charge on the plates is proportional to the applied voltage. Due to the correlation of the depletion width d and the depletion voltage - $d \propto \sqrt{U_{dep}}$ (see eq. (3.24)) - the depletion width d increases with the square-root of the depletion voltage U_{dep}. A change of the width results in a changed capacitance.

But, a depleted sensor diode is not a simple 2D capacitance but a 3D diode. Therefore, the actual behavior of the diode cannot be fully explained by the thought experiment.
To validate both the linear and square-root correlations, a preliminary regression analysis was

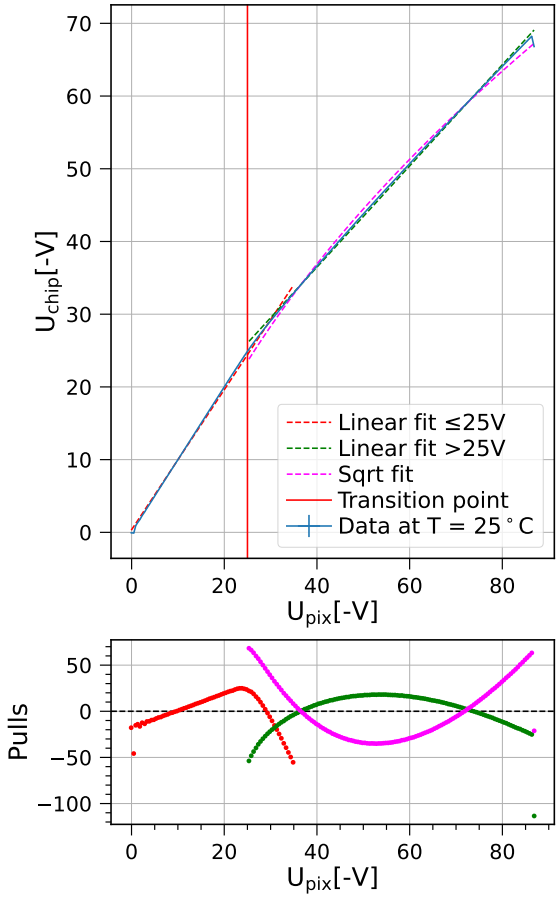


Figure 6.16: VV measurement of TelePix2 with pixel biasing and chip monitoring. The transition point where the linear relation changes is indicated by a red line. Fit functions to both regions are shown.

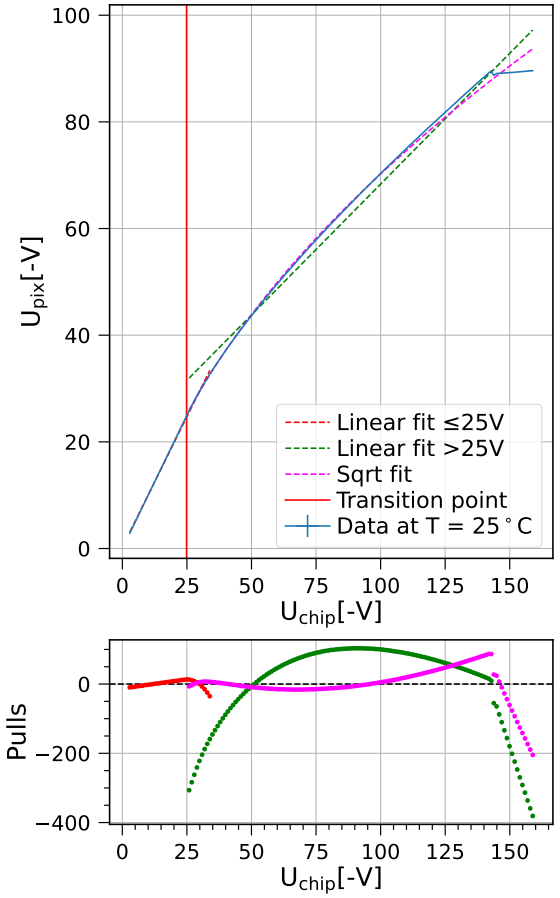


Figure 6.17: VV measurement of TelePix2 with chip biasing and pixel monitoring. The transition point where the linear relation changes is indicated by a red line. Fit functions to both regions are shown.

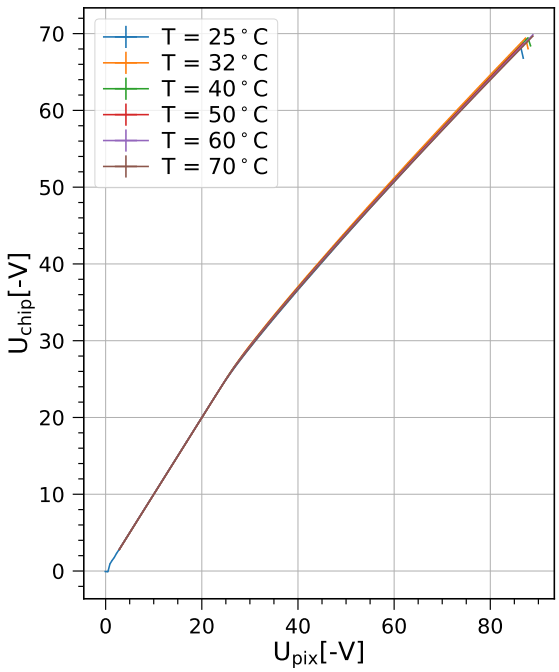
performed on data, as shown in fig. 6.16 and fig. 6.17. A linear regression (colored in red) to the linear region up to the transition point at ≈ 25 V is performed. For the capacitive region a square-root (colored in pink) as well as a linear regression (colored in green) are fitted to data. Both the linear and square-root regressions fail to accurately describe the second region, as visible by the pulls. A slight improvement with the square-root fit is observed visually. However, this provides no definitive evidence for the underlying theory. Further investigation are required to analyze the depletion volume. A possible method is the measurement of its capacitance which is beyond the scope of this thesis.
The third region is dominated by the breakdown and becomes apparent as a kink in the chip-pixel correlation.

An important quantity is the operating temperature T as the leakage current depends on it (see section 3.2.4) and therefore, the sensor performance.
Proving the breakdown-temperature behavior is done by increasing the temperature measured on the PCB stepwise from room temperature up to 70 °C. For each temperature IV and VV curves for both bias possibilities have been taken. A summary of all VV-curves is shown for pixel biasing in fig. 6.18(a) and in fig. 6.18(b) for chip biasing . No change in the correlation between both can be observed. However, the breakdown shows the expected temperature dependence typical for an avalanche breakdown (see section 3.2.4).
For better visualization the breakdown voltage temperature dependence for both bias options is shown in fig. 6.18(c). With increasing temperate a breakdown shift towards higher voltages is observed. Due to increasing lattice vibrations at higher temperatures, the mean free path length of mobile charge carriers in the depletion region is reduced by collisions with phonons. Hence, a higher bias voltage is needed to generate enough electron-hole pairs to create an avalanche breakdown.
It has to be noted that the breakdown at room temperature using chip biasing, as shown in fig. 6.18(c), does not agree with the observed behavior. Due to the significant heat dissipation (as discussed in section 4.2.4), the measured temperature is not fully reliable, likely being higher than anticipated, which could explain the outlier.
Nevertheless, the measured breakdown voltage lies within the expected measurement uncertainty, which is discussed in the following section.

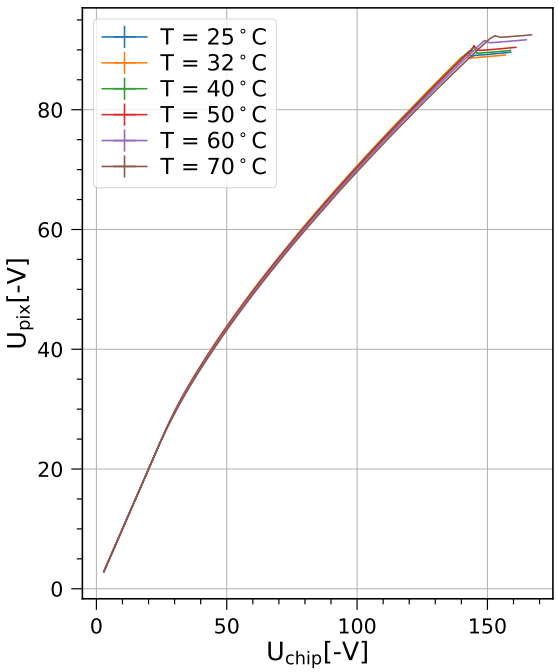
Moreover, the temperature dependence of the leakage current has been studied for TelePix2, aiming to validate the theoretical prediction for a diode and to establish a measurement routine applicable for irradiated devices as well (see section 7.2.1 for comparison measurements). By measuring the correlation as a function of the fluence, it is possible to predict the expected leakage current (see fig. 3.12).
Therefore, the leakage current has been measured at a fixed bias voltage of $U_{chip} - 100\,V$ in dependence of the temperature where the temperature is measured by a digital `BME280` sensor [143], positioned in the vicinity of the DUT on the PCB. Thus, the referred temperature is the temperature on the PCB and not the DUT temperature itself. Again, the actual DUT temperature is higher.
The measured data is shown in fig. 6.19 with a temperature uncertainty of ±2 °C and a current uncertainty of ±1%. A fit to data corresponding to the expected exponential behavior of [34]

$$I_L \propto T^2 \cdot e^{\frac{-E_G}{2k_B T}} \tag{6.2}$$

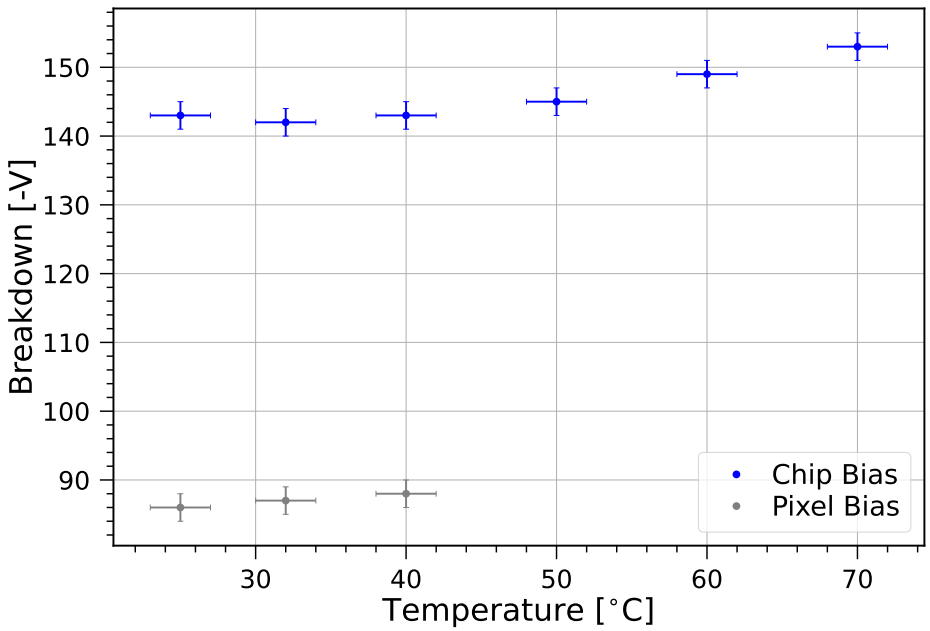
with the bandgap energy of $E_G = 1.21\,eV$ [34] is included. For the fit a constant offset a and a fix constant $b = \frac{E_G}{2k_B}$ are assumed.
Due to TelePix2 self-heating and temperature fluctuations and hence, leakage current fluctuations, the fit describes the data not in a precise manner but a clear trend is visible. At elevated temperatures, the experimental data deviates from the fitted regression. In addition



(a) VV-curves for different temperatures using pixel biasing.



(b) VV-curves for different temperatures using chip biasing.



(c) Breakdown voltage vs. temperature for chip (blue) and pixel (gray) biasing. The uncertainties are primarily determined by the measurement procedure and are estimated as $\Delta U = \pm 2$ V and $\Delta T = \pm 2\,^{\circ}$C.

Figure 6.18: Temperature dependence of VV characteristics and breakdown voltage for TelePix2 under different biasing configurations.

to the measurement precision, surface currents may arise which are not captured by a simple exponential model. Nevertheless, the theoretical prediction of the temperature dependence of the leakage current in diodes provides a valid first-order approximation for HV-MAPS such as TelePix2.
Similar measurements have been performed for irradiated devices and will be discussed in section 7.2.1.

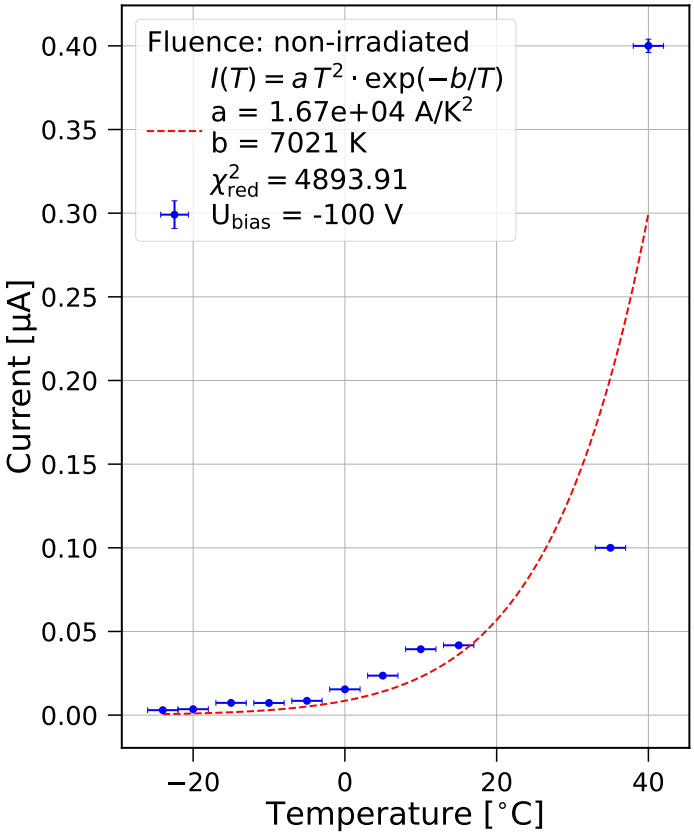


Figure 6.19: Leakage current for different temperatures measured at U_{chip} − 100 V bias voltage. The temperature is measured by a `BME280` temperature sensor [143] placed close to TelePix2 on the PCB. A temperature uncertainty of ±2 °C and current uncertainty of ±1% is assumed. One outlier was measured at 35 °C.

6.3.2 Discussion on Measurement Uncertainties

Due to the heat dissipation of TelePix2 (for more information see section 4.2.4), the temperature measured close to the DUT at the PCB is not equal the DUT temperature. Since no on-chip temperature monitoring is available, the most accurate temperature estimation has been obtained with a thermal camera (see [17] for details). However, the thermal camera is not optimized for the reflecting DUT metal surface. In addition, at cold temperatures the DUT is housed inside a cold box and flushed with nitrogen or dry air to protect for condensation. Thus, measuring the temperature is not feasible with the camera [7]. As a compromise, the PCB temperature has been taken as reference for all presented measurements.
Furthermore, the temperature is affected by several factors in the cooling setup, potentially causing fluctuations. For example, variations in the cooling liquid temperature or in the gas (nitrogen or dry air) flow can contribute. A detailed discussion is presented in [17].
To conclude, the measured temperature is intended as a reference temperature, but not as the operational DUT temperature. Hence, no further uncertainty estimation is given.
Other measurement uncertainties are the bias voltage and measured leakage current. Since the bias voltage is provided by a `iseg SHR` power supply, the provided voltage V_{out} has an uncertainty of $(0.01\,\% \cdot V_{out} + 0.01\,\% \cdot V_{norm})$ with $V_{norm} = 2\,\mathrm{kV}$ [144]. As a conservative approach, the voltage uncertainty is estimated with 0.2 V, including the systematic power supply uncertainty.
The uncertainty on the measured leakage current depends on the power supply measurement resolution and measurement itself, as the leakage is affected by the temperature and depends on the DUT condition. Between different DUTs, the measured leakage current at similar settings can vary, for example due to device-specific defects such as surface scratches. Further, the measurement uncertainty is greater for larger currents due to stronger measurement fluctuations. Therefore, an uncertainty of 0.1 % is estimated including the `iseg SHR` uncertainty of $(0.01\,\% \cdot I_{out} + 0.01\,\% \cdot I_{norm})$ with $I_{norm} = 6\,\mathrm{mA}$ [144].
Finally, the derived breakdown voltage uncertainty is discussed. Because the value is derived at the point where the current change is maximal, the uncertainty depends on the measured current itself. As this in turn has a intrinsic uncertainty, the breakdown uncertainty is affected by it. Because of that, an estimation of the uncertainty is not very meaningful and moreover, not needed to operate the DUT. Thus, no uncertainty is derived. More important is to know the breakdown to operate the DUT close to it to ensure an optimal performance.

[7] A temperature calibration procedure using a non-irradiated TelePix2 sensors with a thermal camera has been executed but not extended towards irradiated devices. In [17] the procedure and results are presented.

6.3.3 Time Resolution

A key requirement for the MightyPix sensor is the accurate association of hits to their corresponding bunch crossings - referred to as in-time efficiency. To achieve an in-time efficiency of 99.9 %, and assuming a Gaussian timing distribution with a $\pm 4\sigma$ acceptance window, a time resolution of ≤ 3 ns is required. Correct assignment of a hit within a 25 ns interval between two consecutive collisions, determined by the 40 MHz bunch crossing frequency, is ensured by this. A schematic illustration is depicted in fig. 6.20. Therefore, the time resolution of HV-MAPS has to be investigated.
Within this section a time resolution measurement performed in the laboratory is explained. The goal is to optimize the settings of TelePix2 to obtain the best optimal time resolution and investigate its performance in dependence of the bias voltage. Before the results are presented, the experimental setup and the analysis procedure are explained.

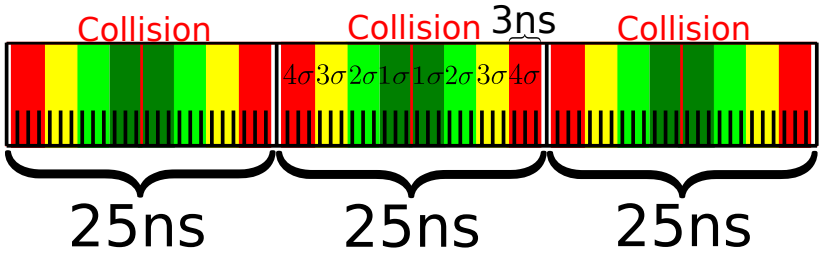


Figure 6.20: Schematic of the needed time resolution to be in-time efficient with 4σ accuracy for a 25 ns bunch crossing frequency [16].

Time Resolution - Experimental Setup

Usually the time resolution is measured with a particle beam at testbeam facilities because a time reference and a particle beam are necessary. However, testbeam campaigns are not done on a daily base and hence, the need for a laboratory setup arises. Therefore, a time resolution measurement setup was designed and commissioned within the Master Thesis of N. Sommerfeld [16] [8].
The setup is independent of the MARS DAQ system but integrated to get a time reference measurement on FPGA level. It consists of a scintillator read-out by two SiPMs. The individual SiPM signals are amplified, discriminated and their coincidence is determined at a dedicated logic board. Its output signal is fed into the adapter board of the MARS DAQ system (see section 5.2.3) and processed as a trigger input signal by the FPGA. In fig. 6.21 a schematic illustration of a typical stack-up consisting of the timing layer including the scintillator (colored in turquoise), the SiPMs (colored in gray) and the amplifier (colored in brown) on top of the TelePix2 DUT and below a radioactive source is depicted. How this looks in reality, is shown in fig. 6.22. Following, cooling of the DUT from the backside is

[8] Details about the design, components, commissioning and calibration measurements are presented in [16].

possible. The setup is used to investigate the time resolution of irradiated samples in the laboratory as well (see section 7.2.2 for corresponding measurements).
An intrinsic time resolution of ≤ 1 ns has been measured [16] for the timing layer. The value is relatively small and therefore neglected in the time resolution correction of TelePix2.
The correction procedure is discussed in the following parts.

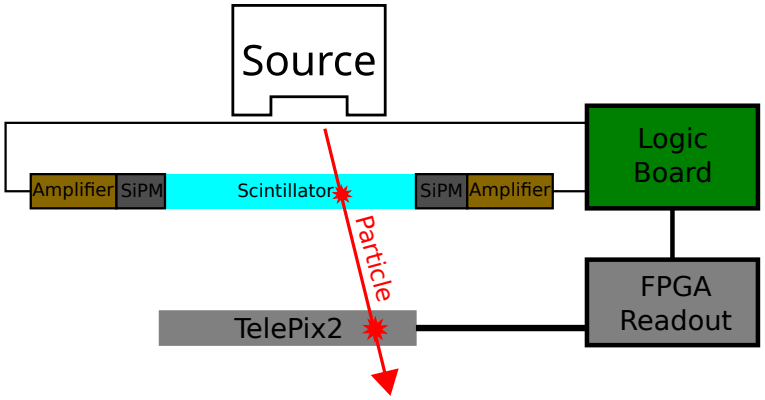


Figure 6.21: Schematic illustration of the timing setup used in the laboratory. Modified from [16].

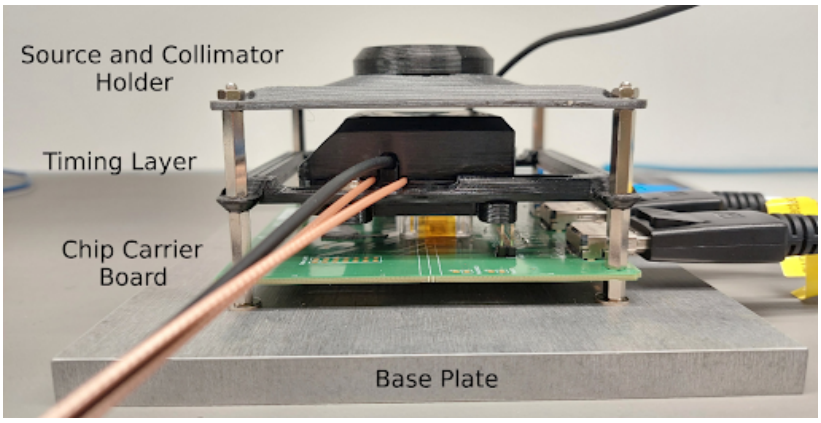


Figure 6.22: Example setup of a MARS DUT carrier board with a stack-up including the timing layer and a source holder with integrated collimator on top [16].

The digital output signal is sampled as a trigger input to the FPGA on a 500 MHz clock. Therefore, the binning limits the accuracy of the measured time resolution to $2\,\text{ns}/\sqrt{12}$ which is corrected for.
Since the timing layer is positioned on top of TelePix2, more particles traverse the timing layer compared to the DUT. Positioning of the timing layer below the DUT can solve the issue. However, efficient back-side cooling of the DUT would not be possible then. Therefore, the first scenario is chosen. Due to the high trigger rate of the timing layer, more timestamps

are available from it than from the DUT. To handle this, all available timing information is assigned on the FPGA. If the DUT sends data, the most recent timestamp from the timing layer is associated with it. Similarly, the FPGA timestamp is buffered (see section 5.3).
The time difference ΔT is defined as

$$\Delta T = TS_{chip} - TS_{TL} \tag{6.3}$$

with the DUT timestamp TS_{chip} and the timing layer timestamp TS_{TL} .
Typically a Sr-90 source is used as particle source and the measurement performed for at least 3 min to record enough statistics. The data analysis is explained next.

Time Resolution - Analysis Procedure

How to obtain the intrinsic time resolution of TelePix2 and other HV-MAPS integrated into the MARS DAQ system will be explained in the following. Since the analysis procedure is discussed in general manner, no specific details on the measurement settings used are provided. For the latter presented results (section 6.3.3), the measurement settings are explained, respectively.
Firstly, the measured time difference is offset corrected. An offset can occur since the timestamp recording has to compensate for system latencies and phase shifts. An example of an offset corrected measurement of the TelePix2 time resolution measurement is shown in fig. 6.23.

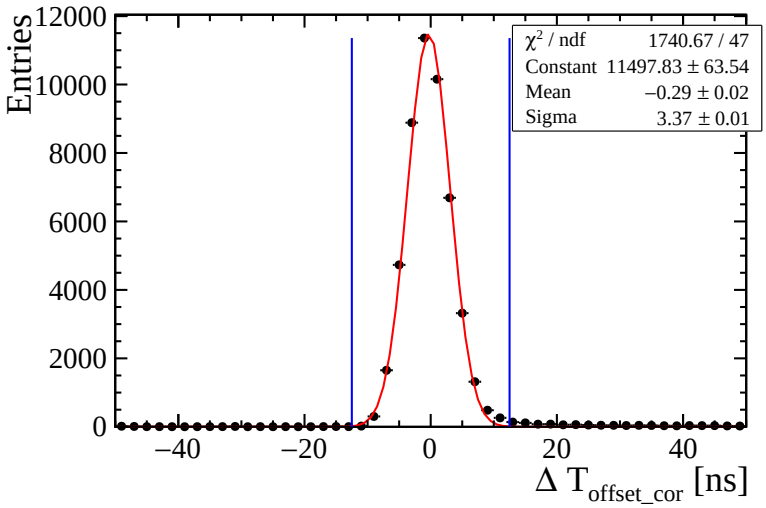
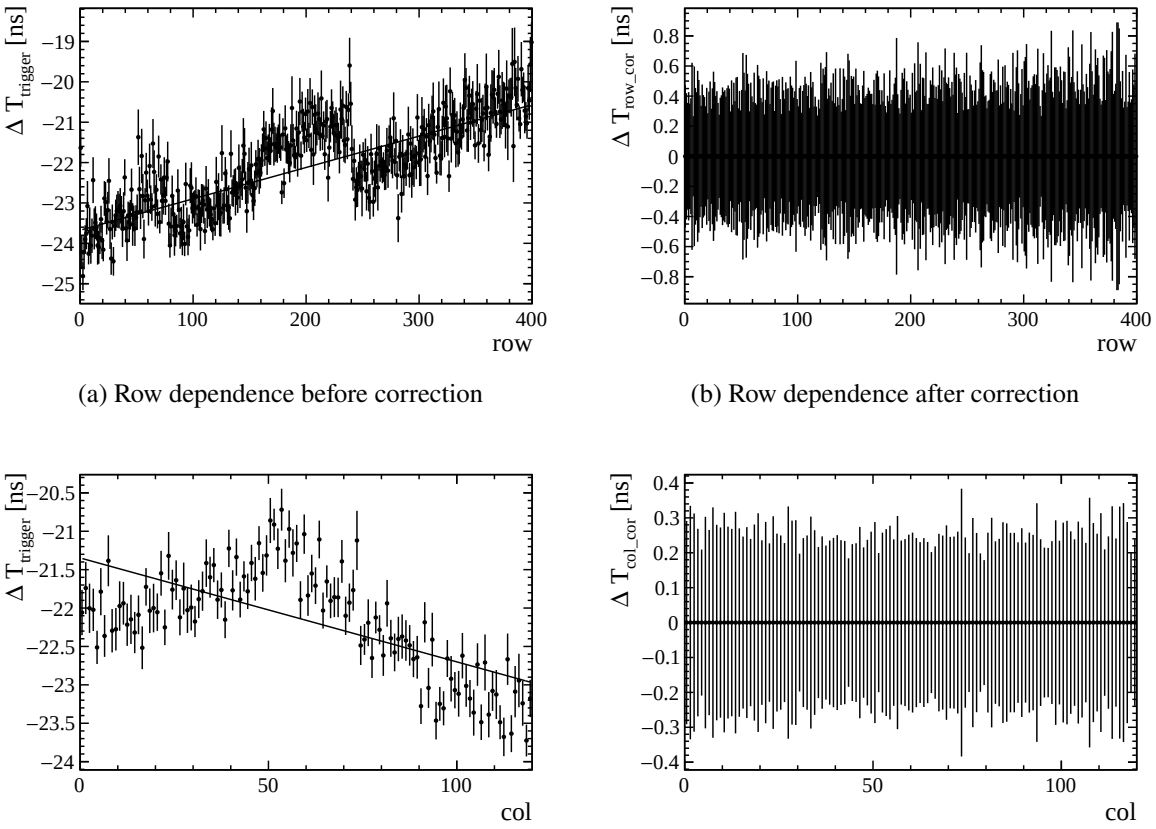


Figure 6.23: Time difference of TelePix2 and the timing layer timestamp after offset correction.

Without any further correction the time resolution including the intrinsic timing layer resolution and timestamp binning of both, DUT and timing layer, is (3.37 ± 0.01) ns where

the uncertainty is the Gaussian fit uncertainty.
Secondly, the time difference is corrected bin-wise for column and row dependencies. In fig. 6.24 both corrections are presented.



(a) Row dependence before correction

(b) Row dependence after correction

(c) Column dependence before correction

(d) Column dependence after correction

Figure 6.24: Profile of the time difference in dependence of rows and columns of TelePix2 before and after a bin-wise correction. A linear regression to data is shown to illustrate the data trend.

On the left hand-side the mean time residuals before and on the right hand-side after correction are shown for all rows in the top row and columns in the bottom.
Four steps for the row dependence are observed corresponding to four metal layers. Since the signal is routed via those, different capacities arise depending on the row address - causing different delays. Further, variations within each layer are visible which can be caused by irregular line spacings.
A simple linear regression, as indicated in fig. 6.24, would not be feasible. Instead each metal layer could be corrected by an individual regression or a bin-wise correction. The latter is done here. After correction the data are well aligned without any significant row dependence.
Studying the column dependence a pattern is observed, too. From the measurement, shown in fig. 6.24(c), central columns have less delay than columns at the edges of TelePix2. A

hypothesis to explain the observation might be the following: The FSM is located in the central part of the TelePix2 periphery. Hence, timestamps generated at hit buffers close to the edges of the DUT have a delayed timestamp compared to those close to the central part. Thus, the observation might be due to a digital effect of delayed clocks. However, the theory cannot be validated since no test structures are available to do so. Nevertheless, a bin-wise correction similar to the row correction is done to overcome the effect.
Thirdly, the row and column corrected time residuals are corrected for time-walk. As explained in section 4.2.2 two timestamps are generated when a hit is detected. The first TS1 detects the ToA when the rising edge of the signal passes the pixel threshold. The second TS2 when the falling edge crosses it. Measuring the time between both TS yields the ToT - a indirect measure of the detected signal charge.
Depending on the signal charge the amplitude varies. For smaller signals a lower amplitude arises while the amplitude is larger for larger signals. Hence, smaller signals have a later ToA than larger signals with a faster ToA. The difference in time is called-time walk. A schematic illustration of the described effect is depicted in fig. 6.25.

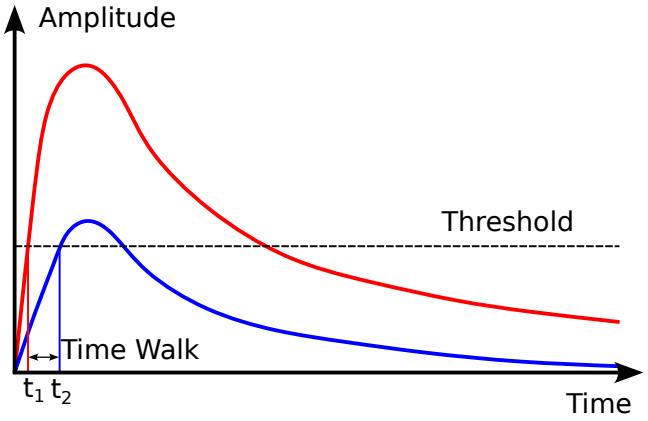
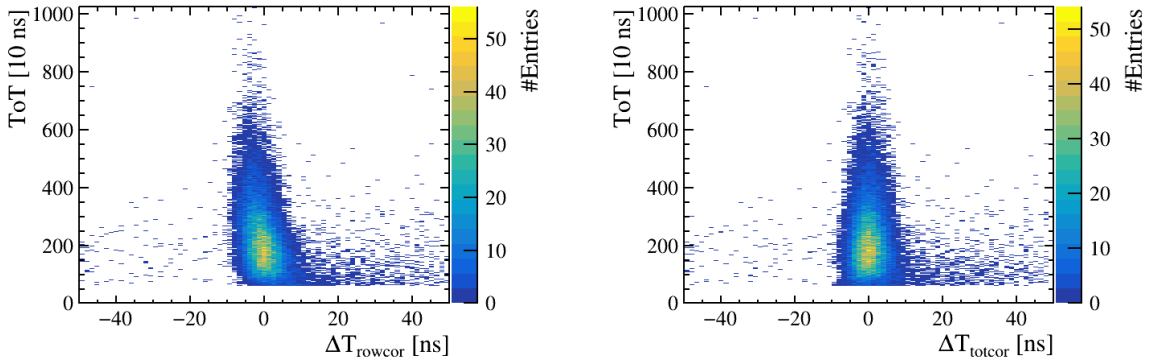


Figure 6.25: Schematic illustration of typical ToT signals leading to time-walk. Time and amplitude are in arbitrary units [16].

Visualization of the effect is possible via the correlation of the ToT and the time residuals shown in fig. 6.26(a). In fig. 6.26(a) the delay of the ToT increases with increasing time difference ΔT. To correct for this, in each ToT bin a Gaussian is fitted to data and the data is shifted by the mean of the fit result to zero. After correction the ToT shows no significant delay with increasing time difference as presented in fig. 6.26(b).
Nevertheless, the time-walk effect depends on the pixel-threshold. With increasing thresholds the time-walk increases as can be seen in fig. 6.25. Thus, the correction might not be sufficient at very high thresholds.

After correction of row, column and time-walk effects, a time resolution (for the example measurement) of $\sigma = (2.95 \pm 0.01)$ ns is obtained. Since this is the total measured time resolution, binning effects and the intrinsic timing layer resolution are included. How those are corrected and the time resolution optimized is discussed next.



(a) Before time-walk correction.

(b) After time-walk correction.

Figure 6.26: ToT dependence of the time residuals.

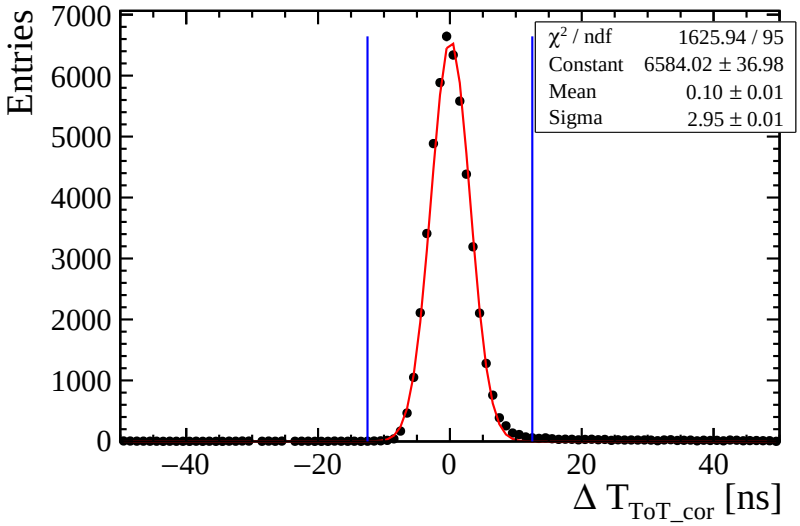


Figure 6.27: Time difference of TelePix2 and the timing layer timestamp after offset, row, column and time-walk corrections.

Time Resolution - Results

In the following the laboratory time resolution measurements of the non-irradiated TelePix2 sensor are presented. Due to the measurement setup and the time stamp binning a further correction to the measurement time resolution σ has to be applied to obtain the intrinsic TelePix2 time resolution σ_{corr}:

$$\sigma_{corr} = \sqrt{\sigma^2 - \left(\frac{5\,\text{ns}}{\sqrt{12}}\right) - \left(\frac{2\,\text{ns}}{\sqrt{12}}\right)} \quad . \tag{6.4}$$

In eq. (6.4) a correction of the DUT time stamp binning of 5 ns is done. In addition, the time stamp binning of the timing layer of 2 ns is corrected for. The intrinsic timing layer resolution is not taken into account since it is $\leq$ 1 ns.
A summary of all introduced corrections to a time resolution measurement performed in the laboratory with standard DAC settings at a bias voltage of −120 V is shown in fig. 6.28.

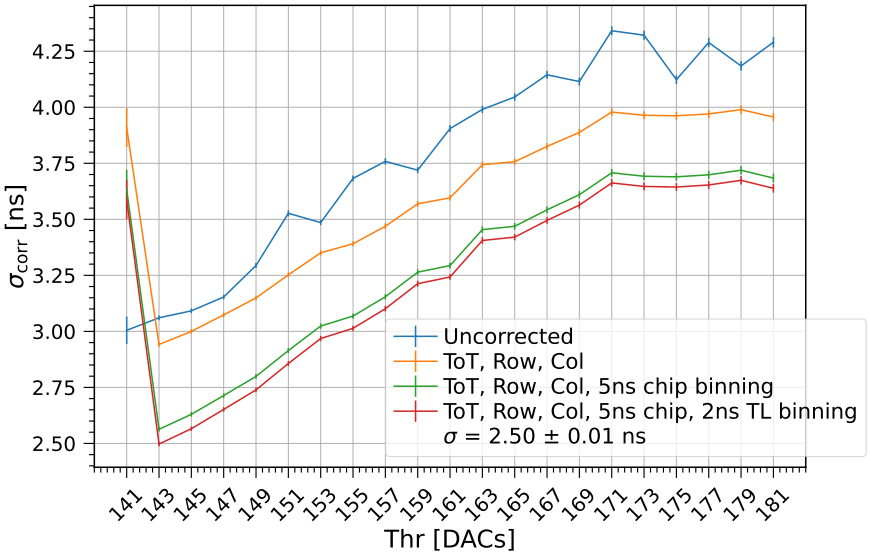


Figure 6.28: Time resolution versus pixel threshold with and without corrections applied to data taken in the laboratory with −120 V chip bias voltage and standard DAC settings of TelePix2.

In blue the recorded time resolution without any correction is shown. How it changes after column, row and time-walk correction is depicted in orange while the final results including binning corrections are shown in red. From the measurement a worse time resolution with increasing pixel threshold is obtained. Even the application of the time-walk correction cannot account for the increase.
The increase, in general, arises due to timewalk. The following reasons might explain the increase even after the correction. Firstly, for higher comparator thresholds smaller ToT

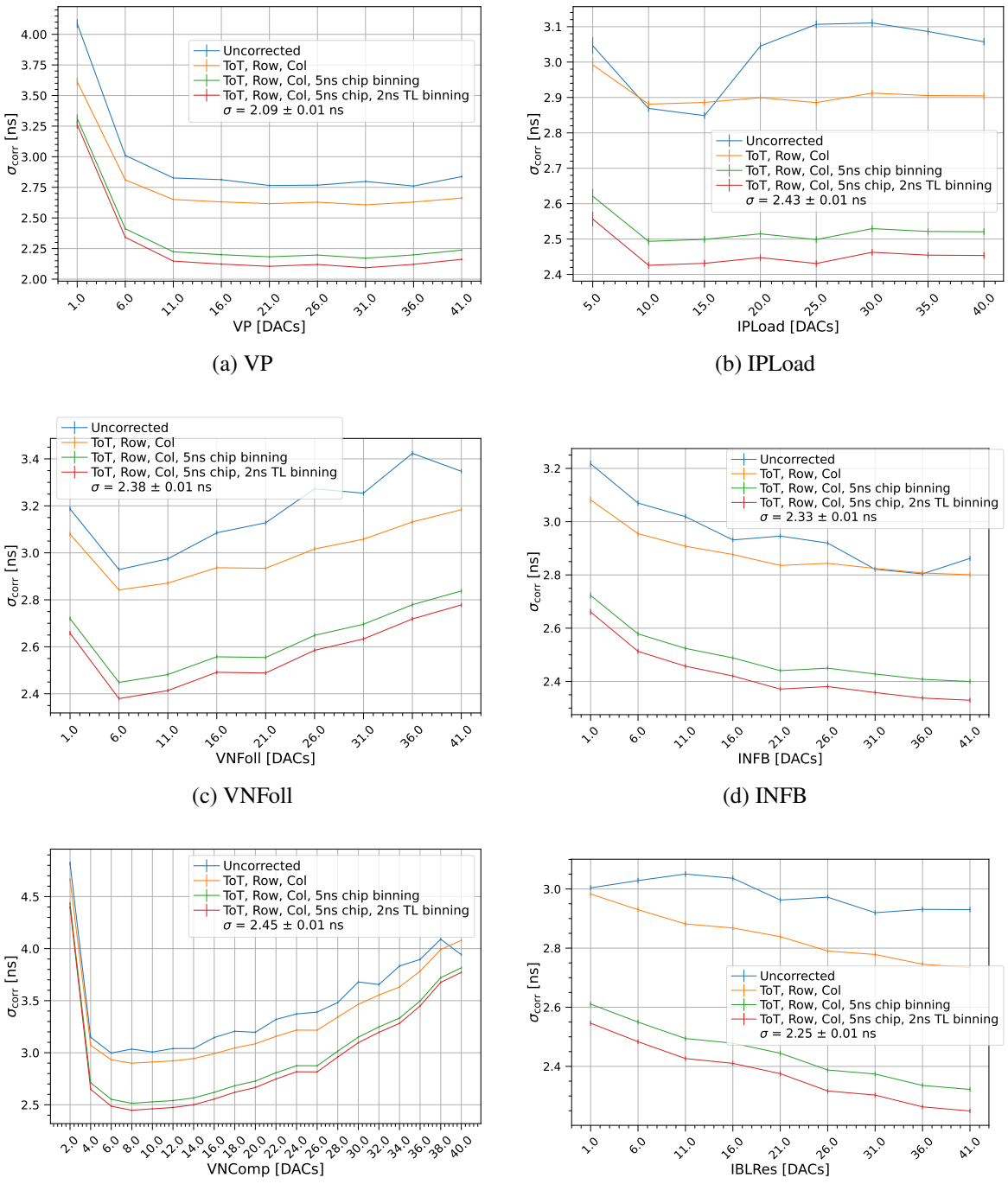
signals are measured. Therefore, the resolution of the ToT is reduced, which can lead to a worse correction.
Secondly, at high thresholds the threshold crossing, shown in fig. 6.25, is less steep. Hence, small jitters of the signal can result in time fluctuations.
Further, the row, column and time-walk corrections may fail at very low pixel thresholds which can occasionally occur - primarily due to limited statistics in the presented measurement. Hence, the time-walk correction based on a Gaussian fit does not work.
Without further optimization of the TelePix2 sensor a time resolution of $\sigma = (2.50 \pm 0.01)$ ns is obtained where the uncertainty is the Gaussian fit uncertainty. Due to the previously discussed measurement setup the measurement uncertainty is larger including the resolution of the timing layer. A detailed measurement uncertainty discussion is not feasible since systematic uncertainties will enter the recorded time resolution of the Mighty-Pixel anyways. Hence, it is more important to understand what influences the time resolution and which corrections are reasonable.
Optimization of the time resolution is done by optimizing the TelePix2 on-chip DAC settings. Therefore, the time resolution measurement was repeated for different DAC settings to obtain the best possible result.
The following DACs have been investigated:

DAC	Electronics	Standard	Optimized
VP	Amplifier bias	10	30
VNFoll	Source follower of the amplifier	3	6
IPLoad	Load resistance of the amplifier	10	11
VNFB	Feedback circuit	10	10
VNComp	Comparator bias	10	10
BLRes	Resistance of the baseline	8	40
Power consumption	Digital	(380 ± 1) mA	(371 ± 1) mA
Power consumption	Analog	(339 ± 1) mA	(548 ± 1) mA

Table 6.2: Overview of investigated DACs, given in DAC units, used to optimize the TelePix2 time resolution and the power consumption for both configurations.

In fig. 6.29 measurements of those over a reasonable DAC range are presented. All measurements have been taken at $U_{\text{chip}} = -120\,\text{V}$ chip bias and are corrected for row, column, time-walk and binning effects. The best obtained result is given within the legend of each.
Two dependencies are observed. Either the time resolution versus DAC settings shows a re-bound structure or the time resolution gets better for higher DAC settings. For the latter this comes with an increased power consumption and hence, it is not reasonable for the Mighty-Pixel since the power budget is limited. Nevertheless, there is some room to optimize the time resolution without increasing the power budget significantly. However, the goal of this measurement was to find the best settings in terms of performance without taken the power budget into account.

For the amplifier and comparator bias, VP and VNComp, the time resolution is optimized once the corresponding transistors are optimally biased and thus, have a fast response time. Vice versa a worse time resolution at low values is obtained due to slow response times.
Analyzing the load resistance of the amplifier, IPLoad, reveals an improved time resolution for DACs between 10-15. Because the transistor is not optimized for higher DAC settings a worsening is observed. Moreover, at higher transistor bias voltages not only signal but also the DUT's noise is amplified, distorting the time resolution.
For the source follower, VNFoll, lower DAC settings yield an improved time resolution.
Since the DAC settings for INFB have to be set at least to 5 to obtain reasonable data, no strong dependence within a reasonable DAC range from 5-30 is observed. This is in compliance with the expectations because INFB affects the falling edge of the signal, which is not relevant for the TOA. In addition, no significant dependence on IBLRes is observed. Similarly, only the falling signal edge is changed by altering the setting.
In summary, DAC investigation is a powerful tool to optimize the time resolution. However, for the final MightyPix sensor the power consumption has to be taken into account. A summary of the optimal DAC settings for TelePix2 is given in table 6.2 in comparison to the standard settings. An increased power consumption of $\approx 18\,\%$ was measured with those settings for TelePix2.



(a) VP (b) IPLoad

(c) VNFoll (d) INFB

(e) VNComp (f) IBLRes

Figure 6.29: Time resolution versus different DACs to optimize for the best possible result. Data have been taken at a bias voltage of −120 V using chip biasing.

The measurement of the time resolution in dependence of the comparator threshold was repeated using the optimized DAC settings. In fig. 6.30 the obtained result for −120 V chip biasing is presented. Similarly, a worse resolution for larger thresholds due to time-walk occurs. Further optimization of the correction would be needed to compensate for this. At a threshold of 166 DAC units the time resolution decreases again due to lower statistics and a non-working fit. Hence, the derived time resolution does not comply with the expectation.
Comparing the best achievable time resolution at the lowest possible threshold - just above the noise floor - an improvement of ≈ 16 % is obtained using optimized instead of standard DAC settings.

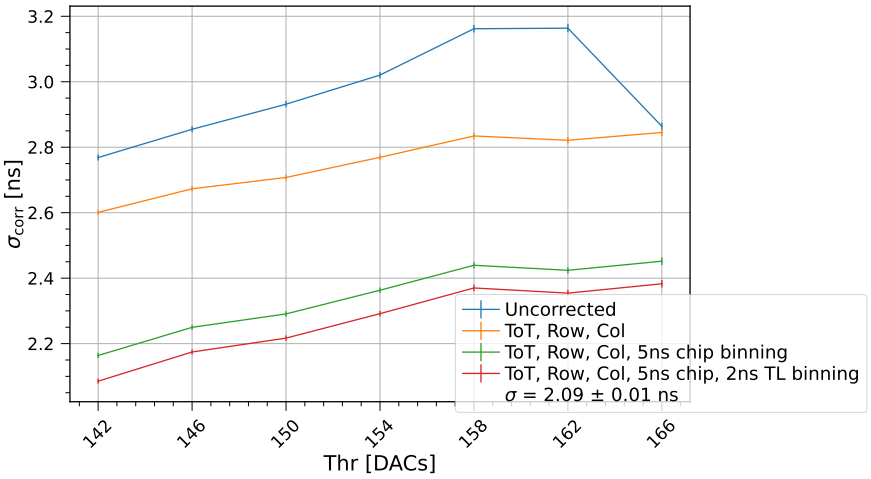


Figure 6.30: Time resolution versus pixel threshold for optimized DAC settings for TelePix2 biased to −120 V at chip biasing.

Besides optimizing the pixel transistor settings, the time resolution is investigated depending on the bias voltage. Since the charge collection efficiency depends on it, an improved time resolution for the maximal possible bias voltage is expected.
Both bias structures, pixel and chip, are studied. In fig. 6.31 and fig. 6.32 both are depicted. As reference the time resolution before any correction is applied is illustrated in blue and after all corrections in red. A pixel threshold of 142 DAC units is chosen to achieve the best result. As expected a clear improvement with increasing bias voltage is observed. Moreover, pixel biasing is not sufficient to achieve the best possible time resolution. However, the result derived at $U_{\text{pix}} = -80\,\text{V}$ (pixel bias) is comparable with the value measured at $U_{\text{chip}} = -80\,\text{V}$ (chip bias) which is in accordance with the VV-curves investigations. Because from those measurements a similar bias potential is expected at the chip bias contact when biasing through the pixel contact.
Since the size of the depletion region depends on the bias voltage and all measurements are taken with an un-thinned DUT, the only limitation is the breakdown voltage. A higher bias voltage would only be possible if the breakdown voltage were higher.
The best possible time resolution obtained for optimized DAC settings for TelePix2 is

(2.04 ± 0.01) ns at $U_{\text{chip}} = -130\,\text{V}$ (chip bias), where the uncertainty is the fit uncertainty. Taking the intrinsic timing layer uncertainty into account an even improved TelePix2 time resolution can be assumed.

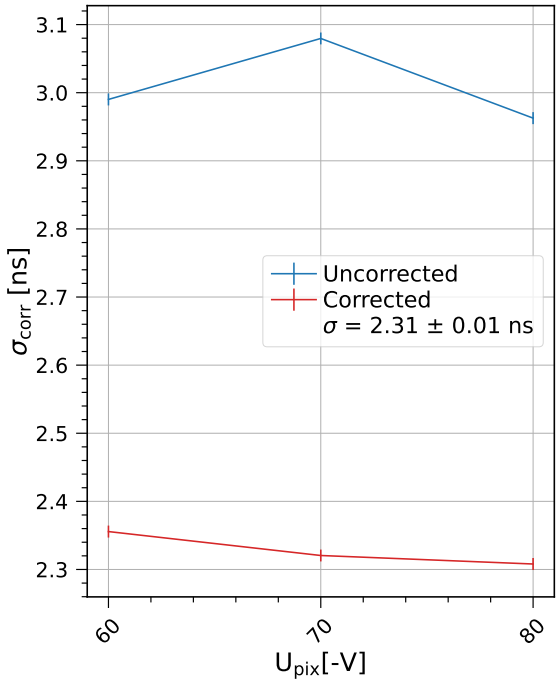


Figure 6.31: Time resolution versus bias voltage using pixel bias.

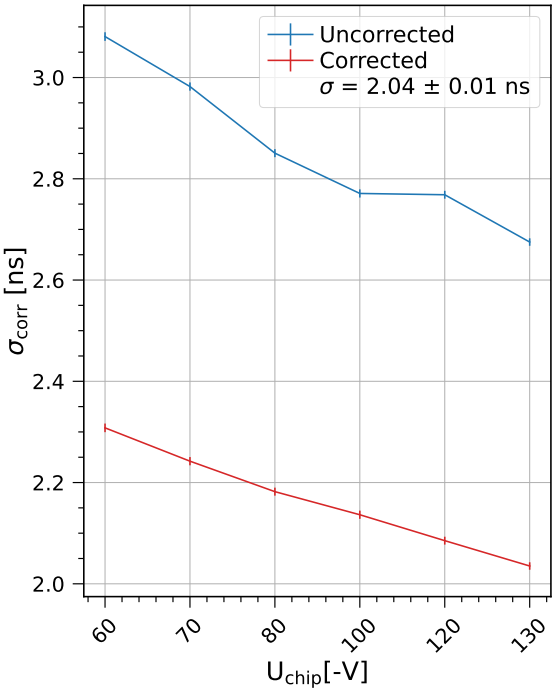


Figure 6.32: Time resolution versus bias voltage using chip bias.

6.4 Summary

Characterization measurements of a non-irradiated TelePix2 sensor as predecessor of the MightyPix2 sensor have been presented. The overall goal was to commission the MARS DAQ system by the performed measurements, establish measurement setups and routines for dedicated use cases and investigate the DUT in terms of bias dependence and time resolution. Commissioning measurements include global calibration measurements of on-chip voltages as the comparator threshold, analog and digital measurements to test the sensor's functionality and response to, e.g. radioactive sources and injection pulses.
Further, a tuning algorithm to optimize the pixel threshold dispersion was implemented in the TelePix2 software and presented. Measurements have shown the expected behavior of the threshold in dependence of the TDACs and tuning strength. The TelePix2 could be fully commissioned for performance measurements.
Investigation of the breakdown and bias behavior in general have shown that pixel biasing is not sufficient to optimally bias TelePix2 since the breakdown happens in the vicinity of the pixel guard ring [9]. Hence, chip bias is chosen as the preferred bias method.
Finally, the time resolution was studied with the goal to achieve a time resolution of $\sigma \leq 3\,\text{ns}$ to fulfill the MightyPix requirements. After optimizing the DAC settings and correction of row, column, time-walk and binning effects, a time resolution of

$$\sigma = (2.04 \pm 0.01)\,\text{ns}$$

has been measured at $U_{\text{chip}} - 130\,\text{V}$ chip biasing. In that sense, TelePix2 would fulfill the MightyPix requirements. Hence, promising results for MightyPix can be expected since the pixel design is very similar.
However, measurements have shown a limitation of the time resolution caused by the bias voltage. Therefore, plans to add multiple guard rings for MightyPix are evaluated.
Further, the influence of radiation damage on the performance has to be investigated which is focus of the following chapters.

[9] A TDAC simulation demonstrating the electrical field strength for comparable HV-MAPS is presented in [112]

CHAPTER 7

Characterization of Bulk Damage on HV-MAPS

At the end of Run 6 the innermost Mighty-Pixel sensors have been exposed to $3 \times 10^{14}\,\mathrm{MeV n_{eq} cm^{-2}}$ NIEL and 40 Mrad TID damage [5]. Therefore, the radiation tolerance of HV-MAPS must be studied in terms of the MightyPix requirements.
Two different irradiation campaigns with protons and x-rays concerning NIEL (discussed in the following) and TID (discussed in chapter 8) damage have been performed with the Run2021 and TelePix2 sensors. Within this chapter detailed investigations on the effect of NIEL damage on the p-type sensor bulk of TelePix2 are presented. TelePix2 has been irradiated in a step-wise irradiation procedure with protons at the Bonn isochronous cyclotron up to the target fluence of $3 \times 10^{14}\,\mathrm{MeV n_{eq} cm^{-2}}$.
Similar to the non-irradiated devices, the investigations focused on the time resolution and bias behavior. A comparable setup as shown in fig. 6.21 has been used for time performance measurements. However, irradiated devices have to be cooled to control the increased leakage currents. Therefore, the measurement setup included the cooling setup shown in fig. 5.4. An overview of the experimental measurement and irradiation setup is given in section 7.1 and section 7.1.1.
The irradiation procedure itself is explained in section 7.1.2. Finally, the results of bias and time resolution measurements are discussed in section 7.2.

7.1 Irradiation Side - Bonn Cyclotron

The proton irradiation campaign was conducted at the Bonn isochronous cyclotron [10]. The in-house facility offers a user-friendly irradiation side with a world-leading precision of the applied fluence on the DUT. Furthermore, a step-wise irradiation procedure with measurements in-between irradiation steps is possible in specialized laboratories. Hence, the Bonn cyclotron has been used as irradiation side for all proton damage studies of TelePix2. Besides protons, the cyclotron is capable of accelerating other positively charged ions as

deuterons and alpha particles. Depending on the target particle type, a different gas is injected into the **E**lectron **C**yclotron **R**esonance ECR ion source from where the particles are extracted and injected into the acceleration complex itself.
Since the cyclotron consists of three Dees, different operation modi are possible. Typically, the $h = 3$ operation mode with the harmonic number h is chosen. Due to the shape of the magnetic yoke the magnetic field increases with increasing momentum of the particle to ensure a constant revolution frequency. As a result, typical energies in the range of 7 to 14 MeV/Nucleon are achieved. Approximately 13 MeV protons were used for presented measurements.

7.1.1 Irradiation Setup and Procedure

TelePix2 has been irradiated in a step-wise manner from $1 \times 10^{12}\,\mathrm{MeVn_{eq}cm^{-2}}$ up to $3 \times 10^{14}\,\mathrm{MeVn_{eq}cm^{-2}}$ in April 2024. Due to time constraints two different devices have been used. The devices that were exposed to which fluence are summarized in the overview table 7.1 of the irradiation.
While only diagnostic measurements of the first four steps have been conducted, the devices exposed to $1 \times 10^{14}\,\mathrm{MeVn_{eq}cm^{-2}}$ and $7.5 \times 10^{13}\,\mathrm{MeVn_{eq}cm^{-2}}$ have been studied in more detail. The final fluence of $3 \times 10^{14}\,\mathrm{MeVn_{eq}cm^{-2}}$ has been applied to DUT 002 in a second irradiation in Fall 2025. Therefore, it was also examined in detail.
Annealing of the devices has been done at the typical 60 °C for 80 min for the last three steps in table 7.1. To inhibit annealing and preserve the radiation damage state, the devices are stored in a freezer when not in use.

Step	Fluence [$\mathrm{MeVn_{eq}cm^{-2}}$]	DUT
1	1×10^{12}	002
2	1×10^{13}	006
3	2.5×10^{13}	002
4	5×10^{13}	006
5	7.5×10^{13}	002
6	1×10^{14}	006
7	3×10^{14}	002

Table 7.1: Summary of the fluence two DUTs have been irradiated to.

For the irradiation itself, the carrier board with the bonded DUT is placed in a Styrofoam box as depicted in fig. 7.1. The box is cooled and constantly flushed with dry nitrogen during irradiation to prevent uncontrolled heating and condensation. Further, unwanted activation of components on the PCB and the PCB itself is reduced by a DUT specific shielding.
To ensure a homogeneous irradiation of the DUT, the DUT is scanned row-wise with constant velocity as illustrated in fig. 7.2. In this scan mode, the fluence is continuously evaluated

online during the procedure. Therefore, a precise irradiation is possible. Moreover, the system recognizes beam instabilities and allows for corrections if, e.g., a non-homogeneity in the scan pattern occurs.

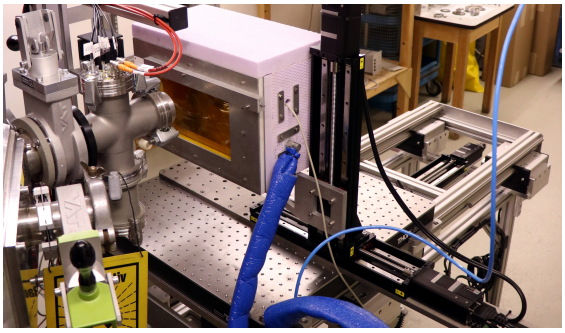


Figure 7.1: Irradiation setup of proton irradiation site at the Bonn cyclotron. The DUT is placed inside the pink styrofoam box, cooled and constantly flushed with nitrogen during the irradiation. Everything besides the sensor itself is covered by a shield to avoid radioactive activation of components [10] [145].

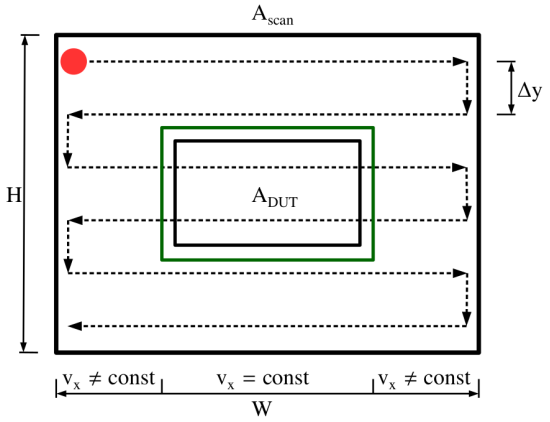


Figure 7.2: Schematic illustration of the irradiation scan procedure. The beam spot constantly scans in height and width over the DUT area [10] [145].

7.1.2 Experimental Procedure

To investigate the TelePix2 performance after proton irradiation, the devices have to be cooled to control the increased leakage damage due to bulk damages (see eq. (3.39)). Therefore, the DUT is cooled via a Peltier element whose warm side is cooled with a water-cooled aluminum block as described in section 5.2. A side view of the setup used for the measurements presented in section 7.2 is depicted in fig. 7.3. On top the DUT carrier board, the timing layer and Sr-90 holding structure are placed, necessary for time resolution measurements. The full stack-up including the aluminum block is positioned inside a 3D printed enclosure from which the bottom half is visible in fig. 7.3. During the measurements, the box is completely closed and flushed with nitrogen. Temperatures of $\approx -40\,^{\circ}\mathrm{C}$ are possible on the PCB near to the DUT when the chiller is cooled to $\approx -20\,^{\circ}\mathrm{C}$. A further reduction in temperature is possible if the enclosure is flushed with cold gaseous nitrogen.

To perform bias and time resolution measurements, the box is firstly flushed and secondly cooled. With an online temperature and humidity monitoring, the environmental conditions are controlled. If stables conditions are ensured, the DUT is powered and biased. After quick sanity checks including a threshold scan and verification of stable data links, the bias dependence is analyzed and time resolution measured for different sensor settings and bias options. The obtained results are presented in the following.

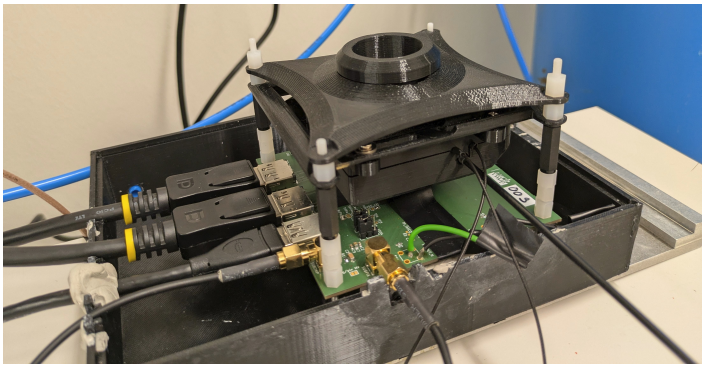


Figure 7.3: Side view of the experimental setup. The DUT carrier board is mounted inside a 3D printed enclosure onto Peltier elements on top of the aluminum water block. A stack-up of the timing layer and Sr-90 source holding structure is placed on top for time resolution measurements. The enclosure is flushed with nitrogen to control the humidity at cold temperatures.

7.2 Impact of Proton Irradiation on the Performance of TelePix2

The overall purpose of the presented results is to demonstrate the radiation tolerance of TelePix2, as predecessor of MightyPix, with regard to NIEL damage and to investigate its time resolution, since the required 3 ns at 3×10^{14} $\mathrm{MeVn_{eq}cm^{-2}}$ must be met.
Moreover, optimal sensor configurations have been investigated - necessary to ensure efficient operation of irradiated devices. In addition, the bias behavior was investigated, which is not only necessary for a high sensor performance, but also important for the entire detector design, since design criteria such as serial power supply chains have to cope with the required high voltage.
Firstly, the bias behavior is discussed in section 7.2.1. Secondly, time resolution measurements for different bias options and sensor configurations are presented in section 7.2.2.

7.2.1 Bias Dependence of Proton-Irradiated TelePix2

At each irradiation step, presented in table 7.1, IV- and VV-curves have been measured to investigate the breakdown behavior and correlation of pixel and chip biasing.
In fig. 7.4 and fig. 7.5 the results obtained for chip biasing up to a fluence of 1×10^{14} $\mathrm{MeVn_{eq}cm^{-2}}$ are presented [1] [2]. Similar results for pixel biasing are shown in appendix A.8.

Comparing the IV behavior for different fluences two effects can be observed. Firstly, the measured leakage current increases with increasing fluence due to bulk damages. Following eq. (3.39) [97]

[1] Due to a technical issue the VV-curve for 7.5×10^{13} $\mathrm{MeVn_{eq}cm^{-2}}$ has not been measured.
[2] For both measurements a discussion on the measurement uncertainties is provided in appendix A.5.

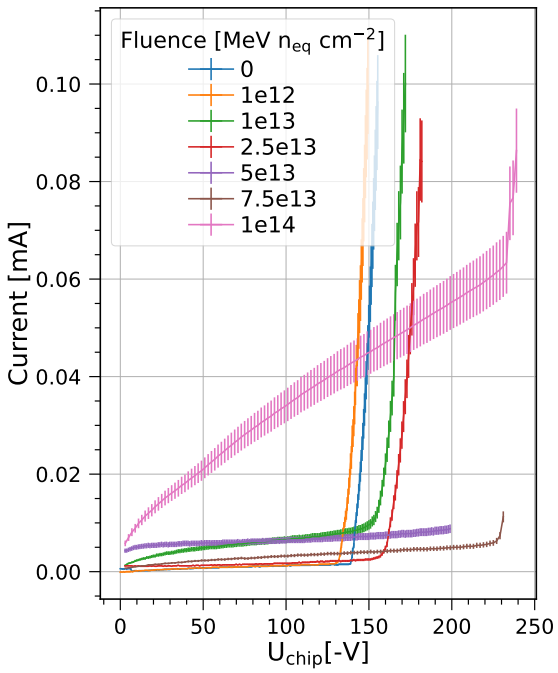


Figure 7.4: Summary of IV measurements for different fluences compared to a non-irradiated device using chip biasing of TelePix2. Measurements have been taken in April 2024.

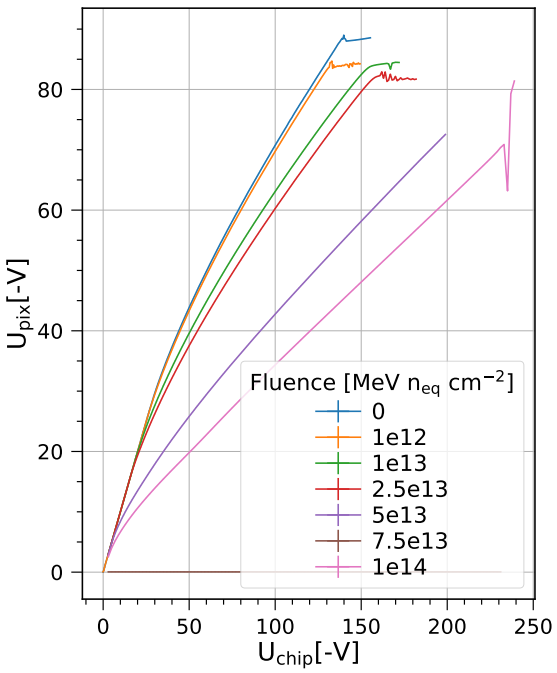


Figure 7.5: Summary of VV measurements for different fluences compared to a non-irradiated device using chip biasing of TelePix2. Measurements have been taken in April 2024.

$$I_{leak} = q_0 \cdot A \cdot \sum_{defects} G_t$$

a linear increase is expected with the defect generation rate G_t. The second observation relates to the breakdown voltage. For higher fluences the breakdown voltage shifts towards higher voltages. Hence, a larger bias voltage has to be applied to operate the sensor close to its breakdown.
It has to be noted that for both observations slight deviations between the measurements are visible. For example, the leakage current for $1 \times 10^{13}\,\mathrm{MeVn_{eq}cm^{-2}}$ is higher than for $2.5 \times 10^{13}\,\mathrm{MeVn_{eq}cm^{-2}}$. The reasons for this are inherent in the measurement itself, as time was limited and the cooling system shown in fig. 7.3 had not yet been finalized when these measurements were taken in April 2024. Therefore, temperature variations have likely occurred. Moreover, the measurements have been performed in-between consecutive irradiations. Hence, the time after irradiation and the first measurement was not consistent between all steps. DUTs with more 'waiting time' have shown overall lower leakage current since the damages directly after irradiation without any controlled annealing affect the sensor behavior a lot. Longer waiting times, on the other hand, had a positive effect on the

measurements due to short living isotopes affecting the leakage current.
Consequently, a more qualitative comparison between the measurements is meaningful here.

In a similar manner VV-curves have been measured using chip biasing. The summary up to a fluence of $1 \times 10^{14}\,\mathrm{MeVn_{eq}cm^{-2}}$ shows a change in the relation between chip and pixel biasing. While a shift of the breakdown towards larger values using chip biasing is observed, an earlier breakdown at the pixel contact occurs. Overall, the voltage measured at the pixel contact decreases a lot with increasing fluence for a given voltage applied at the chip bias contact. Hence, chip biasing is expected to be necessary for an optimal sensor performance. Since the breakdown is driven by the high electrical field in the vicinity of the pixel guard ring, an overall increase of the leakage current influences the breakdown. As a consequence, the breakdown occurs earlier for higher leakage currents - explaining the measurements at the pixel bias contact.
In contrast, the shift of the breakdown voltage toward higher values when using the chip bias contact can be attributed to changes in the bulk properties. Because the effective doping concentration directly influences the depletion depth, a variation can explain the observed behavior as shown in eq. (3.24) [34]:

$$U_{dep} = \frac{ed^2}{2\epsilon\epsilon_o} \cdot N_{eff} \quad .$$

Following, a decreased effective doping concentration affects the depletion depth. In fig. 7.6 the effective doping concentration versus fluence for different bulk resistivities is illustrated.

For the standard resistivity of 370 Ω cm used in TelePix2, the effective doping concentration is expected to exhibit a rebound behavior, reaching a minimum at fluences of approximately 1×10^{14} to $2 \times 10^{14}\,\mathrm{MeVn_{eq}cm^{-2}}$. For example, the effective doping concentration at $1 \times 10^{14}\,\mathrm{MeVn_{eq}cm^{-2}}$ compares to the of a DUT with 1 kΩ cm resistivity without irradiation. Hence, the bias voltage increases as shown in fig. 7.7 and further, yields an increased depletion depth.
An explanation for the changed pixel-chip correlation due a change of the effective doping concentration emerges from the discussions.

A summary of the breakdown voltage versus the fluence is shown in fig. 7.8. As discussed, two different observations for chip and pixel bias have been made. Therefore, and due to fig. 7.7 it is concluded to use chip biasing to ensure an efficient operation of TelePix2. Further, a better performance is expected for proton irradiated devices since the performance is affected by the depletion depth.

Because the final fluence of $3 \times 10^{14}\,\mathrm{MeVn_{eq}cm^{-2}}$ was achieved in a separate irradiation and both devices (002 and 006) have been annealed and taken to a testbeam campaign in December 2024, the bias measurements have been repeated. Due to time constraints shortly before the testbeam, the results presented here have been obtained from laboratory

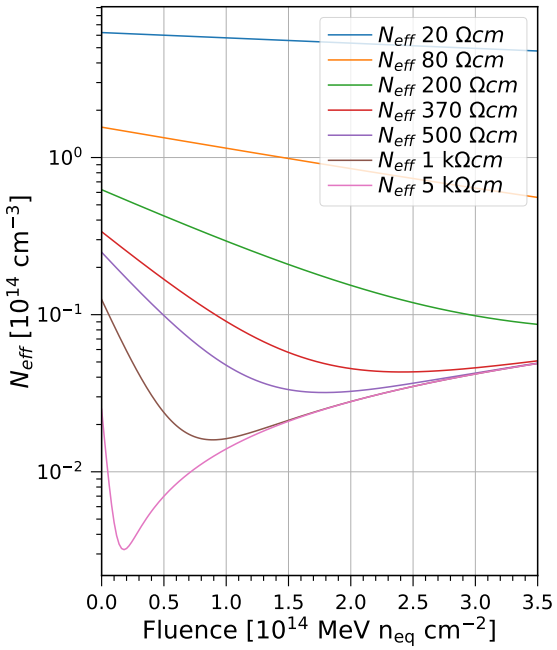


Figure 7.6: Effective doping concentration versus fluence for different bulk resistivities.

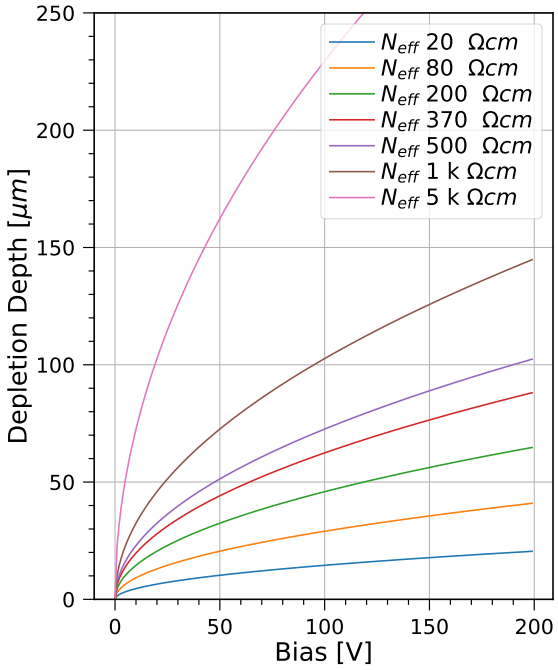


Figure 7.7: Depletion depth versus bias voltage for different bulk resistivities.

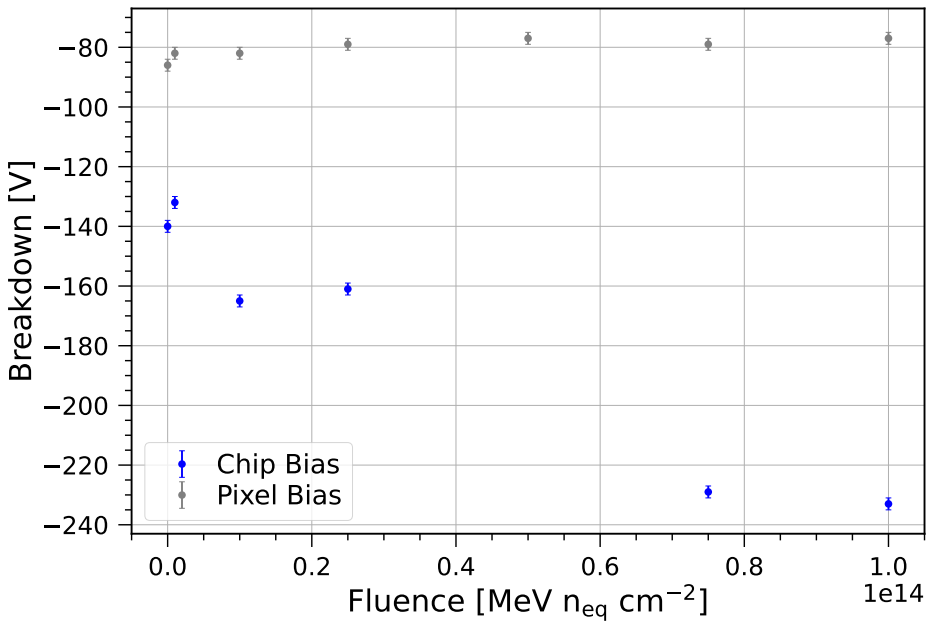


Figure 7.8: Summary of the measured breakdown for different fluences using chip (depicted in blue) and pixel (depicted in gray) biasing. The uncertainty of the breakdown is primarily determined by the measurement procedure and is estimated as $\Delta U = \pm 2\,V$.

investigations with the setup shown in fig. 7.3 in June 2025.
Due to longer annealing times a reduced leakage current for the 1×10^{14} MeVn_{eq}cm^{-2} device is measured as visible in fig. 7.9 for chip biasing [3] [4].

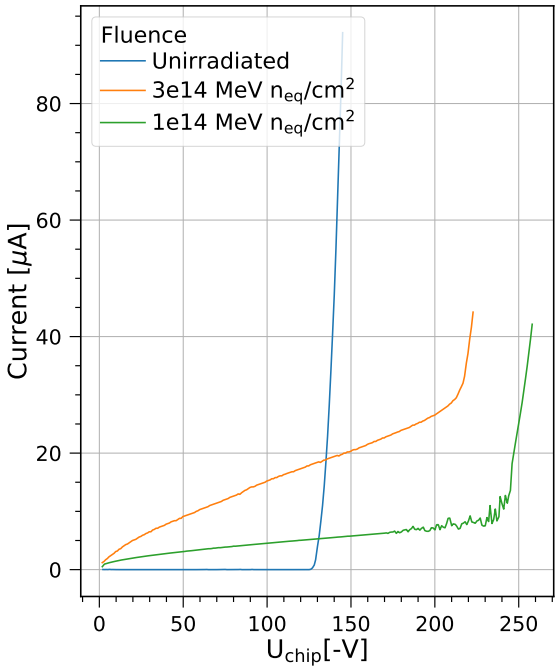


Figure 7.9: Summary of IV measurements for annealed TelePix2 devices compared to a non-irradiated device using chip biasing. For each case, the lowest possible temperature was used (see fig. 7.11). Measurements have been taken in June 2025.

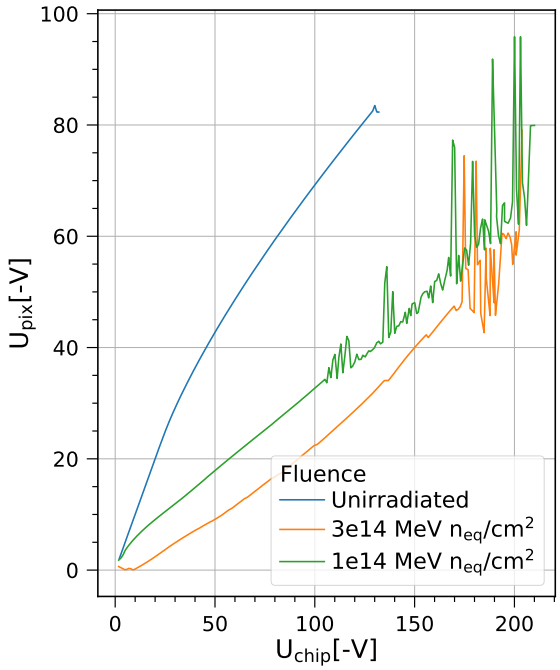


Figure 7.10: Summary of VV measurements for annealed TelePix2 devices compared to a non-irradiated device using chip biasing. For each case, the lowest possible temperature was used (see fig. 7.11). Measurements have been taken in June 2025.

Similar to previous measurements, the leakage current increases with increasing fluence. In addition, fluctuations of the leakage current on the order of ±3 µA are observed at high voltages. Because the high bias voltage enlarges the depletion region, greater fluctuations are expected (A detailed discussion on uncertainties is provided in appendix A.5).
In contrast to fig. 7.4, an earlier breakdown for the highest fluence of 3×10^{14} MeVn_{eq}cm^{-2} is observed. Since the effective doping concentration and consequently, the possible bias voltage depends on the fluence, an increase in doping concentration can explain the observation. From theory and measurements presented in [99] a rebound structure in the effective doping concentration with a minimal concentration at $\approx 2 \times 10^{14}$ MeVn_{eq}cm^{-2} is expected depending on the initial doping concentration and proton energy.

[3] Results using pixel biasing are shown in appendix A.8
[4] A discussion on the measurement uncertainties is provided in section 6.3.2 and appendix A.5.

The VV-curves, presented in fig. 7.10, validate the discussed change in the chip-pixel correlation, as discussed previously. For both irradiated devices greater fluctuations for larger bias voltages are observed - expected due to fluctuations of the leakage current (see appendix A.5). The reason for the leakage current fluctuations are not yet fully understood, but have been observed in several measurements.
Measurements performed with MightyPix1 [11] and the Run2021 [12] sensor have shown comparable results [5].

Besides the breakdown, the leakage current itself has to be investigated to ensure a high-performance detector. From measurements of several irradiated devices it could be concluded that too high leakage currents $\mathcal{O}(10\,\mu\text{A}) \approx 0.21\,\text{nA/pixel}$ affect the sensor performance. At higher currents, the sensor amplifier starts to oscillate resulting in unwanted noise and worse performance in terms of time resolution. To control the leakage current and keep it at a reasonable level, the DUT has to be cooled. The target temperature of the DUT is important for the Mighty-Pixel, as it influences the design of the detector, especially the cooling of the modules. Moreover, it has to be taken into account that not all sensors will be exposed to the same fluence at the same time. Hence, a key investigation is to understand the performance-temperature dependence of HV-MAPS.
However, TelePix2 is not the ideal candidate for precise temperature dependent measurements due to its high self-heating and no on-chip temperature monitoring.
But, a first attempt was done by measuring the leakage current in dependence of the temperature and fluence. Under the assumption that the NIEL hypothesis holds for p-type devices and the depletion depth is known, predictions of the expected leakage current for a given fluence become possible [6].
Similar to the measurement of a non-irradiated TelePix2 sensor, presented in section 6.3.1, the leakage current has been measured for a bias voltage of $U_{\text{chip}} = -100\,\text{V}$ using chip bias. The value has been chosen because it is close to the standard laboratory operation voltage of $U_{\text{chip}} = -120\,\text{V}$ and is below the breakdown of the photon irradiated device (see section 8.4.1). A summary including all investigated devices is shown in fig. 7.11.

Besides, the proton irradiated samples, also one x-ray irradiated and hence, surface damaged device has been analyzed.
All devices show the expected exponential temperature dependence of eq. (6.2) [34]

[5] Both irradiation campaigns have been performed at the Bonn isochronous cyclotron under the supervision of the author. Moreover, the measurement setup for MightyPix1 as well as the start of the analysis has been provided by the author.

[6] An initial effort to normalize the leakage current to the depleted volume at a fixed temperature was done. However, the accuracy of the temperature measurement is not sufficient. In addition, the depleted volume can only be determined from theoretical predictions (more information are provided in section 3.2). A measurement of the depletion depth is possible by measuring the sensor capacitance in dependence of the bias voltage. The measurement is planned for the future, but was not conducted within the scope of this thesis.

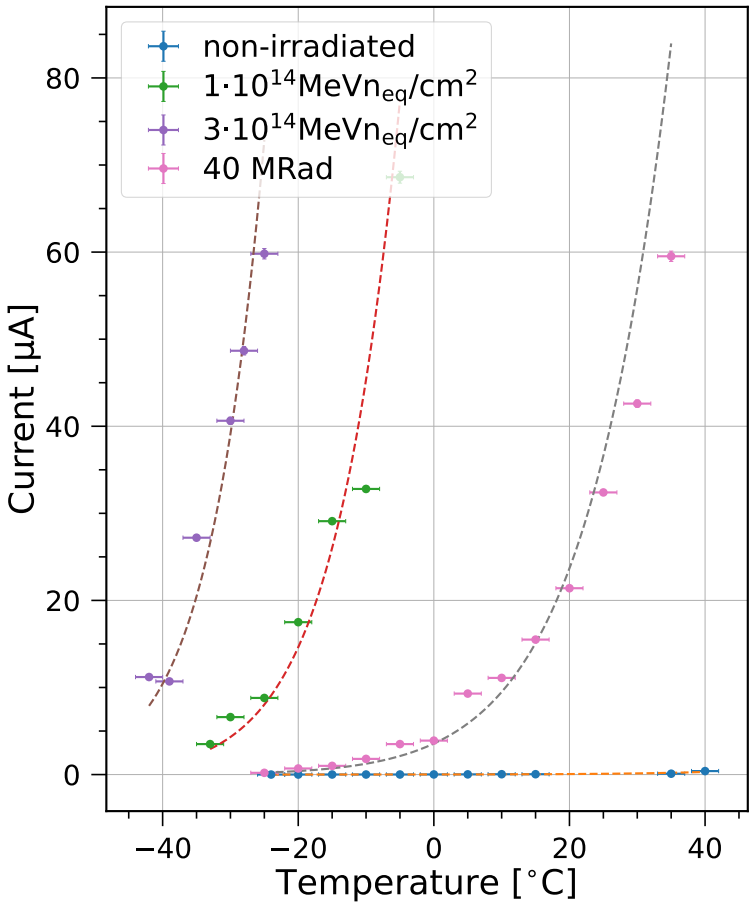


Figure 7.11: Leakage current versus temperature for different radiation damages and fluences. Due to the comparable low leakage current on the non-irradiated DUT the exponential behavior is not visible here, but in fig. 6.19.

$$I_L \propto T^2 \cdot e^{\frac{-E_G}{2k_B T}} \quad . \tag{7.1}$$

When comparing the DUTs irradiated with protons, the overall higher leakage current observed in the IV measurements is also confirmed here. A change of the depleted volume and increased amount of bulk damage can explain the observation. Moreover, an effect on the leakage current for both irradiation types is observed. It has to be noted that surface damage is discussed in more detail in the next chapter (see chapter 8).
Nevertheless, the increased leakage current for the DUT exposed to 40 MRad TID shows an effect of surface damage on the leakage that was not initially expected, but can be explained by an accumulation of electrons at the Si-$Si0_2$ interface, which influences the electrical field. However, compared to the samples irradiated with protons, the effect of proton irradiation on

leakage damage is more severe.
Furthermore, the measurement shows the necessity to operate high irradiated devices at very cold temperatures to keep the leakage current below 10 to 20 µA.

7.2.2 Time Resolution Measurement

The time resolution was investigated during two separate laboratory measurement campaigns. First, after the irradiation in April 2024 with a non-optimized cooling solution for the DUTs exposed to fluences of $7.5 \times 10^{13}\,\mathrm{MeV n_{eq} cm^{-2}}$ and $1 \times 10^{14}\,\mathrm{MeV n_{eq} cm^{-2}}$. For both, measurements studying the bias and sensor configuration dependence have been conducted. Secondly, the measurements have been repeated in June 2025 using the optimized cooling solution for the DUTs exposed to $1 \times 10^{14}\,\mathrm{MeV n_{eq} cm^{-2}}$ and $3 \times 10^{14}\,\mathrm{MeV n_{eq} cm^{-2}}$ with the goal to obtain the best possible time resolution.
Further, a high leakage current of the DUT exposed to $3 \times 10^{14}\,\mathrm{MeV n_{eq} cm^{-2}}$ has been observed at the testbeam campaign in December 2024. Therefore, the DUT could not be biased via chip biasing at that point (see chapter 9). Thus, the measurements taken in June 2025 also aimed to investigate a possible defect of the sensor.

First, the results from April 2024 will be discussed. Both devices have been cooled as much as possible at the time. A reference temperature cannot be given here because the cooling solution was not optimized and characterized itself. However, the leakage current was on the order of $O(10\,\mu\mathrm{A})$.
To determine the time resolution, a Sr-90 source similar as for measurements of the non-irradiated device has been used. The same corrections as discussed in section 6.3.3 were applied.
In fig. 7.12 the results before (depicted in blue) and after (depicted in red) are shown for a fluence of $7.5 \times 10^{13}\,\mathrm{MeV n_{eq} cm^{-2}}$ for different bias voltages using chip biasing. Similarly, in fig. 7.13 the results for a fluence of $1 \times 10^{14}\,\mathrm{MeV n_{eq} cm^{-2}}$ are presented. For both standard DAC settings and a comparator threshold of 145 DAC units were used.

A clear improvement of the time resolution with increasing bias voltage is obtained. An increased bias voltage enhances the electric field strength, leading to a larger depletion region. Hence, the charge collection efficiency is improved. As a consequence, a limitation in the time resolution is inferred by the breakdown of the DUT.
Changing the guard ring design to improve biasing would result in a better performance. However, adding more guard rings will reduce the active area of the DUT. The design was discussed by the Mighty-Pixel coordination team in collaboration with the designers at KIT. One conclusion from this discussion is that additional space for more guard rings will be available [146]. Nevertheless, for both sensors time resolutions of

$$\sigma_{corr} = (2.91 \pm 0.01)\,\mathrm{ns} \qquad (7.5 \times 10^{13}\,\mathrm{MeV n_{eq} cm^{-2}})$$
$$\sigma_{corr} = (2.68 \pm 0.01)\,\mathrm{ns} \qquad (1 \times 10^{14}\,\mathrm{MeV n_{eq} cm^{-2}})$$

have been obtained - fulfilling the required time resolution of $\sigma \leq 3\,\mathrm{ns}$.
Comparing both with each other, a slightly worse time resolution for the lower fluence is observed. A general higher noise level of the $7.5 \times 10^{13}\,\mathrm{MeV n_{eq} cm^{-2}}$ can explain the result.

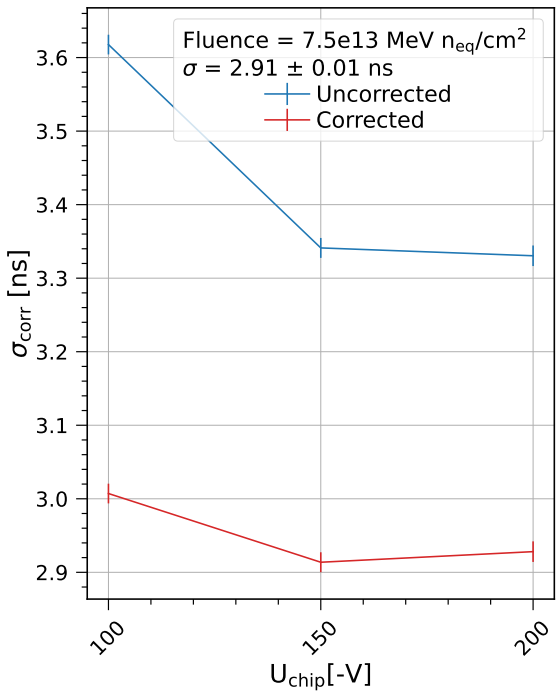


Figure 7.12: Time resolution for a fluence of $7.5 \times 10^{13}\,\mathrm{MeV n_{eq} cm^{-2}}$ in dependence of applied chip biasing before (depicted in blue) and after (depicted in red) correction. The uncertainty on the time resolution is the Gaussian fit uncertainty. Measurements were taken in April 2024.

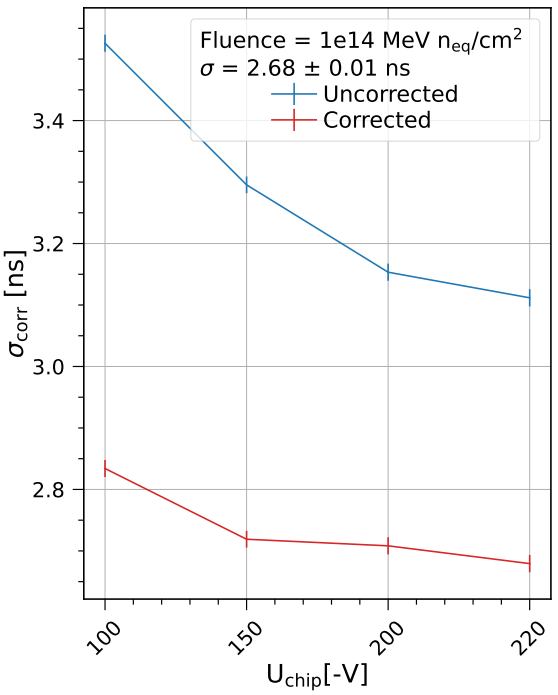


Figure 7.13: Time resolution for a fluence of $1 \times 10^{14}\,\mathrm{MeV n_{eq} cm^{-2}}$ in dependence of applied chip biasing before (depicted in blue) and after (depicted in red) correction. The uncertainty on the time resolution is the Gaussian fit uncertainty. Measurements have been taken in April 2024.

Furthermore, not enough statistics with irradiated samples is available. Hence, a chip-to-chip variation in orders of 0.2 ns may be possible. To prove this, further samples are necessary.

Next, the results of the measurements obtained in June 2025 are discussed. Again the same corrections have been applied and the devices are cooled as much as possible whereby the coldest temperature shown in fig. 7.11 for each device has been used. The goal of the measurements is to confirm the testbeam results, discussed in chapter 9, and obtain the best possible time resolution.
Therefore, four different scenarios were studied: (1) Standard bias voltage of $U_{\mathrm{chip}} = -120\,\mathrm{V}$ with standard DAC settings, (2) standard bias voltage with best DAC settings, (3) high bias voltage of $U_{\mathrm{chip}} = -210\,\mathrm{V}$ with standard DAC settings and (4) high bias voltage with best DAC settings. By best DAC settings the settings determined in table 6.2 are meant. A comparator threshold of 145 DAC units has been set for all measurements. In fig. 7.14 the summary of the corrected time resolution results for both sets of DACs is shown.
For both scenarios the higher bias voltage yields a better time resolution due to faster charge

collection. Moreover, for all four cases the results fulfill the required time resolution of ≤ 3 ns.
A time resolution of ≤ 2 ns is achieved for optimized DAC settings and a bias voltage of $U_{\text{chip}} = -210$ V.
Comparing the result using standard DAC settings with the results obtained from April 2024, a similar time resolution is determined - validating the measurements with each other and showing continuity which is crucial for long term operation of the devices.

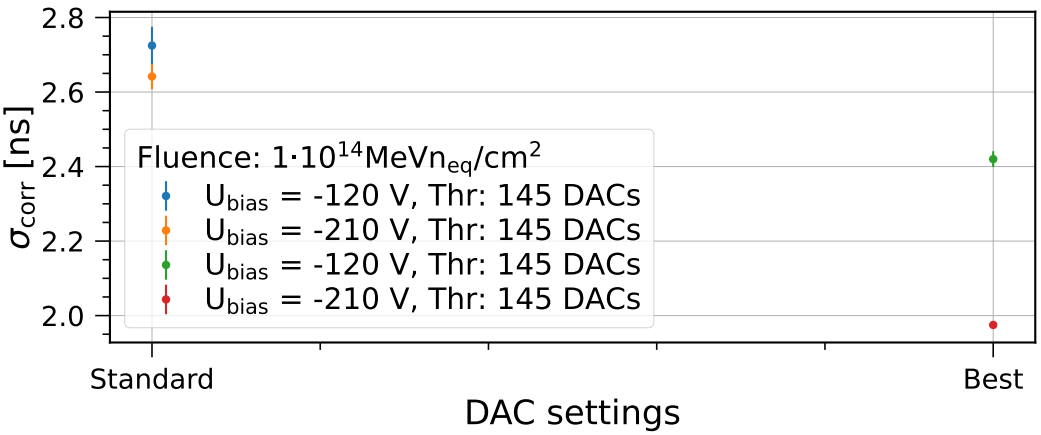
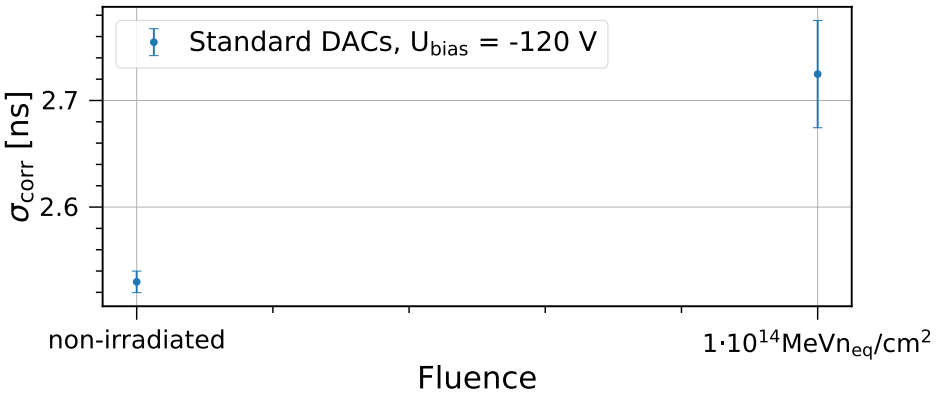
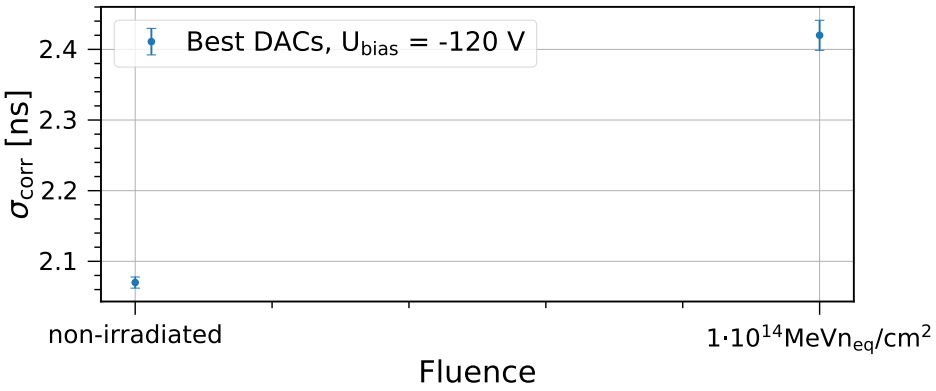


Figure 7.14: Corrected time resolution for a fluence of 1×10^{14} MeVn$_{\text{eq}}$cm^{-2} for standard and best DAC settings for standard and best bias voltage using chip biasing at a comparator threshold of 145 DAC units. The error bars indicate the statistical uncertainties on the measured value.

Finally, the results using standard and best DAC settings are compared between the non-irradiated TelePix2 and the device exposed to 1×10^{14} MeVn$_{\text{eq}}$cm^{-2} for a standard bias voltage of $U_{\text{chip}} = -120$ V. For both the same comparator threshold of 145 DAC units has been used and each sensor was cooled as much as possible.
In fig. 7.15(a) the comparison using standard DACs is presented and in fig. 7.15(b) for best DAC settings.
In both cases, the time resolution worsens for the irradiated device keeping the bias voltage fix. An explanation can be found in the effects of radiation damage. As shown in fig. 7.7, the depletion depth is enhanced with higher bulk resistivity at a constant bias of $U_{\text{chip}} = -120$ V. Assuming an effective doping concentration of $N_{eff} = 370\,\Omega$ cm, the depletion depth is approximately 65 µm. For an effective doping concentration of $N_{eff} = 1$ kΩ cm at a fluence of 1×10^{14} MeVn$_{\text{eq}}$cm^{-2}, the depletion depth increases to roughly 105 µm.
Hence, more charge can be collected. However, radiation damages affect the charge collection. Due to trapping (see section 3.3.1) the charge collection efficiency is deteriorated. To overcome this, drift times have to be reduced and charge collection times improved - achievable by increasing the bias voltage.
Nevertheless, the measured time resolution keeping the standard bias voltage fulfills the requirements of 3 ns.



(a) Standard DAC settings



(b) Best DAC settings

Figure 7.15: Comparison of corrected time resolution of TelePix2 at $U_{\text{chip}} = -120\,\text{V}$ for different fluences using (a) standard and (b) best DAC settings. A comparator threshold of 145 DAC units has been set. The error bars indicate the statistical uncertainties on the measured value.

As mentioned one goal of the repeated measurements was to measure the time resolution of TelePix2 exposed to $3 \times 10^{14}\,\mathrm{MeV n_{eq} cm^{-2}}$ which was not possible at the testbeam in December 2024. Cooling the device in the laboratory to $-40\,^{\circ}\mathrm{C}$ enabled the possibility to control the leakage current up to $\approx$ 10 to 20 µA. However, the device was still too noisy. Therefore, the time resolution could not be measured using the setup shown in fig. 7.3. Further, a non-homogeneous occupancy, presented in fig. 7.16, was observed for a measurement time of 3 min using Sr-90. Instead a horseshoe-shaped occupancy has been measured, showing low charge collection in the central part of the sensor. Pixels with very low occupancy in the central part of the sensor are masked white and noisy pixels with a occupancy larger than the maximum red.

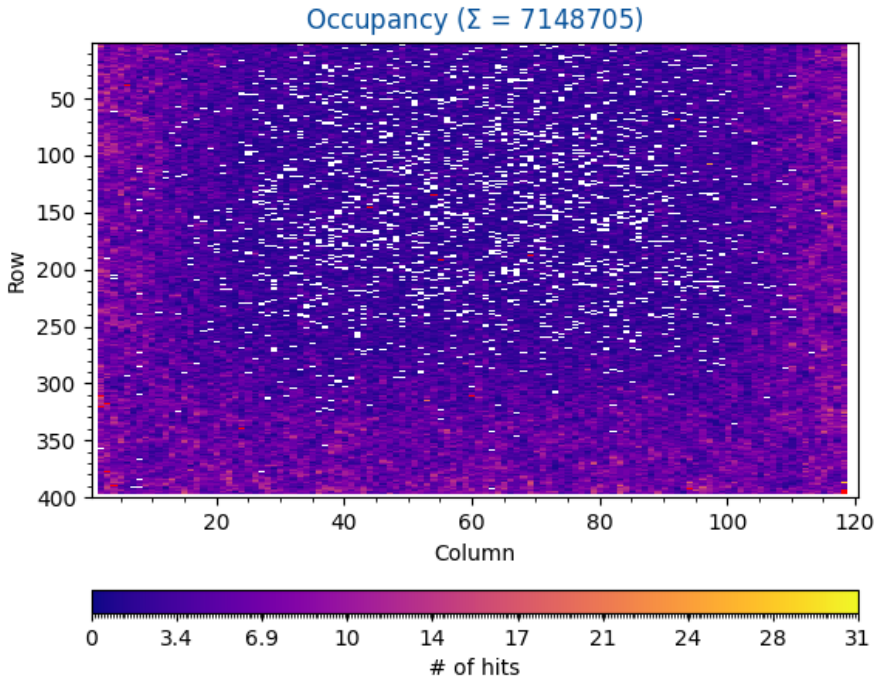


Figure 7.16: Occupancy map of TelePix2 exposed to $3 \times 10^{14}\,\mathrm{MeV n_{eq} cm^{-2}}$. Chip biasing with -150 V, a comparator threshold of 150 DAC units and a temperature of $\approx -40\,^{\circ}\mathrm{C}$ have been set.

Depending on the bias voltage, the size of the horseshoe differs. For lower bias voltages the in-efficient area increases since less charge is collected. Vice versa keeping the same voltage and increasing the temperature, results in a larger area too due to higher leakage currents and hence, less effective charge collection. A similar observation was obtained during the testbeam campaign (see fig. 9.20).
To mitigate the observed issue, the device was further cooled to approximately $-80\,^{\circ}\mathrm{C}$ by flushing the enclosure with cooled nitrogen, thereby enabling a time resolution measurement. However, the measurement is driven by the leakage. Therefore, a bias voltage of maximal

$U_{\text{chip}} = -120\,\text{V}$ was possible. With standard DAC settings and a comparator threshold of 150 DAC units, a time resolution of $\sigma_{\text{corr}} = (3.28 \pm 0.02)$ ns was obtained.
For optimized DAC settings an enhancement up to (2.58 ± 0.01) ns was measured.
Comparing the obtained results with those of the non-irradiated and up to $1{\times}10^{14}\,\text{MeV}\text{n}_{\text{eq}}\text{cm}^{-2}$ proton irradiated TelePix2 sensors in table 7.2, a worsening for the highest irradiated DUT is observed. Two effects have to be taken into account.
Firstly, a higher comparator threshold has been set to ensure a reliable performance of the DUT. As a consequence, a worse time resolution is expected. Secondly, a higher amount of bulk damage is expected, resulting in an increased charge trapping probability and change of the effective doping concentration (see fig. 7.6). Keeping the bias voltage unchanged, the time resolution is worsen due to charge trapping. Similar to the DUT irradiated to a fluence of $1 \times 10^{14}\,\text{MeV}\text{n}_{\text{eq}}\text{cm}^{-2}$, a higher bias voltage would be needed to mitigate the effect but due to the high leakage current the bias voltage cannot be increased without further cooling of the DUT.

Fluence	DACs	Bias	Threshold	Time resolution
-	Best	−130 V	142 DAC units	(2.04 ± 0.01) ns
-	Best	−120 V	145 DAC units	(2.07 ± 0.01) ns
-	Standard	−120 V	145 DAC units	(2.53 ± 0.01) ns
$1 \times 10^{14}\,\text{MeV}\text{n}_{\text{eq}}\text{cm}^{-2}$	Best	−210 V	145 DAC units	(1.97 ± 0.01) ns
$1 \times 10^{14}\,\text{MeV}\text{n}_{\text{eq}}\text{cm}^{-2}$	Best	−120 V	145 DAC units	(2.41 ± 0.02) ns
$1 \times 10^{14}\,\text{MeV}\text{n}_{\text{eq}}\text{cm}^{-2}$	Standard	−120 V	145 DAC units	(2.72 ± 0.05) ns
$3 \times 10^{14}\,\text{MeV}\text{n}_{\text{eq}}\text{cm}^{-2}$	Best	−120 V	150 DAC units	(2.58 ± 0.01) ns
$3 \times 10^{14}\,\text{MeV}\text{n}_{\text{eq}}\text{cm}^{-2}$	Standard	−120 V	150 DAC units	(3.28 ± 0.02) ns

Table 7.2: Comparison of the time resolution of a non-irradiated and proton irradiated TelePix2 sensor. Details about the DAC configuration are provided in appendix A.11.

A comparison of all conducted time resolution measurements including results obtained at the testbeam is given in section 9.4.2.

7.3 Summary

The effect of bulk damage on the p-type bulk of TelePix2 has been investigated in terms of performance measurements required to ensure the radiation tolerance of HV-MAPS for the Mighty-Pixel.
Therefore, a step-wise irradiation campaign in April and Fall of 2024 at the Bonn isochronous cyclotron was conducted exposing two devices from $1 \times 10^{12}\,\mathrm{MeVn_{eq}cm^{-2}}$ to $3{\times}10^{14}\,\mathrm{MeVn_{eq}cm^{-2}}$. The irradiation was separated into two parts due to time constraints such that the final irradiation of device 002 from $7.5 \times 10^{13}\,\mathrm{MeVn_{eq}cm^{-2}}$ to $3 \times 10^{14}\,\mathrm{MeVn_{eq}cm^{-2}}$ was done in a second step in Fall 2024. Annealing for 60 min at 80 °C has been applied to the final irradiated devices.
The performance has been studied in terms of bias behavior and time resolution. As expected the effective doping concentration changed with increasing fluence affecting the bias behavior. To ensure an optimal operation of the DUTs, an increased bias voltage using chip biasing is critical. Further, the exponential dependence between leakage current and temperature is confirmed for proton irradiated TelePix2 sensors.
Investigation of the time resolution has yielded a time resolutions of $\leq$ 3 ns keeping the standard bias voltage and DAC settings up to a fluence of $1 \times 10^{14}\,\mathrm{MeVn_{eq}cm^{-2}}$. The best possible result has been measured with a bias voltage of $U_{\mathrm{chip}} = -210$ V, comparator threshold of 145 DAC units and best DAC settings according to table 6.2 with a value of

$$\sigma = (1.97 \pm 0.01)\,\mathrm{ns} \quad (1 \times 10^{14}\,\mathrm{MeVn_{eq}cm^{-2}})$$

and the fit uncertainty of ±0.01 ns. For the DUT exposed to a fluence of $3{\times}10^{14}\,\mathrm{MeVn_{eq}cm^{-2}}$ a time resolution of

$$\sigma = (2.58 \pm 0.01)\,\mathrm{ns} \quad (3 \times 10^{14}\,\mathrm{MeVn_{eq}cm^{-2}})$$

was measured for a bias voltage of $U_{\mathrm{chip}} = -120$ V, a comparator threshold of 150 DAC units and standard DAC settings.
From the performed measurements the leakage current was found to be the critical parameter, limiting the sensor performance. If the leakage current is too high, amplifier oscillations have been observed leading to non-functionality of the device due to a high noise level. Therefore, irradiated samples have to be cooled to keep the performance comparable with non-irradiated devices. Moreover, the improved time resolution is limited by the breakdown voltage similar to the non-irradiated device. Hence, an improved bias design would increase the performance of TelePix2.
Consequently, promising results from MightyPix are expected. However, consequences for the Mighty-Pixel detector design follow from the measurements.
Firstly, the increase in bias voltage for irradiated devices has to be taken into account for

the electrical design of the detector. Further, higher bias voltages affect the minimal space between neighboring chips in terms of high voltage protection.
Secondly, the required cooling affects the overall stave design since very cold temperatures are necessary for central sensors. However, no statement about the operation temperature can be done yet since TelePix2 intrinsic power consumption is higher than anticipated for MightyPix. But a trend towards operation temperatures between 0 to $-10\,^{\circ}\mathrm{C}$ is expected. Confirmed are those by measurements conducted with ATLASPix3.0(1), publicized in [9]. Consequently, temperature dependent measurements of MightyPix will be part of its single-chip testing phase. In addition, irradiation campaigns including SEUs, powered and biased proton irradiations are planned.

CHAPTER 8

Characterization of Surface Damage on HV-MAPS

Probing the radiation tolerance of HV-MAPS involves the investigation of surface damage effects. For the Mighty-Pixel a radiation tolerance in terms of TID damage of up to 40 MRad (see chapter 6) is required. Studying the effect of surface damage on the performance of the sensor has been done at multiple irradiation campaigns using the Run2021 and TelePix2 sensors as DUTs.
For both sensor variations the irradiation campaigns were carried out at the x-ray tube at the FTD in Bonn.
Main goals are studying the performance after irradiation and investigation of the sensor behavior during the irradiation itself. Because surface damage or colloquially known as TID damage is expected to affect mostly the transistor behavior, a change of their working points and the power consumption is expected. A maximal effect is expected to occur on the order of 1 MRad (see section 3.3.2).
Low and high voltage currents have been monitored during all campaigns to probe the radiation tolerance. Additionally, a step-wise irradiation approach - similar to the proton irradiation campaigns - was chosen to study the devices, irradiated to different levels, and to understand how the damage affects the performance.
Investigation of the performance was conducted by threshold scans, bias performance studies and time resolution measurements. However, for each campaign the measurement program was slightly adapted depending on the aspects in focus. In section 8.2 each campaign and set of measurements to accomplish the corresponding goals are discussed.
Monitoring of the currents was not only done to study the effect of surface damage on the power consumption but also with regard to the Mighty-Pixel design - since a change in the power budget during operation time heavily affects the overall detector design. Hence, it is crucial to know how the power consumption changes with irradiation and thus, operation time.
Before the irradiation procedure is discussed in section 8.3, the experimental setup is

introduced in section 8.1. The discussion of the derived results in section 8.4 is split into discussing the bias behavior, low voltage power consumption, time resolution, threshold dispersion and annealing studies. The specific sensor used for each measurement is explicitly stated in the corresponding sections.
All presented studies within this section have been done for the first time for HV-MAPS designed at KIT and produced in the 180 nm TSI process. Therefore, no comparisons with similar measurements can be done. Nevertheless, expectations from theory will be embedded into the discussion of the results.

8.1 Experimental Setup

The x-ray irradiation campaign was conducted using the in-house x-ray cabinet at the FTD Bonn [13]. In the following the working principle is described:
Due to heating of the cathode electrons are thermally released and accelerated towards the anode by an electric field - caused by a high voltage bias. At the anode most of the electron's energy is lost by thermal emission. But, a fraction is converted into x-rays - used to irradiate devices.
The available x-ray tube can be operated between 2 to 60 kV with a current between 2 to 58 mA [147]. As anode material tungsten is used and beryllium at the exit windows of the x-ray tube. The beam is collimated and low-energy photons are filtered by a 150 µm [13] Aluminum filter.
A side view of the x-ray cabinet housing the x-ray tube (located in the top right) and the DUT enclosure box is shown in fig. 8.1. The DUT is placed below the center of the beam spot. To align the horizontal position, two alignment lasers are available. Depending on the target dose rate, the height has to be adjusted. Therefore, a calibration is done before the start of the irradiation using a PIN-diode [148]. The diode itself was calibrated at CERN to obtain the expected dose rate as a function of the tube current [147]. A linear relation was determined. Therefore, the calibrated PIN-diode was used to evaluate the required distance between the x-ray tube and the DUT in order to obtain the target dose rate.

In fig. 8.2 an example calibration measurement at a height of 25 cm measured with 40 kV and 50 mA tube current is presented. A peak dose rate of 474 kRad h^{-1} at the red marked position is expected. Overall the calibration was done for an area of 40 x 40mm^2 to ensure a homogeneous dose rate over the complete TelePix2 area of 20.015 x 13.130 mm^2. By the corresponding projections of both dimensions an overall homogeneous area can be identified. However, a lower rate is expected in the left half of the calibration window. Consequently, the device has been positioned such that it is exposed homogeneously.
Since two main different dose rates have been used for TelePix2 and Run2021, two different heights were chosen. However, both devices were positioned with the periphery and wire bonds pointing towards the center of the calibration window such that the active pixel matrix is irradiated homogeneously.

Both devices (TelePix2 and the Run2021 sensor) were mounted on top of an aluminum

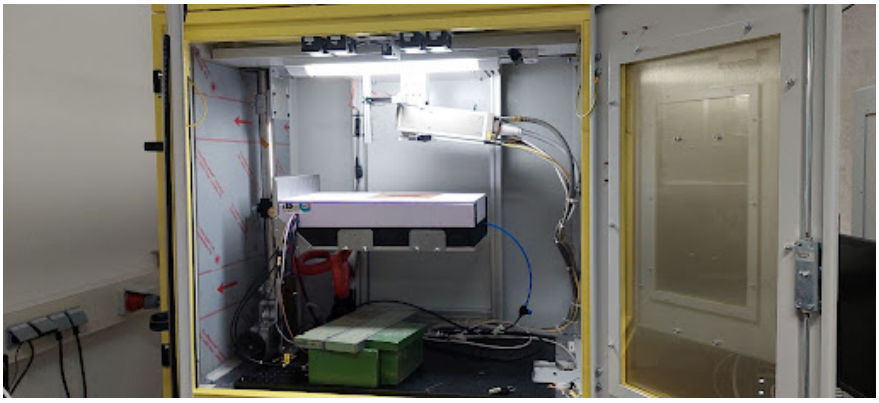


Figure 8.1: Side view of the x-ray cabinet. The DUT is placed inside the pink styrofoam box on top of an aluminum block to cool the PCB from the bottom side.

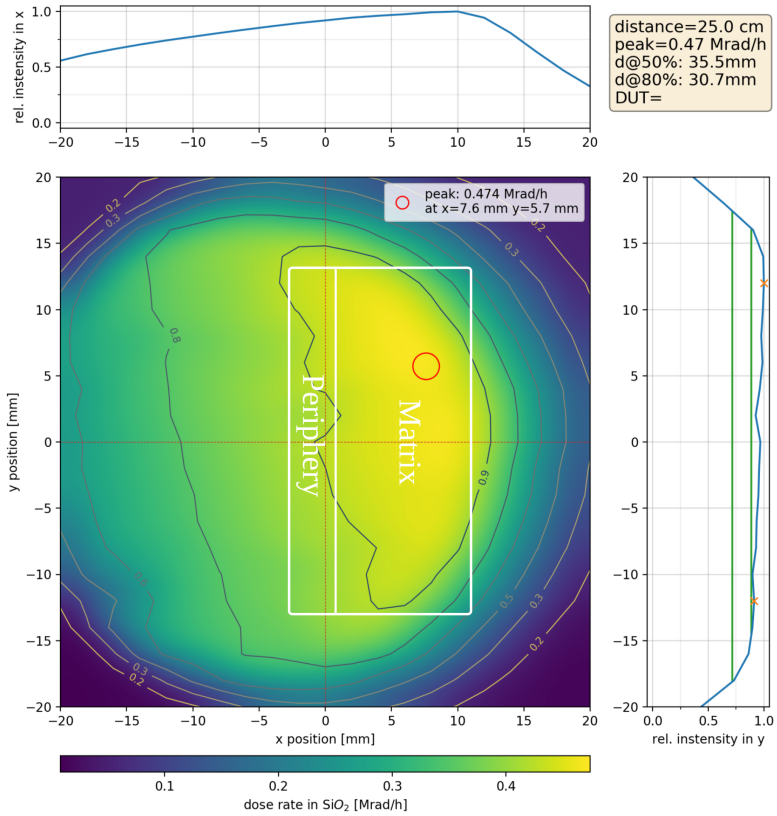


Figure 8.2: Calibration measurement for the TelePix2 irradiation campaign. The calibration diode was positioned at a height of 25 cm. Projections of the intensity in x, y-dimensions are displayed. A peak rate of 474 kRad h^{-1} at the red marked position is expected. The position of TelePix2 is indicated.

water block and placed inside a styrofoam enclosure. From the measurement point of view, no cooling of the devices is required. Nevertheless, the DUT will probably be operated at temperatures of 0 to $-10\,^{\circ}$C at the Mighty-Pixel. Therefore, the operation temperature during irradiation was set to $-10\,^{\circ}$C, measured on the PCB, to stick close to the experiment's environmental conditions. Further, the enclosure was flushed with nitrogen to prevent condensation.
A remark on the temperature has to be made here. Since TelePix2 self-heating (explained in section 4.2.4), the DUT temperature itself was higher than $-10\,^{\circ}$C. Colder temperatures are not possible with the available setup. One way to improve the cooling would be to exchange the available cooling setup with the one presented in fig. 5.4. However, this has not been done but should be considered for future measurements.
An exemplary picture of the Run2021 sensor mounted on the aluminum block inside the enclosure is depicted in fig. 8.3. For the irradiation of TelePix2 the setup looked comparable.

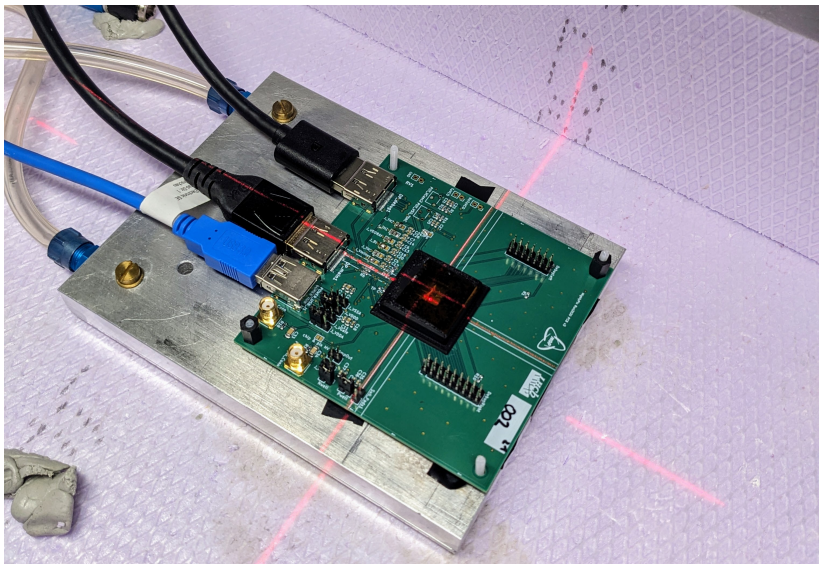


Figure 8.3: Top view of the Run2021 sensor - mounted on top of an aluminum water block to cool the DUT from the bottom side - positioned inside an enclosure box.

To prevent sensitive electronics, e.g. FPGAs, for radiation damage, the x-ray cabinet offers a cable tunnel, allowing electronic devices to be placed outside. During the campaign MARS's flexible design allowed cables to be fed through the cable tunnel such that the DAQ system was positioned outside. In addition, the power supplies were also placed outside.

8.2 Irradiation Campaigns

In total four x-ray irradiation campaigns were conducted: Two with TelePix2 and two with the Run2021 sensor. To explain the reasons and configurations for each, the historical evolution from the first to the last campaign is explained in the following. A comprehensive summary of all with the goal of each and performed measurements is given in table 8.1 and table 8.2. For all, a PCB temperature of $-10\,^{\circ}\mathrm{C}$ was set.

#	DUT	When	Goal	Final Dose
1	TelePix2	July 2024	Emulate TID damage and first look into TID	40 MRad
2	TelePix2	November 2024	Deeper investigations for more realistic DUT settings	40 MRad
3	Run2021	December 2024	Investigation of DAC behavior	40 MRad
4	Run2021	May 2025	Slow rate with detailed DAC behavior investigation	1.05 MRad

Table 8.1: Summary of all x-ray irradiations done within this thesis.

#	Rate	Measurements	Settings
1	$474\,\mathrm{kRad\,h^{-1}}$	Power consumption, bias behavior	Fully operational, adjusted bias
2	$474\,\mathrm{kRad\,h^{-1}}$	Power consumption, bias behavior, z-curves, time resolution	No amplifier, no comparator & timestamp clock bias, max threshold & VMinus, reduced bias
3	$474\,\mathrm{kRad\,h^{-1}}$	Power consumption, z-curves, DAC behavior	No amplifier & comparator bias, max threshold & VMinus, no bias
4	$6\,\mathrm{kRad\,h^{-1}}$	Power consumption, bias behavior, threshold dispersion, DAC behavior, annealing	Max threshold & VMinus, reduced bias

Table 8.2: Summary of all settings during the x-ray irradiations performed in this thesis.

The first step-wise x-ray irradiation campaign has been performed with the TelePix2 sensor as the DUT in July 2024 with the goal to get a first impression on the effect of TID on the technology of HV-MAPS foreseen for the Mighty-Pixel. Therefore, the target dose is 40 MRad as expected for the innermost pixels at the Mighty-Pixel. Due to time constraints

concerning the availability of the x-ray tube and the goal to mimic the expected dose in a reasonable amount of time, a high dose rate of 474 kRad h^{-1} was chosen. However, the expected TID rate for the innermost sensors at the Mighty-Pixel is $\approx$ 1 kRad h^{-1} [1] [146].
Because no x-ray irradiation with those type of HV-MAPS produced in a 180 nm process was done before, no references and information about optimal sensor settings during irradiation itself are available. Hence, it was chosen to keep the standard settings and bias the DUT to its nominal voltage of $U_{\text{chip}} = -120$ V.
However, the bias voltage had to be adjusted over the irradiation campaign at higher dose levels since high leakage currents occurred and the breakdown happened earlier. Between each irradiation step the bias behavior was studied by IV- and VV-curves. In addition, analog studies of the amplifier and comparator outputs were carried out, and the power consumption of both the high- and low-voltage supplies was monitored. However, further studies with the final irradiated device could not be performed because the DUT was damaged after irradiation.
Consequently, a second irradiation of another TelePix2 sensor has been carried out in November 2024 to investigate the effect of surface damage in more detail with incorporation of lessons learned from the first campaign. Similar to the first, a high rate of 474 kRad h^{-1} was chosen. Since high leakage currents and a too high power consumption during the first irradiation have been observed (see appendix A.9), the DUT was operated with an unbiased amplifier and comparator to prevent uncontrolled currents. Further, the comparator threshold and VMinus have been set to their maximum level to avoid currents between the analog and digital part of the device. Besides preventing unwanted currents, this operation mode of the amplifier and comparator is closer to the real operation conditions of the Mighty-Pixel, as the chosen rate is approximately 474 times higher than the expected LHCb peak TID rate of 1 kRad h^{-1}. In addition, the timestamp clock was turned off during the irradiation to reduce the power consumption and hence, self-heating - resulting in a lower DUT temperature. The bias voltage was reduced to -80 V due to the observed shift of the breakdown from the first irradiation campaign.
Investigation of the damage was done by monitoring the low and high voltage power consumption and studying the bias behavior and threshold dispersion. In addition, the time resolution was measured after the last iteration step. To investigate the DUT performance further, the device was taken to a testbeam campaign (see chapter 9). A detailed discussion of the results obtained by this irradiation campaign will be given in section 8.4.
Since TelePix2 large heat dissipation and an obtained increase in the threshold dispersion as well as a softening of the slope of the z-curve, a third x-ray irradiation campaign has been done in November/December 2024 - but with the Run2021 sensor. Main focus was on the power consumption and DAC behavior. Because the Run2021 sensor offers the possibility to access on-chip transistor voltages via so-called *Debug Outputs*, it is possible to measure the change of the transistor voltage for a given DAC setting. Therefore, the DAC measurement

[1] Assuming an accumulation of 40 MRad over a run time of 5 yr results in a dose rate of approximately 1 kRad h^{-1}. The simple calculation does not include run stops and times without beam.

was performed at each irradiation step. The chosen DUT could not be biased due to an issue with the biasing for this specific sensor. Hence, it was assumed that only the surface of the DUT was damaged and not the bulk. Measurement of the DACs was done by the Bachelor student L. Ernst [2]. Unfortunately, the monitored power consumption got lost due to technical difficulties. Therefore, no results will be discussed.
Because of the mentioned issues another irradiation with the Run2021 sensor was carried out in May 2025. Again the DAC measurement was repeated at each irradiation step. Obtained results and the measurement setup are presented in the Bachelor thesis of M. Liebetrau [14]. Besides previous campaigns, the chip configuration and irradiation environment was chosen to be as close as possible to the experiment. Hence, a low irradiation rate of $6\,\mathrm{kRad\,h^{-1}}$ (Six times higher than the Mighty-Pixel peak rate), a temperature of $-10\,^{\circ}\mathrm{C}$ and an operational DUT were used, whereby the comparator threshold and VMinus were set to their maximum value of 1.8 V to protect the DUT of the constant amplifier output due to the high particle rate. Further, the irradiation was only done up to a dose of 1.05 MRad since the typical TID peak, observable in the power consumption, is known to occur in that order of magnitude. The question to be answered by stopping there was how the DUT will anneal other time. To summarize, the fourth irradiation had the following goals: An irradiation close to the experimental environment with a slow x-ray rate, investigation of the DAC behavior during the irradiation and after a certain time of annealing, measuring the power consumption during the irradiation and over the full annealing time, measurement of the threshold dispersion before and after tuning, investigation of the bias behavior and studying the annealing and its effect on the DUT performance.

Main focus are on the second high rate TelePix2 and low rate Run2021 irradiation. The results obtained by those will be discussed in section 8.4. From both, the overall goal - besides investigating the effect of surface damage on the performance of HV-MAPS - is to give an estimation on the expected power budget for the Mighty-Pixel and guidance on what to consider for the detector design to ensure a stable detector performance.

[2] By the time writing the thesis the Bachelor thesis is not finished and hence, no reference is given here.

8.3 Irradiation Plan

For all irradiation campaigns a step-wise approach was chosen to enable the possibility of measurements at each dose level to investigate the effect of surface damage in more detail. An example irradiation plan used for both TelePix2 irradiations is shown in table 8.3. Similar, the first irradiation of the Run2021 was set up. For the low rate Run2021 irradiation the steps are quite similar but the irradiation was stopped at 1.05 MRad to study the annealing behavior.
Since the effect of TID damage is expected to have maximum at $\approx$ 1 MRad in the power consumption, a logarithmic step-size was chosen to get denser data points at low dose levels. Measurements were conducted between each step to investigate the effect of surface damage on the DUT's performance. Before the start of the first measurement at least 20 to 30 min were allotted to allow for electrical annealing to not disturb the measurements by short-time annealing effects. However, the waiting time was chosen arbitrary since no references are available. It was observed that longer annealing times, especially at higher dose levels, would have been beneficial. But due to time constraints it was not reasonable.

Step	Total dose [kRad]
0	0
1	3
2	20
3	50
4	100
5	300
6	600
7	1000
8	2500
9	5000
10	7500
11	10000
12	15000
13	25000
14	40000

Table 8.3: Summary of all dose levels the TelePix2 has been irradiated to.

8.4 Results

As mentioned in section 8.2 the overall goal of all conducted TID studies with respect to the Mighty-Pixel project is to investigate the effect of surface damage on the performance of HV-MAPS. Consequently, the bias behavior (see section 8.4.1) and time resolution (see section 8.4.5) have been studied for the TelePix2 and Run2021 sensor. Further, it is crucial to know the expected power consumption of the sensors over their full run-time since the detector design depends on it. Because a change in the power consumption - depending on the transistor design and dose level - is expected, the power consumption during the irradiation campaigns has been investigated for both devices (see section 8.4.2).
A shift of the working points of damaged transistors in the chip electronics is expected from the theory of TID (see section 3.3.2). As a consequence, a change of the threshold dispersion and overall amplifier and comparator behavior might occur. Hence, the threshold dispersion was measured with and without tuning of the sensor matrix during the irradiation campaign of the Run2021 sensor (see section 8.4.6). To further investigate the effect of surface damage on transistor level, the behavior of on-chip DACs for the Run2021 sensors was studied within the Bachelor thesis of M. Liebetrau [14]. A comprehensive summary is given in section 8.4.7. More details are provided in [14].
Besides measurements executed during the irradiation campaign, the annealing behavior of the low rate irradiated Run2021 sensor was studied. In contrast to the well-known annealing behavior of bulk damaged sensors (see section 3.3.1), annealing of surface damaged sensors is not well understood. Among others, a main reason is the difference between the various manufacturing processes and chip designs. However, the goal of the annealing studies is to understand if the observed changes in performance are reversible and if so, how long it takes (see section 8.4.3).
Moreover, an attempt to determine the annealing rate of the power consumption was made. Together with the measured power consumption during the irradiation for the Run2021 and TelePix2 sensor, a first estimation of the expected power consumption of the Mighty-Pixel for Run 5 and Run 6 has been derived (see section 8.4.4). Simulations leading to those results have been developed by M. Liebtrau [14].

8.4.1 Bias Behavior

At first, the bias behavior of the TelePix2 sensor is discussed. After each irradiation step IV- and VV-curves have been measured using the chip bias contact. Both measurements are presented in fig. 8.4 and fig. 8.5.

The measurements have been performed after a waiting time of at least 20 to 30 min at the same environmental conditions as during the irradiation. The only difference is the change of the DUT configuration from its irradiation state (see table 8.2) to its nominal operating mode, in order to investigate the performance under standard conditions.
In fig. 8.4 a change in the breakdown and overall IV-curve shape with increasing dose level is observed. Firstly, with increasing dose level the breakdown occurs earlier. Secondly, the

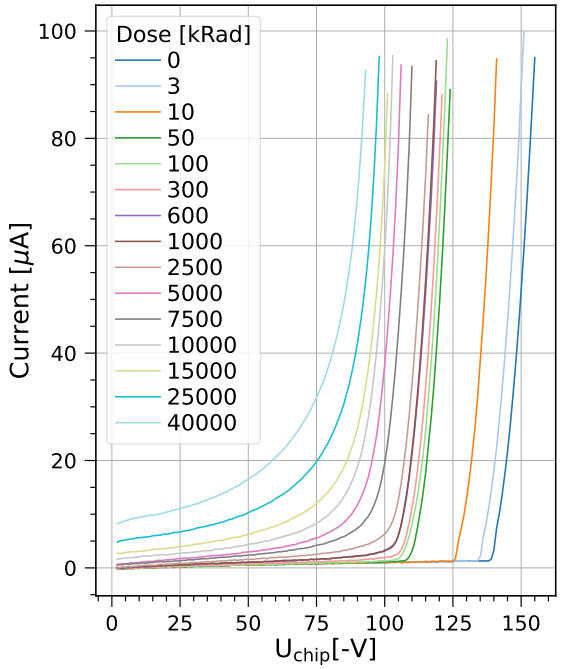


Figure 8.4: IV-curves measured after each irradiation step for TelePix2 after a minimum annealing time using chip biasing.

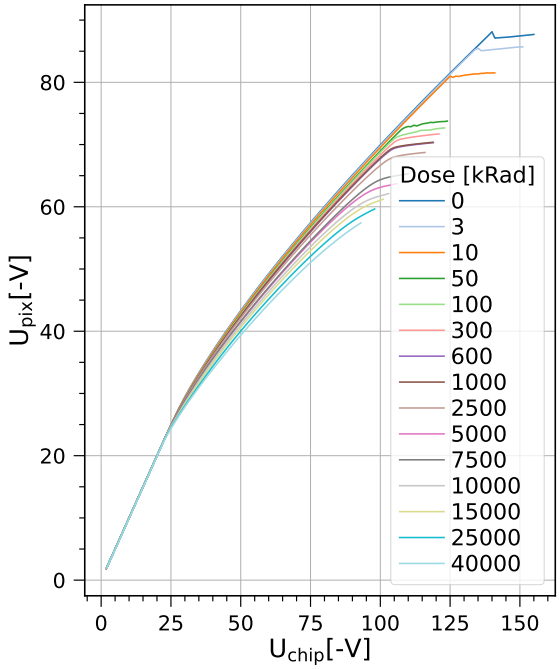


Figure 8.5: VV-curves measured after each irradiation step for TelePix2 after a minimum annealing time using chip biasing.

overall leakage current and hence, noise level increases. And thirdly, the breakdown does not show a sharp rise in the leakage current as expected for an avalanche breakdown but a softening of the slope.
From theory an effect on ASIC electronics, mostly transistors, is expected and not on the sensor bulk. However, the measurements shows a correlation between both. Two things have to be kept in mind to understand the observation:
Firstly, most TID studies have been performed on transistor level or for pure readout ASICs of hybrid sensors. But TelePix2 is a complex, monolithic device. Consequently, its bulk and surface cannot be disentangled as easily and effects in each can influence the other.
Secondly, TID changes the amount and type of traps in the SiO_2-Si interface and the Si-bulk itself. As a consequence, the movement of free charge carriers in the bulk is affected.
A preliminary hypothesis is proposed: Positively charged traps (interface and oxide traps (see section 3.3.2) attract free electrons close to the SiO_2-Si interface region - resulting in a conductive electron layer [3]. Therefore, the electric field around the p-stop pixel implant is changed such that the breakdown happens earlier due to the field change and softer due to trapping of charge carrier. The higher leakage current can be explained by the conductive electron layer and overall higher amount of charge carriers, too.

[3] A comparable TCAD simulation demonstrating the effect of electron accumulation in HV-MAPS is presented in [112]

In contrast to bulk damaged sensors (see fig. 7.5), no significant change in the correlation between chip and pixel bias is observed from the VV-measurements depicted in fig. 8.5. Due to the overall increased leakage current and possible change of the electric field caused by the electron layer, the earlier breakdown with increasing dose level is observed in the measurement. In addition, the higher leakage current affecting the pixel-chip correlation slightly.

To visualize the shift in the breakdown better, a summary of the breakdown versus dose level is illustrated in fig. 8.6 for pixel biasing (colored in gray) and chip biasing (colored in blue). The most drastic change occurs between 0 to 1 MRad which is consistent with the expectation of the TID theory.
At higher dose levels the calculation of the breakdown is due to the softening not accurate and mostly dominated by the increased leakage current.
Further, one data point for pixel biasing at a low dose shows a breakdown at 0 V because of a technical difficulty not spotted during the irradiation. Therefore, the data point is not considered further.

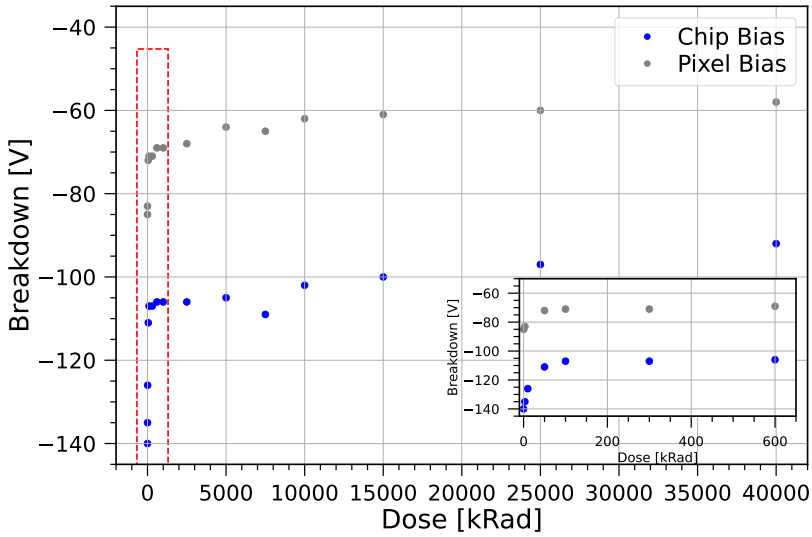


Figure 8.6: Summary of determined breakdowns versus dose for chip (colored in blue) and pixel (colored in gray) biasing. The uncertainty of the breakdown is primarily determined by the measurement procedure and estimated as $\Delta U = \pm 2$ V.

Since the measurements have been conducted shortly after each irradiation step, the IV- and VV-measurement have been repeated seven months after the irradiation to investigate an annealing effect on the bias behavior and to compare the result with a non-irradiated and proton irradiated TelePix2 sensor. In addition, a back-shift of the breakdown towards its initial value after two months was observed at the testbeam campaign such that a further shift due to the longer annealing time is expected.
In fig. 8.7, a clear difference in the breakdown voltage is observed between the TelePix2 sensor

exposed to 40 MRad - measured seven months after irradiation - and an undamaged sensor. However, the leakage current is at its initial level compared to the measurement displayed in fig. 8.4. Comparing the results with the proton irradiated samples a large dispersion between the radiation types is observed - supporting that TID damage affects mostly the chip electronics and NIEL damages its bulk. Further, the comparison of the VV-curves in fig. 8.8 emphasizes this thesis since the correlation between chip and pixel biasing which is given by the bulk is not significantly changed by TID damage.
However, a remaining question is what happens under more experiment-like conditions where the DUT is powered and biased during irradiation. Therefore, one next step of the radiation tolerance research of HV-MAPS is to perform a powered and biased proton irradiation at a low beam current. Due to time reasons and constraints on available DUTs it is not done within this thesis but planned for the future at the Bonn cyclotron.

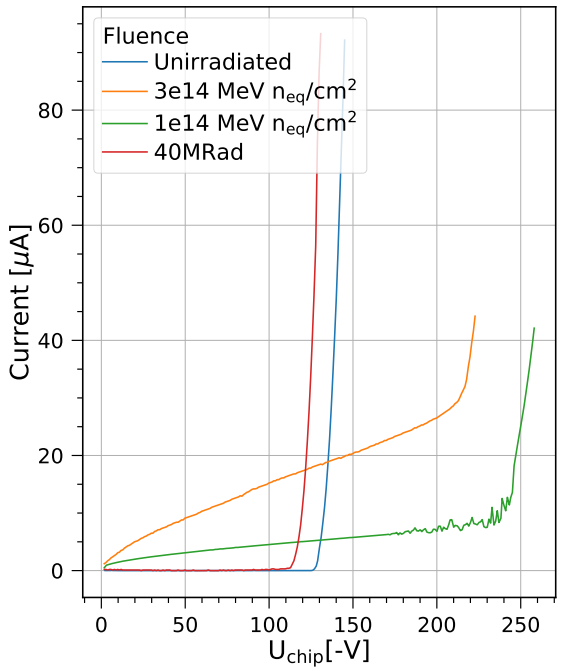


Figure 8.7: Comparison of IV-curves for different irradiation types and doses obtained with TelePix2 conducted at low temperatures. In fig. 7.9 the measurement without the surface damaged DUT is presented.

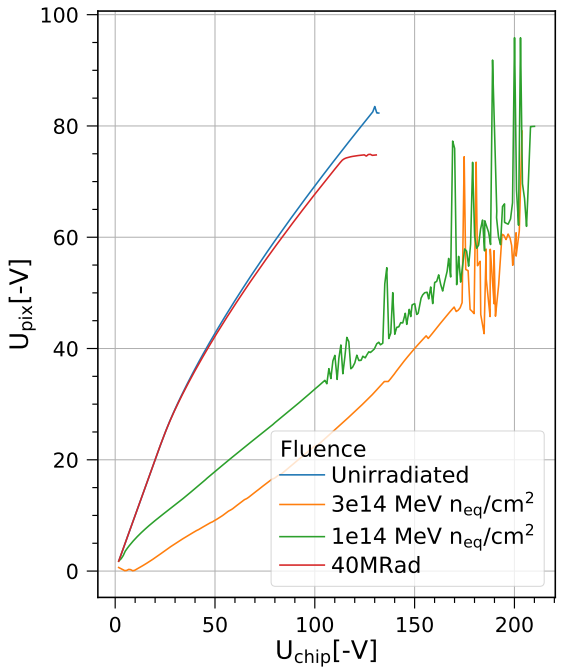


Figure 8.8: Comparison of VV-curves for different irradiation types and doses obtained with TelePix2 at low temperatures. In fig. 7.10 the measurement without the surface damaged DUT is presented.

Run2021

Secondly, the bias behavior of the low rate irradiated Run2021 sensor is discussed. Main goal of the measurements is to validate the results obtained with TelePix2 and observe a possible TID rate dependence. In fig. 8.9 the results of the IV-measurements executed after each irradiation step and in fig. 8.10 the VV-curves using chip biasing are presented.
Similar to the TelePix2 measurements, the DUT was configured to its standard operation mode for the measurements and the environmental conditions kept stable.
Independent of the irradiation rate ($6\,\mathrm{kRad\,h^{-1}}$ for the Run2021 and $474\,\mathrm{kRad\,h^{-1}}$ for the TelePix2 sensor) the same bias behavior is observed. With increasing dose level the breakdown occurs earlier and the slope softens [4]. However, the overall noise level is lower, keeping the smaller DUT size into account. A possible increase of the leakage current for higher dose levels cannot be confirmed with this irradiation campaign since the maximal dose level is 1.05 MRad.
Similar to TelePix2, the pixel-chip correlation is not changed by TID as shown in fig. 8.10. For both measurements fluctuations are observed. In case of the IV-curves, the leakage current fluctuations increase with increasing dose - expected due to a higher noise level caused by moving charge carriers. In contrast to the measurements obtained with TelePix2 (see fig. 8.4), a more precise power supply has been used. Therefore, small fluctuations on the order of $\mathcal{O}(\pm 0.5\,\mu\mathrm{A})$ are recorded. As shown previously (see section 6.3.1), fluctuations of the monitored voltage, visible in fig. 8.10, occur in the breakdown regime. A possible explanation is the increased leakage current in that region affecting the monitored voltage (see appendix A.5 for more details).

To conclude, the Run2021 bias behavior confirmed the measurements obtained with TelePix2 in terms of IV- and VV-measurements regardless of the irradiation rate. As a consequence, it is crucial to investigate surface damage with MightyPix2 with respect to the bias behavior in more detail since a change of the breakdown effects the sensor performance. Furthermore, more temperature dependent studies are mandatory because the leakage is heavily temperature dependent as shown in fig. 7.11. Therefore, similar studies with MightyPix2 at its operational temperatures are foreseen.

[4] Since the breakdown behavior is similar to TelePix2, the breakdown voltages are not extracted as in fig. 8.6.

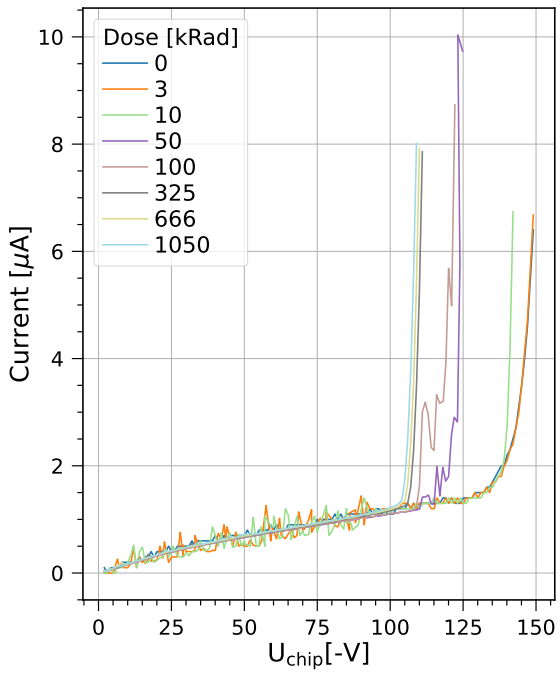


Figure 8.9: IV-curves measured after each irradiation step for Run2021 after a minium time of annealing (O(10 to 20 min)) using chip biasing.

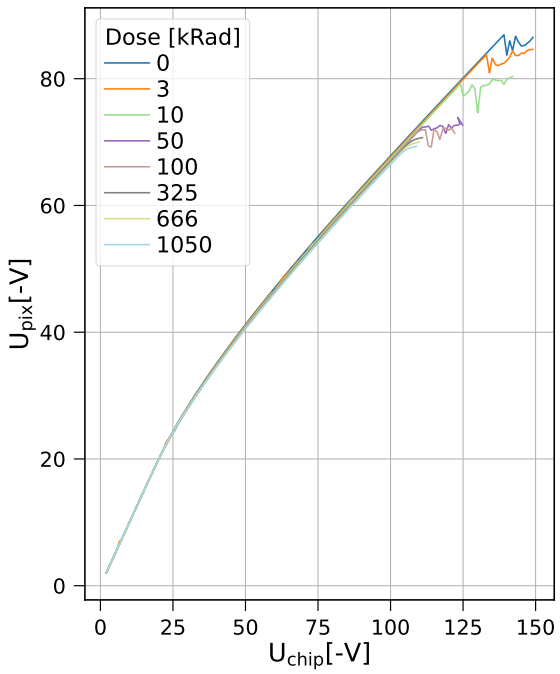


Figure 8.10: VV-curves measured after each irradiation step for Run2021 after a minium time of annealing (O(10 to 20 min)) using chip biasing.

8.4.2 Low Voltage Power Consumption

Besides the bias behavior, the power consumption was investigated for both sensors. From the theory of TID damage (see section 3.3.2 for more details) a change of the power consumption depending on the transistor flavor (NMOS, PMOS) is expected because of the formed interface and oxide traps. For NMOS transistors a re-bound structure with a peak in the power consumption around 1 MRad is expected due to a fast formation of positively charged oxide traps and slow formation of negatively charged interface traps which counteract each other. For PMOS transistors both kind of traps are positively charged, leading to a monotonic decrease in the power consumption.
However, the investigated devices are built of both transistor types and single transistor currents cannot be measured. The only way to obtain information is to measure the currents in the digital (VDDD) and analog (VDDA) power domain. But a change in each would have consequences on the planned serial power scheme and detector design.
Investigation of a possible change with irradiation was done by recording the current over the full irradiation campaign. A dependence of the power consumption on the irradiation settings is expected. Two crucial parameters are: (1) Temperature, and (2) irradiation rate.
As stated in section 8.2, a temperature of $-10\,^{\circ}$C was chosen in order to meet the MightyPixel environmental conditions. However, a higher temperature during irradiation would beneficially affect the power consumption, as more annealing would occur (see section 3.3.2).

A high irradiation rate is expected to increase the number of traps, thereby impacting the power consumption. Since high currents during the irradiation are expected for the chosen rate, the current for the measurement, presented in fig. 8.11, was obtained shortly before the next irradiation started, while the DUT was set to its standard configuration mode and biased. To show the change in the low voltage current, a normalization of each power domain to its initial value before irradiation is applied.

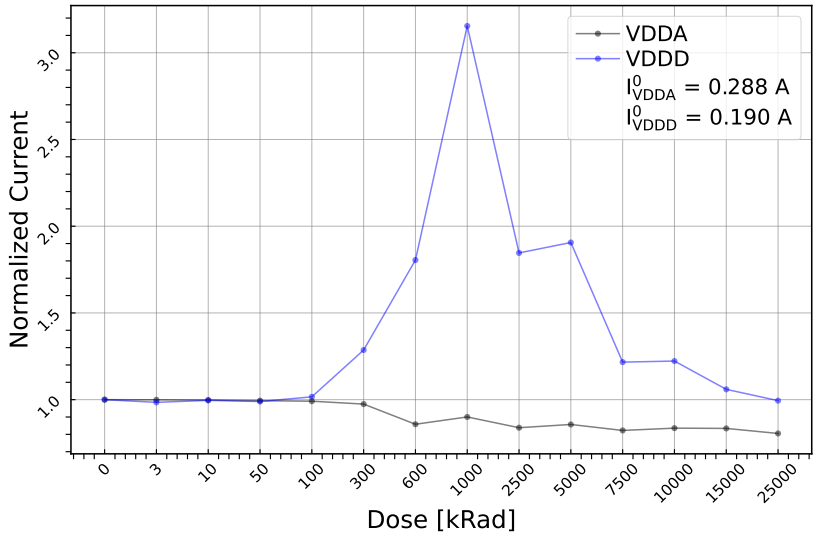


Figure 8.11: Normalized current versus doses separated in digital (colored in blue) and analog (colored in gray) part for TelePix2. The normalization to the current obtained at 0 kRad is given in the legend.

For TelePix2 a re-bound structure in the digital part is observed while the analog current decreases with increasing dose level. At a first glance the digital behavior seems to be dominated by NMOS while the analog by PMOS transistors. But during the irradiation the analog transistors (amplifier and comparator) were not powered to avoid damage of the electronics. Since TID occurs if the transistors are powered, less damage changing the power consumption was done during irradiation. Evidence to support this theory comes from the first TelePix2 irradiation campaign. In appendix A.9 the corresponding low voltage measurement is presented where a similar shape of the digital and analog voltage behavior is observed.
Further evidence is given by the low rate irradiation of the Run2021 sensor presented in fig. 8.12. Between 600 to 1 000 kRad a re-bound shape of the normalized current is observed for both voltage domains.
Besides the change in the power consumption obtained with TelePix2, the drastic increase - up to 3 times the initial value - is major and not tolerable in the experiment (see section 2.4). Because of TelePix2 high power consumption and design flaw, it is not clear if the effect is DUT specific. Additionally, a high irradiation rate was chosen which has an effect on the trap generation rate. Hence, one aspect investigated at the low rate irradiation, using the

Run2021 sensor, was to measure the current at a more reasonable rate. As visible in fig. 8.12 a maximum increase of the initial current of up to 30 % is measured in the digital domain.

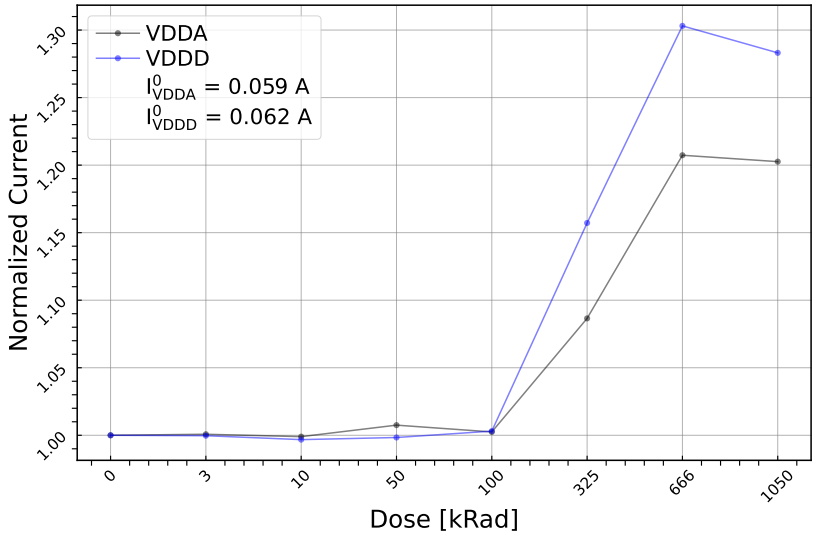


Figure 8.12: Normalized current versus doses separated in digital (colored in blue) and analog (colored in gray) part for Run2021. The normalization to the current obtained at 0 kRad is given in the legend.

Comparing both measurements with each other a clear rate dependence is visible. Therefore, the question is: Which current is expected at the maximum Mighty-Pixel peak rate of 1 kRad h^{-1}?
However, the peak rate is only expected for the innermost devices from the radiation damage simulation. Hence, a lower rate towards the outer modules is anticipated. From both measurements a reduced peak current following the decreasing rate can be assumed. To estimate the expected current in dependence of the TID rate, two things have to be simulated. Firstly, the expected TID rate in dependence on the Mighty-Pixel design and integrated luminosity and secondly, a current-TID rate dependence including annealing is mandatory. The first is done by simulations based on the LHCb `Fluka` simulation [149] and the Mighty-Pixel module description [150]. For the latter, the presented measurements obtained with the Run2021 and TelePix2 sensors as well as the annealing study presented in section 8.4.3 have to be used. For both - irradiation and annealing - the temperature is a crucial parameter, which has to be taken into account. The procedure and results are discussed in section 8.4.4. Before a dedicated annealing study is discussed, a short discussion on the annealing included within both irradiation campaigns is done:
TID annealing occurs whenever the transistors are powered or heated (see section 3.3.2). Hence, a certain fraction of annealing happens already during the irradiation and the measurements. In the later experiment a comparable situation exists, such that the low rate irradiation emulates a reasonable scenario. In addition, there will be technical stops and times without any beam at the LHCb experiment where the MightyPix sensors can electrically anneal as long as they are powered. However, this might not be possible at the experiment.

Due to the measurements in-between each irradiation step during the performed campaigns the scenario is emulated as well. However, a detailed study of the annealing behavior is crucial because for some sensors, especially those positioned at the outer Mighty-Pixel modules, the annealing will dominate over the TID damage because of the low dose rate.

8.4.3 Run2021 - Annealing Studies

As mentioned in the previous section, a dedicated annealing study of the Run2021 sensor after the last irradiation step to 1.05 MRad was carried out. Besides the attempt to determine an annealing rate, the overall annealing behavior was in focus of the investigation.
Therefore, the DUT was operated at stable environmental conditions of $T = -10\,^{\circ}\mathrm{C}$ and constant humidity over a long time period. The power consumption has been monitored over the full measurement time and performance measurements including the bias behavior and threshold dispersion have been performed on regular basis. Moreover, the on-chip DAC behavior was measured. In section 8.4.7 those results and in section 8.4.6 the threshold dispersion is discussed in more detail. Within this section the focus is on the power consumption and bias measurements.
The measurement of the normalized current versus annealing with a normalization to the current before annealing is presented in fig. 8.13. For both voltage domains a slow decrease of the power consumption towards its initial value is observed. After $\approx 4\,\mathrm{d}$ the DUT was transported to the laboratory and hence, turned off and on again - resulting in a drop in its power consumption which recovered within 2 d. Deeper investigations are needed to understand the observation.
After 30 d the digital power consumption is still 10% higher compared to its pre-irradiation state.

In a similar manner, an annealing study of the bias behavior was carried out. Therefore, IV-curves using chip biasing were measured on regular basis. Figure 8.14 shows the obtained measurements over the full annealing period up to the point this thesis is written. A slow shift of the breakdown towards its initial value of $\approx -140\,\mathrm{V}$ is observed. However, after one month of annealing the breakdown is still below $-120\,\mathrm{V}$ - comparable with the observations from TelePix2 where the breakdown after more than six months after irradiation is still lower than before irradiation.
Furthermore, the assumption of trapped charge carriers, that have changed the electric field and are only released slowly again, aligns with this observation.
Consideration of the observations is crucial for the Mighty-Pixel design and operation because a change in the bias voltage affects the sensor performance. Since not all sensors will experience the same change at the same time due to a position dependent TID, the bias scheme foreseen for the Mighty-Pixel has to cope with this. Nevertheless, a proton irradiation campaign with a powered and biased DUT combining NIEL and TID is missing to give a more accurate estimation of the breakdown shift in the Mighty-Pixel. Moreover, the measurement has to be repeated with MightyPix2 because the surface damage depends on the foundry and transistor implementations.

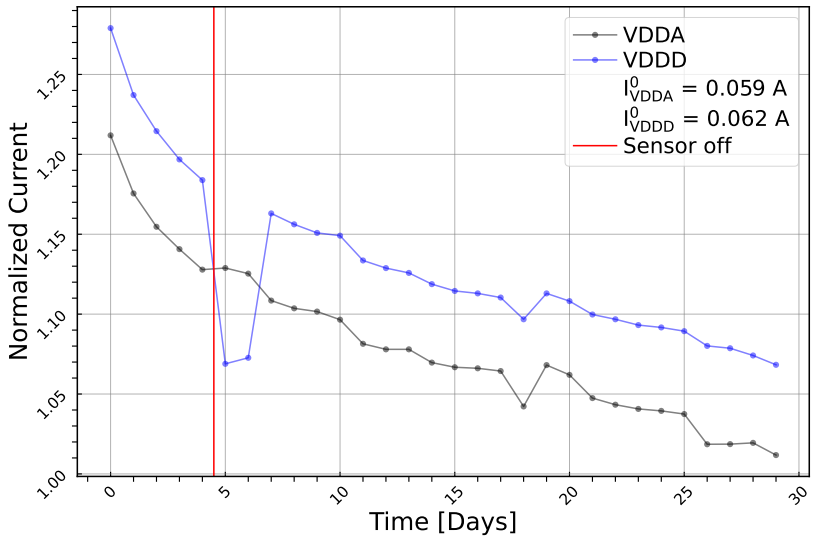


Figure 8.13: Measurement of the recorded current normalized to the current before irradiation of the Run2021 sensor. The environmental settings ($T = -10\,^{\circ}$C) of the DUT have been kept constant over the measurement time.

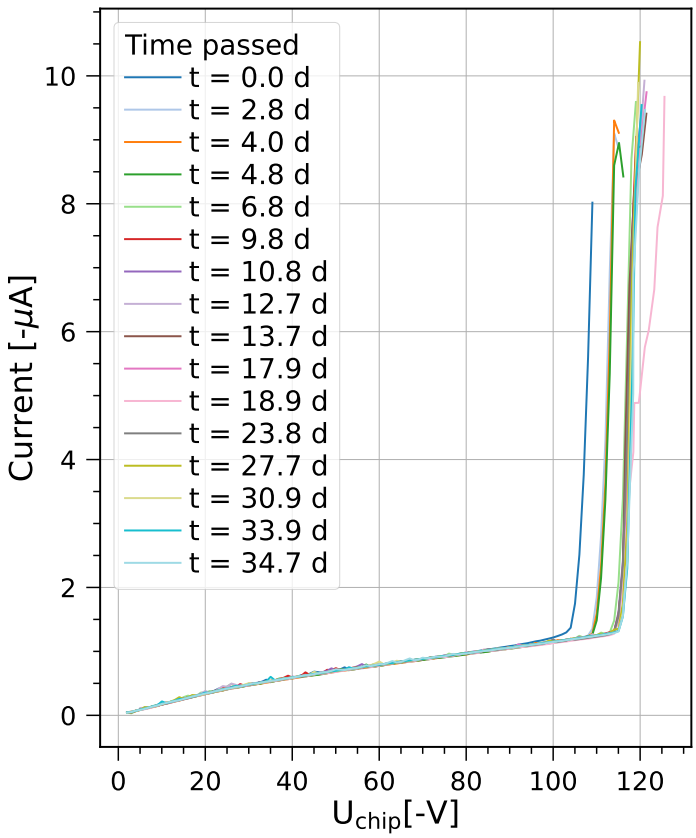


Figure 8.14: Summary of the IV-curves measured during the annealing process of the Run2021 sensor.

8.4.4 Simulation of the Expected Power Consumption of the Mighty-Pixel

Crucial for the Mighty-Pixel design is to know the expected power consumption. Since the measurements of the power consumption have shown a dependence on the TID rate, the influence has to be considered. However, the measurement of the power consumption was performed at a constant TID rate of $6\,\mathrm{kRad\,h^{-1}}$. In the experiment a position dependent rate is expected for the detector geometry. Hence, a peak rate of $1\,\mathrm{kRad\,h^{-1}}$ is only expected for the innermost sensors close to the beam-pipe while the rate decreases for outer modules. Because of that, the amount of TID is position dependent. Consequently, the power consumption changes not only over operation time but also over the detector geometry.
Furthermore, the TID peak, expected to occur around 1 MRad, will occur at different times at different sensors such that not only the power distribution has to cope with this but also the sensor performance is effected. To ensure the required performance, a deep understanding is mandatory.
Therefore, the expected power consumption for the Mighty-Pixel over its run-time taking TID into account has been simulated within the Bachelor thesis by M. Liebetrau [14].
In a first step the expected fluence over time is simulated for the first layer of the Mighty-Pixel based on the module description in [150] and the dose simulation in [149]. The expected dose distribution at an integrated luminosity of $250\,\mathrm{fb^{-1}}$ at the Mighty-Pixel is depicted in fig. 8.15. As assumed a decrease in the total dose towards outer modules is obtained with a peak dose of up to $\approx 40\,\mathrm{MRad}$ at the innermost modules.

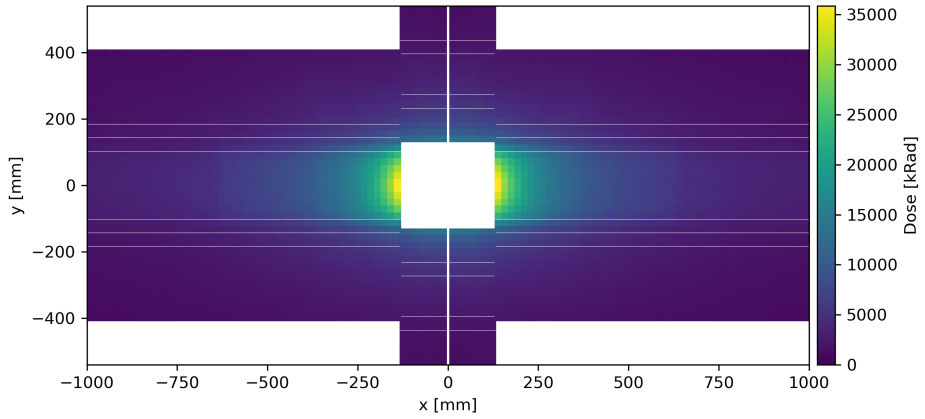


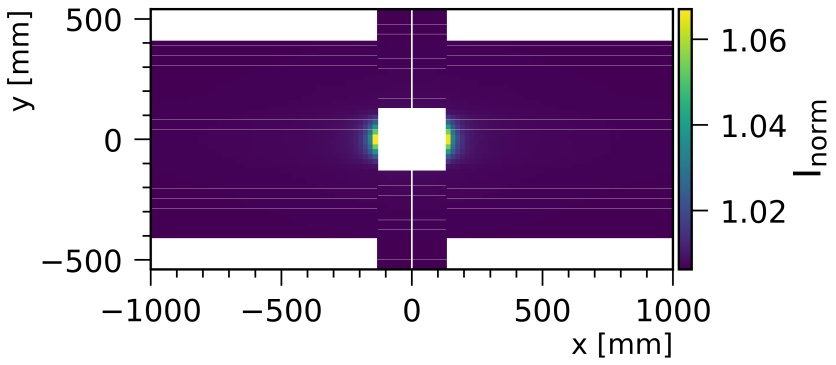
Figure 8.15: Simulation of the expected dose after $L_{int} = 250\,\mathrm{fb^{-1}}$ of the first layer of the Mighty-Pixel [14].

In a second step, the expected power consumption is mapped onto the dose distribution. The data measured with the TelePix2 and Run2021 sensors are considered. Since the particle rate for the TelePix2 campaign was very high and thus, the measured peak power consumption too, the data has been normalized to the peak power consumption of the Run2021 sensor. It

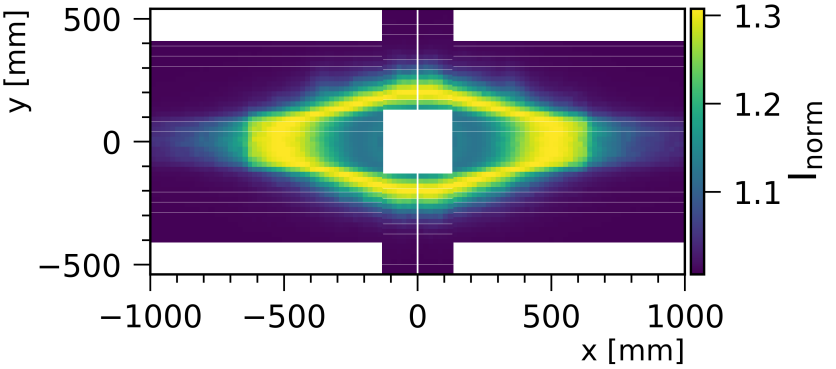
should be noted that the estimate is very rough, but in the absence of further measurements, this approach was chosen.
Following the position and run-time dependent dose distribution, the digital current distribution, presented in fig. 8.16, shows a similar pattern where the change of the power consumption behaves like a wave over time and position.

Remaining questions are the influence of annealing on the power consumption and the expected peak power consumption. Since the DUTs have been irradiated step-wise with measurements in-between, technical stops where the sensors can anneal are emulated in the irradiation campaigns. The more complicated question of the expected peak power consumption cannot be answered completely because of two reasons:
Firstly, the used rates for the irradiation campaigns are higher than the expected rate at the experiment. Secondly, the MightyPix has a different digital design than the TelePix2 and Run2021 sensors and is fabricated at another foundry. Because of the second reason the irradiation campaign has to be repeated with MightyPix2.
To estimate the rate dependent peak power distribution, an attempt to determine the dependence of the power consumption and x-ray rate has been made. Therefore, the normalized digital power consumption of both devices, TelePix2 and Run2021, versus time is determined and shown in fig. 8.17. A further measurement at a different rate would be needed to estimate the current rate. However, no further irradiation campaigns would have been possible within the scope of this thesis. Instead, the annealing rate obtained with the Run2021 sensor (included as dark red markers in fig. 8.17), is taken into account.
As visible, the annealing rate cannot be used to describe the current rate. Consequently, no analytic model was derived to model the power consumption in dependence of the irradiation rate.
Nevertheless, it seems like a current rate dependence would be determinable if more statistics are available. As a consequence, a further irradiation campaign at a different rate is planned for the future.

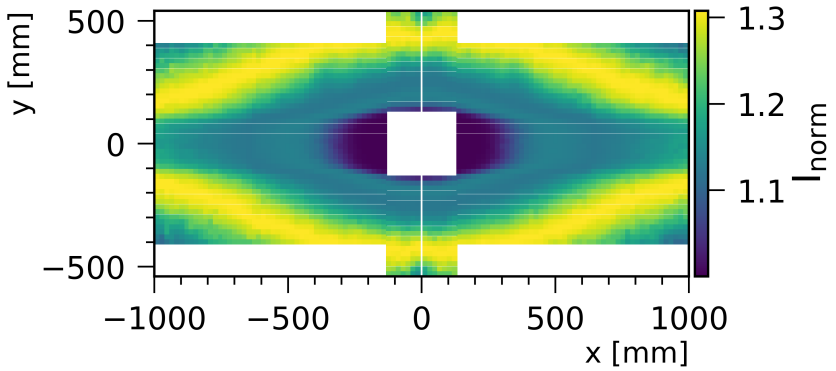
In summary, the obtained power consumption of the TID irradiation campaigns could be used to give a first estimate on the expected power distribution of the Mighty-Pixel over its life-time.



(a) $L_{int} = 5\,\mathrm{fb}^{-1}$



(b) $L_{int} = 50\,\mathrm{fb}^{-1}$



(c) $L_{int} = 200\,\mathrm{fb}^{-1}$

Figure 8.16: Simulation of the expected digital power consumption at the first layer of the Mighty-Pixel for different luminosities using the data obtained by the second TelePix2 irradiation campaign. The data has been normalized to the Run2021 data to get more reasonable results. Only annealing during the irradiation and measurements is considered [14].

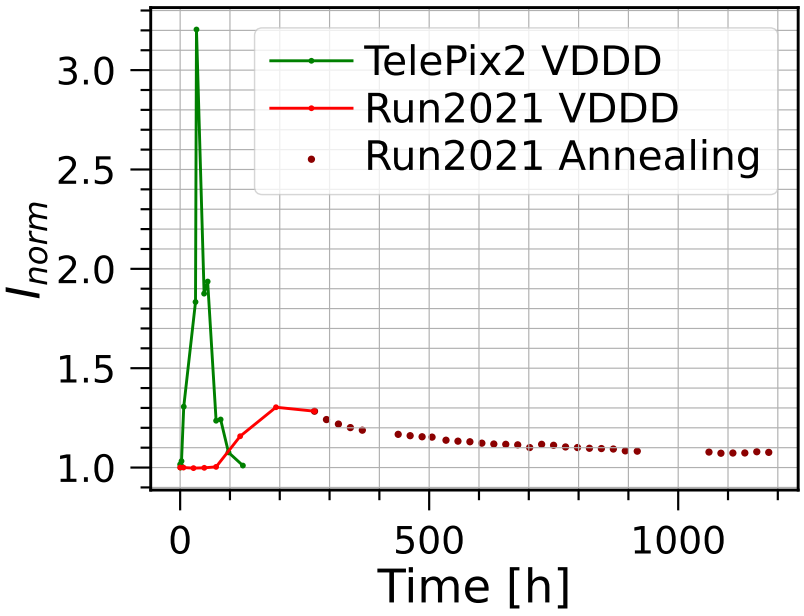


Figure 8.17: Normalized digital current versus time obtained from the TelePix2 and low rate Run2021 irradiation. The annealing rate of the digital current of the Run2021 sensor is included [14].

8.4.5 DUT Performance - Time Resolution

A key element of the performance of HV-MAPS for the Mighty-Pixel is the time resolution. Because of that the influence of surface damage on the time resolution is crucial to ensure the required time resolution of ≤ 3 ns.
Similar to the proton irradiated devices (see section 7.2.2), the time resolution of TelePix2 has been studied for different configurations of the TelePix2 sensor exposed to 40 MRad. The same setup as shown in section 7.1.1 was used and the temperature set as low as possible (see fig. 7.11). Corrections are applied as before: Firstly, the offset, column, row and ToT dependence is corrected and secondly, the binning.
In fig. 8.18 the corrected time resolution of TelePix2 for four different configurations keeping a constant bias voltage of $U_{\text{chip}} = -100$ V is shown:
(1) Standard DAC settings and comparator threshold of 145 DAC units, (2) standard DAC settings and comparator threshold of 140 DAC units, (3) best DAC settings and comparator threshold of 145 DAC units and (4) best DAC settings and comparator threshold of 140 DAC units.
The first scenario would correspond to the default operation scenario at a slightly lower bias voltage than nominal. A time resolution slightly worse than the anticipated goal of 3 ns is determined. But keeping the DUT configuration unchanged and lowering the comparator threshold results in an improved time resolution as expected. However, such a low comparator threshold could not be set for the non-irradiated device without entering the noise floor of the device. Either a change of the effective comparator threshold or a change of the

amplifier gain [5] can explain the observation. Further evidence is given by the hit-efficiency measurement conducted at the testbeam campaign (see section 9.3).
Improvement of the time resolution is possible by changing the DAC configuration to the configuration obtained in table 6.2. At a low comparator threshold a time resolution of $\leq 2.4\,\text{ns}$ could be measured - fulfilling the required time resolution of the Mighty-Pixel.

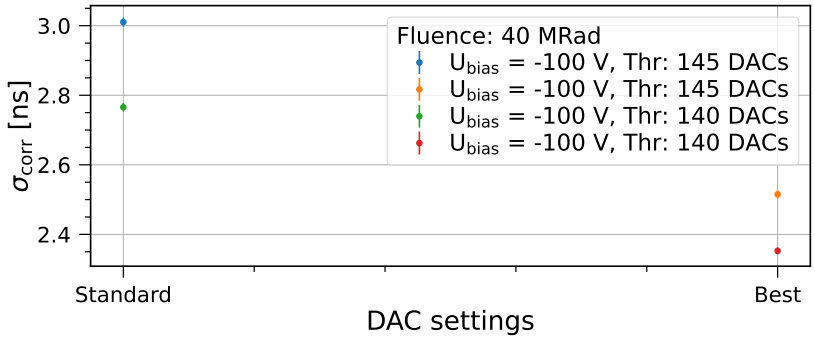


Figure 8.18: Corrected time resolution versus DAC configuration of TelePix2 for two different comparator thresholds using a bias voltage of $U_{\text{chip}} = -100\,\text{V}$. The DUT was cooled as much as possible (see fig. 7.11 for comparison).

A comparison of the derived and corrected time resolutions of TelePix2 without irradiation, exposed to a fluence of $1 \times 10^{14}\,\text{MeVn}_{\text{eq}}\text{cm}^{-2}$ and a dose of 40 MRad using standard DAC settings at a comparator threshold of 145 DAC units is presented in fig. 8.19. For both types of radiation damage the time resolution worsens keeping the same DUT configuration. However, all results are below or on the order of 3 ns. An improvement for all devices is achieved by optimizing the sensor settings at the cost of a higher power consumption.
In fig. 8.20 the comparison using the optimized DAC configuration is depicted. Again a worsening of the time resolution keeping the bias voltage unchanged is observed.
Nevertheless, all determined results fulfill the required time resolution.

For both comparisons the worse time resolution can be explained by radiation induced damages. For the proton irradiated device the sensor bulk is affected such that free charge carriers are trapped and the charge collection efficiency is deteriorated. In the case of the surface damaged device, the worse resolution cannot be explained by trapping centers in the bulk. However, other traps as interface and oxide traps can trap free charge carriers influencing the charge collection efficiency. Further, the observed change of possible comparator thresholds and efficiency slope (see section 9.3) due to a worse amplifier gain (see appendix A.9.6) can explain the changed sensor performance.
To overcome both types of damages and enhance the DUT performance, dedicated changes of the DUT operation mode are beneficial. For the bulk damaged device the main driver is the bias voltage - essential to reduce drift times and enhance the charge collection efficiency. In contrast to that, the bias voltage cannot be increased for the surface damaged device. Instead,

[5] A first estimation of the amplifier gain for TelePix2 was conducted and is presented in appendix A.9.6.

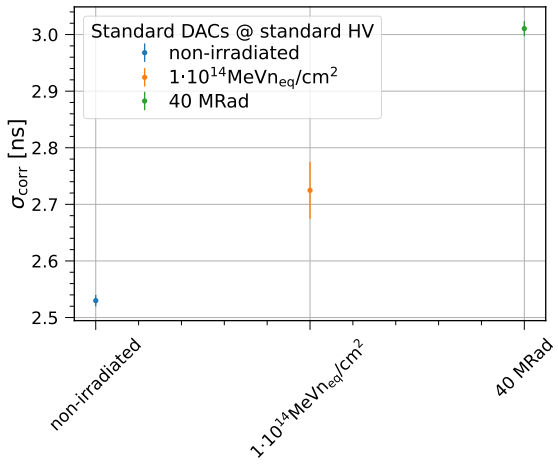


Figure 8.19: Comparison of the corrected time resolution of TelePix2 for different radiation damages using standard DAC settings and a standard bias voltage of $U_{\text{chip}} = -120\,\text{V}$ (non-irradiated and bulk damaged DUT) and $U_{\text{chip}} = -100\,\text{V}$ (surface damaged DUT).

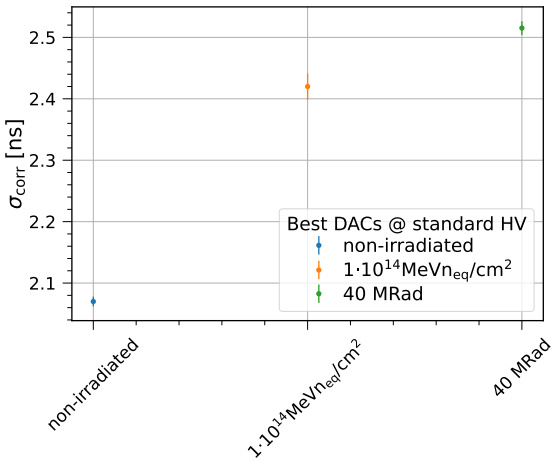


Figure 8.20: Comparison of the corrected time resolution of TelePix2 for different radiation damages using best DAC settings and a standard bias voltage of $U_{\text{chip}} = -120\,\text{V}$ (non-irradiated and bulk damaged DUT) and $U_{\text{chip}} = -100\,\text{V}$ (surface damaged DUT).

Damage	DACs	Threshold	Bias	Time resolution
0	Best	145 DAC units	$-120\,\text{V}$	(2.01 ± 0.01) ns
$1 \times 10^{14}\,\text{MeVn}_{\text{eq}}\text{cm}^{-2}$	Best	145 DAC units	$-210\,\text{V}$	(1.97 ± 0.01) ns
40 MRad	Best	140 DAC units	$-100\,\text{V}$	(2.35 ± 0.01) ns

Table 8.4: Comparison of the best time resolution obtained for TelePix2 for different radiation damages. The time resolution uncertainty is obtained by the uncertainty of the Gaussian fit.

the main driver is the sensor configuration.
A summary of the best obtained results for all investigated devices using the optimized sensor configuration is presented in table 8.4. The best result is obtained for the TelePix2 sensor exposed to $1 \times 10^{14}\,\text{MeVn}_{\text{eq}}\text{cm}^{-2}$ with a time resolution of ≤ 2 ns. Since the largest possible bias voltage was applied to this device, the largest depletion depth of approximately 140 µm (accordingly to fig. 7.7) is expected. As a result, the charge collection efficiency is maximal.

In summary, all studied devices do fulfill the required time resolution of the Mighty-Pixel using standard DAC configurations and a comparable bias voltage - demonstrating the usability of HV-MAPS for the Mighty-Pixel in terms of time resolution for the anticipated radiation damage.
Moreover, it is possible to tune the devices such that improved results can be achieved. However, it has to be kept in mind that tuning always influences the power consumption.

Hence, a trade-off between best possible performance and tolerable power consumption has to be made.
As stated in section 4.2.4, TelePix2 has a large intrinsic heat dissipation. Therefore, operating the sensor at the coldest required temperature is reasonable. However, this results in varying operating temperatures across the measurements. Consequently, the operating temperature for the Mighty-Pixel cannot be estimated with TelePix2. Nevertheless, operation at low temperatures is preferred for both types of radiation damage to keep the leakage current low. As a consequence, the presented measurements have to be repeated with MightyPix2. Another missing measurement of the time resolution is after powered and biased proton irradiation, which is planned for MightyPix2.
But, important quantities for an efficient operation of MightyPix2 can be derived from the measurements with TelePix2. Firstly, the bias voltage is a key driver, in order to enhance the depletion depth, which is essential for efficient charge collection. Secondly, the noise floor must be reasonable low to achieve a sufficient time resolution and thirdly, a trade-off between power consumption and performance is crucial.

8.4.6 DUT Performance - Threshold Dispersion

Investigations of the threshold dispersion for the low rate irradiated Run2021 have been carried out. Therefore, the matrix of the DUT has been tuned at each irradiation step. The threshold dispersion as well as the mean comparator threshold were measured before and after tuning.
A change in the threshold dispersion and shift of the z-curve would occur, if the working points of the injection capacitance, amplifier or comparator would change unevenly due to TID. Since the metal injection capacitance is positioned inside the metal layers of the sensor, no change due to TID is expected.
For the tuning a similar matrix tuning algorithm as illustrated in fig. 6.11 is used for the Run2021 sensor. The dispersion and mean comparator threshold are obtained for a TDAC value of 3 DAC units by injection of a test signal into all pixels and a Gaussian fit to the distribution of the turning point of all determined z-curves. The measurement was not done for TelePix2, as the tune algorithm was not fully developed at the point of its irradiation. Moreover, time needed to tune TelePix2 is not available during the dense irradiation plan - but a comparison of the threshold dispersion before and after irradiation is discussed later within this section.
In fig. 8.21, the mean comparator threshold in dependence of the dose for a TDAC setting of three is shown. The uncertainty for μ is dominated by the statistical uncertainty $\sigma/\sqrt{N_{inj}}$ with the standard deviation σ and the number of injection N_{inj} [6]. With increasing dose level the mean comparator threshold shifts towards lower values. The obtained result matches the measurements with TelePix2, where after the irradiation up to 40 MRad lower comparator thresholds are possible.

[6] As explained in section 6.2.4, the fit uncertainty is not currently implemented in MARS analysis.

Tuning the threshold back to its initial setting is possible by increasing the tune strength - taken an increased power consumption into account. However, the initial setting might yield a difference performance of the DUT after irradiation. To quantify the observed shift, a calibration with electrons (as explained in section 6.2.1) is required.

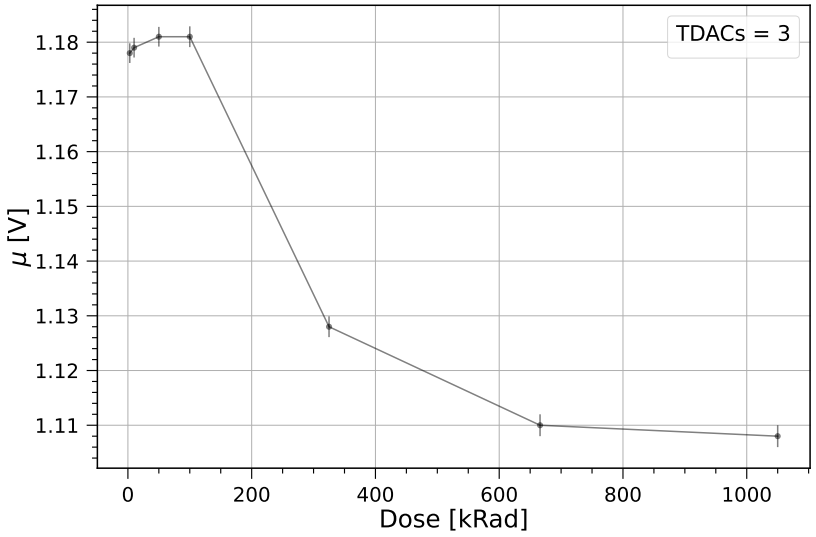


Figure 8.21: Shift of the mean comparator threshold, externally set, obtained by injecting analog test signals in all pixels in dependence of the dose - measured with the Run2021 sensor. The uncertainty for μ is the statistical uncertainty $\sigma/\sqrt{N_{inj}}$ with the standard deviation σ and the number of injection N_{inj}.

In addition, the threshold dispersion σ has been determined. As shown in fig. 8.22, no significant increase in the dispersion with irradiation is observed which does not correspond to the expectations from TelePix2 where a large threshold dispersion is obtained (see fig. 8.25). The statistical uncertainty and a second y-axis showing the corresponding values in DAC units are included.
The dispersion of approximately 2.7 DAC units is comparable to the dispersion ($\sigma \approx$ 2.6 DAC units) of a non-irradiated TelePix2, as shown in fig. 6.12. A possible reason for the increased dispersion are larger variations in the bigger TelePix2 sensor compared to the smaller Run2021 sensor. Further studies are required to explain the observation.

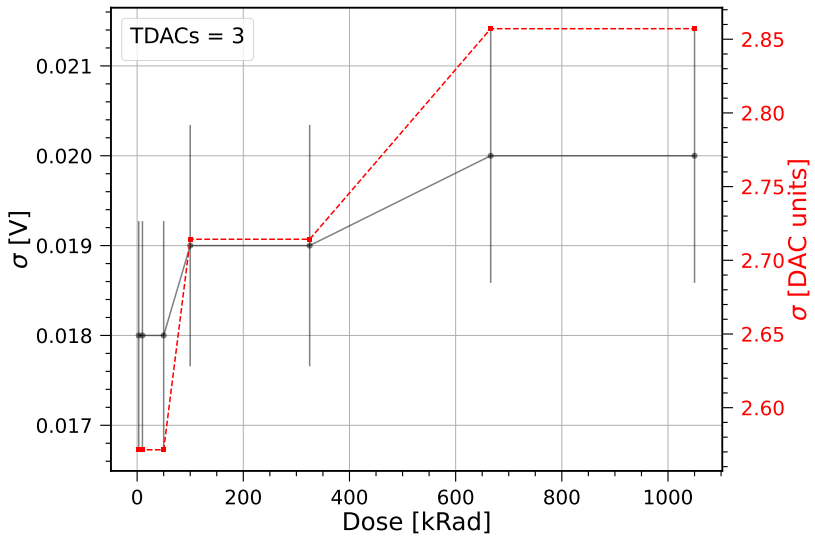


Figure 8.22: Threshold dispersion versus dose level obtained by injecting test signals in all pixels with increasing irradiation doses measured with the Run2021 sensor. The uncertainty for μ is the statistical uncertainty. A second y-axis showing the corresponding values in DAC units is provided.

Because no direct access to the involved chip electronics is possible, an explanation cannot be given without deeper investigations. The main observations obtained with both sensors, the Run2021 and TelePix2, are summarized in the following and a first hypothesis is proposed [7]:

- A large threshold dispersion of $\sigma \approx 6$ DAC units for TelePix2, exposed to 40 MRad is observed but not for the Run2021 sensor ($\sigma \approx 2.7$ DAC units).
- A change in the efficiency (see section 9.3) for TelePix2 has been measured as well as a softening of the efficiency curve (see section 9.3).
- For the Run2021 and TelePix2 sensors, a shift of the z-curve was measured. In contrast to z-curve measured for TelePix2, no significant change of the slope was obtained for the Run2021 sensor. The measurements of the Run2021 sensor, both non-irradiated and exposed to 1 MRad, are shown in fig. A.15 and fig. A.16, respectively. For the TelePix2 sensor, the corresponding measurements are presented in fig. A.17 (1 MRad) and fig. A.18 (40 MRad).
- A shift of the mean of the threshold distribution towards lower threshold values for the same amplitude of test signal occurred for both devices.
- Lower comparator thresholds are possible without entering the noise floor of the DUT and lastly, a larger injection voltage is required for TelePix2 to perform a threshold scan.

[7] The measurements performed with TelePix2 are explained in the following sections. Nevertheless, the obtained results are previewed here.

Taking the observations into account, a change in the amplifier gain might explain the observations obtained for the threshold range and the injection signal.
If the amplifier gain would be worsened by TID, a higher injection signal is required to generate signals above the comparator threshold. In addition, the noise floor would be entered at lower comparator thresholds, as the amplification of the leakage current, leading to the noise, is lower as well.
The differences between the Run2021 and TelePix2 senors could be explained by the trap formation mechanism. Oxide traps change the transistor threshold, which reduces the threshold of an NMOS transistor. At higher doses interface traps start to form, counteracting the oxide traps and leading to a slower slope of the transistor threshold.
Because of the low target dose of 1 MRad of the Run2021, the transistor threshold is dominated by oxide traps, while for TelePix2 the interface traps are dominating.
To validate this Ansatz, a measurement of the transistor voltage versus leakage current is required. However, no direct measurement of the current is possible - but for the Run2021 sensor some on-chip DACs are accessible. Hence, the output voltage of the DACs in dependence of the power consumption was measured (see section 8.4.7).
Furthermore, a possible change of the amplification, as previously discussed, could be caused by traps. A first attempt to determine the amplifier gain and investigate the observed behavior in more detail was conducted and is presented in appendix A.9.6.

Annealing Studies of the Threshold Dispersion of the Run2021 Sensor

As for the studies on the power consumption and bias behavior, annealing effects on the threshold dispersion have also been investigated. The goal is to investigate the change of the mean threshold over time for the Run2021 sensor. As introduced in section 8.4.3, the environmental conditions have been kept stable and the DUT was powered and biased over the full annealing period.
On regular basis threshold scans of specific test pixels and the full matrix have been conducted. From each z-curve measurement the turning point is extracted and a Gaussian fit to the distribution performed. The mean of the fit is considered to determine its evolution over time - shown in fig. 8.23. As a reference the mean threshold of the non-irradiated device (colored in blue) is included. For all measurements the TDACs have been set to 0.
A re-bounding structure of the mean comparator threshold over time is observed. Within the first two weeks - after the last irradiation up to 1.05 MRad - the mean threshold shifted back towards its initial value. However, a shift towards the opposite direction occurred afterwards, followed by a significant back shift after 40 d.

From the theoretical predictions of TID a slow annealing process is expected. Assuming oxide traps to dominate the DUT performance, as discussed previously, a slow annealing of the holes is expected, which could explain the slow change. However, the re-bound structure cannot be explained. In contrast, the shape looks like oppositely charged traps interact with each other. As no further reference measurements are available and no possibilities to investigate the observation in more detail, no statement can be made here. More data points

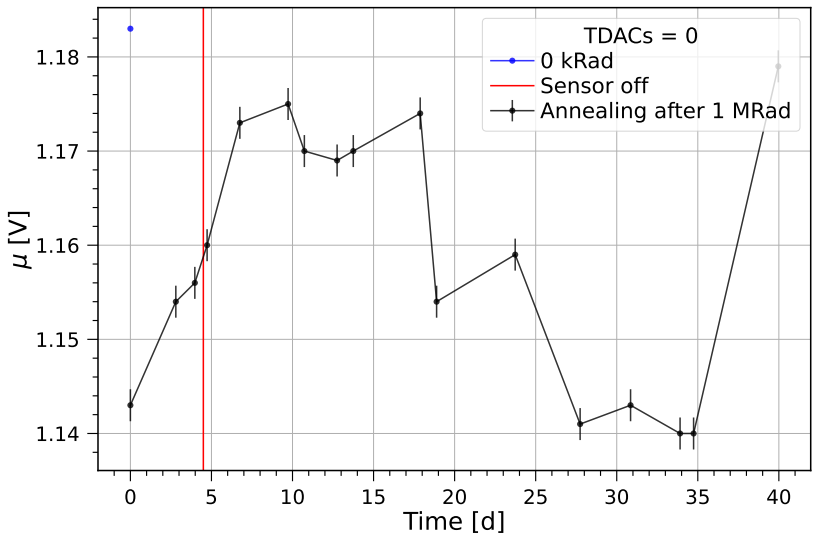


Figure 8.23: Mean comparator threshold versus annealing time obtained by injecting test signals in all pixels. As reference, the mean threshold of a non-irradiated Run2021 sensor is included in blue. The uncertainty of μ is the statistical uncertainty $\sigma/\sqrt{N_{inj}}$ with the standard deviation σ and the number of injections N_{inj}.

are required to explain the observation.

Threshold Dispersion Studies of TelePix2

As mentioned at the beginning of the threshold dispersion discussion, tuning of the pixel matrix at each irradiation step is not feasible for TelePix2. But, the tuning was repeated six months after the last irradiation step. Hence, uncontrolled annealing in the meantime took place.
By threshold scans of dedicated test pixels a shift of the threshold towards lower values was observed. In addition, a large analog injection signal is necessary and the threshold distribution widened. Because of that, the calibration measurement of the mean comparator threshold versus TDAC step for different VNDAC strengths was repeated to validate the operation of the TDACs. Figure 8.24 shows the result. Similar to the non-irradiated device, not all Gaussian fits to the mean comparator threshold succeed such that some data points are missing. Nevertheless, a clear trend for each tune strength is observable. Because a large analog injection signal is required, the threshold level differs compared to the calibration shown in fig. 6.10. Moreover, only 25 test pixels have been used for the measurement [8].

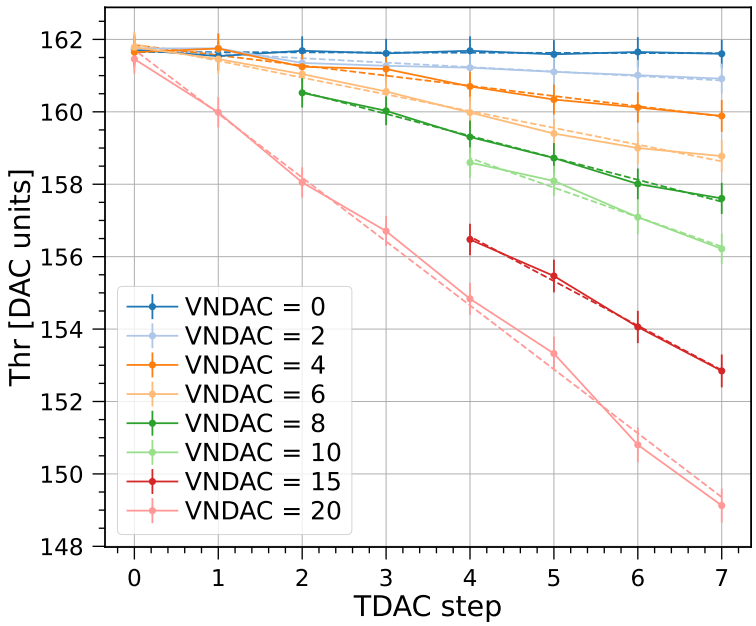


Figure 8.24: Mean pixel threshold versus TDAC for different VNDAC settings in DAC units for 25 test pixels after irradiating TelePix2 to 40 MRad. A linear regression is fitted to data to show the linear dependence of threshold and TDAC. The uncertainty of μ is the statistical uncertainty $\sigma/\sqrt{N_{inj}}$ with the standard deviation σ and the number of injections N_{inj}. The injection is done analog.

Comparing the determined slopes to those measured for the non-irradiated TelePix2

[8] For the non-irradiated device, a larger test sample was used. The reduced number of pixels has two reasons: First, measurements with the non-irradiated device showed that fewer test pixels are sufficient. Second, the large threshold dispersion makes measurements with the irradiated DUT more difficult.

in table 8.5, no significant change due to TID at low VNDAC values is visible. However, for larger tune strengths a slight deviation is obtained. But for the surface damaged TelePix2 a lower set of test pixels was used for the calibration because of the large threshold dispersion. Concluding, no significant change in the operation of the TDACs has been observed at a TID of 40 MRad for TelePix2 - validating the radiation tolerance of the transistors responsible for the comparator tuning.

VNDAC [DAC units]	Slope pre-irradiation [(DAC units)/TDAC]	Slope after 40 MRad [(DAC units)/TDAC]
0	0.01	0.00
2	-0.16	-0.12
4	-0.27	-0.28
6	-0.43	-0.46
8	-0.54	-0.61
10	-0.80	-0.82
15	-1.09	-1.23
20	-1.18	-1.77

Table 8.5: Comparison of the change of threshold per TDAC step for different VNDACs of a non-irradiated and up to 40 MRad x-ray irradiated TelePix2 sensor.

A threshold dispersion of $\sigma \approx 6$ DAC units after irradiation is observed. Compared to a dispersion of $\sigma \approx 2.6$ DAC units before irradiation, presented in fig. 8.25, a significant increase is attributed to irradiation.

For the measurement of the irradiated device, a reduced amount of pixel of 300 had to be used. In addition, a large tuning strength was set. Although an improvement is determined by the tuning, the chosen strength is not sufficient to reduce the dispersion towards its initial value. Increasing the tune strength further would be possible, but the power consumption would increase which is not feasible for the final detector.
Furthermore, a regular matrix tuning might not be possible within the experiment since it is too time consuming. Therefore, the increased pixel spread has to be accepted which is possible as long as the overall sensor performance is sufficient and its noise reasonable. Hence, tuning the local comparator thresholds to suppress noisy pixels, as described in section 6.2.4, is the more suitable approach.

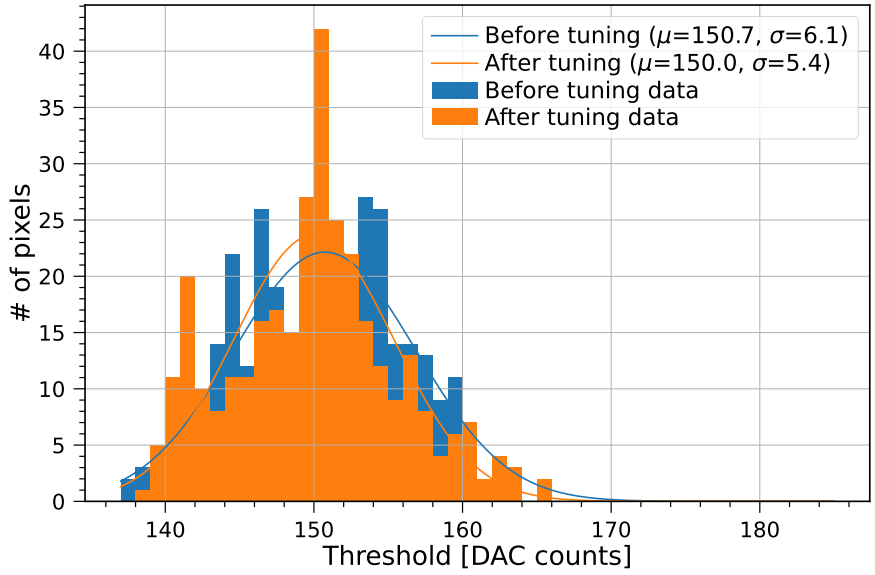


Figure 8.25: Threshold dispersion before (colored in blue) and after tuning (colored in orange). A threshold goal of 150 DAC units was anticipated for 300 pixels using VNDAC = 15 DAC units.

8.4.7 Run2021 - On-Chip DAC behavior

Due to the observed influence of surface damage on the sensor performance, discussed previously, a study of the on-chip DACs was done to investigate the effect of surface damage on the transistors in HV-MAPS in more detail.
Measurements of the on-chip DAC behavior have been conducted by M. Liebetrau [14] under the supervision of the author.
For the Run2021 sensor some on-chip DACs are accessible. At those measurement points the output voltage of the DACs applied to the analog circuit is measurable. Hence, the measured voltage versus the set voltage in DAC units can be obtained in dependence of the power consumption.
The measurement was done at each irradiation step for all on-chip DACs included in the amplifier, feedback and comparator circuit as well as for the hit digitizers. With an `Arduino Nano Every` an automatized measurement procedure has been set up - described in [14].
No significant change between the measured and set DAC value correlation has been measured. Therefore, the implementation with respect to TID damage is sufficient for the experiment. An exemplary measurement of the set to measured DAC correlation is shown for the amplifier bias DAC *VN* in fig. 8.26.

The standard value of *VN* is 10. The change of the corresponding measured voltage versus fluence is depicted for this configuration in fig. 8.27. Measurement errors are dominated by the measurement itself and have been estimated accordingly. As discussed previously, no significant change in the measured voltage (colored in blue) with increasing dose is visible, but an increase in the measured digital (colored in green) and analog (colored in green)

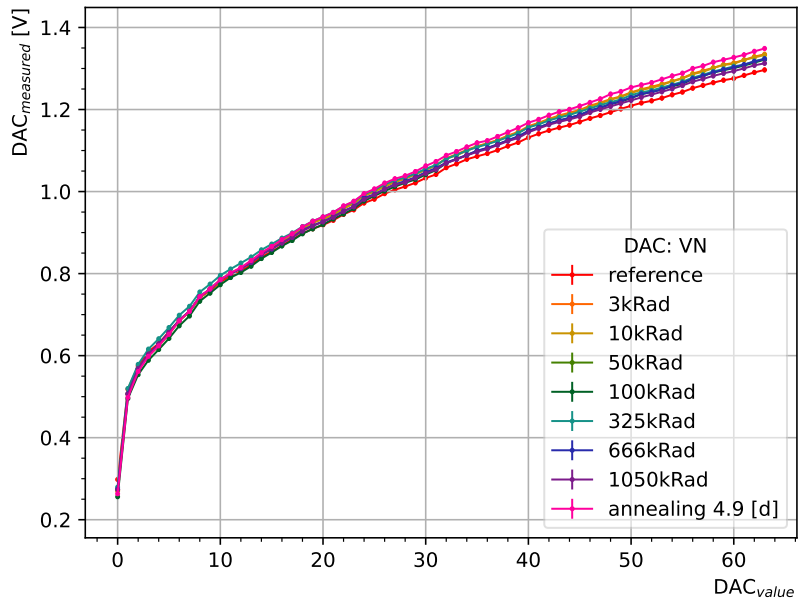


Figure 8.26: Correlation of the measured voltage of the amplifier bias *VN* for its possible settings for each dose level and after 5 d of annealing [14].

current is observed.

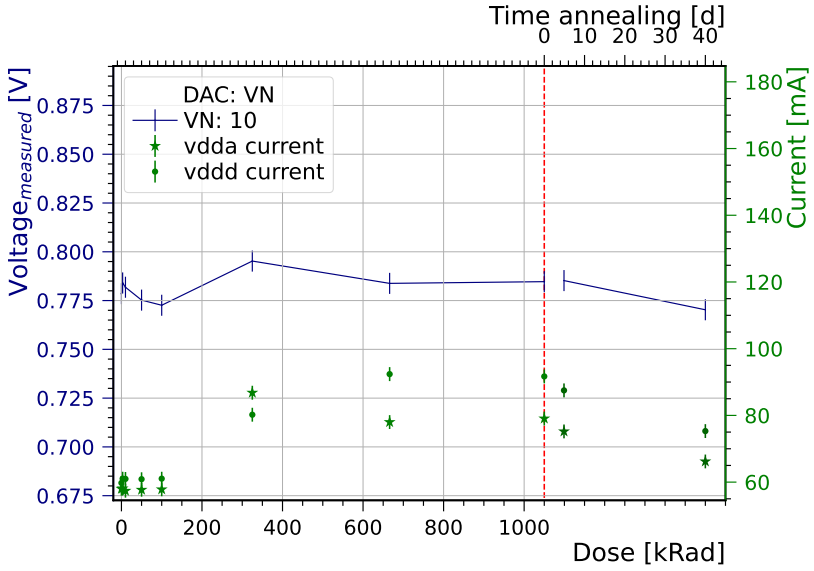


Figure 8.27: Measured voltage and power consumption of the amplifier bias *VN* set to its nominal value of 10 versus dose. The measurement was repeated after some annealing time, shown on the second x-axis [14]. The measurement uncertainties are included.

As discussed in section 8.4.6, a transistor characterization is essential to determine the

effect of surface damage on its gate voltage. However, such a measurement is not possible with the available HV-MAPS. An attempt to investigate their electronics in more detail is made by the measurement of the amount of the current - drawn by the DAC - as part of the total current versus transistor voltage, accessible by the *Debug Outputs*. A representative result for the amplifier bias is depicted in fig. 8.28.

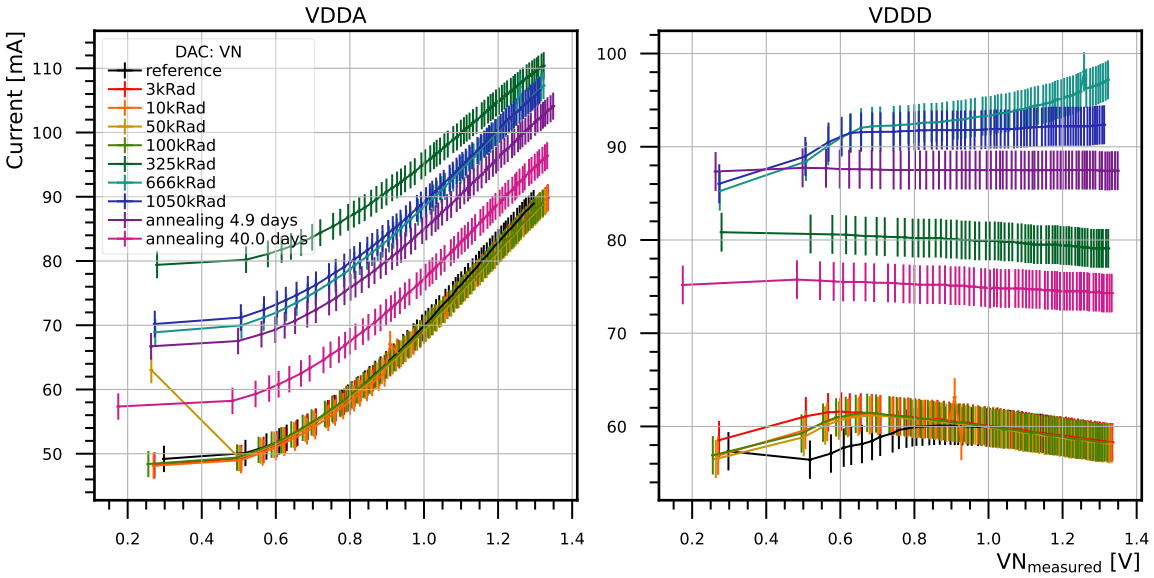


Figure 8.28: Measured current, separated in digital and analog power domain, versus the measured voltage of the debug output of the amplifier bias *VN* in dependence of the dose. The measurement has been repeated after 5 and 40 days annealing time. The systematic uncertainties of the power supply are included [14].

The measured current is separated into the digital (depicted on the right hand-side in fig. 8.28) and analog (depicted on the left hand-side in fig. 8.28) power domain. Since the amplifier bias is powered by the analog power domain, a change of the current-voltage dependence in the analog domain is observed but not in the digital. Increasing the amplifier bias voltage results in an increased current. Further, the overall current level increases with increasing radiation dose. Already after five days of annealing time, the current level shifted back into direction of its nominal level - but after 40 d annealing time the level is still higher than nominal.
By the determined dependence the increase of the overall power consumption, shown in fig. 8.12, with increasing dose can be explained. In addition, a slight change in the slope is observed. Due to higher transistor leakage currents, caused by TID, the slope is altered. The behavior has been observed for all analog DACs (more results are presented in [14]). Since TelePix2 has been irradiated to a higher dose than the Run2021 sensor, a stronger change in the slope can be extrapolated for TelePix2. As a consequence, the change in the efficiency-curve would be explainable. However, no final conclusion can be given because

the measurement cannot be repeated with TelePix2. In addition, a more detailed study on the transistor behavior would be beneficial. Therefore, a measurement of the transistor threshold and leakage would be required which is not possible with the available DUTs.
The measurement has been repeated for each accessible DAC. Therefore, a current-dose dependence for each DAC is available. In fig. 8.29 the normalized current for all DACs, set to their standard configuration, value is presented. Each data point corresponds to the current measured for the corresponding DAC setting. An increase of the overall power consumption with increasing dose is observed - matching the total measured power consumption in fig. 8.12. A slight deviation between the currents is observed due to different temperatures during the measurements. While the temperature for the measurement presented in fig. 8.12 was kept at $-10\,^{\circ}\mathrm{C}$, all measurements of the on-chip DACs were conducted at room temperature because of the required measurement setup, where connectors to dedicated probe points had to be attached (see [14] for more information).
But in summary, the measured power consumption matches the total power consumption. To investigate the absolute increase in power consumption in more detail, the difference in power consumption for each DAC setting relative to the standard configuration was measured at each dose level. The results are presented in appendix A.9. While the overall power consumption increases with dose, as shown in fig. 8.29, the variation of the absolute power consumption per DAC exhibits no significant deviation.

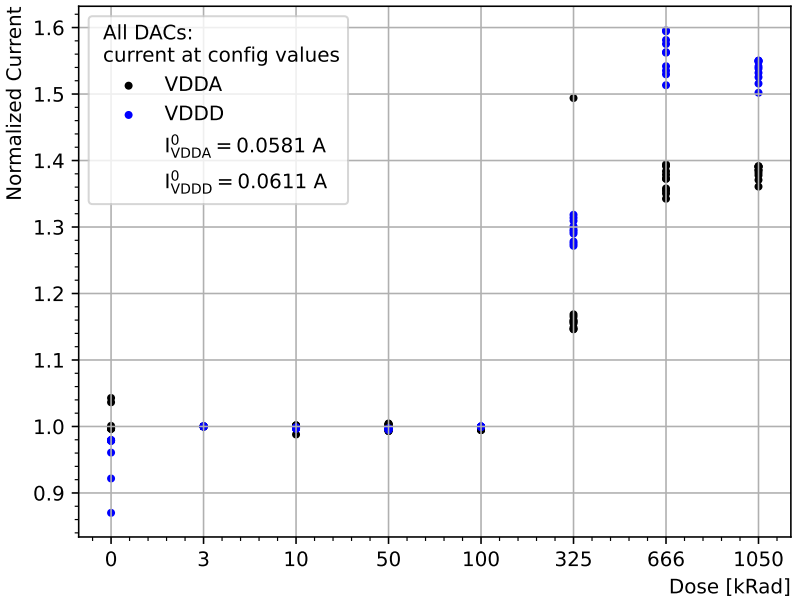


Figure 8.29: Normalized current versus dose for all DACs set to their standard values [14].

8.5 Summary

The effect of surface damage on the TelePix2 and Run2021 sensor as predecessors of the MightyPix was investigated in terms of performance measurements including time resolution measurements, bias behavior studies and the threshold dispersion. In total four x-ray irradiation campaigns, two for each sensor type, have been carried out at the in-house available x-ray tube at the FTD in Bonn.
To prove the radiation tolerance in terms of TID, three irradiation campaigns up to the maximum peak dose of 40 MRad were conducted with a high TID rate of 474 kRad h^{-1} to accumulate the dose within a reasonable amount of time. Further, a low rate irradiation with 6 kRad h^{-1} was done since a rate dependence for the expected effects of TID is known and the peak rate at the Mighty-Pixel is anticipated to be on the order of 1 kRad h^{-1}.
Each irradiation campaign was set up in a step-wise manner to allow measurements in-between and emulate annealing times of the DUT comparable with annealing times due to times without beam at the Mighty-Pixel.
Investigation of the time resolution for TelePix2, irradiated to 40 MRad, has yielded a best value of

$$\sigma = (2.35 \pm 0.01)\,\text{ns}$$

at a comparator threshold of 140 DAC units at a bias voltage of $U_{\text{chip}} = -100\,\text{V}$ for optimized DAC settings which fulfills the required time resolution of the Mighty-Pixel.
Measurements of the bias behavior and power consumption have shown a TID dependence. While the bias behavior, studied for TelePix2 and the Run2021, has yield a similar behavior independent of the TID rate, a dose dependence of the power consumption was observed. With increasing TID, the breakdown occurs earlier and is softer compared to an typical avalanche breakdown. A back-shift after a certain amount of annealing was measured within dedicated annealing studies. However, the initial breakdown could not be restored - influencing the sensor performance.
The power consumption shows the expected TID behavior with a peak in the power consumption around 1 MRad. Important for the Mighty-Pixel is the expected peak power consumption and its distribution over the detector and run-time. Therefore, the power consumption measurement of both DUTs has been used to simulate the power consumption distribution of the Mighty-Pixel over its lifetime. A wave-like distribution over time and position at the detector following the dose distribution is determined. As a consequence, the power distribution scheme foreseen for the Mighty-Pixel has to cope with this to ensure an efficient long-term detector performance.
Due to the rate, chip design and foundry dependencies of the peak power consumption a final statement cannot be made yet. The dependence on the chip design and foundry will be answered by a repetition of the measurement with MightyPix2. To estimate the rate dependence, an attempt to derive a current rate was made. However, the current rate could

not be derived using the available data. As a consequence, another irradiation campaign with a different rate is planned.
Furthermore, the effect of surface damage on the performance has been studied in more detail since it is crucial to understand the effects on HV-MAPS. Therefore, the threshold dispersion of both devices was investigated and a detailed characterization of the on-chip DAC behavior of the Run2021 sensor was performed.
Measurement of the z-curves to obtain the mean comparator threshold and threshold dispersion have shown a TID dependent behavior. While at low TIDs oxide traps lead to a shift of the threshold, the slope is affected at higher TIDs. Similar at low TIDs the threshold dispersion did not change, while at high TIDs an enhanced dispersion was measured. To further investigate the observations, the on-chip DACs, accessible for the Run2021 sensor, have been studied in more detail. Although the DAC behavior did not change with irradiation in general, the power consumption did change.
Nevertheless, all presented measurements were done for the first time for HV-MAPS designed at KIT and produced in an 180 nm TSI process. Hence, no reference measurements to validate or negotiate the results are available. Most measurements can be explained by the theory of TID damage. However, those have been mostly done for dedicated test structures and not HV-MAPS. As a consequence, the given explanations should be taken with caution.
To conclude, the presented TID campaigns and results show how crucial it is to investigate surface damage. Although promising results with TelePix2 and the Run2021 sensor have been obtained, it is mandatory to repeat the measurements with MightyPix2 and investigate the rate dependence further.

CHAPTER 9

Performance Studies of TelePix2 in a Testbeam

In previous sections the performance of HV-MAPS, in particular TelePix2, has been discussed. All studies had the overall goal to demonstrate the technology being compatible with the Mighty-Pixel requirements. However, not all requirements can be studied in the laboratory. To determine the hit-efficiency and in-time efficiency, the DUTs have to be characterized at a beam test facility. In addition, testbeams are required to probe the response to a particle beam. Therefore, the performance in terms of time resolution and hit-efficiency has been studied at a testbeam campaign in December 2024 at the DESY II testbeam facility [140] (see section 9.1). Moreover, the testbeam has been used to commission the MARS DAQ system as a DAQ system for testbeams. Besides integration of the hardware into the available beam telescope, the firmware had to be adjusted (see section 5.3) and dedicated software developed to integrate MARS into the same software system, the EUDAQ2 [151] - used for the beam telescope.
The integration into the EUDAQ2 software framework is described in section 9.2.1. To analyze the collected data, the offline data analysis framework `Corryvreckan` [135] was used. Because the framework expects a `root`-format data input, the data collected with MARS, stored in a `hdf5` data format, must be converted. In section 9.2.2 the conversion is explained.
Before discussion of the results with focus on the hit-efficiency (see section 9.3) and time resolution (see section 9.4), the experimental setup is introduced in section 9.2. Finally, a comparison to the results obtained by measurements in the laboratory is provided in section 9.4.2.

9.1 The DESY II Testbeam Facility

The DESY II synchrotron offers an electron/positron beam. A dedicated beam for the testbeam facilities is produced from the primary. Therefore, photons are produced via Bremsstrahlung by a carbon fiber target which is placed inside the circulating beam. Produced photons are in turn converted into electrons/positrons via a metal plate target. The produced beam is then dispersed by a dipole magnet. Depending on the magnet current and polarity, the beam polarity and energy can be selected. An energy in the range of 1 to 6 GeV is selectable. Finally, the testbeam beam is collimated.
For the testbeam campaign presented within this thesis an average beam energy of 4 GeV with particle rate of 30 to 40 kHz/(1 x 2)cm^2 has been chosen. The rate was measured with the TelePix2 DUT, used as the time reference layer, and is compatible with the rate measured by the scintillators.

9.2 Experimental Setup

The hit-efficiency and time resolution has not only been investigated for a non-irradiated TelePix2 sensor but also for the irradiated devices presented in chapter 7 and chapter 8. Therefore, the influence of bulk and surface damage on the sensor performance could be studied. A summary of all devices used at the testbeam campaign and the bias voltage used for the measurements is given in table 9.1.
For the TelePix2 sensor exposed to 3×10^{14} MeVn$_{eq}$cm^{-2} different bias options have been tested due to difficulties in the operation of the DUT - discussed in section 7.2 and further explained in section 9.3. For the other DUTs the bias voltage was chosen accordingly to measurements done in the laboratory.

DUT	Radiation Damage	Bias
TelePix2	0	−120 V (Chip bias)
	0	−100 V (Chip bias)
TelePix2	1×10^{14} MeVn$_{eq}$cm^{-2}	−180 V (Chip bias)
TelePix2	3×10^{14} MeVn$_{eq}$cm^{-2}	−170 V (Chip bias)
	3×10^{14} MeVn$_{eq}$cm^{-2}	−180 V (Chip bias)
	3×10^{14} MeVn$_{eq}$cm^{-2}	−70 V (Pixel bias)
TelePix2	40 MRad	−100 V (Chip bias)

Table 9.1: Overview of all DUTs characterized at the testbeam campaign. For each, the bias voltage and the radiation damage is given. All devices are unthinned with $\approx 740\,\mu$m thickness.

To study the hit-efficiency, a particle track has to be reconstructed. Hence, not only a particle beam is required but also reference measurements to reconstruct a track. Therefore,

the DUT is placed within a testbeam telescope - consisting of six reference layers providing information about the hit position. In addition, the beam telescope is equipped with scintillators to trigger and consequently, gather a reference time information.
Since the used EUDET type beam telescope comes with MIMOSA26 [118] sensors, no common information about the time and hit position is available from these sensors. MIMOSA26 sensors are read-out in a rolling shutter manner - resulting in large event frames with essentially no time information. Therefore, a time reference layer combining hit and time information is necessary. For that, a second TelePix2 - read-out and configured with a second MARS DAQ system - has been used. Because TelePix2 has been designed for this purpose, the device is excellent for the task of providing fast time information.
A schematic overview of the beam telescope with the scintillator, time reference and DUT is depicted in fig. 9.1. Three telescope layers are positioned upstream and three downstream of the DUT. The scintillators have been placed downstream to ensure that the telescope layers and the DUT have detected the particle, too - suppressing data where only the scintillators have detected a hit.

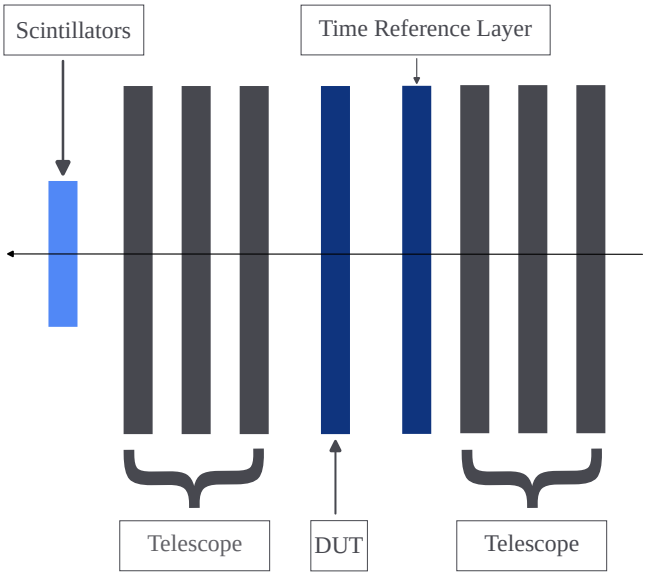


Figure 9.1: Schematic overview of the measurement setup consisting of six layers of beam telescope (colored in gray), a scintillator layer (colored in light blue), a time reference layer (colored in dark blue) and the DUT layer (colored in dark blue). For the time reference layer another TelePix2 sensor has been used.

The real setup is shown in fig. 9.2. A 3D printed holding structure (in green and visible on the left in fig. 9.2) is used to hold the scintillator [1] and mount them on the telescope rail. For the time reference layer an adapter to the original telescope planes was used.
Since the DUTs are operated at cold temperatures, the DUT carrier board is positioned inside

[1] The used scintillators are from Bonn and typically form the timing layer (see fig. 6.22).

an enclosure box (colored in black and yellow) - flushed with nitrogen to prevent condensation. To cool the DUTs, the same hybrid cooling solution as presented in fig. 5.4 has been used. A top view of the PCB mounted on it and positioned inside the enclosure is shown in fig. 9.4. In addition, a temperature and humidity sensor is attached to the PCB in the vicinity of the DUT to monitor the temperature and more important the humidity during the measurements.



Figure 9.2: Side view of the measurement setup. The beam is coming from the right and going towards the left. 3D printed structures are used to mount the DUT, the time reference layer and the scintillators on the telescope arm.

To reduce multiple scattering, the enclosure box has an opening window covered with a film of `Kapton` in front of the DUT. A side view close-up of it and the time reference layer is shown in fig. 9.3.

For both TelePix2 layers (the DUT and the time reference layer) two separate MARS DAQ systems have been used to configure and operate the DUTs and read-out the data because the system is not yet ready to operate multiple sensors at once. However, both systems have been connected for the first time to the same back-end computer.

To secure both setups and to allow a positioning of the adapter and FPGA card outside of the beam, long `Display Port` cables are used to connect the DUT/reference layer to the corresponding adapter card. In addition, the power supplies were placed outside the telescope as well.

Since two MARS DAQ systems, the beam telescope and scintillators are used at the same time, a common software framework to organize all at the same time is crucial. The EUDAQ2 software framework is dedicated for this purpose. How MARS is integrated, is explained in section 9.2.1.

Further, all parts have to be operated at the same clock because otherwise no correlation

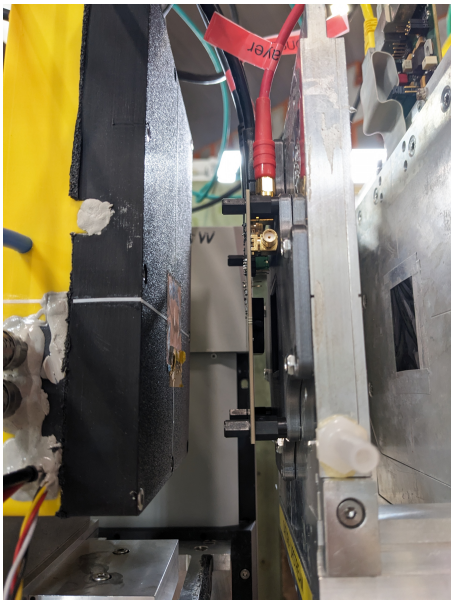


Figure 9.3: Close up of the opening window of the enclosure box and the time reference layer.

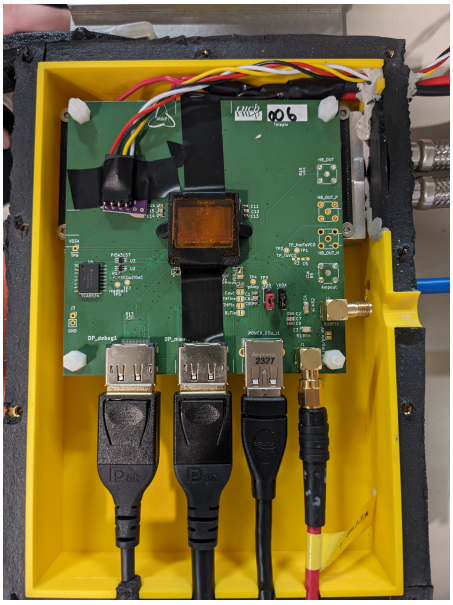


Figure 9.4: Top view of the DUT mounted on the water block and inside its enclosure.

between the different collected data can be made. Hence, all are connected to a **T**rigger **L**ogic **U**nit TLU. A common clock is distributed to the telescope, time reference and DUT layer. If the scintillators detect a hit, a trigger is sent by the TLU to the time reference and DUT layer causing a timestamp in the MARS firmware which can be used to obtain the time resolution. Depending on the operation mode of the telescope (EUDET or AIDA-style (for more information: [118])) further signals are sent from the TLU. During the testbeam campaign the EUDET mode has been used for the telescope. In total, the TLU has distributed the following signals: a common clock, trigger and reset signals. For the DUT, the AIDA mode was chosen. To veto further triggers as long as the DUT is busy, a busy signal is sent to the TLU.

9.2.1 Integration of MARS into the EUDAQ2 Software Framework

The EUDAQ2 software framework has been developed to operate the DAQ system of the EUDET-type beam telescopes. Configuration, initialization and data collection are controlled by the system. For each task dedicated modules are responsible. A schematic overview of the system is shown in fig. 9.5. A producer for each device is required. Data is collected by dedicated data collectors as well as log information by a log collector. All processes are controlled and observed using a monitoring system.

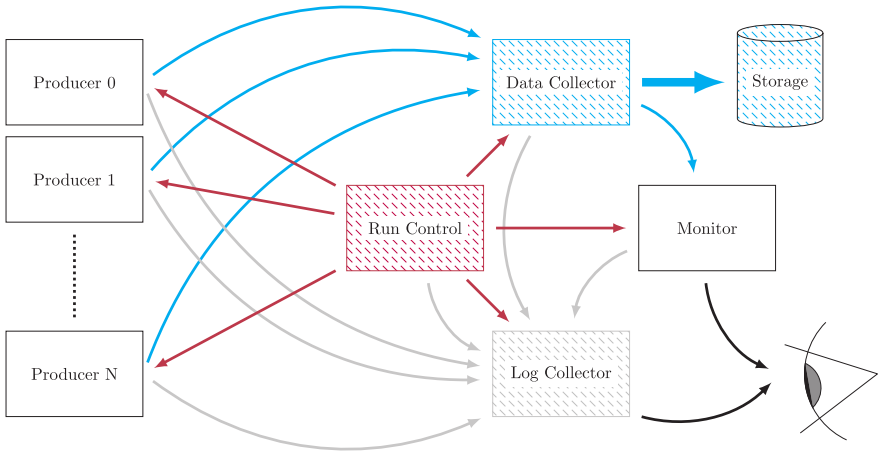


Figure 9.5: Schematic overview of the EUDAQ2 software framework with its different modules to control all devices, collect data and log files as well as a monitor to control the processes [151].

Besides the telescope, the scintillators are also integrated into the EUDAQ2, such that the trigger and timestamp data is stored as well. Since the DUT and time reference layer are configured via the MARS DAQ system and data collected with it, an integration of the MARS DAQ into the EUDAQ2 control system is mandatory to ensure a simultaneous and synchronized operation. Therefore, a producer for each device is required. Further, dedicated data collectors could be integrated. But, due to the performed offline data analysis, there is no need for it. Hence, data of the DUT and time reference layer were collected by MARS and stored in a `hdf5` data format. The conversion necessary for the offline analysis is described in section 9.2.2.
Following the detailed description in [151], a producer module was developed [2]. Its task is to establish an interface between the EUDAQ2 and MARS DAQ. Hence, both systems have to know each other. Therefore, the python interface of the EUDAQ2 system is used.
The developed producer offers several functions essential to operate the DUT using the available **G**raphical **U**ser **I**nterface GUI. Initialization, configuration, start/stop of a run, data handling and status information are implemented. In addition, not only single scans can be started but also scan routines.

[2] For the time reference layer a similar producer was developed. Due to the similarities only the DUT producer is described.

The integration of the MARS DAQ system was fully commissioned during the testbeam campaign and led to the results presented in section 9.3 and section 9.4.

9.2.2 Integration of MARS into the Corryvreckan Testbeam Analysis Framework

For the offline data analysis the `Corryvreckan` [135] framework is used - a dedicated testbeam data analysis system. It offers a wide range of analysis options and the integration of the EUDET-type testbeam telescopes. Several event loader modules are available, required to load the data of the corresponding device and further process it. For data collected with the EUDAQ2 data collector, in this case the data collected by the TLU and telescope, the available event loaders were used. A new event loader based on an existing `hdf` event loader [152] was developed because the style of data format of the MARS DAQ system differed compared to the expected input in [152].
Its task is to convert the collected data into a `root` data format. Main information used within the offline analysis are timestamp and spatial information. Besides, timestamps from the DUT, also scintillator and FPGA timestamps (according to section 5.3) are stored by MARS and converted by the event loader.
The converted data format is used for the reconstruction of tracks - required for the efficiency studies presented in section 9.3 and time resolution determination in section 9.4.

9.3 Efficiency Studies of TelePix2

Studying the hit-efficiency is mandatory to determine the performance of the DUT. A hit-efficiency ≥ 99 % of the MightyPix over its sensitive area is required to ensure efficient tracking essential for LHCb's Upgrade II physics program.
With `Corryvreckan` the determination of the hit-efficiency of the complete device or for a dedicated **R**egion-**o**f-**I**nterest ROI or single pixels, called in-pixel efficiency, is possible. The efficiency is defined as

$$\epsilon = \frac{k}{N} \tag{9.1}$$

with the number of tracks k associated with a hit in the DUT and the total number N of all reconstructed tracks passing the DUT. The errors are calculated with the Clopper-Pearson method [153].
Due to imperfect alignment of the DUT, the time reference layer and the telescope sensors, a ROI is defined based on their overlapping physical coverage. Further, noisy pixels are masked and excluded from the track reconstruction.
Important for the later operation of the sensor at the Mighty-Pixel is to know the optimal working point. Therefore, the efficiency has been studied in dependence of the comparator threshold and different types of radiation damage. Before the discussion of the results the analysis procedure is explained.

9.3.1 Analysis Procedure

In the following the analysis procedure, used to determine the hit-efficiency and time resolution of the DUTs, is introduced. To reconstruct a particle track, the hit position at each layer must be known.
Each detection layer must provide adequate spatial overlap with the others, and their positions must be precisely known. In the first step, a physical alignment of all layers (telescope, time reference and DUT) is performed. However, mismatches and rotations may still occur. These are corrected during the offline analysis.
The offline analysis begins with aligning the telescope, where the telescope geometry is emulated to reproduce its configuration. `Corryvreckan` offers a geometry file for this purpose. All positions, rotation angles and further information, e.g. a masks for noisy pixels, are defined.
Proper alignment of the telescope - and later the DUT - can be validated through correlation plots. If a correlation is observed between a layer and a defined reference layer (for this analysis the first telescope layer was chosen), a fine alignment is performed as a second step. Accurate alignment is crucial, since slight misalignments can cause wrongly associated pixels - deteriorating the track reconstruction.
Once the telescope is aligned, the DUT is aligned with respect to the reference layer.

How the correlation and alignment procedure are done, is explained in the following.

Correlations

Examples of the correlation between the telescope reference layer (in this analysis the first layer of the telescope is chosen) and another telescope layer and the DUT are presented. The goal is to observe a correlation - crucial to ensure a spatial alignment of the telescope layers and the DUT. To verify the correlation, a comparison in global units and local units is performed.
In fig. 9.6 the correlation in local units of the telescope sensor columns of the telescope is depicted. Similar, the correlation of the rows is presented in fig. 9.7. For both, a clear correlation is visible. However, due to a non-perfect alignment the correlation does not originate in column/row (0/0) but is slightly shifted. A correction is performed in the alignment.

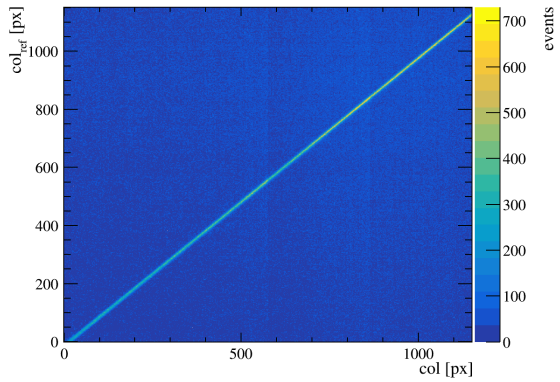


Figure 9.6: Example of a column-column correlation of a MIMOSA layer with the telescope reference layer.

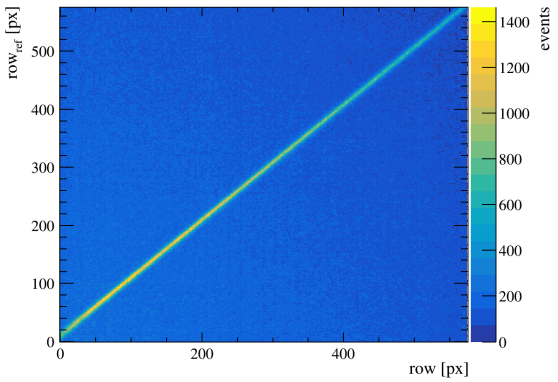


Figure 9.7: Example of a row-row correlation of a MIMOSA layer with the telescope reference layer.

Similar, the correlation of the columns of the DUT with those of the reference layer and the row correlation are shown in fig. 9.8 and fig. 9.9. Due to a different matrix arrangement, the correlation does not origin at (0,0). In addition, a misalignment, which is corrected for at a later step, is observed.

Further, data quality assurance is done by investigation of the global correlation in x, y of the DUT and telescope layer with the reference layer. An example of both the second MIMOSA layer and the telescope reference layer are shown in fig. 9.10 and fig. 9.11.
Since the correlation shows the spatial difference of clusters on the reference layer and any telescope layer, a peak around 0 mm is expected - validated by the presented measurements. It does not have to be centered around zero due to a physical displacement. The peak position is shifted for downstream layers due to a physical misalignment of the up- and downstream telescope arms. Additionally, a triangular background due to random coincidences of both is

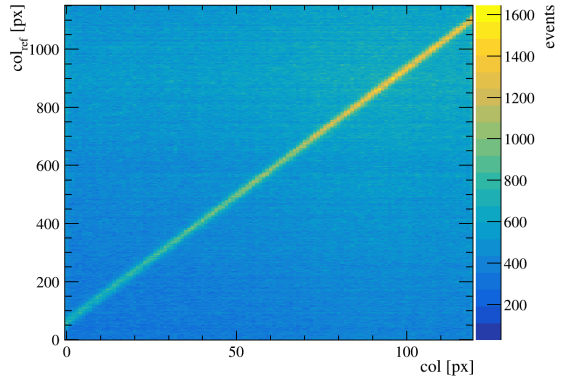


Figure 9.8: Example of a column-column correlation of the DUT with the telescope reference layer.

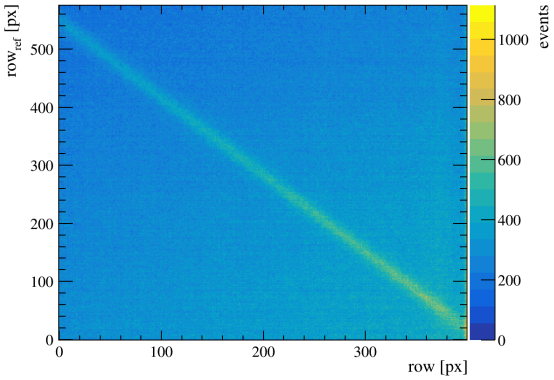


Figure 9.9: Example of a row-row correlation of the DUT with the telescope reference layer.

observed.

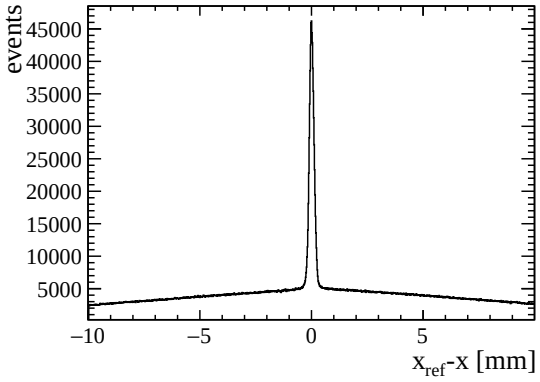


Figure 9.10: Example of the correlation in x of a MIMOSA layer with the telescope reference layer.

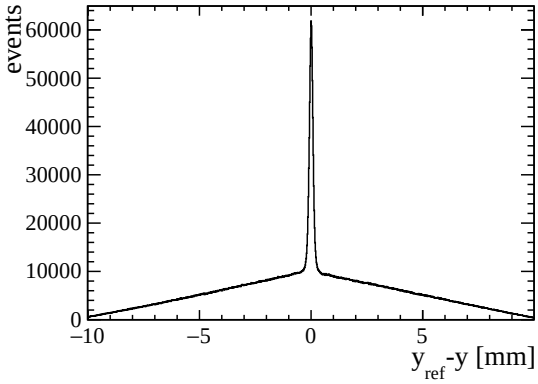


Figure 9.11: Example of the correlation in y of a MIMOSA layer with the telescope reference layer.

In addition, the width of the correlation increases for downstream layers due to multiple scattering, as evident in the correlation of the DUT and the time reference layer shown in fig. 9.12 and fig. 9.13. Nevertheless, all layers validate the expected correlations such that a track reconstruction is possible. Next, the alignment procedure is described.

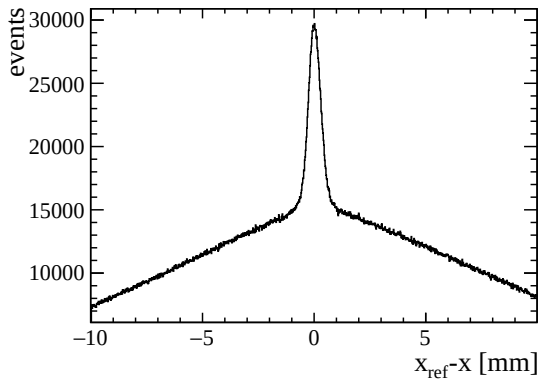


Figure 9.12: Example of the correlation in x of the DUT layer with the telescope reference layer.

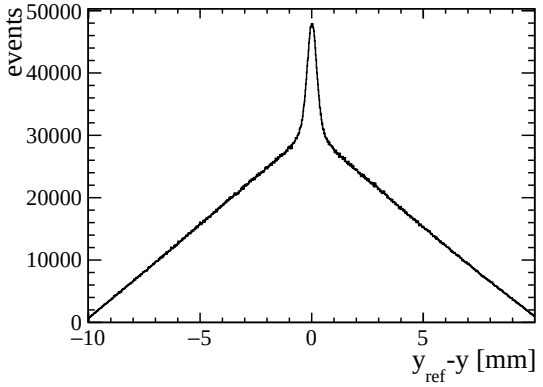


Figure 9.13: Example of the correlation in y of the DUT layer with the telescope reference layer.

Alignment

The telescope is aligned in software to mitigate physical misalignment and rotations - crucial for a high track quality. Once the telescope is aligned with respect to the reference layer, the DUT is aligned with respect to it. Therefore, a similar alignment procedure is executed. At each step a **G**eneral **B**roken **L**ine GBL fit is performed to reconstruct a track (more information is provided in [135]). To optimize the track quality, the residuals are evaluated to center them around zero. The residuals for the aligned DUT are shown in fig. 9.14 and fig. 9.15. The width of the distribution is determined by the spatial resolution of the DUT convolved with the track resolution of the telescope at the position of the hit in the DUT. A worse resolution in x than in y is observed due to a worse spatial resolution of $\sigma_x \approx 47.6\,\mu\text{m}$ for a pixel pitch of 165 µm of TelePix2 compared to $\sigma_y \approx 7.2\,\mu\text{m}$ for a pixel pitch of 25 µm in y.
If the DUT is well aligned, the residuals are centered around zero. Next, cuts for the tracking algorithm have to be defined.

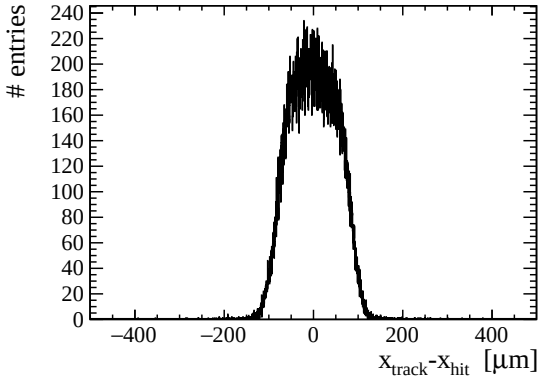


Figure 9.14: Residuals of the aligned DUT with respect to the telescope reference layer in x.

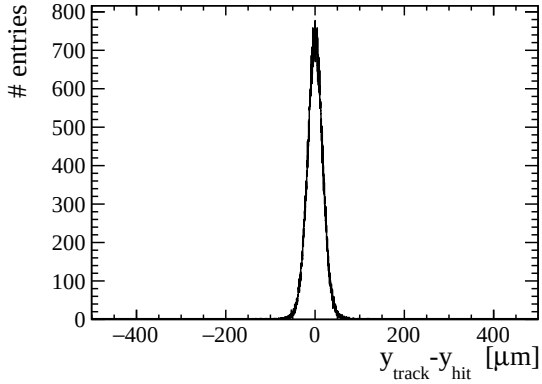


Figure 9.15: Residuals of the aligned DUT with respect to the telescope reference layer in y.

Cut Selection

`Corryvreckan` offers the definition of various cuts at different reconstruction steps to optimize the track reconstruction.
To associate clusters in the DUT to a reference with high quality, several cuts can be optimized to improve the quality. An iterative optimization has been performed with the goal to obtain the most accurate hit-efficiency.
Therefore, the spatial cuts in x, y, the cut on the allowed time window and the χ^2/DoF of the reconstructed tracks were analyzed. For each, the cut was varied and the hit-efficiency calculated. The best found cut values have been applied to all studies for all DUTs.
In fig. 9.16 the cut optimization of the spatial cut in x and fig. 9.17 in y are presented. Both show an overall high efficiency for all tested values besides a slight decrease at lower values. Since the spatial cut defines an ellipse of the maximum allowed spatial distance between clusters on the DUT and a reference track, a lower value reduces the search window and results in a worse efficiency. On the other hand, the search window is enhanced by softening of the cut. Further opening of the search window would not be beneficial because the probability for fake tracks would increase.

In the same way the time cut is optimized. By the time cut the maximum allowed time difference between a DUT cluster and reference track is defined. Figure 9.18 shows a decrease in efficiency for a hard time cut due to less events being within the allowed time window. If the time cut is lower than 115 µs, hits collected within one readout frame of the MIMOSA26 sensors would be cut. Hence, the time cut should be at least one readout frame long.
With the optimized spatial and time cut, the χ^2/DoF of the track is studied, shown in fig. 9.19. Since the track quality can be proven by χ^2/DoF, a low value yields a high quality. As a consequence, tracks with high χ^2/DoF worsen the efficiency. Because of that tracks with $\chi^2/\text{DoF} \geq 4$ are excluded from the analysis.

A summary of all final cuts is presented in table 9.2. Besides the previously discussed cuts

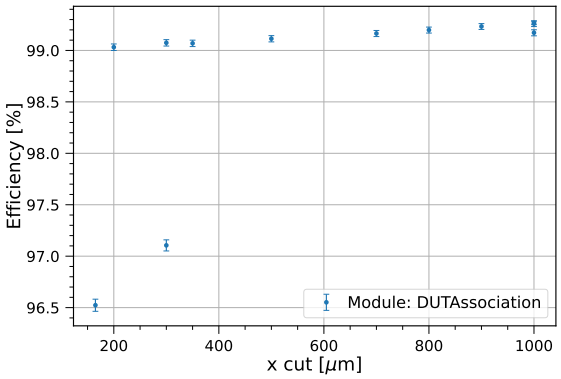


Figure 9.16: Hit efficiency versus spatial cut in x.

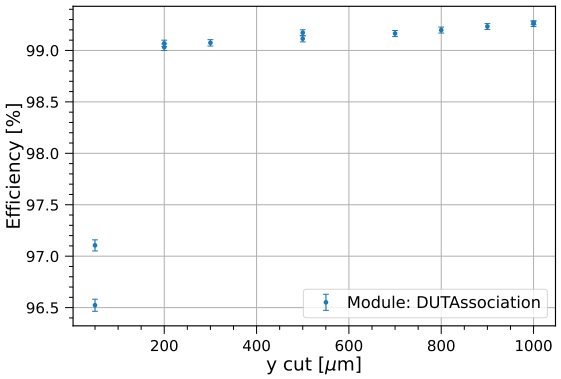


Figure 9.17: Hit efficiency versus spatial cut in y.

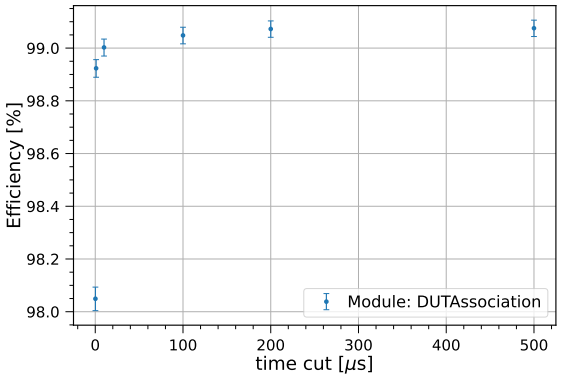


Figure 9.18: Hit efficiency versus time cut.

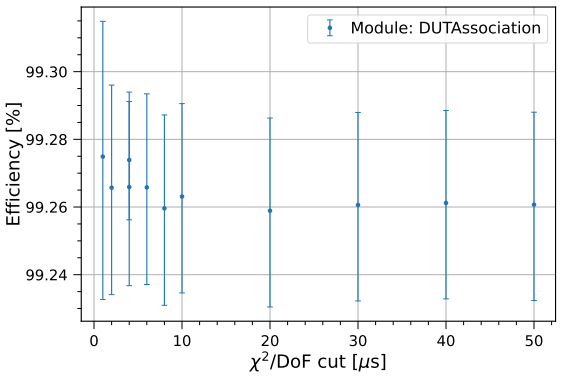


Figure 9.19: Hit efficiency versus χ^2 cut.

for the analysis of the DUT, cuts for the telescope track reconstruction have been optimized as well. Although the track reconstruction is done without the DUT, the spatial cuts are driven by the pixel pitch of TelePix2 because the time reference layer is included in the tracking and clusters are required. If the time reference layer would not have been needed, the spatial cuts would be stricter due to the better spatial resolution of the MIMOSA26 sensors.

Corryvreckan Module	Cut	Value
Tracking	Spatial	300 µm, 300 µm
Tracking	Time	120 µs
DUTAssosciation/DUTAnlysis	Spatial	1 000 µm, 1 000 µm
DUTAssosciation/DUTAnlysis	Time	200 µs
DUTAssosciation/DUTAnlysis	χ^2/DoF	4

Table 9.2: Summary of chosen cuts for the Corryvreckan testbeam analysis.

A final remark on the time cut for the time resolution analysis has to be made. For each scan, jumps in the timestamps for all TelePix2 sensors have been observed without any

correlation between the DUT and the time reference layer (see appendix A.10). Such a behavior was never observed in the laboratory when the FPGA clock is used as input for the PLL. At the testbeam the TLU clock was used instead. A possible explanation could be an instability of the input clock which cannot by handled by MARS's firmware properly. An improved termination of the input clock could solve the issue.
Since the observed jumps are in the order of $\mathcal{O}(\text{ns})$, a correction is not possible. As a trade-off a harsh timestamp cut of 15 ns was applied and runs, where the cut is not sufficient, excluded from the analysis.

9.3.2 Hit-Efficiency of TelePix2

With the discussed cuts the hit-efficiency has been studied in dependence of the comparator threshold and radiation damage. For all measurements the DUT was cooled, such that the leakage current was on the order of $\mathcal{O}(10 \text{ to } 20\,\mu\text{A})$ per sensor, corresponding to a PCB temperature of $\approx -40\,^{\circ}\text{C}$ for the proton irradiated devices. For the x-ray irradiated and non-irradiated devices warmer temperatures were sufficient. For all, the set temperature cannot be taken as a reference for the operation of the Mighty-Pixel due to TelePix2 large self-heating (see section 4.2.4 for more information). However, a trend towards low temperatures for the operation of irradiated devices can be derived. Similar to measurements performed in the laboratory (see chapter 6, chapter 7, chapter 8), the DUTs had too high leakage currents at higher temperatures and were non-operational.
For all devices the bias voltage was set accordingly to the results obtained in the laboratory. A standard bias voltage of $U_{chip} = -120\,\text{V}$ was applied for the non-irradiated device, a reduced voltage of $U_{chip} = -100\,\text{V}$ for the 40 MRad DUT and an increased voltage of $U_{chip} = -180\,\text{V}$ for the $1 \times 10^{14}\,\text{MeV}\text{n}_{\text{eq}}\text{cm}^{-2}$ DUT.
As mentioned in section 7.2.2 and the beginning of the chapter, issues with the $3 \times 10^{14}\,\text{MeV}\text{n}_{\text{eq}}\text{cm}^{-2}$ DUT were observed. In contrast to preparatory laboratory measurements before the testbeam campaign, the DUT could not be biased close to the breakdown via the chip bias contact because of too high leakage currents. Bias voltages of at least $U_{chip} = -170\,\text{V}$ or $U_{chip} = -180\,\text{V}$ (see table 9.1) would are required to operate the DUT efficiently. Due to the high leakage the operation was not possible. Biasing the DUT via the pixel ring was possible up to $U_{pix} = -70\,\text{V}$ and a minimum comparator threshold of 155 DAC units. However, from laboratory measurements (see section 7.2.1) a worse correlation between chip and pixel bias is known for irradiated devices. Further, the DUT must be biased via the chip bias contact to ensure a deep depletion and efficient charge collection. Therefore, biasing via the pixel contact is not sufficient to operate the DUT with a high hit-efficiency. In addition, the obtained occupancy, presented in fig. 9.20, showed a horseshoe-shaped pattern with low occupancy in the central region and high in the outer parts of the pixel matrix.
At later laboratory measurements (see fig. 7.16), the behavior could be validated. However, biasing via the chip contact is possible in the laboratory due to a better cooling of the DUT.

From the measurements, a too high operation temperature at the testbeam is concluded. As a consequence, neither hit-efficiency nor time resolution measurements of this device are discussed.

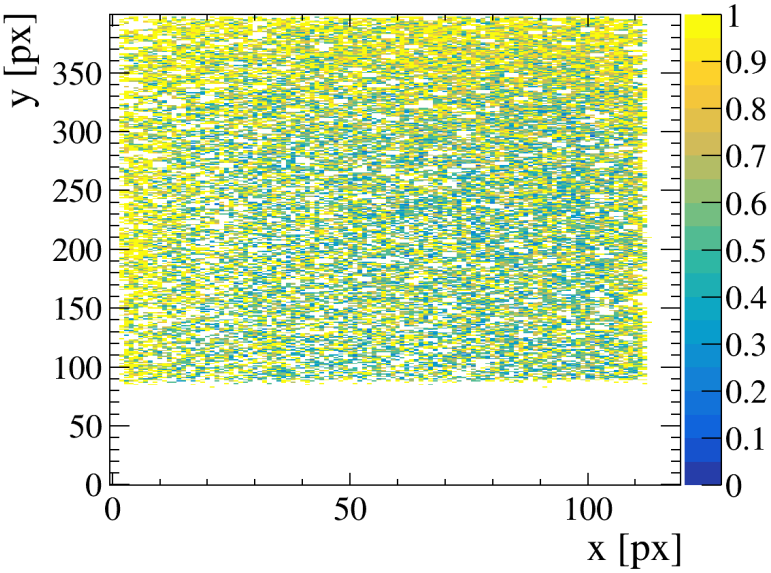


Figure 9.20: Efficiency map of the up to $3 \times 10^{14}\,\mathrm{MeVn_{eq}cm^{-2}}$ proton irradiated DUT biased by $U_{pix} = -70\,\mathrm{V}$ and a comparator threshold of 168 DAC units. An inefficient region in the central part is visible.

In contrast, a homogeneous occupancy over the full matrix was observed for the non-irradiated, $1 \times 10^{14}\,\mathrm{MeVn_{eq}cm^{-2}}$ proton irradiated and 40 MRad x-ray irradiated DUTs. In figs. 9.21 to 9.23 the efficiency maps of those devices are presented. For each, the result obtained at the lowest possible comparator threshold is shown. Noisy pixels are masked white.
No inefficient region is observed for any of the DUTs. In agreement with the hit-efficiency curve, presented in fig. 9.24, the irradiated devices show a more homogeneous efficiency compared to the non-irradiated TelePix2. An explanation is provided in the corresponding discussion.

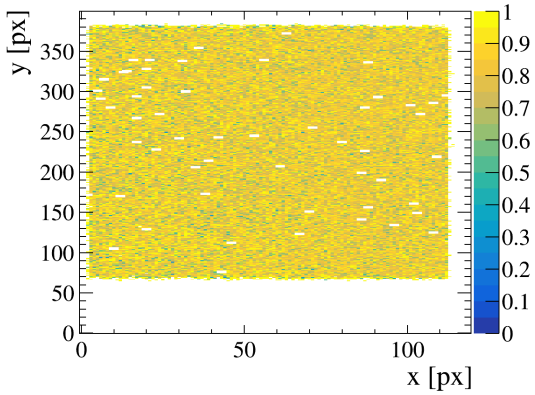


Figure 9.21: Efficiency map of the non-irradiated DUT biased by $U_{chip} = -120\,\mathrm{V}$ and a comparator threshold of 145 DAC units.

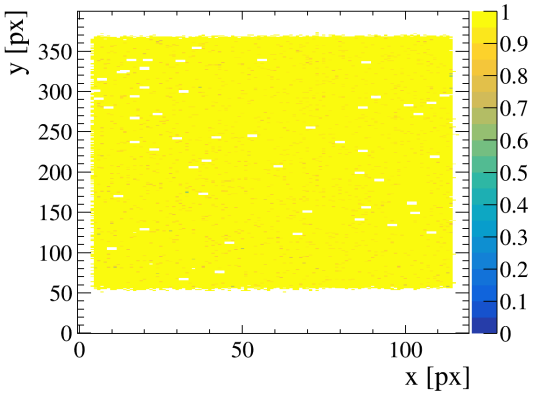


Figure 9.22: Efficiency map of the up to 1×10^{14} $\mathrm{MeVn_{eq}cm^{-2}}$ proton irradiated DUT biased by $U_{chip} = -180\,\mathrm{V}$ and a comparator threshold of 153 DAC units.

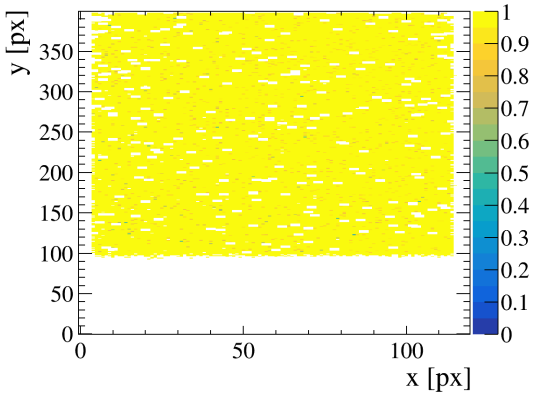


Figure 9.23: Efficiency map of the up to 40 MRad x-ray irradiated DUT biased by $U_{chip} = -100\,\mathrm{V}$ and a comparator threshold of 143 DAC units.

The result of the hit-efficiency in dependence of the comparator threshold is shown fig. 9.24.

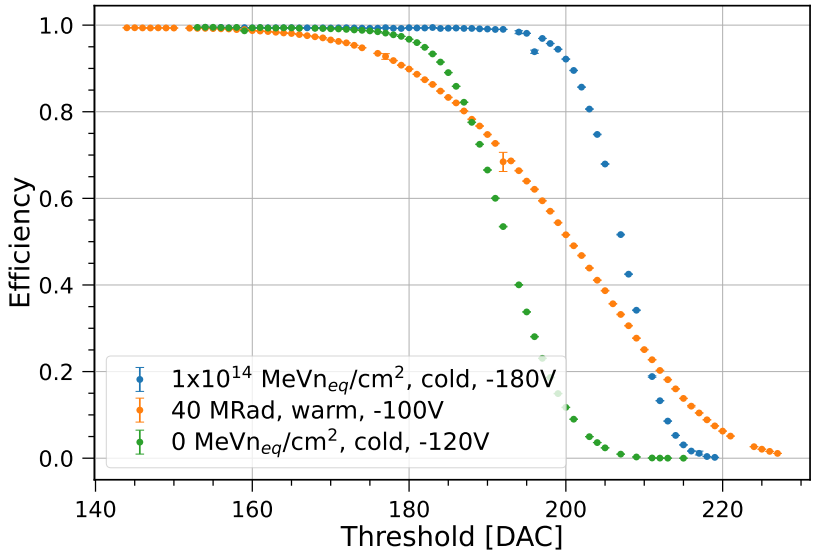


Figure 9.24: Comparison of the hit-efficiency for the different irradiated TelePix2 sensors in dependence of the comparator threshold. The DUTs have been biased close to their breakdown.

Coloured in green the efficiency of the non-irradiated device is shown. With increasing comparator threshold the efficiency decreases because only signals with a large charge deposition have a signal above the threshold. Hence, the efficiency decreases. The minimal possible comparator threshold is defined by the noise level of the DUT. But due to a saturation of the MARS DAQ system the limit could not be reached. As a consequence, the minimal possible threshold was at approximately 150 DAC units. The issue was solved during the testbeam campaign by increasing the data buffers in the firmware such that higher particle rates can be processed with MARS. Because of time constraints the measurement could not be repeated with the optimized firmware.
Nevertheless, an efficiency of $\geq$ 99 % could be measured for the non-irradiated TelePix2 sensor.
A wider efficiency plateau is observed for the TelePix2 sensor irradiated with protons up to a fluence of 1×10^{14} MeVn$_{\text{eq}}$cm^{-2} (colored in blue in fig. 9.24). Since the depletion region increases for the higher bias voltage, following fig. 7.6, the charge is collected more efficiently and a larger amount of signal is generated. Therefore, a better performance is obtained.
In contrast, no change in the efficiency plateau is observed for the x-ray irradiated device (colored in orange) but a change in the slope of the efficiency-curve. In addition, lower comparator thresholds are possible. Two reasons are responsible for this:
Firstly, the mentioned firmware improvement was implemented at the point when the measurement was conducted. Secondly, lower threshold voltages have been measured for z-curve measurements in the laboratory, too (see section 8.4.6 for comparison). As discussed in section 8.4.6, lower thresholds might be possible due to a reduced amplifier gain as a

consequence of TID damage of the involved transistors - resulting in a lower possible transistor threshold. Moreover, the changed slope of the efficiency curve can be explained by increased leakage currents of the transistors effecting their performance.
In fact, the obtained efficiency of $98.74^{+0.02}_{-0.02}$ % [3] of the TID DUT at a comparator threshold of 160 DAC units is worse compared to the obtained efficiency of $99.35^{+0.01}_{-0.01}$ % of the non-irradiated DUT at the same comparator threshold. Hence, the hit-efficiency is probably altered due to TID.
By lowering the comparator threshold to 145 DAC units a hit-efficiency of $99.34^{+0.01}_{-0.01}$ % was measured. Consequently, changes in the DUT operation due to radiation damage are beneficial to maintain the required hit-efficiency. However, a thorough understanding of this effect is essential, as the detector contains a large number of sensors, and adjusting the sensor configuration on a per sensor level entails significant overhead. If the configurations have to be adjusted too frequently, the adjustment may not be feasible.
Additionally, an investigation of the effect must be done with MightyPix2, as the TID damage might differ compared to TelePix2. In addition, the observation has to be further investigated to understand the changed slope.

[3] The asymmetric error is obtained by the Clopper-Person method.

9.4 Time Resolution Studies of TelePix2

Besides the hit-efficiency, the time resolution of TelePix2 in dependence of the comparator threshold and radiation damage has been studied with the goal to obtain a time resolution of ≤ 3 ns as required for the MightyPix.
To do so, the time difference ΔT of the time when a hit is detected by the DUT T_{hit} and a reference are needed. The reference is determined by the timestamp of the reconstructed track T_{track}, resulting in

$$\Delta T = T_{\text{track}} - T_{\text{hit}} \quad . \tag{9.2}$$

Usually, the track timestamp is provided by the scintillators causing a trigger signal and further processed by the TLU. Because of the TLU configuration the TLU frequently entered 'busy' mode, resulting in fewer trigger timestamps being sent by the TLU than by the DUT. Therefore, too less statistics from the TLU is available for a time resolution analysis. For future testbeam campaigns the observed issue has to be eliminated. A possible solution is to configure the TLU such that all received busy signals will be ignored.
As an alternative, the timestamp information of the time reference layer is used to associate time information to the reconstructed track. Since the measured time difference is the total value of all time resolutions, it includes the intrinsic DUT and time reference time resolution and binning effects (see section 6.3.3 for a detailed explanation of how to correct binning effects). Therefore, the intrinsic time resolution of the time reference layer is mandatory to be known to correct for it. The following procedure explains how the intrinsic time reference resolution was determined:
The DUT TelePix2 and time reference TelePix2 sensors have been configured similarly and the time resolution σ_{TR} of the time reference layer was determined at its nominal comparator threshold of 147 DAC units by

$$\sigma_{\text{TR}} = \sqrt{\frac{\sigma_{\text{total}}^2}{2} - \left(\frac{5\,\text{ns}}{\sqrt{12}}\right)^2} \tag{9.3}$$

including the total measured time resolution σ_{total} and a timestamp binning of 5 ns of each device. An intrinsic time resolution of the time reference layer of $\sigma_{\text{TR}} \approx 2.71$ ns resulted - used as a correction parameter in all time resolution studies.
Due to issues of the time reference layer recorded at the end of the testbeam campaign, only results for the non-irradiated and $1 \times 10^{14}\,\text{MeV}\text{n}_{\text{eq}}\text{cm}^{-2}$ device are shown and not for the TID sensor.
The issue was observed in the time correlations in the offline analysis. Because of unknown reasons a shoulder (see appendix A.10) in the time correlation occurred - worsening the intrinsic time resolution. A reasonable correction could not be determined.

Measurements in the laboratory using the same device did not show the behavior. Reconfiguration and power cycling during the testbeam campaign could probably have solved the issue.
The presented results of the measured time resolution of TelePix2 were only corrected for binning effects and the intrinsic time reference layer. No further corrections as row, column and ToT (see section 6.3.3 for more information about those) have been done due to several reasons:
Firstly, the corrections, especially the ToT correction, are not feasible for the experiment because its too time consuming. Secondly, the time reference layer and DUT have the same pixel matrix design such that row and column dependencies cancel out in the time reference. Thirdly, as shown in section 6.3.3, the effect of row/column correction on the time resolution is minor and lastly, the corrections are not essential because the determined time resolution does fulfill the requirements without.

9.4.1 Time Resolution of TelePix2

The dependence of the uncorrected time resolution (colored in gray) and corrected (colored in blue) on the comparator threshold is shown in fig. 9.25. As reference the required 3 ns time resolution is indicated in red. Further, the comparator threshold is calibrated in mV using the calibration measurement presented in fig. 6.2.

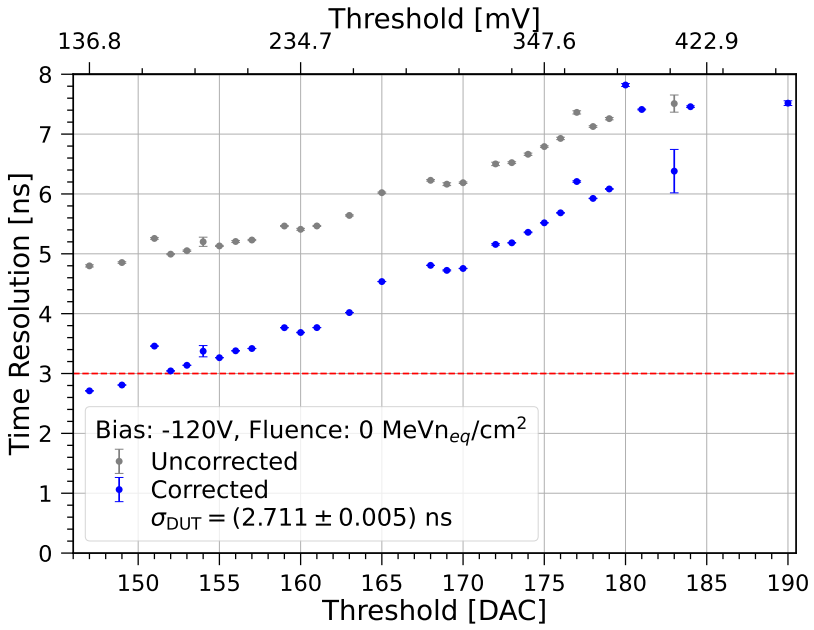


Figure 9.25: Dependence of the intrinsic time resolution on the comparator threshold of a non-irradiated TelePix2 sensor biased to $U_{chip} = -120$ V. The required 3 ns time resolution is indicated by a red line. The statistical uncertainties are included. Due to fluctuations in the measurement some outliers are visible.

Only at low comparator thresholds the required 3 ns are fulfilled. Since the time resolution is not timewalk corrected, the increasing timewalk for higher thresholds worsens the time resolution. In addition, fewer signals surpass the detection threshold and those exceeding it exhibit a later ToA - explained in the following: For high detection thresholds, small variations in the signal peak have a greater effect on the ToA information (use fig. 6.25 for comparison) resulting in a degraded time resolution. The behavior is compatible with the time resolution measured in the laboratory. A detailed comparison is given in section 9.4.2.
In the same way the time resolution of the TelePix2 sensor - exposed to a fluence of $1 \times 10^{14}\,\mathrm{MeVn_{eq}cm^{-2}}$ - was measured. Due to time constraints the dependence on the comparator threshold was only measured for the high bias voltage scenario of $U_{\mathrm{chip}} = -180\,\mathrm{V}$ and not for the standard bias voltage.
Figure 9.26 shows the obtained intrinsic time resolution in dependence of the threshold. The required time resolution of 3 ns is again indicated by a red line.
Overall, a time resolution of $\leq$ 3 ns for a wide comparator threshold range is measured. Furthermore, an improved minimal time resolution of (1.835 ± 0.001) ns is determined at the lowest possible comparator threshold of 149 DAC units.
The improvement can be explained by the higher bias voltage, which reduces the drift time and drastically improves the charge collection efficiency. Reduction of the timewalk effect can be explained by a stronger electric field, reducing the drift time, and a larger depletion region, enhancing the amount of collected signal.

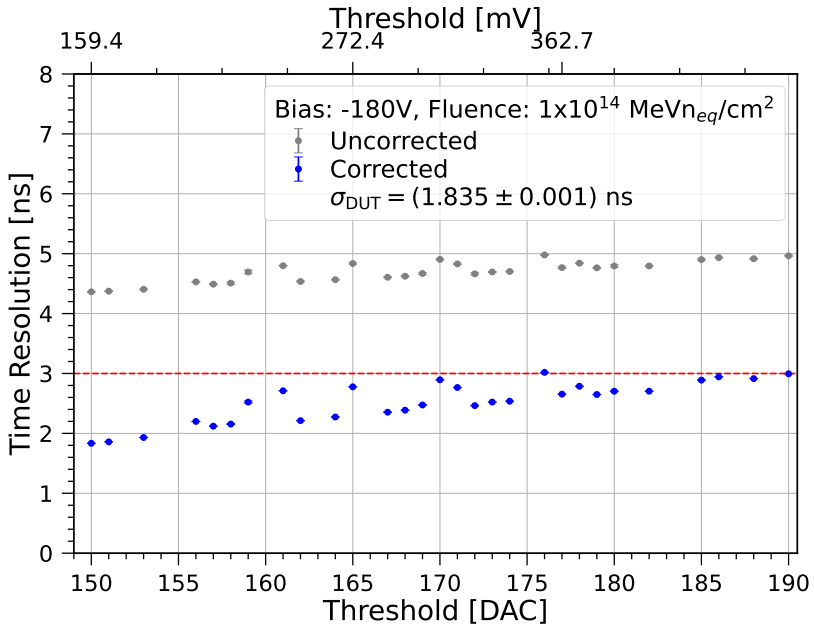


Figure 9.26: Dependence of the intrinsic time resolution of a TelePix2 sensor exposed to a fluence of $1 \times 10^{14}\,\mathrm{MeVn_{eq}cm^{-2}}$ biased to $U_{\mathrm{chip}} = -180\,\mathrm{V}$ on the comparator threshold. The required 3 ns time resolution is indicated by a red line. The statistical uncertainties are included.

In summary, both time resolution measurements demonstrate the usability of HV-MAPS at the Mighty-Pixel in terms of time resolution up to a fluence of 1×10^{14} $\mathrm{MeVn_{eq}cm^{-2}}$.

9.4.2 Comparison with Laboratory Measurements

How comparable the testbeam and laboratory measurements are, is discussed in the following. A summary of the best time resolution of TelePix2 for each measurement type is given in table 9.3. Results marked in red and blue are intended for comparison.

Type	Fluence	DACs	Bias	Threshold	Time resolution
Laboratory	-	Best	−130 V	142 DAC units	(2.04 ± 0.01) ns
Laboratory	-	Best	−120 V	145 DAC units	(2.07 ± 0.01) ns
Laboratory	-	Standard	−120 V	145 DAC units	(2.53 ± 0.01) ns
Laboratory	1×10^{14} MeVn$_{eq}$cm^{-2}	Best	−210 V	145 DAC units	(1.97 ± 0.01) ns
Laboratory	1×10^{14} MeVn$_{eq}$cm^{-2}	Best	−120 V	145 DAC units	(2.41 ± 0.02) ns
Laboratory	1×10^{14} MeVn$_{eq}$cm^{-2}	Standard	−120 V	145 DAC units	(2.72 ± 0.05) ns
Laboratory	1×10^{14} MeVn$_{eq}$cm^{-2}	Standard*	−180 V	149 DAC units	(2.38 ± 0.02) ns
Laboratory	3×10^{14} MeVn$_{eq}$cm^{-2}	Best	−120 V	150 DAC units	(2.58 ± 0.01) ns
Laboratory	3×10^{14} MeVn$_{eq}$cm^{-2}	Standard	−120 V	150 DAC units	(3.28 ± 0.02) ns
Laboratory	40 MRad	Best	−100 V	140 DAC units	(2.35 ± 0.01) ns
Laboratory	40 MRad	Best	−100 V	145 DAC units	(2.52 ± 0.01) ns
Laboratory	40 MRad	Standard	−100 V	145 DAC units	(3.01 ± 0.01) ns
Testbeam	-	Standard	−120 V	147 DAC units	(2.711 ± 0.005) ns
Testbeam	1×10^{14} MeVn$_{eq}$cm^{-2}	Standard*	−180 V	149 DAC units	(1.835 ± 0.001) ns

Table 9.3: Summary of the time resolution of TelePix2 obtained by all conducted measurements. Details about the DAC configurations (Standard, standard*, best) are provided in appendix A.11.

As discussed in section 8.4.5 the time resolution worsens keeping the standard bias voltage and standard DAC settings with radiation damage. For bulk damage the worsening can be mitigated by increasing the bias voltage and thus, decreasing the probability of charge trapping and enhancing drift times. For surface damage the worsening cannot be corrected by changing properties concerning the sensor bulk since the damage effects the sensor electronics. Therefore, adjusting the comparator threshold and sensor configuration is needed to improve the time resolution. Optimizing the sensor configuration in general improves the time resolution for all three devices characterized in the laboratory taking an increased power consumption into account.
Results obtained at the testbeam campaign are in the following compared to those from the laboratory (see colored results in table 9.3). For the non-irradiated device similar DAC settings have been used. At a slightly higher comparator threshold set at the testbeam a slightly worse time resolution compared to the laboratory measurement is obtained validating the agreement of both.
For the irradiated device a deviation between the testbeam and laboratory measurement with similar settings is observed. At a comparator threshold of 149 DAC units, testbeam DAC settings, marked as Standard* (an overview of the different sensor configurations is presented

in appendix A.11), and a bias voltage of $U_{\text{chip}} = -180\,\text{V}$ a time resolution of (2.38 ± 0.02) ns at a fluence of $1 \times 10^{14}\,\text{MeVn}_{\text{eq}}\text{cm}^{-2}$ is measured in the laboratory and (1.835 ± 0.001) ns at the testbeam. One possible explanation might be an over-correction of the testbeam measurement. But due to the agreement of the other measurements with each other an over-correction is not probable. Instead, another explanation can be found in the particle source. While the testbeam measurements were performed at an electron beam, a Sr-90 source has been used in the laboratory where parts of the emitted electrons are low-energy electrons traversing the measurement setup with a lower velocity [4]. However, the systematic effect would occur in all laboratory measurements. Therefore, further investigations are necessary to explain the discrepancy.

9.5 Summary

A time resolution of ≤ 3 ns and hit-efficiency of ≥ 99 % are required for the Mighty-Pixel up to a fluence of $3 \times 10^{14}\,\text{MeVn}_{\text{eq}}\text{cm}^{-2}$ and 40 MRad. Therefore, the performance has to be investigated.
In December 2024 a testbeam campaign at the DESY II testbeam facility was carried out using the predecessor of the MightyPix sensor - TelePix2. Its performance was studied with focus on the hit-efficiency and time resolution in dependence of the radiation damage. In table 9.1 a summary of all characterized devices is shown.
To operate the DUTs, the MARS DAQ system has been used which was fully commissioned as a testbeam DAQ system within the campaign. Integration of the system into the EUDAQ2 software framework was mandatory to configure the DUT and the testbeam EUDET-type telescope - equipped with MIMOSA26 sensors - at the same time. Further, scan routines are controlled by the EUDAQ2. For the offline data analysis the `Corryvreckan` software framework is used. Since a `root` type data input format is required, a MARS specific event loader had to be implemented. With the integration into both systems, the MARS DAQ system is fully operational as a testbeam DAQ system.
All measurements were done with the purpose to obtain the best possible performance. Therefore, the different DUTs were cooled to different temperatures depending on the radiation damage. As a consequence, the operating temperature of MightyPix remains undetermined. Hence, dedicated temperatures studies are crucial for MightyPix2.
The hit-efficiency and time resolution could not be studied for the TelePix2 sensor exposed to a fluence of $3 \times 10^{14}\,\text{MeVn}_{\text{eq}}\text{cm}^{-2}$. Because of high leakage currents, the DUT could not be biased efficiently. Later measurements in the laboratory have shown a similar behavior for non-sufficient cooling and hence, a high leakage current. Improved cooling is deemed necessary to ensure the DUT's operability.
For the other DUTs, a high hit-efficiency of $\geq 99\%$ was achieved. However, the hit-efficiency is affected by the type of radiation damage. Bulk damage changes the effective

[4] In [16] a detailed study of the Sr-90 energy spectrum has been done.

doping concentration, allowing a higher bias voltage and hence, improves the charge collection efficiency beneficially. In contrast, surface damage altered the behavior of the sensor electronics, affecting both the slope of the hit-efficiency curve and the comparator threshold range. An initial hypothesis based on laboratory measurements attributes the observations to increased transistor leakage currents and shifts in transistor threshold voltages (see appendix A.9.6 for more information). Nevertheless, further investigations are inevitable.
The time resolution has been determined for the non-irradiated and up to $1 \times 10^{14}\,\mathrm{MeV n_{eq} cm^{-2}}$ irradiated TelePix2 sensor. For each, a time resolution below the required 3 ns is measured:

$$\sigma_{\mathrm{non-irrad}} = (2.711 \pm 0.005)\,\mathrm{ns}$$
$$\sigma_{\mathrm{1e14}} = (1.835 \pm 0.001)\,\mathrm{ns} \quad .$$

While the result for the non-irradiated DUT is comparable with the measurements from the laboratory, as discussed in table 9.3, the results for the irradiated device differs. Further investigations are required to understand the discrepancy.
In summary, the performance of TelePix2 in dependence of the radiation damage was successfully studied and demonstrates usability of HV-MAPS in terms of hit-efficiency and time resolution of the MightyPix. Furthermore, the MARS DAQ system was successfully commissioned as a testbeam DAQ system.
For future testbeam campaigns the temperature dependence has to be taken into account. Moreover, the performance has to be studied for DUTs powered during a proton irradiation such that TID and NIEL damage occur at the same time. In addition, the noise rate and in-time efficiency have to be investigated. By in-time efficiency the efficiency of a hit being assigned to the correct bunch crossing is meant. Due to the mentioned timestamp jumps and time cut of 15 ns (see table 9.2) the in-time efficiency was not studied within this thesis.

CHAPTER 10

Conclusion and Outlook

The LHCb experiment located at the LHC at CERN will enter the HL-LHC era with the beginning of Run 5. To exploit the full flavor physics potential and enable unparalleled precision measurements of rare particle processes, the LHCb experiment has to undergo a major detector upgrade with the beginning of Long Shutdown 4.
Seeking answers for the matter-antimatter asymmetry, is one of several parts of the various physics program of LHCb. Measurements concerning the **C**harge-**P**arity CP condition of the **S**tandard **M**odel of particle physics are mandatory to explain the asymmetry. Designed as a beauty and charm-factory, LHCb found a first evidence for CPV in 2017 in the decay $\Lambda_b^0 \to p\pi^-\pi^+\pi^-$ and $\Lambda_b^0 \to p\pi^-K^+K^-$ with a significance of $3.3\,\sigma$ [39]. Further studies, using Run 1 and Run 2 data, have found hints for CPV in the charmed sector as well [42].
However, the significance of those and other CPV measurements conducted at LHCb are consistent with the SM and thus, not sufficient to claim CPV. Further exploration of CPV and its validation are only possible by improving the measurement significance. Therefore, more data is needed. The full physics potential of LHCb can only be exploited by an increase of the instantaneous luminosity. Hence, the instantaneous luminosity will by raised by one order of magnitude from $1 \times 10^{33}\,\mathrm{cm}^{-2}\mathrm{s}^{-1}$ to $1 \times 10^{34}\,\mathrm{cm}^{-2}\mathrm{s}^{-1}$ [1] with the start of Run 5, resulting in at least $300\,\mathrm{fb}^{-1}$ [5] collected data at the end of the detector's lifetime. Consequently, the mean number of hard proton-proton interactions per bunch crossing will increase from 6 to 40 [5].
Crucial for LHCb's physics program is the distinction of primary and secondary vertices belonging to one decay chain. An increased pile-up will degrade tracking accuracy. To ensure - and even exploit - the tracking accuracy, the full detector system must be upgraded, including radiation tolerant and high granularity detectors that provide fast time information. The Mighty-Tracker, consisting of the Mighty-Pixel and Mighty-SciFi detectors, is a key element of the Upgrade II detector. A radiation tolerance of up to $3 \times 10^{14}\,\mathrm{MeVn_{eq}cm}^{-2}$ NIEL and 40 MRad TID damage are required [5]. In addition, a time resolution of ≤ 3 ns and a hit-efficiency of $\geq 99\%$ are crucial to ensure the correct hit to bunch crossing association [5]. Investigation measurements on the performance of prototype HV-MAPS, planned to be

installed for the Mighty-Pixel, with respect to the Mighty-Pixel requirements have been presented within this thesis.
As a prototype sensor the TelePix2 sensor [6], developed as a Region-of-Interest Trigger for EUDET-type telescopes, has been characterized. The DUT offers a comparable analog pixel design to the MightyPix. Consequently, TelePix2 is an optimal candidate to execute performance studies.

The design of TelePix2 with respect to further predecessor HV-MAPS and the MightyPix has been introduced in chapter 4. Understanding the design of HV-MAPS was crucial to execute performance measurements and understand how to operate HV-MAPS. In addition, the understanding was mandatory to develop the DAQ system MARS (chapter 5) [7].
Due to non-existence of a DAQ systems covering all requirements foreseen to operate the MightyPix at the laboratory and at testbeam campaigns, the necessity to develop a new DAQ system arose.
MARS comprises a flexible and modular design approach including hardware, firmware and software and is dedicated for HV-MAPS within the Mighty-Pixel project. The goal to develop a flexible system usable in the laboratory and at testbeam campaigns was achieved by separating it into three building blocks and designing each component to be intrinsically modular.
Up to now three different HV-MAPS (Run2020, Run2021 and TelePix2) have been successfully implemented into MARS and are running in the laboratory. In addition, the DAQ system was embedded into an EUDET-type testbeam telescope at the DESY II [8] testbeam facility including not only a hardware implementation into the telescope but also a software implementation into the EUDAQ2 [142] testbeam software framework. Furthermore, an integration of the data obtained with MARS into the offline data analysis tool Corryvreckan [135] was realized. Both integrations have been discussed in chapter 9.
To summarize, MARS is a newly developed DAQ system and fully commissioned to be used for single chip testing in the laboratory and at testbeam campaigns. In the future, the potential of the system will be further exploited by implementation of other HV-MAPS, e.g. MightyPix2, and parallel configuration, operation and read-out of multiple HV-MAPS essential to characterize hybrids of the Mighty-Pixel where five sensors are placed on one PCB. In addition, MARS will be used at collaborating institutes for future R&D as part of the Mighty-Pixel project.

By the commissioning of MARS, the author could establish a diverse measurement program to study the performance of HV-MAPS. As stated previously, the TelePix2 sensor was the main characterized DUT. The sensor has a chip size of 20.015 x 13.130 mm^2 and a pixel size of 165 x 25 μm^2. In total, the pixel matrix consists of 120 columns and 400 rows. Each pixel is designed as an active pixel cell housing a CSA and comparator implemented in CMOS logic. The digital periphery is located at the bottom of the sensor with a line-to-line connection between the End-of-Columns buffers and pixel cells. TelePix2 was produced in a 180 nm process on a 200 to 400 Ω cm p-type Czochralski wafer at TSI [71].

Performance studies with the emphasis on non-irradiated, proton and x-ray irradiated TelePix2 sensors have been presented in chapters 6 to 8, respectively.

Measurements performed with non-irradiated DUTs had the additional goal to commission the MARS DAQ system (chapter 6). By calibration and performance measurements the system has been validated. In addition, a tuning algorithm to minimize the threshold dispersion was implemented and successfully tested.
The performance studies had the focus on the bias behavior of TelePix2 and time resolution measurements. Therefore, the TelePix2 bias structure, consisting of a pixel and chip bias ring, has been studied independent of each other and with respect to each other. As a main result, the breakdown of the sensor diode could be located in the vicinity of the p^+ implant of the pixel bias contact. Consequently, chip biasing had to be used to obtain the best possible performance of the DUT.
Development of a time resolution measurement and optimization of the obtained result, yielded a time resolution of $\sigma = (2.04 \pm 0.01)$ ns after all corrections were applied for a bias voltage of $U_{\text{chip}} = -130\,\text{V}$. A constraint in the time resolution due to a limited bias voltage was found. To exceed this constraint, the guard ring design has to be improved.

The radiation tolerance in terms of NIEL damage up to a fluence of $3 \times 10^{14}\,\text{MeVn}_{\text{eq}}\text{cm}^{-2}$ has been studied with TelePix2 (chapter 7). Therefore, a step-wise irradiation campaign starting at a fluence of $1 \times 10^{12}\,\text{MeVn}_{\text{eq}}\text{cm}^{-2}$ and ending at the target fluence has been performed at the Bonn isochronous cyclotron [10]. At each step sanity measurements examining the bias behavior were conducted. As a main result an increase of the leakage current with increasing fluence was measured following the NIEL scaling hypothesis. Similarly, a strong temperature dependence of the leakage current and an exponential increase with temperature were obtained. By investigation of the breakdown behavior and chip-to-pixel bias correlation, a change in the effective doping concentration with fluence following the theoretical expectations has been observed.
Further, the time resolution for TelePix2 exposed to a fluence of $1 \times 10^{14}\,\text{MeVn}_{\text{eq}}\text{cm}^{-2}$ of $\sigma = (1.97 \pm 0.01)$ ns using optimized sensor settings and applying a bias voltage of $U_{\text{chip}} = -210\,\text{V}$ was derived. Similarly, the time resolution at a fluence of $3{\times}10^{14}\,\text{MeVn}_{\text{eq}}\text{cm}^{-2}$ was measured. However, the measurement was dominated by the leakage current, limiting the bias to a maximum of $U_{\text{chip}} = -120\,\text{V}$ for the standard sensor configuration. As a result, a time resolution of $\sigma = (2.58 \pm 0.01)$ ns was obtained.
The leakage current was found to be the critical parameter. Therefore, an accurate temperature controlled measurement setup is essential for proton irradiated devices.
In summary, the effect of NIEL on the p-bulk substrate of TelePix2 was successfully investigated. From the Mighty-Pixel time resolution requirement point of view, the technology of HV-MAPS was successfully tested to be radiation tolerant.
In future, the measurement campaigns must be repeated with MightyPix2 with emphasis on the temperature dependence as well as power consumption.

To prove the radiation tolerance in terms of TID damage up to a dose of 40 MRad, multiple step-wise x-ray irradiation campaigns at the x-ray tube at the Bonn FTD [13] were performed (chapter 8). While three of them followed a high rate approach of 470 kRad h^{-1} (about 470× the peak rate at the Mighty-Pixel) to reach the target dose within a reasonable time, the Run2021 sensor was irradiated at a low rate of 6 kRad h^{-1} to study TID effects under more experiment-like conditions. At all campaigns the bias behavior and power consumption in dependence of the dose was studied. The on-chip DAC behavior was investigated in more detail at the low rate irradiation campaign. In addition, a long-term annealing study was conducted.
The expected TID peak at approximately 1 MRad was observed at all measurements independent of the irradiation rate. However, a difference in the peak power consumption depending on the rate but also on the used DUT and its settings has been determined. Due to variations between the measurements and between the used DUTs and the MightyPix, no statement on the exactly expected peak power consumption for the Mighty-Pixel can be made. Nevertheless, a simulation, showing the dependence of the peak power consumption on the irradiation rate, and hence, on the location of each MightyPix at the Mighty-Pixel for its full lifetime was set-up, based on the obtained results. From that can be concluded that TID damage has to be taken into account for the design of the Mighty-Pixel staves and, in particular, of the serial power chain.
Further, a measurement of the time resolution of a TelePix2 sensor exposed to a dose of 40 MRad was conducted. Using the optimized sensor configuration and a bias voltage of $U_{\text{chip}} = -100\,\text{V}$, a time resolution of (2.35 ± 0.01) ns was obtained.
From all irradiation campaigns an effect on the sensor electronics due to TID was observed. The most drastic changed was found in the comparator threshold range. After irradiation, the minimal possible comparator threshold was shifted towards lower values. A possible explanation might be a reduced amplifier gain or signal loss due to surface damage.
In future, the amplifier gain has to be investigated in more detail. In addition, further TID studies are foreseen to investigate the rate dependence as well as temperature dependence during the irradiation itself but also of the DUT under operation in more detail. In particular, TID damage has to be studied for the MightyPix since its effect depends heavily on the sensor design and manufacturer. Therefore, TID studies with MightyPix2 are unavoidable.

A measurement of the hit-efficiency and time resolution for all three kinds of TelePix2 sensors (non-irradiated, proton and x-ray irradiated) were conducted at the DESY II testbeam facility [8] (chapter 9). The MARS DAQ system has been commissioned at the testbeam campaign and used for the operation of all DUTs. For each a hit-efficiency of $\geq 99\%$ and time resolution for the non-irradiated and up to $1 \times 10^{14}\,\text{MeV}\text{n}_{\text{eq}}\text{cm}^{-2}$ proton irradiated devices of $\sigma \leq 3$ ns has been measured. All conducted time resolution measurements are compatible with those obtained in the laboratory. In addition, the leakage current and hence possible bias, being the limiting factor was confirmed.

In summary, the performance of several HV-MAPS with emphasis on their radiation

tolerance has been investigated within the Mighty-Pixel project using the newly developed MARS DAQ system. All measurements have shown the success of the technology and its usability for the Mighty-Pixel in terms of radiation tolerance and time resolution. Furthermore, the foundation was established in Bonn to enable detailed characterization of the MightyPix and related HV-MAPS.
However, there is a lot of work remaining. Among the objectives of the Mighty-Pixel project are investigations into temperature dependence, power consumption, the AMS aH18 production process, **S**ingle **E**vent **U**psets (SEUs), biased NIEL irradiations, comprehensive TID studies, characterization of hybrids and staves, as well as integration into the LHCb DAQ system and production and testing of all detector components.
To conclude physicists will always remain fascinated and driven by the desire to satisfy their curiosity. The Mighty-Pixel provides the opportunity to define challenges, to understand them, and to seek solutions in pursuit of the best possible outcome.
As a final remark, the work presented in this thesis has been guided by this principle, with the goal of contributing to the optimization of HV-MAPS for the Mighty-Pixel.

Bibliography

[1] The LHCb collaboration, *LHCb Upgrade II Scoping Document*, tech. rep., CERN, 2024, URL: https://cds.cern.ch/record/2903094 (cit. on pp. v, vii, 2, 13–15, 17–19, 21, 23–29, 121, 239).

[2] I. Perić, *A novel monolithic pixelated particle detector implemented in high-voltage CMOS technology*, Nuclear Instruments and Methods in Physics Research Section A: Accelerators, Spectrometers, Detectors and Associated Equipment **582** (2007) 876, VERTEX 2006, ISSN: 0168-9002, URL: https://www.sciencedirect.com/science/article/pii/S0168900207015914 (cit. on pp. v, vii, 2, 76).

[3] https://www.psi.ch/de/mu3e, Accessed: 2025-04-24 (cit. on pp. v, vii, 2, 77).

[4] https://adl.ipe.kit.edu/english/101.php, Accessed: 2025-04-24 (cit. on pp. v, vii, 77).

[5] The LHCb collaboration, *Framework TDR for the LHCb Upgrade II: Opportunities in flavour physics, and beyond, in the HL-LHC era*, tech. rep., CERN, 2021, URL: https://cds.cern.ch/record/2776420 (cit. on pp. v, vii, 2, 14, 15, 18–27, 29, 121, 155, 239).

[6] L. Huth et al., *TelePix2: Full scale fast region of interest trigger and timing for the EUDET-style telescopes at the DESY II Test Beam Facility*, 2025, arXiv: 2503.08177 [hep-ex], URL: https://arxiv.org/abs/2503.08177 (cit. on pp. v, vii, 2, 77, 80, 240).

[7] H. Schmitz, L. Dittmann, S. Neubert and K. Padeken, *Development of a new Readout System for HVCMOS Sensors for the LHCb Mighty Tracker*, Nuclear Instruments and Methods in Physics Research Section A: Accelerators, Spectrometers, Detectors and Associated Equipment **1065** (2024) 169491, ISSN: 0168-9002, URL: https://www.sciencedirect.com/science/article/pii/S0168900224004170 (cit. on pp. v, vii, 2, 4, 95, 240).

[8] R. Diener et al., *The DESY II test beam facility*,
Nuclear Instruments and Methods in Physics Research Section A: Accelerators, Spectrometers, Detectors and Associated Equipment **922** (2019) 265,
ISSN: 0168-9002, URL: https://www.sciencedirect.com/science/article/pii/S0168900218317868
(cit. on pp. 3, 80, 240, 242).

[9] K. Padeken, *The LHCb Mighty Tracker*, PoS **Pixel2022** (2023) 084,
URL: http://cds.cern.ch/record/2871825 (cit. on pp. 4, 33, 173).

[10] https://www.zyklotron.hiskp.uni-bonn.de/index.html,
Accessed: 2025-05-22 (cit. on pp. 4, 155, 157, 241).

[11] S. Rüssmann,
Studien zu Strahlenschäden an HVMAPS im Rahmen des LHCb Upgrade 2,
Bachelor thesis, 2025 (cit. on pp. 4, 163).

[12] N. Sommerfeld, unpublished thesis, expected 2027, PhD thesis: University of Bonn
(cit. on pp. 4, 163).

[13] https://github.com/SiLab-Bonn/X-ray_machine, Accessed: 2025-06-26
(cit. on pp. 4, 176, 242).

[14] M. M. Liebetrau, *Characterisation of Surface Damage Effects on HV-MAPS for the LHCb Mighty-Pixel Project*, 2025, URL: https://confluence.team.uni-bonn.de/spaces/PHYLHCB/pages/194478676/Finished+Projects?preview=/194478676/389160700/BachelorarbeitMax.pdf
(cit. on pp. 4, 181, 183, 193, 195, 196, 206–209).

[15] C.-D. Arslan, *Developments for the LHCb Mighty Tracker Readout System aiming at the Characterization of MAPS*, University of Bonn, 2023,
URL: https://uni-bonn.sciebo.de/s/duHHWnrsYwuoA46 (cit. on p. 4).

[16] N. Sommerfeld, *Design and Commissioning of a Silicon Chip Timing Setup*,
University of Bonn, 2023, URL: https://confluence.team.uni-bonn.de/display/PHYLHCB/Finished+Projects
(cit. on pp. 4, 103, 142, 143, 146, 236).

[17] J. P. Guenther,
Entwicklung einer hybriden Kühlung zum Betrieb von Silizium-Pixeldetektoren, 2024,
URL: https://confluence.team.uni-bonn.de/display/PHYLHCB/Finished+Projects (cit. on pp. 4, 100, 101, 141).

[18] http://www.fluka.eu/Fluka/www/html/fluka.php?, Accessed: 2025-07-24
(cit. on p. 4).

[19] L. J. Exner, *Didaktische Elementarisierung von Hadronenspektroskopie im Rahmen einer Netzwerk Teilchenwelt-Masterclass*, University of Bonn, 2023, URL: https://confluence.team.uni-bonn.de/display/PHYLHCB/Finished+Projects?preview=/194478676/194478687/Exner%5C%2C%5C%20Lukas%5C%20Julian.pdf (cit. on p. 4).

[20] O. Aberle et al., *High-Luminosity Large Hadron Collider (HL-LHC): Technical design report*, CERN Yellow Reports: Monographs, Geneva: CERN, 2020, URL: https://cds.cern.ch/record/2749422 (cit. on pp. 7, 9, 10, 19).

[21] https://cerncourier.com/a/fcc-the-physics-case/, Accessed: 2025-03-28 (cit. on p. 7).

[22] https://home.cern/science/accelerators/accelerator-complex, Accessed: 2025-03-28 (cit. on p. 7).

[23] *The High-Luminosity LHC Project. 298th Meeting of Scientific Policy Committee*, tech. rep., 2016, URL: https://cds.cern.ch/record/2199189 (cit. on p. 7).

[24] https://atlas.cern/about, Accessed: 2025-03-28 (cit. on p. 7).

[25] https://home.cern/science/experiments/cms, Accessed: 2025-03-28 (cit. on p. 7).

[26] https://home.cern/science/experiments/alice, Accessed: 2025-03-28 (cit. on p. 7).

[27] E. Lopienska, *The CERN accelerator complex, layout in 2022. Complexe des accélérateurs du CERN en janvier 2022*, (2022), General Photo, URL: https://cds.cern.ch/record/2800984 (cit. on p. 8).

[28] O. Brüning and L. Rossi, *The High Luminosity Large Hadron Collider*, WORLD SCIENTIFIC, 2015, eprint: https://www.worldscientific.com/doi/pdf/10.1142/9581, URL: https://www.worldscientific.com/doi/abs/10.1142/9581 (cit. on pp. 7, 10).

[29] The LHCb collaboration, *The LHCb Upgrade I*, JINST **19** (2024) P05065, arXiv: 2305.10515 [hep-ex] (cit. on pp. 8, 11, 16, 18, 20–26).

[30] *Letter of Intent for the LHCb Upgrade*, tech. rep., CERN, 2011, URL: https://cds.cern.ch/record/1333091 (cit. on pp. 8, 13).

[31] The ATLAS collaboration, *Observation of a new particle in the search for the Standard Model Higgs boson with the ATLAS detector at the LHC*, Phys. Lett. B **716** (2012) 1, arXiv: 1207.7214 [hep-ex] (cit. on p. 8).

[32] The CMS collaboration, *Observation of a New Boson at a Mass of 125 GeV with the CMS Experiment at the LHC*, Phys. Lett. B **716** (2012) 30, arXiv: 1207.7235 [hep-ex] (cit. on p. 8).

[33] P. W. Higgs, *Broken Symmetries and the Masses of Gauge Bosons*, Phys. Rev. Lett. **13** (1964) 508, ed. by J. C. Taylor (cit. on p. 8).

[34] H. Kolanoski and N. Wermes, *Teilchendetektoren, Grundlagen und Anwendungen*, 1st ed., Springer, 2016, ISBN: 978-3-662-45349-0, URL: https://doi.org/10.1007/978-3-662-45350-6 (cit. on pp. 8, 9, 13, 36, 38–54, 57, 58, 70–75, 128, 138, 160, 163).

[35] D. Choudhury and B. Mukhopadhyaya, "The Large Hadron Collider: Overall Motivation", *Physics at the Large Hadron Collider*, ed. by A. Datta et al., New Delhi: Springer India, 2009, ISBN: 978-81-8489-295-6, URL: https://doi.org/10.1007/978-81-8489-295-6_1 (cit. on p. 9).

[36] https://home.cern/news/opinion/accelerators/updated-schedule-cerns-accelerators, Accessed: 2025-04-07 (cit. on p. 10).

[37] http://lhc-commissioning.web.cern.ch/schedule/LHC-long-term.htm, Accessed: 2025-04-07 (cit. on p. 10).

[38] *News*, (2014), URL: https://cds.cern.ch/record/2064576 (cit. on p. 11).

[39] The LHCb Collaboration, *Measurement of matter-antimatter differences in beauty baryon decays*, Nature Phys. **13** (2017) 391, All figures and tables, along with any supplementary material and additional information, are available at https://lhcbproject.web.cern.ch/lhcbproject/Publications/LHCbProjectPublic/LHCb-PAPER-2016-030.html, arXiv: 1609.05216, URL: https://cds.cern.ch/record/2216363 (cit. on pp. 11, 239).

[40] The LHCb collaboration, *Search for CP violation and observation of P violation in $\Lambda_b^0 \to p\pi^-\pi^+\pi^-$ decays*, Phys. Rev. D **102** (5 2020) 051101, URL: https://link.aps.org/doi/10.1103/PhysRevD.102.051101 (cit. on p. 11).

[41] The LHCb collaboration, *Study of Λ_b^0 and Ξ_b^0 Decays to $\Lambda h^+ h^{'-}$ and Evidence for CP Violation in $\Lambda_b^0 \to \Lambda K^+ K^-$ Decays*, Phys. Rev. Lett. **134** (10 2025) 101802, URL: https://link.aps.org/doi/10.1103/PhysRevLett.134.101802 (cit. on p. 11).

[42] The LHCb collaboration, *First Evidence for Direct CP Violation in Beauty to Charmonium Decays*, Phys. Rev. Lett. **134** (10 2025) 101801, URL: https://link.aps.org/doi/10.1103/PhysRevLett.134.101801 (cit. on pp. 11, 239).

[43] The LHCb collaboration, *Precise determination of the B_s^0–$\overline{B}_s^0$ oscillation frequency. Precise determination of the B0s-B0sbar oscillation frequency*, Nature Phys. **18** (2022) 1, All figures and tables, along with any supplementary material and additional information, are available at https://cern.ch/lhcbproject/Publications/p/LHCb-PAPER-2021-005.html (LHCb public pages), arXiv: 2104.04421, URL: https://cds.cern.ch/record/2764338 (cit. on p. 12).

[44] N. Cabibbo, *Unitary Symmetry and Leptonic Decays*, Phys. Rev. Lett. **10** (12 1963) 531, URL: https://link.aps.org/doi/10.1103/PhysRevLett.10.531 (cit. on p. 12).

[45] M. Kobayashi and T. Maskawa, *CP Violation in the Renormalizable Theory of Weak Interaction*, Prog. Theor. Phys. **49** (1973) 652 (cit. on p. 12).

[46] The LHCb collaboration, *Strong constraints on the rare decays $B_s \to \mu^+\mu^-$ and $B^0 \to \mu^+\mu^-$*, Phys. Rev. Lett. **108** (2012) 231801, arXiv: 1203.4493 [hep-ex] (cit. on p. 12).

[47] The Belle collaboration, *Observation of a Narrow Charmoniumlike State in Exclusive $B^\pm \to K^\pm\pi^+\pi^- J/\psi$ Decays*, Phys. Rev. Lett. **91** (26 2003) 262001, URL: https://link.aps.org/doi/10.1103/PhysRevLett.91.262001 (cit. on p. 12).

[48] The LHCb collaboration, *Observation of $J/\psi p$ Resonances Consistent with Pentaquark States in $\Lambda_b^0 \to J/\psi K^- p$ Decays*, Phys. Rev. Lett. **115** (7 2015) 072001, URL: https://link.aps.org/doi/10.1103/PhysRevLett.115.072001 (cit. on p. 12).

[49] The LHCb collaboration, *Observation of a Narrow Pentaquark State, $P_c(4312)^+$, and of the Two-Peak Structure of the $P_c(4450)^+$*, Phys. Rev. Lett. **122** (22 2019) 222001, URL: https://link.aps.org/doi/10.1103/PhysRevLett.122.222001 (cit. on p. 12).

[50] The LHCb collaboration, *Study of the doubly charmed tetraquark T_{cc}^+*, Nature Commun. **13** (2022) 3351, arXiv: 2109.01056 [hep-ex] (cit. on p. 12).

[51] The LHCb collaboration, *Observation of an exotic narrow doubly charmed tetraquark*, Nature Phys. **18** (2022) 751, arXiv: 2109.01038 [hep-ex] (cit. on p. 12).

[52] The LHCb collaboration, *Physics case for an LHCb Upgrade II - Opportunities in flavour physics, and beyond, in the HL-LHC era*, tech. rep., ISBN 978-92-9083-494-6: CERN, 2016, arXiv: 1808.08865, URL: https://cds.cern.ch/record/2636441 (cit. on pp. 14, 15).

[53] Mindaugas Šarpis,
Pentaquark Search in $\Lambda_b^0 \to \Lambda_c^+ D\bar{D}^{*0}K^-$ Decays and LHCb Open Data Release,
PhD thesis: Rheinische Friedrich-Wilhelms-Universität Bonn, 2024,
URL: https://hdl.handle.net/20.500.11811/11225 (cit. on p. 14).

[54] https://indico.cern.ch/event/1491351/contributions/6377140/attachments/3039374/5368929/U2Wshop2025_ALai.pdf,
Upgrade2 Workshop 2025, accessed: 2025-04-10 (cit. on p. 19).

[55] https://indico.cern.ch/event/1491351/contributions/6377146/attachments/3039635/5368777/0_20250326_Mighty_Tracker_EV_e.pdf,
Upgrade2 Workshop 2025, accessed: 2025-04-11 (cit. on pp. 20, 21, 97).

[56] https://www.epfl.ch/labs/lphe/en/lhcb/the-scifi-tracker/,
Accessed: 2025-04-19 (cit. on p. 21).

[57] https://www.hamamatsu.com/jp/en.html, Accessed: 2025-04-15
(cit. on p. 21).

[58] The LHCb Collaboration, *LHCb Tracker Upgrade Technical Design Report*,
tech. rep., 2014, URL: https://cds.cern.ch/record/1647400 (cit. on p. 22).

[59] P. A. Čerenkov, *Visible Radiation Produced by Electrons Moving in a Medium with Velocities Exceeding that of Light*, Phys. Rev. **52** (4 1937) 378,
URL: https://link.aps.org/doi/10.1103/PhysRev.52.378 (cit. on p. 23).

[60] F. L. Anderson, *Huygens' Principle geometric derivation and elimination of the wake and backward wave*, Scientific Reports **11** (2021),
URL: https://doi.org/10.1038/s41598-021-99049-7 (cit. on p. 23).

[61] https://indico.cern.ch/event/1491351/contributions/6377153/attachments/3039814/5369202/2025_03_27%20-%20Fiorini%20-%20RICH%20design%20and%20technology.pdf,
Upgrade2 Workshop 2025, accessed: 2025-04-14 (cit. on p. 23).

[62] https://indico.cern.ch/event/1491351/contributions/6377159/attachments/3039835/5369248/Rich_Torch_RoadmapTDR.pdf,
Upgrade2 Workshop 2025, accessed: 2025-04-14 (cit. on p. 24).

[63] https://indico.cern.ch/event/1491351/contributions/6377161/attachments/3039844/5369334/lhcb_upgrade_ii_workshop_philipp_roloff_27_03_2025.pdf, Upgrade2 Workshop 2025, accessed: 2025-04-14
(cit. on p. 25).

[64] https://indico.cern.ch/event/1491351/contributions/6377162/attachments/3039845/5369599/MUON\spacefactor\@m{}U2__workshopHeidelberg2025-FD.pdf,
Upgrade2 Workshop 2025, accessed: 2025-04-14 (cit. on p. 25).

[65] https://indico.cern.ch/event/1491351/contributions/6377165/attachments/3040195/5370008/20250326.u2_workshop.online.pdf, Upgrade2 Workshop 2025, accessed: 2025-04-14 (cit. on p. 26).

[66] https://indico.cern.ch/event/1491351/contributions/6377146/attachments/3039635/5368777/0_20250326_Mighty_Tracker_EV_e.pdf, Upgrade2 Workshop 2025, accessed: 2025-04-15 (cit. on pp. 27, 30–33).

[67] https://indico.cern.ch/event/1491351/contributions/6377147/attachments/3039631/5368772/Mighty_SciFi_Heidelberg_U2_2025_GH.pdf, Upgrade2 Workshop 2025, accessed: 2025-04-15 (cit. on p. 29).

[68] https://mightypix2.docs.cern.ch, MP2 User Manual, accessed: 2025-04-17 (cit. on pp. 32, 33, 92, 121).

[69] L. Dittmann, unpublished thesis, PhD thesis: Heidelberg University, 2025 (cit. on p. 33).

[70] S. Scherl, N. Striebig, K. Hennessy, I. Perić and E. Vilella, *MightyPix at the LHCb Mighty Tracker — verification of an HV-CMOS pixel chip's digital readout*, Journal of Instrumentation **19** (2024) C04045, URL: https://dx.doi.org/10.1088/1748-0221/19/04/C04045 (cit. on p. 33).

[71] https://www.tsi.com/electronics-manufacturing/market-segments/semiconductor_manufacturing, Accessed: 2025-04-17 (cit. on pp. 33, 80, 240).

[72] https://ams-osram.com/de/, Accessed: 2025-04-17 (cit. on p. 33).

[73] https://pdg.lbl.gov/2019/reviews/rpp2018-rev-passage-particles-matter.pdf, Accessed: 2025-03-07 (cit. on pp. 36–38).

[74] E. Rutherford, *The scattering of alpha and beta particles by matter and the structure of the atom*, Phil. Mag. Ser. 6 **21** (1911) 669 (cit. on pp. 36, 39).

[75] https://pdg.lbl.gov/2022/reviews/rpp2022-rev-passage-particles-matter.pdf, Accessed: 2025-03-10 (cit. on pp. 38, 39, 41, 43).

[76] P. V. Vavilov, *Ionization losses of high-energy heavy particles*, Sov. Phys. JETP **5** (1957) 749 (cit. on p. 39).

[77] L. Landau, *On the energy loss of fast particles by ionization*, J. Phys. (USSR) **8** (1944) 201 (cit. on p. 39).

[78] H. A. Bethe, *Molière's Theory of Multiple Scattering*, Phys. Rev. **89** (6 1953) 1256, URL: https://link.aps.org/doi/10.1103/PhysRev.89.1256 (cit. on p. 39).

[79] R. Ballabriga, M. Campbell and X. Vilasis-Cardona,
The Design and Implementation in 0.13*μm CMOS of an Algorithm Permitting Spectroscopic Imaging with High Spatial Resolution for Hybrid Pixel Detectors*, () (cit. on p. 43).

[80] E. Martins, *Essentials of Semiconductor Device Physics*, Wiley, 2022,
ISBN: 9781119884118,
URL: https://books.google.de/books?id=gVm_zgEACAAJ (cit. on pp. 44–46).

[81] L. Rossi, P. Fischer, T. Rohe and N. Wermes,
Pixel detectors: from fundamentals to applications,
Particle acceleration and detection, Berlin: Springer, 2006,
URL: http://cds.cern.ch/record/976471 (cit. on pp. 44, 51, 52, 72, 74, 75).

[82] A. Juengel, *Transport Equations for Semiconductors*, 2004,
URL: https://www.tuwien.at/index.php?eID=dumpFile&t=f&f=188883&token=179fbec419dd61079dce733efe0bfaf3bcef665b (cit. on p. 44).

[83] R. Schimassek,
Entwicklung und Charakterisierung von Integrierten Sensoren für die Teilchenphysik = Development and Characterisation of Integrated Sensors for Particle Physics,
PhD thesis: Karlsruher Institut für Technologie (KIT), 2021, 215 pp.
(cit. on pp. 44, 55, 78).

[84] Z. Zhang and S. Satpathy, *Electromagnetic wave propagation in periodic structures: Bloch wave solution of Maxwell's equations*, Phys. Rev. Lett. **65** (21 1990) 2650,
URL: https://link.aps.org/doi/10.1103/PhysRevLett.65.2650
(cit. on p. 44).

[85] J. Lin et al.,
An investigation of gamma radiation detection with a CMOS imaging sensor,
Scientific Reports **14** (2024) (cit. on p. 47).

[86] R. Schimassek,
Test der Funktionsfähigkeit digitaler Pixelmodule für das CMS-Upgrade, 2014
(cit. on pp. 49, 95).

[87] E. Young,
Ultrafast acoustic strain generation and effects in semiconductor nanostructures,
PhD thesis, 2014 (cit. on p. 50).

[88] P. MARS, *Temperature dependence of avalanche breakdown voltage Temperature dependence of avalanche breakdown voltage in p—n junctions†*,
International Journal of Electronics **32** (1972) 23,
eprint: https://doi.org/10.1080/00207217208938266,
URL: https://doi.org/10.1080/00207217208938266 (cit. on p. 51).

[89] W. Shockley, *Currents to Conductors Induced by a Moving Point Charge*, Journal of Applied Physics **9** (1938) 635, ISSN: 0021-8979, eprint: https://pubs.aip.org/aip/jap/article-pdf/9/10/635/18304047/635_1_online.pdf, URL: https://doi.org/10.1063/1.1710367 (cit. on p. 53).

[90] S. Ramo, *Currents Induced by Electron Motion*, Proceedings of the IRE **27** (1939) 584 (cit. on p. 53).

[91] T. Bisanz, I.-M. Gregor, F. Hügging and J. Weingarten, *Elektronik im Physikstudium: Eine Einführung geeignet zur Vorlesung, im Praktikum und im Labor*, Springer, 2024, URL: http://cds.cern.ch/record/2907608 (cit. on pp. 54, 55).

[92] https://www.mks.com/n/mosfet-physics, Accessed: 2025-08-29 (cit. on p. 55).

[93] A. Herkert, *Characterization of a Monolithic Pixel Sensor Prototype in HV-CMOS Technology for the High-Luminosity LHC*, PhD thesis: The Faculty of Physics and Astronomy (Heidelberg), 2020 (cit. on pp. 55, 78).

[94] V. Bezhenova and A. Michalowska-Forsyth, *Aspect ratio of radiation-hardened MOS transistors: Modelling of the equivalent channel dimensions of integrated MOS transistors in radiation-hardened enclosed layout*, e & i Elektrotechnik und Informationstechnik **135** (2018) (cit. on pp. 55–57).

[95] M. Moll, *Radiation damage in silicon particle detectors: Microscopic defects and macroscopic properties*, PhD thesis: Hamburg U., 1999 (cit. on pp. 57–65).

[96] David-Leon Pohl, *3D-Silicon and Passive CMOS Sensors for Pixel Detectors in High Radiation Environments*, PhD thesis: Rheinische Friedrich-Wilhelms-Universität Bonn, 2020, URL: https://hdl.handle.net/20.500.11811/8743 (cit. on p. 58).

[97] M. Moll, *Displacement Damage in Silicon Detectors for High Energy Physics*, IEEE Transactions on Nuclear Science **65** (2018) 1561 (cit. on pp. 59–62, 64, 158).

[98] https://www.zyklotron.hiskp.uni-bonn.de/index.html, Accessed: 2025-03-14 (cit. on p. 59).

[99] M. Moll, *Acceptor removal - Displacement damage effects involving the shallow acceptor doping of p-type silicon devices*, PoS **Vertex2019** (2020) 027, URL: https://cds.cern.ch/record/2747752 (cit. on pp. 59, 63, 162).

[100] W. Shockley and W. T. Read, *Statistics of the Recombinations of Holes and Electrons*, Phys. Rev. **87** (5 1952) 835, URL: https://link.aps.org/doi/10.1103/PhysRev.87.835 (cit. on p. 60).

[101] R. N. Hall, *Electron-Hole Recombination in Germanium*, Phys. Rev. **87** (2 1952) 387, URL: https://link.aps.org/doi/10.1103/PhysRev.87.387 (cit. on p. 60).

[102] F. Hartmann, "Radiation Damage in Silicon Detector Devices",
Evolution of Silicon Sensor Technology in Particle Physics: Basics and Applications,
Cham: Springer Nature Switzerland, 2024, ISBN: 978-3-031-59720-6
(cit. on pp. 65, 68, 76).

[103] G. Lutz, *Semiconductor Radiation Detectors: Device Physics*,
New York: Springer, 1999, ISBN: 978-3-540-64859-8 (cit. on pp. 66, 71).

[104] J. R. Schwank et al., *Radiation Effects in MOS Oxides*,
IEEE Transactions on Nuclear Science **55** (2008) 1833 (cit. on pp. 66–68).

[105] H. J. Barnaby, *Total-Ionizing-Dose Effects in Modern CMOS Technologies*,
IEEE Transactions on Nuclear Science **53** (2006) 3103 (cit. on pp. 66, 67).

[106] L. Gonella,
TID Tolerance of commercial 130nm CMOS Technologies for HEP experiments,
Presented 27 Oct 2006, Turin U., 2006,
URL: https://cds.cern.ch/record/2252791 (cit. on pp. 67, 68).

[107] J. Topping, *Investigations on the Theory of the Brownian Movement*,
Physics Bulletin **7** (1956) 281,
URL: https://dx.doi.org/10.1088/0031-9112/7/10/012 (cit. on p. 71).

[108] L. Vigani et al.,
Study of prototypes of LFoundry active CMOS pixels sensors for the ATLAS detector,
Journal of Instrumentation **13** (2018) C02021,
URL: https://dx.doi.org/10.1088/1748-0221/13/02/C02021
(cit. on p. 73).

[109] L. Gonella, *The ATLAS ITk detector system for the Phase-II LHC upgrade*,
Nuclear Instruments and Methods in Physics Research Section A: Accelerators,
Spectrometers, Detectors and Associated Equipment **1045** (2023) 167597,
ISSN: 0168-9002, URL: https:
//www.sciencedirect.com/science/article/pii/S0168900222008890
(cit. on p. 72).

[110] A. Schoening et al., "MuPix & ATLASpix: Architectures and Results", *Proceedings of The 28th International Workshop on Vertex Detectors — PoS(Vertex2019)*,
28th International Workshop on Vertex Detectors, VERTEX 2019 (Lopud, Kroatien, 13th–18th Oct. 2019), 54.02.03; LK 01,
Scuola Internazionale Superiore di Studi Avanzati (SISSA), 2020 024 (cit. on p. 77).

[111] H. Augustin et al.,
TelePix – A fast region of interest trigger and timing layer for the EUDET Telescopes,
Nuclear Instruments and Methods in Physics Research Section A: Accelerators,
Spectrometers, Detectors and Associated Equipment **1048** (2023) 167947,
ISSN: 0168-9002, URL: https:

//www.sciencedirect.com/science/article/pii/S0168900222012396 (cit. on p. 77).

[112] A. Gonzales, *TCAD Simulations and Characterization of High-Voltage Monolithic Active Pixel Sensors*, Heidelberg, 2023, URL: https://archiv.ub.uni-heidelberg.de/volltextserver/33792/1/Thesis_v1_Annie_submitted.pdf (cit. on pp. 78, 154, 184).

[113] F. Foerster, *HV-MAPS Readout and Direct Memory Access for the Mu3e Experiment*, Heidelberg, 2014, URL: https://www.physi.uni-heidelberg.de/Publications/MasterFoerster.pdf (cit. on p. 78).

[114] H. Augustin, *Characterization of a novel HV-MAPS Sensor with two Amplification Stages and first examination of thinned MuPix Sensors*, Heidelberg, 2014, URL: https://www.physi.uni-heidelberg.de/Publications/Thesis.Augustin.pdf (cit. on p. 78).

[115] D. Imming, *HV-MAPS Family*, Courtesy of David Imming. Adapted by Lucas Dittmann., 2025 (cit. on p. 79).

[116] https://www.blogs.uni-mainz.de/fb08p2/the-p2-experiment/, Accessed: 2025-04-24 (cit. on p. 78).

[117] http://www.lfoundry.com/, Accessed: 2025-04-24 (cit. on p. 78).

[118] H. Jansen et al., *Performance of the EUDET-type beam telescopes*, EPJ Techniques and Instrumentation **3** (2016) 7, URL: https://epjtechniquesandinstrumentation.springeropen.com/articles/10.1140/epjti/s40485-016-0033-2 (cit. on pp. 80, 116, 215, 217).

[119] I. Perić, *TelePix User Manual*, Internal User Manual of TelePix written by I. Perić., 2023 (cit. on pp. 81, 88).

[120] I. Perić et al., *High-Voltage CMOS Active Pixel Sensor*, IEEE Journal of Solid-State Circuits **56** (2021) 2488 (cit. on p. 82).

[121] T. Hirono, *Private communication*, 2025 (cit. on pp. 83, 86).

[122] B. Maisano, *Validation of an NMOS Comparator Design in High Voltage Monolothic Active Pixel Sensors for LHCb Upgrade II Mighty-Tracker Performances*, University of Heidelberg, 2025 (cit. on p. 91).

[123] M. Daas et al., *BDAQ53, a versatile pixel detector readout and test system for the ATLAS and CMS HL-LHC upgrades*, Nuclear Instruments and Methods in Physics Research Section A: Accelerators, Spectrometers, Detectors and Associated Equipment **986** (2021) 164721, ISSN: 0168-9002, URL: https://www.sciencedirect.com/science/article/pii/S0168900220311189 (cit. on pp. 95, 107, 113).

[124] https://github.com/SiLab-Bonn/basil, Accessed: 2025-05-05 (cit. on p. 95).

[125] Christian Bespin Valero, *Characterization of the TJ-Monopix2 Depleted Monolithic Active Pixel Sensor for High-Energy Physics Experiments*, PhD thesis: Rheinische Friedrich-Wilhelms-Universität Bonn, 2024, URL: https://hdl.handle.net/20.500.11811/12562 (cit. on pp. 95, 113).

[126] P. Baesso, D. Cussans and J. Goldstein, *The AIDA-2020 TLU: a flexible trigger logic unit for test beam facilities*, Journal of Instrumentation **14** (2019) P09019, URL: https://dx.doi.org/10.1088/1748-0221/14/09/P09019 (cit. on p. 97).

[127] https://www.enclustra.com/en/products/fpga-modules/mercury-kx1/, Accessed: 2025-05-06 (cit. on pp. 97, 101).

[128] https://gitlab.cern.ch/mightypix, Accessed: 2025-05-06 (cit. on p. 97).

[129] https://lhcb-mighty-tracker-daq.docs.cern.ch/useful_links/, Accessed: 2025-08-04 (cit. on pp. 97, 118).

[130] https://docs.rs-online.com/66f2/0900766b8154d2ae.pdf, Accessed: 2025-07-14 (cit. on p. 101).

[131] https://github.com/BeeBeansTechnologies/SiTCP_Netlist_for_Kintex_UltraScale, Accessed: 2025-05-08 (cit. on p. 102).

[132] https://www.ti.com/lit/an/sbaa565/sbaa565.pdf?ts=1754251254996, Accessed: 2025-08-04 (cit. on p. 108).

[133] https://www.hdfgroup.org/solutions/hdf5/, Accessed: 2025-05-16 (cit. on p. 114).

[134] https://gitlab.cern.ch/mightypix/mars_daq/-/tree/master/mars_daq?ref_type=heads, Accessed: 2025-05-16 (cit. on pp. 114, 261).

[135] D. Dannheim et al., *Corryvreckan: a modular 4D track reconstruction and analysis software for test beam data*, Journal of Instrumentation **16** (2021) P03008, URL: https://dx.doi.org/10.1088/1748-0221/16/03/P03008 (cit. on pp. 116, 213, 219, 223, 240).

[136] https://github.com/SiLab-Bonn/pixel_clusterizer/tree/master, Accessed: 2025-05-19 (cit. on p. 116).

[137] https://gitlab.cern.ch/mightypix/telepix_daq/, Accessed: 2025-05-08 (cit. on p. 117).

[138] https://gitlab.cern.ch/mightypix/MightyPixdaq, Accessed: 2025-05-08 (cit. on p. 117).

[139] https://gitlab.cern.ch/mightypix/run2021_mars, Accessed: 2025-05-08 (cit. on p. 117).

[140] https://particle-physics.desy.de/test_beams_at_desy, Accessed: 2025-05-08 (cit. on pp. 118, 213).

[141] https://gitlab.cern.ch/mightypix/telepix_daq/-/tree/testbeam_december?ref_type=heads, Accessed: 2025-05-08 (cit. on p. 118).

[142] Y. Liu, *EUDAQ2 User Manual*, tech. rep., CERN, 2018, URL: https://cds.cern.ch/record/2314266 (cit. on pp. 118, 240).

[143] https://www.bosch-sensortec.com/media/boschsensortec/downloads/datasheets/bst-bme280-ds002.pdf, Accessed: 2025-06-18 (cit. on pp. 138, 140).

[144] https://iseg-hv.com/files/media/docitems_file_20240423111613.pdf, Accessed: 2025-06-02 (cit. on pp. 141, 265).

[145] D. Sauerland, R. Beck, J. Dingfelder, P. Eversheim and P. Wolf, "Proton Irradiation Site for Si-Detectors at the Bonn Isochronous Cyclotron", *Proc. IPAC'22* (Bangkok, Thailand), International Particle Accelerator Conference 13, JACoW Publishing, Geneva, Switzerland, 2022 MOPOST030 130, ISBN: 978-3-95450-227-1, URL: https://jacow.org/ipac2022/papers/mopost030.pdf (cit. on p. 157).

[146] K. Padeken, *Private communication*, 2025 (cit. on pp. 166, 180).

[147] A. Qamesh, *X-ray Irradiation and Calibration of the RD53A Pixel Read-out Chip*, University of Bonn, 2029, URL: https://web.physik.uni-bonn.de/group/view.php?&group=2&lang=en&c=t&id=670 (cit. on p. 176).

[148] https://indico.cern.ch/event/956616/contributions/4068849/attachments/2126064/3579530/PIN_diode_calibration_2018.pdf, Accessed: 2025-08-14 (cit. on p. 176).

[149] https://lbfenceint.cern.ch/simrad/file/plot?fileIds=641, Accessed: 2025-06-30 (cit. on pp. 190, 193).

[150] https://gitlab.cern.ch/lhcb-mightytracker/mighty-tracker-design-tools, Accessed: 2025-06-30 (cit. on pp. 190, 193).

[151] Y. Liu and E. D. Team, *EUDAQ2 User Manual*, version 2.0.1, Accessed: 2025-05-23, EUDET, 2017, URL: https://eudaq.github.io/manual/EUDAQUserManual_v2.pdf (cit. on pp. 213, 218).

[152] https://gitlab.cern.ch/corryvreckan/corryvreckan/-/tree/master/src/modules/EventLoaderHDF5?ref_type=heads, Accessed: 2025-07-07 (cit. on p. 219).

[153] https://root.cern.ch/doc/master/classTEfficiency.html#ae80c3189bac22b7ad15f57a1476ef75b, Accessed: 2025-07-30 (cit. on p. 220).

APPENDIX A

Appendix

A.1 MARS - Latest FPGA Carrier Board

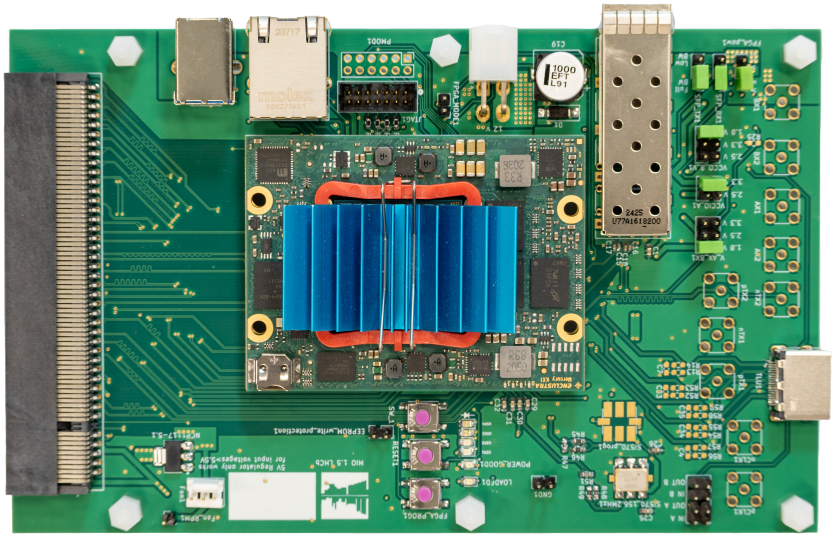


Figure A.1: Top view of the latest version of the FPGA carrier board. The FPGA is covered by a blue heat sink.

A.2 Universities using MARS

In table A.1 an overview of universities using the MARS DAQ system is presented.

Universities	Available	In-Use
Bonn	x	x
Dortmund	x	x
Edinburgh	x	
RAL	x	x
Freiburg		
France (in2p3)		

Table A.1: Summary of institutes using the MARS DAQ system. If MARS is actively used, it is marked as ”in-use”. If not, it is available and will be used in the future. Institutes listed here without an available system are planning to get MARS.

A.3 Get Started with MARS

To use MARS to characterize HV-MAPS, two things are required: (1) Available hardware and (2) installation of the software/firmware package.
How to install the software and firmware is explained in the *ReadMe* description provided in [134]. Next, the following steps need to be executed:

1. Generation of the bitstream to program the FPGA or direct usage of the available bitstream.
2. Connection of the FPGA carrier board to the back-end PC and powering of it.
3. Validation of the connection and low voltage.
4. Configuration of the FPGA by uploading the bitstream. If everything went well, test LED lights and the Ethernet connection LEDs light up.
5. Verification of the Ethernet connection by sending a ping.
6. Connection of the adapter board to the FPGA carrier and low voltage.
7. Verification of applied voltages and clock signals. At this step the user is able to measure every signal received by the DUT.
8. After validation of all signals, the DUT carrier board is connected while all external voltages are turned-off.
9. Powering of the DUT and confirmation of all voltages available at the DUT carrier board.
10. Biasing of the DUT while the leakage current has to be monitored.
11. Configuration of the DUT. Different start-up `Jupyter` notebooks are available.
12. Confirmation of all voltages and threshold on the DUT carrier board, e.g the threshold of the comparator.
13. If everything is set-up correctly and the DUT is configured to its default settings, the data link has to be controlled using the `Jupyter` notebook.
14. If the data link is stable, the DUT is fully operational.

Depending on used `Display Port` cables, the data link might be instable. To figure out the optimal settings, the data link in dependence on the *LVDS* and *LVDSDel* driver strength has to be measured. Further, a switch from external to internal clock (PLL) together with turning the bias block on and off might help to get a stable link. If the PLL is used, but the link is instable, *VPpump* has to be adjusted.

A.4 Configurable on-chip DACs of TelePix2

Sensor component	DAC	Purpose
State machine	slowdownend	Duration of the LDCol1 state
State machine	timerend	Slow down of state machine used to program the duration of the sync state
Clocking scheme	ext_clk_en	Enables the external clock as base clock
Clocking scheme	pll_en	Enables the PLL
Clocking scheme	invert_clk_pll	Inverts the clock
Clocking scheme	ckdivend	Speed of the TS1 counter can be adjusted
Clocking scheme	ckdivend2	Speed of the TS2 counter can be adjusted
Hit buffer	WrRam_TDAC	3 bits used to tune the comparator threshold
Hit buffer	WrRam_Comp	1 bit to enable the comparator output
Hit buffer	RAMWrEnable	1 bit to enable RAM writing

Table A.2: Summary of configurable on-chip DACs of the digital periphery. For each DAC the name, its location in the sensor and purpose is given.

Sensor Component	DAC	Purpose
Bias circuit	INBias	Controls bias strength of n-well
CSA	VN & VP	Bias current of the CSA input
CSA	IPLoad	Bias of the input transistor of the CSA and feedback circuit (changes bias of resistive load)
CSA	VNFoll	Current source of the CSA output source follower
CSA	IPFoll	Current source of the CSA output
CSA	VCasc/VCasc2	Bias of the cascaded amplifier (fixed at $\approx$ 1.1 V to stabilize potential)
Feedback	VNFB	Controls current of feedback loop
Comparator	BL	Baseline voltage compared to CSA signal
Comparator	BLRes	Controls current of capacitor; shapes CSA output
Comparator	THPix	Global threshold for all comparators
Comparator	IPDAC	Controls current drawn by TDACs in hit-buffer cells
Comparator	VMinus	Low level of signal driver line (higher VMinus reduces crosstalk but also signal strength)
Receiver	VNBiasRec	Threshold of the receiver
Receiver	VPBiasRec	Pull-up current of the receiver
Edge detector	VNDel	Delay setting for hit edge detector
Data serializer	VNLVDS	Output signal strength (via LVDS driver voltage)
Data serializer	VNLVDSDel	Pre-emphasis driver strength for VNLVDS
VCO	VPVCO	Bias voltage to Voltage Controlled Oscillator (VCO)
VCO	VPPump	Charge pump bias (used when PLL out of sync)
PLL	VNVCO	Bias voltage to PLL

Table A.3: Summary of configurable on-chip DACs and voltages of the in-pixel electronics. Each DAC is listed with its location and function.

A.5 Discussion on the Uncertainties of IV- and VV-Measurements

In all IV- and VV-measurements fluctuations for both the leakage current and the monitored voltage were observed. Since two different HV power supplies [144] - differing in precision - were used, the precision of the recorded fluctuations vary accordingly.
For measurements using the Run2021 sensor, the higher precision power supply with a resolution of 0.1 nA was used mostly, as the observables are about one order of magnitude smaller compared to TelePix2 - due to the sensor's ten-times smaller size. Conversely, the less precise power supply with a resolution of 0.1 µA was used for TelePix2 measurements. As a result, small fluctuations in the leakage current of the Run2021 sensor, e.g. fig. 8.9, were recorded but not for the TelePix2. To be more specific, only larger fluctuations are recorded with the used power supply.
For both devices, larger leakage current fluctuations were measured for both types of radiation damage - surface and bulk - caused by the higher noise level due to radiation damage.
In addition, fluctuations in the monitored voltage during VV-measurements were observed. While the VV-curves of surface damaged (see fig. 8.5) devices showed fluctuations mostly in the breakdown regime, bulk damaged devices (see fig. 7.10) exhibited more throughout the measurement. One possible explanation is the increased noise level of the bulk damaged device. Nevertheless, further investigation is required.
A final remark on the VV-measurement is necessary. Since the power supplies operate as a current source, they are not intended for use as monitoring devices. In more detail, the internal resistance is smaller than the resistance of the sensor's depleted substrate. Consequently, a non-negligible amount of current flows through the power supply.
Therefore, a systematic uncertainty arises in all measurements due to the non-standard usage.

A.6 Commissioning Measurements of TelePix2

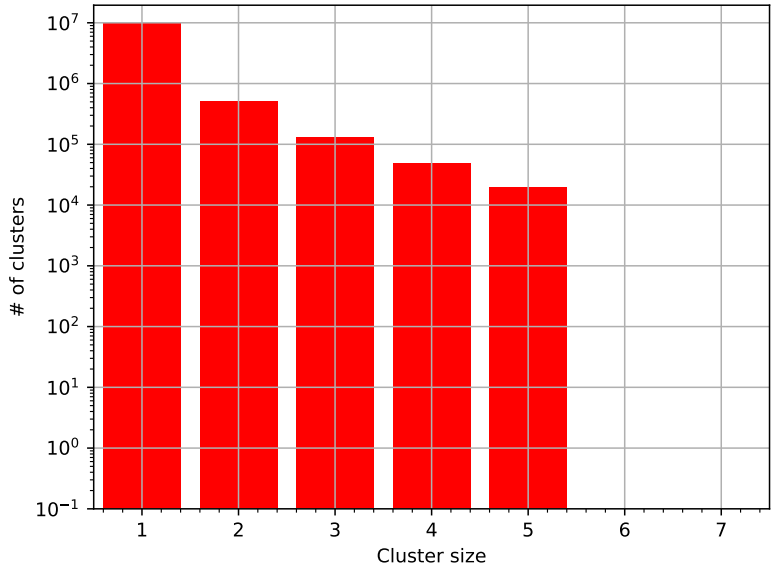


Figure A.2: Measured cluster size with a Sr-90 β-particle source. Most clusters are of size 1. Due to inclined tracks, larger clusters are observed.

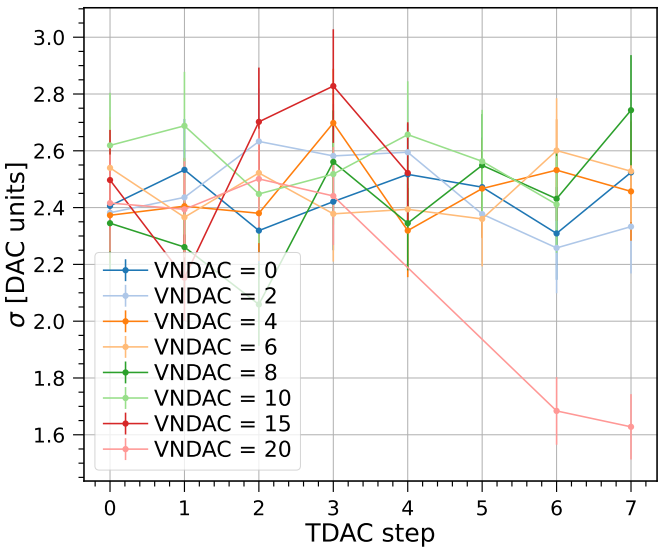


Figure A.3: Threshold dispersion versus TDAC for different VNDAC settings in DAC units. The uncertainty of μ is the statistical uncertainty. The measurement shows no significance dependence of the dispersion on *VNDAC* - except for *VNDAC*= 20 DAC units, which is caused by a failed fit, as shown below.

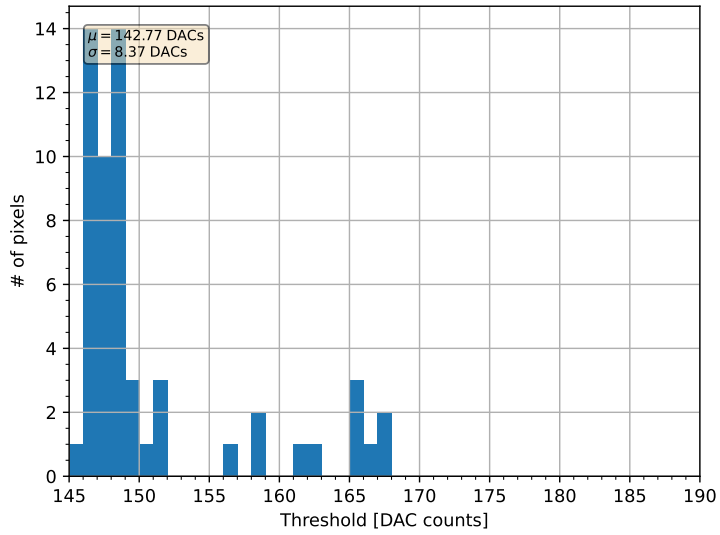


Figure A.4: Example of the threshold distribution of 400 pixels. A Gaussian distribution could not be fitted to data because most entries lie outside the measurement range. Measurement settings are: VNDAC= 20 DAC units and TDAC = 7.

A.7 Matrix Tuning of the Run2021 Sensor

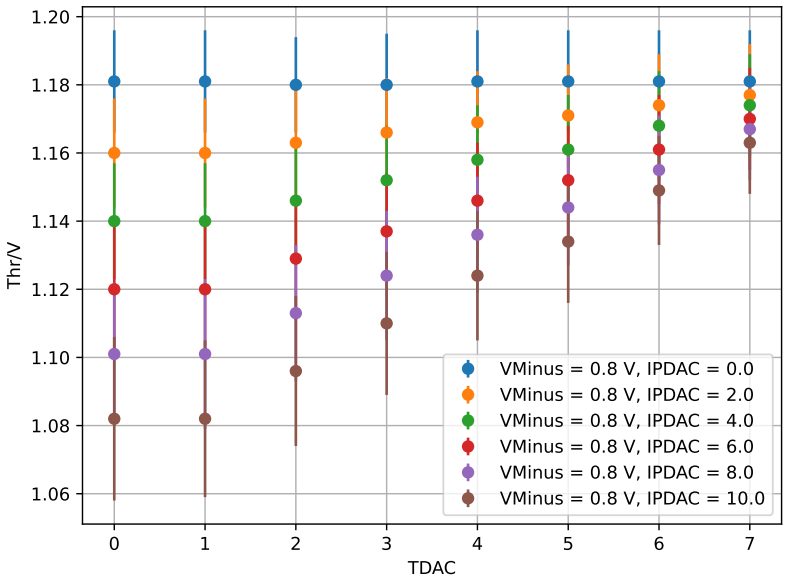


Figure A.5: Strength of the threshold change per TDAC value for different *IPDAC* values. For the Run2021 sensor, the on-chip DAC *IPDAC* defines the current drawn by the TDACs. Compared to the TelePix2 sensor, the TDACs are implemented at the hit buffers and not the pixel itself.

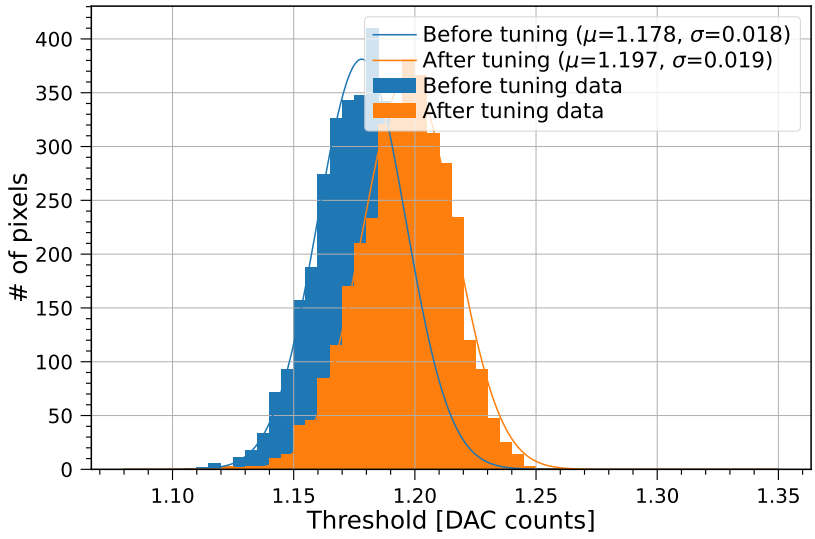


Figure A.6: Result of the matrix tuning algorithm for the Run2021 sensor using a tune strength of *IPDAC* = 4. The target threshold of 1.2 V is reached after tuning of the full pixel matrix.

A.8 Characterization of Bulk Damage on HV-MAPS

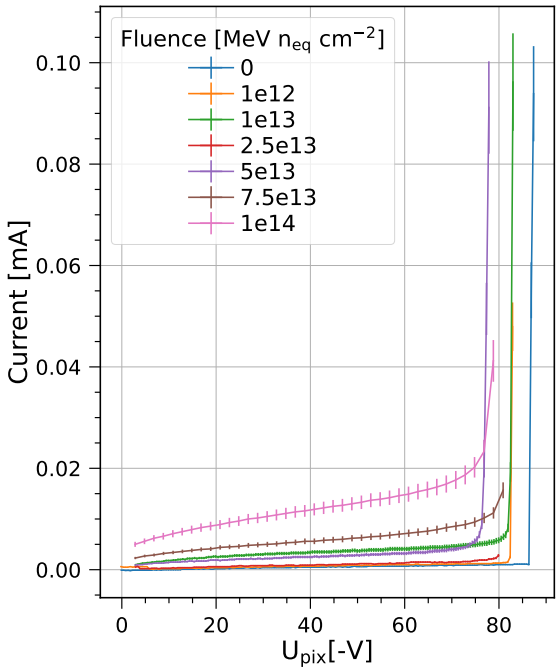


Figure A.7: Summary of the leakage current in dependence of the fluence using pixel biasing. For increasing fluences the leakage current increases such that the breakdown occurs earlier.

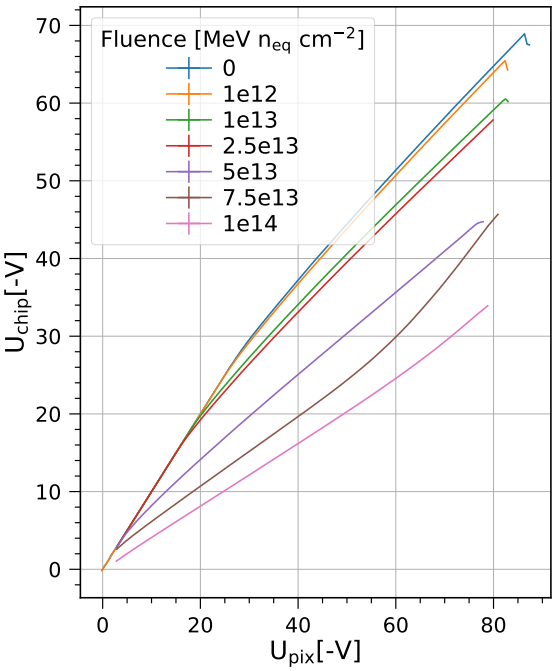


Figure A.8: Summary of all measured VV-curves using the pixel bias while monitoring the voltage at the chip bias. Due to radiation damage and an increased leakage current, the breakdown at the pixel bias occurs earlier, preventing the formation of a sufficient depletion depth. As a consequence, the measured voltage at the chip bias connection worsens compared to the non-irradiated DUT.

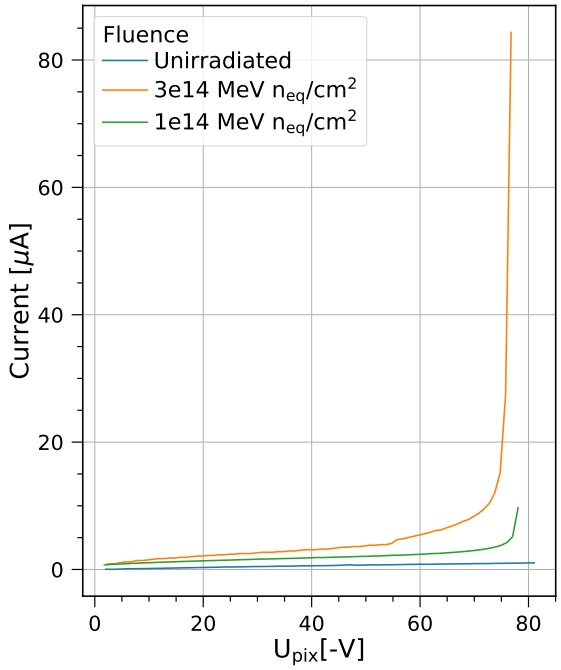


Figure A.9: Summary of IV measurements for annealed TelePix2 devices compared to a non-irradiated device using pixel biasing. Measurements have been taken in June 2025.

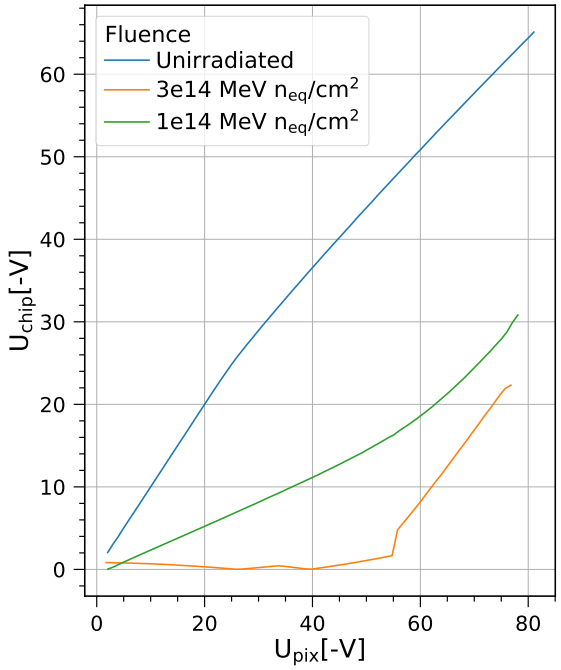


Figure A.10: Summary of VV measurements for annealed TelePix2 devices compared to a non-irradiated device using pixel biasing. Measurements have been taken in June 2025.

A.9 Characterization of Surface Damage on HV-MAPS

A.9.1 Calibration of the Comparator Threshold

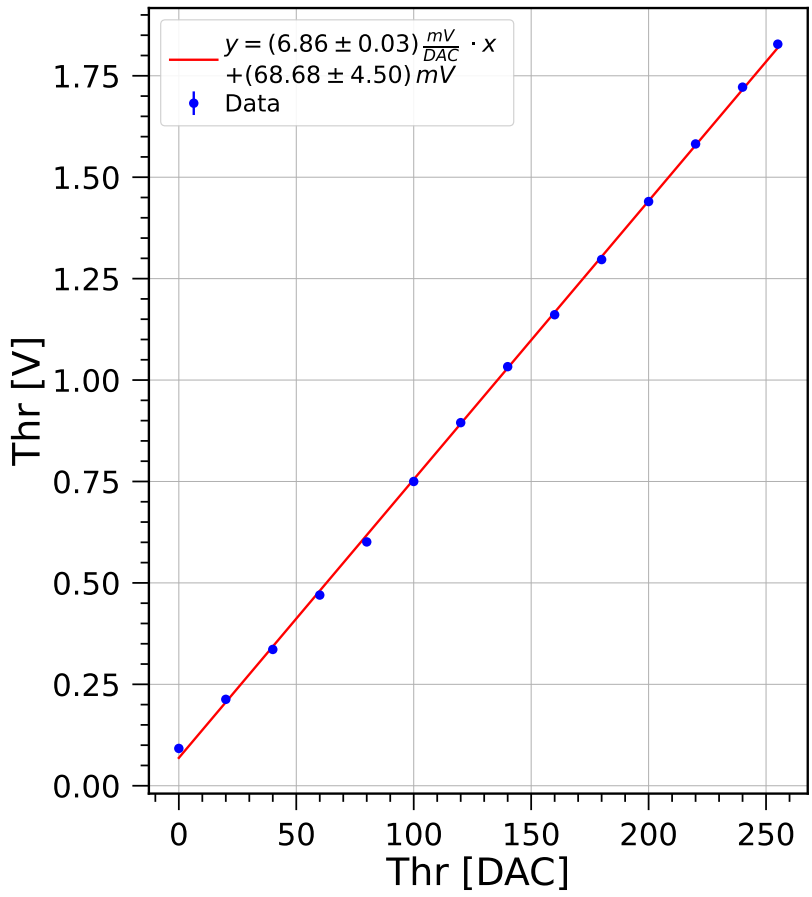


Figure A.11: Calibration measurement of the comparator threshold for the possible DAC value range using a TelePix2 sensor exposed to 40 MRad.

A.9.2 Power Consumption of the First TelePix2 Irradiation

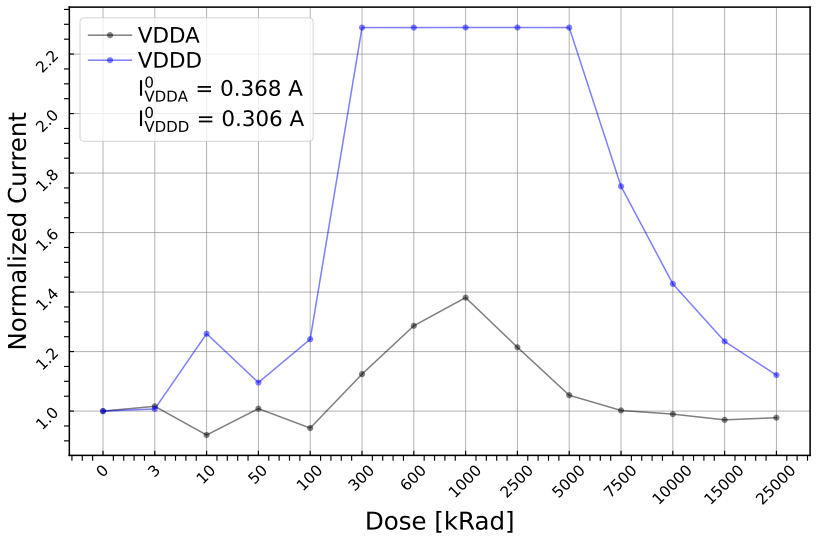


Figure A.12: Normalized current versus dose of the digital (colored in blue) and analog (colored in gray) power domain obtained at the first TID campaign with TelePix2. The normalization to the current measured at 0 kRad is given in the legend. Due to the DUT settings, high currents were drawn, causing the power supply to reach its compliance limit in the digital power domain.

A.9.3 Annealing Measurement of the Threshold Dispersion of the Run2021 Sensor

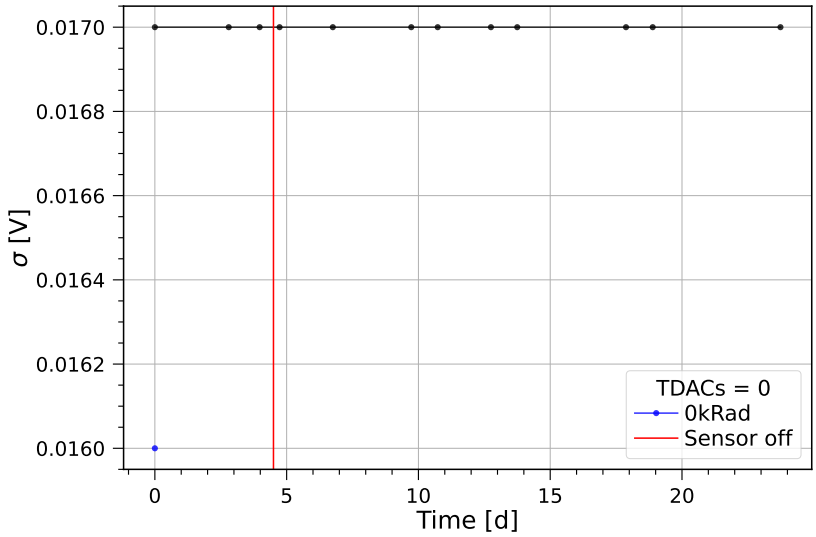


Figure A.13: Threshold dispersion σ versus annealing time conducted by injecting test signals into all pixels. As a reference the threshold dispersion of a non-irradiated Run2021 sensor is included (depicted in blue). No change of the dispersion with annealing time is observed.

A.9.4 Summary of the On-Chip DAC Measurement of the Run2021 Sensor

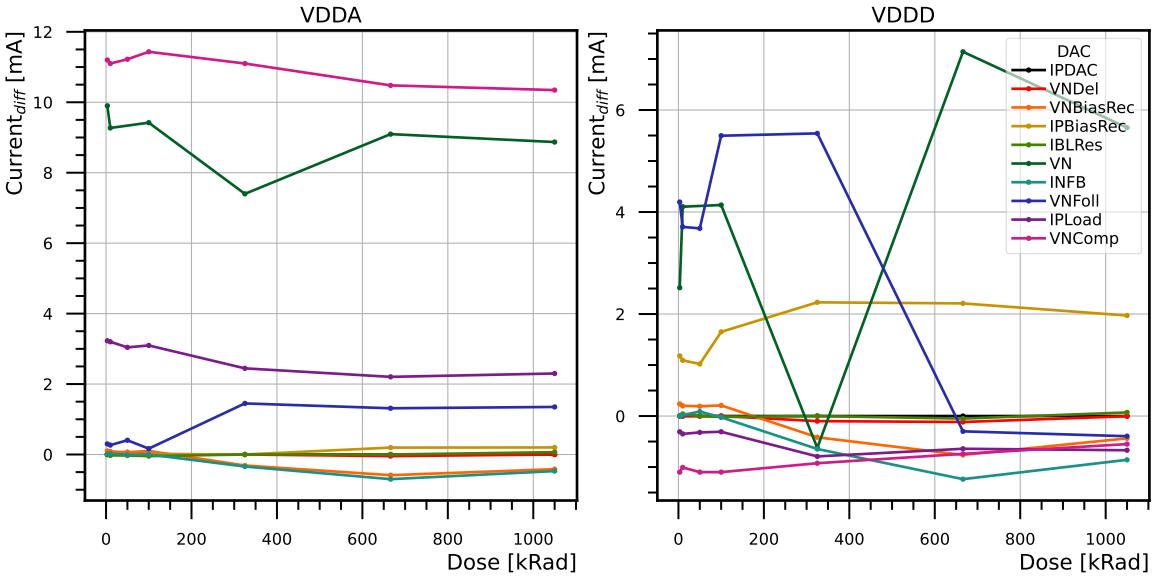


Figure A.14: Change in the current difference for all DACs as a function of the dose. The current difference I_{diff} is defined as the current measured at the nominal DAC setting $I_{nominal}$ minus the current with the DAC turned off I_{off}. No significant dependence of I_{diff} on the dose is observed for most DACs. For *VN* and *VNFoll* a change in the digital power domain is observed. Due to the design of the amplifier, an interplay between both cannot be excluded. In addition, the measurement was only done once and cannot be repeated. Consequently, no statement on the origin of the observed behavior can be made.

A.9.5 Comparison of the Threshold Scans between the Run2021 and TelePix2 Sensors

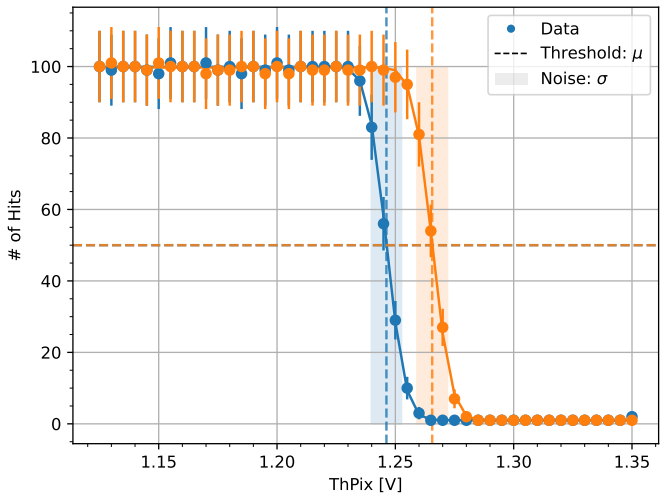


Figure A.15: Threshold scan of two pixels of a non-irradiated Run2021 sensor using analogue injection. The statistical uncertainties are provided.

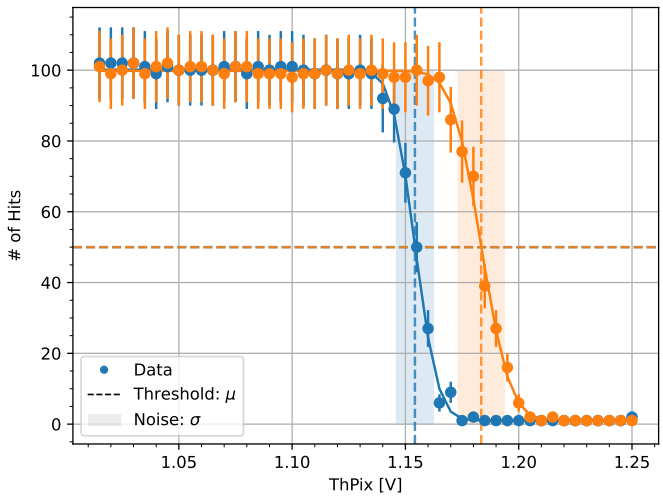


Figure A.16: Threshold scan of two pixels of the Run2021 sensor exposed to 1 MRad using analogue injection. The statistical uncertainties are provided. A change of the mean comparator threshold is observed, while the slope did not change significantly.

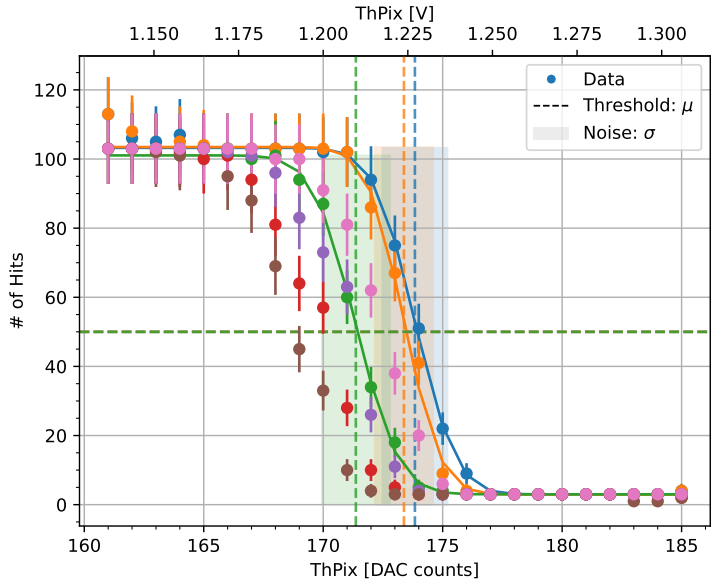


Figure A.17: Threshold scan of the TelePix2 sensor exposed to 1 MRad using analogue injection. Results for different pixels are color coded. The statistical uncertainties are provided. Fits with a low χ^2/DoF are included.

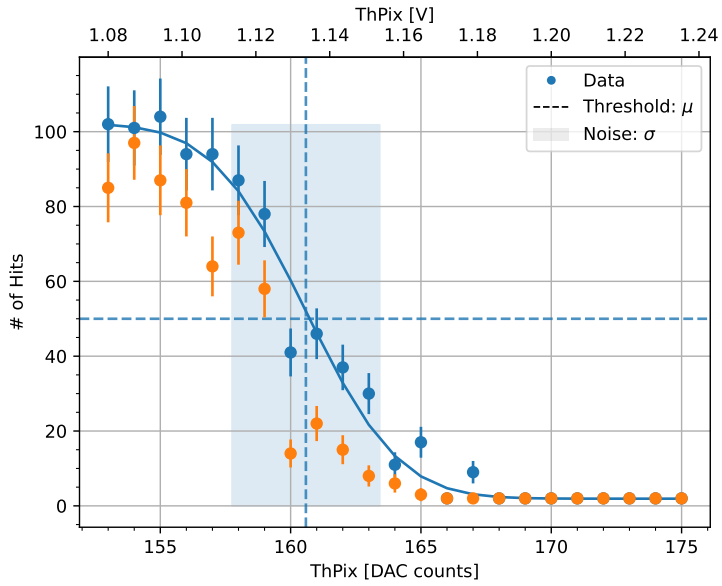


Figure A.18: Threshold scan of the TelePix2 sensor exposed to 40 MRad using analogue injection. Results for different pixels are color coded. The statistical uncertainties are provided. A change of the mean comparator threshold, as well as a softening of the slope, are observed. Fits with a low χ^2/DoF are included.

A.9.6 Investigation of the Amplifier Gain

The measurements presented in chapter 8 and chapter 9 have shown a change of the performance of the TelePix2 sensor exposed to 40 MRad compared to a non-irradiated device. In summary, an earlier breakdown, a lower hit-efficiency, a worse time resolution, a changed range of possible comparator thresholds and altered slope of the z-curves were measured. A first approach to explain the observations was derived. As a hypothesis a change of the amplifier gain is proposed.
If the amplifier gain would be worsened due to TID damage, the reduced hit-efficiency and the change of the comparator threshold range can be explained. To prove this hypothesis, the amplifier gain of TelePix2 was measured. Therefore, the following procedure was performed:

- Threshold (z-curves) scans for different injection strengths were executed for one pixel.
- The turning point μ, corresponding to the effective comparator threshold, was determined and corrected for the baseline.
- The dependence of the corrected threshold for different injection strengths was analyzed.

A comparison between the x-ray (colored in orange) and non-irradiated (colored in blue) devices is presented in fig. A.19. For both, a comparable gain and saturation of the amplifier using a digital injection is obtained. However, the intercept for the x-ray irradiated device is shifted and not at the origin. In addition, the intercept for the non-irradiated device is also not at the origin. But, this initial measurement, conducted for one pixel, indicates a promising first step. More systematic investigations are required. Nevertheless, a clear difference between both devices is observed.

To exclude the digital injection as possible source for the observation, the measurement was repeated for the x-ray irradiated device using analog injection. In fig. A.20 the result is depicted. A comparable gain and intercept are obtained. Comparing the analog injection strength with the digital injection, a slight deviation is observed. In addition, a lower limit of the gain is observed where the gain is not linear, which is expected from the design of the amplifier.

Taking both measurements into account, the amplifier gain is probably not altered by TID damage. A resulting hypothesis is a change of the comparator threshold and/or a damage of the injection circuit. The comparator threshold is excluded by the calibration presented in fig. A.11. To investigate the hit-efficiency in more detail, the response of the devices to Fe-55 was measured. Therefore, the ToT spectra were measured for both sensors the x-ray and non-irradiated. A comparison is presented in fig. A.21. For the measurement the same DAC settings, a bias voltage of $U_{\text{chip}} = -80\,\text{V}$ and a measurement time of 3 min were used.

By the comparison, the change of the comparator threshold is excluded because otherwise, the peak of the ToT spectra would be shifted. In addition, the measurement confirms a reduced signal rate of the x-ray irradiated device. Besides a reduced amount of signal, the

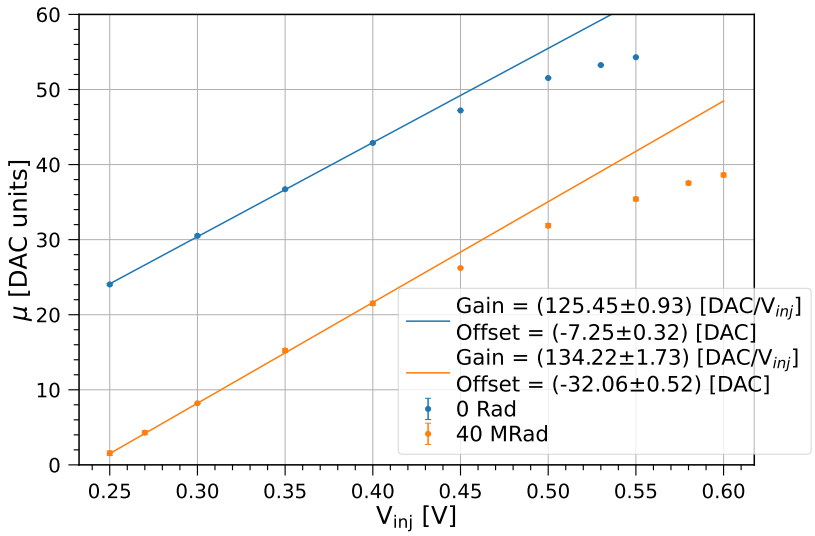


Figure A.19: Baseline corrected threshold μ versus injection strength V_{inj} for a non-irradiated and x-ray irradiated TelePix2 sensor using digital injection. The statistical uncertainties are included.

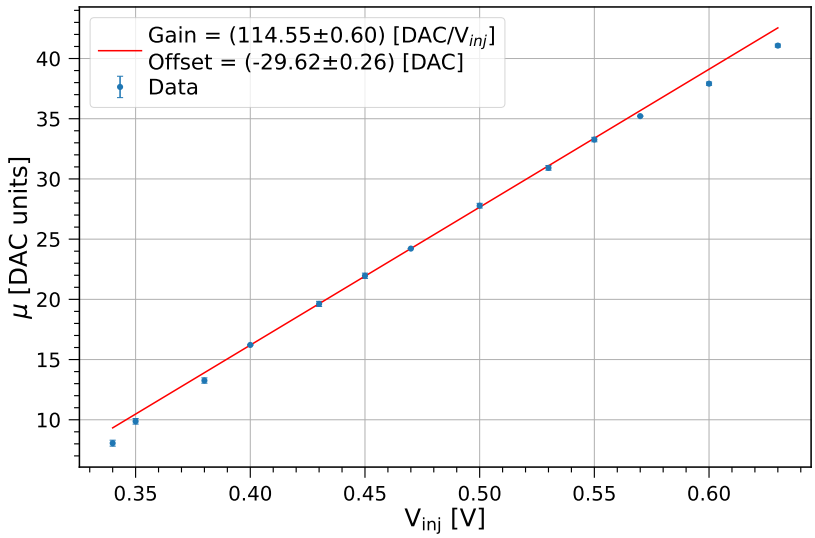


Figure A.20: Baseline corrected threshold μ versus injection strength V_{inj} for a x-ray irradiated TelePix2 sensor using analog injection. The statistical uncertainties are included.

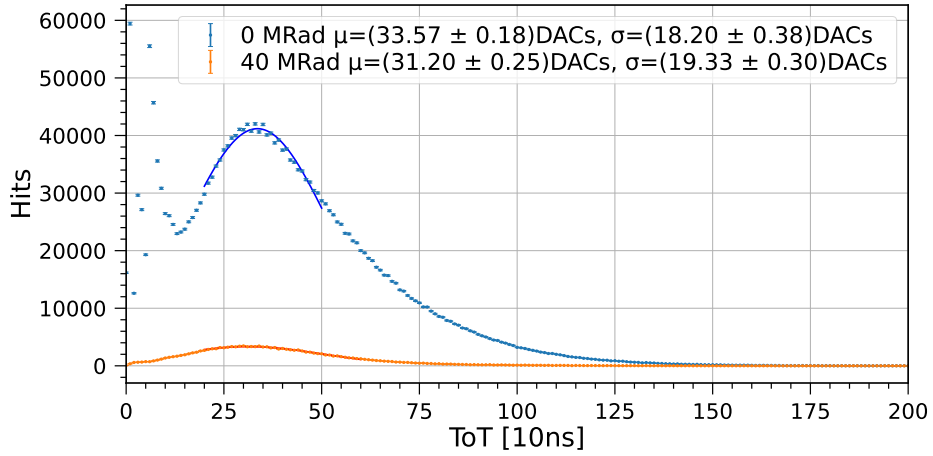
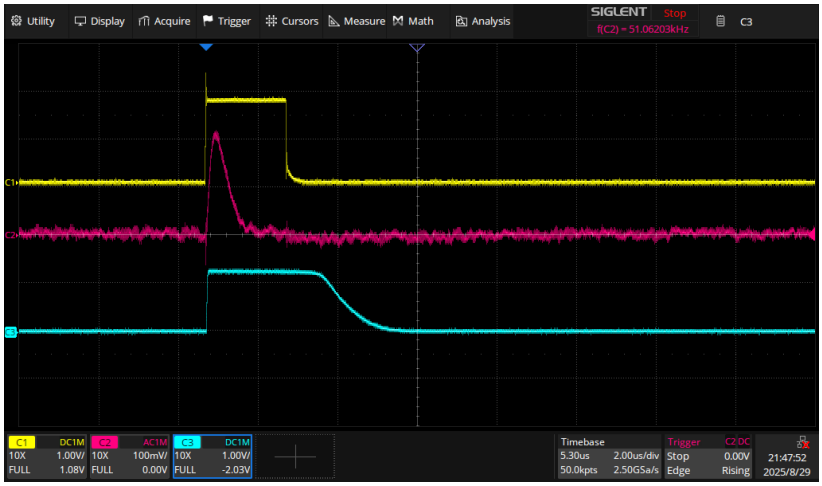


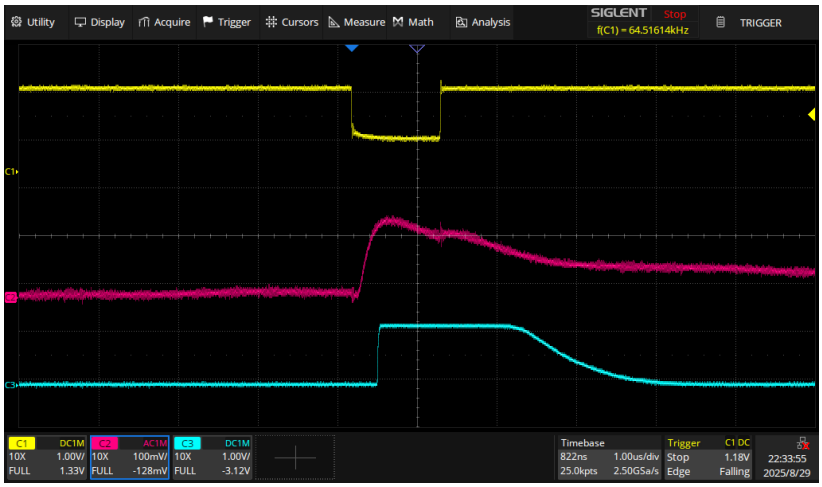
Figure A.21: Comparison of the ToT spectrum recorded using Fe-55. Standard DAC settings, a bias voltage of $U_{\text{chip}} = -80\,\text{V}$ and measurement time of 3 min was used for both DUTs.

noise peak, obtained with the non-irradiated device at low ToT values, is not visible using the x-ray irradiated sensor.
In summary, a similar behavior as for the gain measurement is observed. To investigate the DUTs in more detail, the amplifier output signal was analyzed using an oscilloscope.
No significant difference of the amplifier output shape compared to the non-irradiated sensor is observed using Sr-90 or Fe-55 as a particle source. However, a reduced signal rate was recorded. In a similar manner, the amplifier output was measured using the injection circuit. A significant discrepancy between the non-irradiated and x-ray irradiated device is observed, shown in fig. A.22. The top picture shows the amplifier output and hitbus signal of a non-irradiated DUT using digital injection. In the lower picture analog injection was used for the TID damaged device. A clear change of the amplifier rise and fall becomes apparent.

In summary, a different shape of the amplifier output signal and following ToT signal are observed using the injection circuit, but not when a particle source is used. Furthermore, a reduced amount of signal is obtained regardless of the signal source.
Therefore, the following explanation approach is proposed:
The altered behavior using the injection circuit might be explained due to a damage of it, resulting in a slower discharge of the injection capacitance.
The reduced number of signals might be explained by a damage of the input transistors of the amplifier circuit (shown in fig. 4.4) or a constant current source reducing the signal. To proof the latter, the effective baseline voltage was measured with an oscilloscope. Therefore, the source follower of the amplifier was not biased to suppress its output. The hitbus output was measured with the oscilloscope while decreasing the comparator threshold. At the point where the comparator input and threshold are equal, the hitbus switches from low to high. As the amplifier output is suppressed, the switch occurs when the comparator threshold equates to the effective baseline voltage. Within an uncertainty of 3 to 5 DAC units no significant discrepancy between the devices was measured for all possible configurations of on- and



(a) 0 kRad - digital injection



(b) 40 MRad - analog injection

Figure A.22: Example of an injection signal (colored in yellow), the corresponding *AmpOut* (colored in pink) and *HitBus* (colored in turquoise) output signals for a non-irradiated and x-ray irradiated TelePix2 sensor. Vertical and horizontal scales are depicted in the picture.

off-chip voltages (see chapter 4 for more information about on- and off-chip voltages).
The presented measurements in this sections are only initial investigations. Consequently, further tests are required in order to disentangle the observed behavior.

A.10 Performance Studies of TelePix2 in a Testbeam - Observed Time Shifts

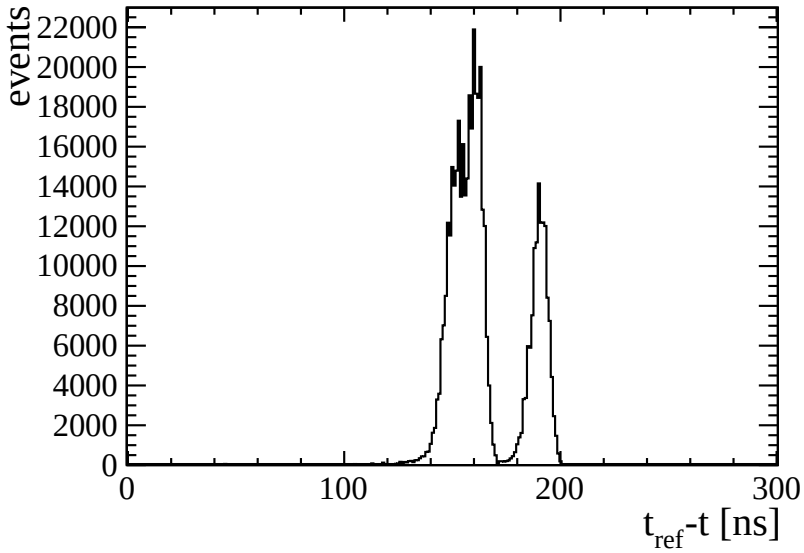


Figure A.23: Time correlation between the TelePix2 DUT and the telescope reference layer measured at the testbeam campaign in December 2024. A jump in the time correlation as well as a shoulder in the main correlation peak was observed. While the time jump can be corrected by applying a strict selection cut, the shoulder cannot without removing valid data.

A.11 Sensor Configuration Settings

DAC name	Standard	Standard*	Optimized
IBLRes	8	8	40
VNCompFine	8	8	8
VP	10	10	30
INFB	10	5	10
VNFoll	3	5	6
VNRegC	0	0	0
VNDel	10	10	10
IPBigFine	0	0	0
IPDAC	0	0	0
VN	0	0	0
INFoll2	0	0	0
INBias	0	0	0
IPLoad	6	6	11
VNComp2	0	0	0
vpvco	5	5	5
vnvco	20	20	20
vpdclmux	32	32	32
vndclmux	32	32	32
vpdeldcl	32	32	32
vndeldcl	32	32	32
vpdelpreemp	32	32	32
vndelpreemp	32	32	32
vpdcl	40	40	40
vndcl	32	32	32
vnlvds	1	1	1
vnlvdsdel	5	5	5
vppump	40	40	40
IPRegCasc	0	0	0
IPSmallFine	0	0	0
VNComp	10	10	10
IPFoll	0	0	0
VNDAC	0	0	0
IPBiasRec	30	30	30
VNBiasRec	30	30	30

Table A.4: Overview of the standard, standard* (testbeam) and optimized DAC settings used for TelePix2 to obtain the presented measurements.

A.12 Glossary

ALICE - **A** **L**arge **I**on **C**ollider **E**xperiment
ASIC - **A**pplication **S**pecific **I**ntegrated **C**ircuit
ATLAS - **A** **T**oroidal **L**HC **A**pparatu**S**
ATLAS ITk - **ATLAS** **I**nner **T**rac**k**er
CERN - **C**onseil **E**uropéen pour la **R**echerche **N**ucléaire - European Council for Nuclear Research
CKM - **C**abibbo-**K**obayashi-**M**askawa Matrix
CMOS - **C**omplementary **M**etal-**O**xide-**S**emiconductor
CMS - **C**ompact **M**uon **S**olenoid
Cocotb - **Co**routine based **Co**simulation **T**est**b**ench
CP - **C**harge-**P**arity
CPV - **C**harge-**P**arity **V**iolation
CRB - **C**onfiguration **R**egister **B**lock
CSA - **C**harge **S**ensitive **A**mplifier
DAC - **D**igital-to-**A**nalog **C**onverter
DAQ - **D**ata **Acq**uisition
DCR - **D**ark **C**ount **R**ate
DDR - **D**ouble **D**ata **R**ate
DESY - **D**eutsches **E**lektron-**Sy**nchrotron
DUT - **D**evice **U**nder **T**est
EB - **E**vent **B**uilder
ECAL - **E**lectromagnetic **CAL**orimeter
ECR - **E**lectron **C**yclotron **R**esonance
ECS - **E**xperimental **C**ontrol **S**ystem
EoC - **E**nd-**o**f-**C**olumn
FE-ASIC - **F**ront-**E**nd **ASIC**
FIB - **F**ocused **I**on **B**eam
FIFO - **F**irst-**I**n-**F**irst-**O**ut Buffer
FPGA - **F**ield **P**rogrammable **G**ate **A**rray
FTDR - **F**ramework **T**echnical **D**esign **R**eport
FWHM - **F**ull **W**idth at **H**alf-**M**aximum
GBL - **G**eneral **B**roken **L**ine
GECCO - **GE**neric **C**onfiguration and **CO**ntrol
GEM - **G**aseous **E**lectron **M**ultiplier
GPIO - **G**eneral **P**urpose **I**nput/**O**utput
GPU - **G**raphics **P**rocessing **U**nit
HCAL - **H**adronic **CAL**orimeter
HDI - **H**igh **D**ensity **I**nterconnect
HEP - **H**igh **E**nergy **P**hysics
HL-LHC - **H**igh-**L**uminosity **L**arge **H**adron **C**ollider

HLT - **H**igh-**L**evel **T**rigger
HV - **H**igh **V**oltage
HV-MAPS - **H**igh-**V**oltage **M**onolithic **A**ctive **P**ixel **S**ensor
IEL - **I**onizing **E**nergy **L**oss
LHC - **L**arge **H**adron **C**ollider
LHCb - **L**arge **H**adron **C**ollider **b**eauty
LS - **L**ong **S**hutdown
MAPS - **M**onolithic **A**ctive **P**ixel **S**ensor
MARS - **M**ighty **A**SIC **R**eadout **S**ystem
MCP-PMTs - **M**icro**C**hannel **P**late **P**hoto**M**ultiplier **T**ube
MIP - **M**inimum **I**onizing **P**article
MOSFET - **M**etal-**O**xide-**S**emiconductor **F**ield-**E**ffective **T**ransistor
MP - **M**ighty-**P**ixel
MPV - **M**ost **P**robable **V**alue
MT - **M**ighty-**T**racker
MWPC - **M**ulti-**W**ire **P**roportional **C**hamber
NIEL - **N**on-**I**onizing **E**nergy **L**oss
NP - **N**ew **P**hysics
PCB - **P**rinted **C**ircuit **B**oard
PID - **P**article **I**dentification **D**etector
PKA - **P**rimary **K**nock on **A**toms
PLL - **P**hase **L**ocked **L**oop
PS - **P**roton **S**ynchrotron
PSB - **P**roton **S**ynchrotron **B**ooster
QA - **Q**uality **A**ssurance
RCU - **R**eadout **C**ontrol **U**nit
R&D - **R**esearch and **D**evelopment
RF - **R**adio-**F**requency
RICH - **R**ing **I**maging **CH**erenkov detector
RTA - **R**eal-**T**ime **A**nalysis
SciFi - **Sci**ntillating **Fi**ber detector
SEU - **S**ingle **E**vent **U**pset
SiPM - **Si**licon **P**hoto-**M**ultiplier
SM - **S**tandard **M**odel
SNR - **S**ignal-to-**N**oise **R**atio
SpaCal - **Spa**ghetti **Cal**orimeter
SPI - **S**erial **P**eripheral **I**nterface
SPS - **S**uper **P**roton **S**ynchrotron
SR - **S**hift **R**egister
SRH - **S**hockley-**R**ead-**H**all model
TDAC - **T**une **DAC**
TDC - **T**ime-to-**D**igital **C**onverter

TID - **T**otal **I**onizing **D**ose
TLU - **T**rigger **L**ogic **U**nit
ToA - **T**ime-**o**f-**A**rrival
TOF - **T**ime-**O**f-**F**light
TORCH - **T**ime **O**f internally **R**eflected **C**herenkov light
ToT - **T**ime-**o**ver-**T**hreshold
TS - **T**ime**S**tamp
UDP - **U**ser **D**atagram **P**rotocol
UP - **U**pstream **P**ixel
UT - **U**pstream **T**racker
VCO - **V**oltage **C**ontrolled **O**scillator
VELO - **VE**rtex **LO**cator

List of Tables

2.1 Summary of the experimental requirements of the Mighty-Pixel and hence MightyPix. Numbers are taken from [66]. 32

4.1 Overview of specifications of HV-MAPS used for measurements within this thesis (ATLASPix3(.1), Run2020, Run2021, TelePix2) compared to the specifications of MightyPix1 and MightyPix2. Specifications include production foundry, dimensions, readout electronics, sensor interfaces and implemented data readout. 93

6.1 Summary of standard voltage settings for a default operation of a non-irradiated TelePix2 sensor using the MARS DAQ system. 123
6.2 Overview of investigated DACs, given in DAC units, used to optimize the TelePix2 time resolution and the power consumption for both configurations. 149

7.1 Summary of the fluence two DUTs have been irradiated to. 156
7.2 Comparison of the time resolution of a non-irradiated and proton irradiated TelePix2 sensor. Details about the DAC configuration are provided in Anhang A.11. 171

8.1 Summary of all x-ray irradiations done within this thesis. 179
8.2 Summary of all settings during the x-ray irradiations performed in this thesis. 179
8.3 Summary of all dose levels the TelePix2 has been irradiated to. 182
8.4 Comparison of the best time resolution obtained for TelePix2 for different radiation damages. The time resolution uncertainty is obtained by the uncertainty of the Gaussian fit. 198
8.5 Comparison of the change of threshold per TDAC step for different VNDACs of a non-irradiated and up to 40 MRad x-ray irradiated TelePix2 sensor. . . 205

9.1 Overview of all DUTs characterized at the testbeam campaign. For each, the bias voltage and the radiation damage is given. All devices are unthinned with $\approx 740\,\mu$m thickness. 214
9.2 Summary of chosen cuts for the Corryvreckan testbeam analysis. 225

9.3 Summary of the time resolution of TelePix2 obtained by all conducted measurements. Details about the DAC configurations (Standard, standard*, best) are provided in Anhang A.11. 235

A.1 Summary of institutes using the MARS DAQ system. If MARS is actively used, it is marked as ”in-use”. If not, it is available and will be used in the future. Institutes listed here without an available system are planning to get MARS. 260
A.2 Summary of configurable on-chip DACs of the digital periphery. For each DAC the name, its location in the sensor and purpose is given. 263
A.3 Summary of configurable on-chip DACs and voltages of the in-pixel electronics. Each DAC is listed with its location and function. 264
A.4 Overview of the standard, standard* (testbeam) and optimized DAC settings used for TelePix2 to obtain the presented measurements. 283